Top Quarks and Diamonds

Author(s):
Bäni, Lukas

Publication Date:
2017

Permanent Link:

https://doi.org/10.3929/ethz-b-000222412 →

Top Quarks and Diamonds

Lukas Bäni

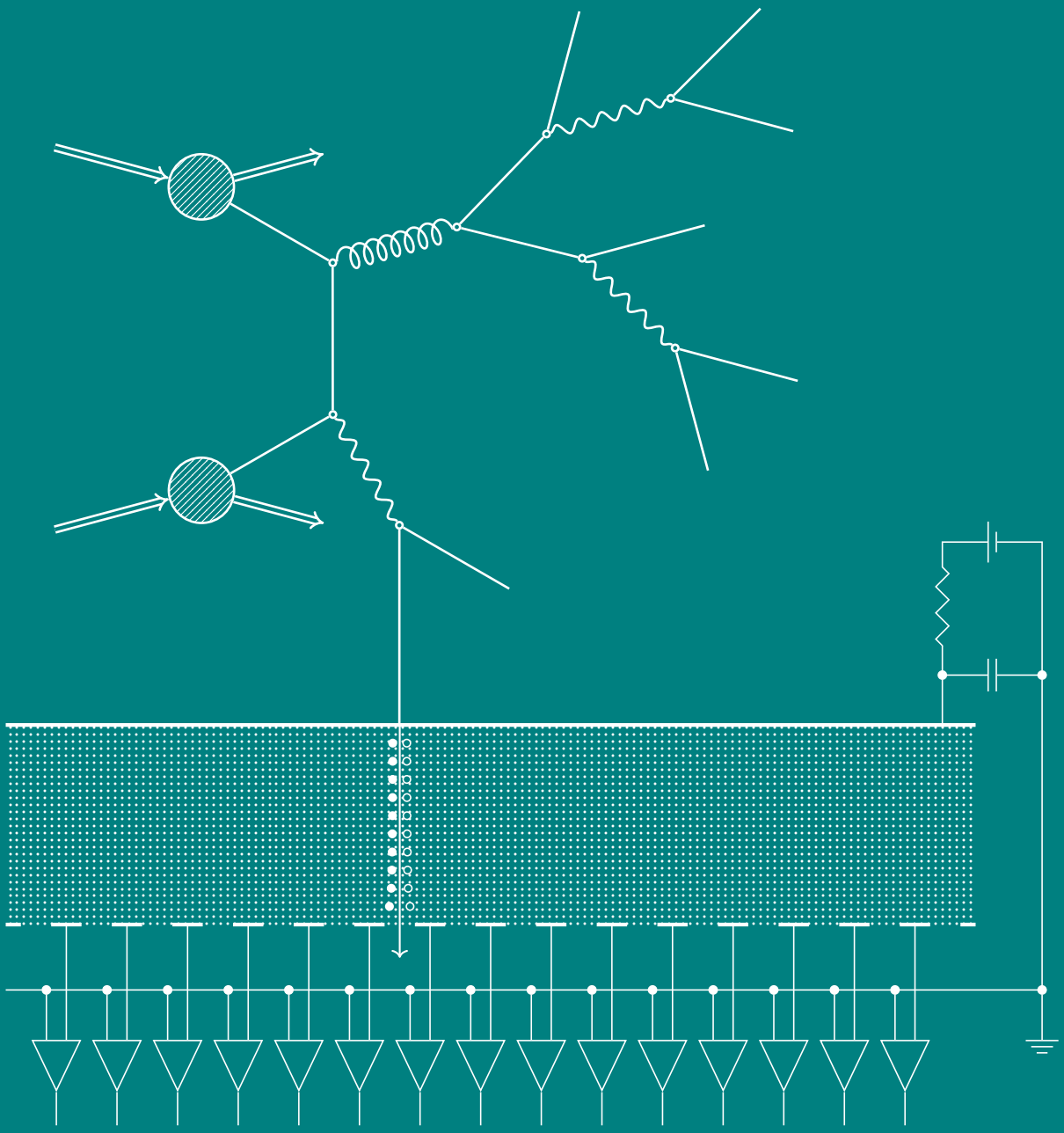

Diss ETH
24 561

DISS. ETH NO. 24 561

Top Quarks and Diamonds

A thesis submitted to attain the degree of

Doctor of Sciences of ETH Zurich
(Dr. sc. ETH Zurich)

presented by

Lukas Bäni

Dipl. Phys. ETH Zurich

born on 12.07.1984

citizen of Basel BS

accepted on the recommendation of

Prof. Dr. Rainer Wallny, examiner
Prof. Dr. Günther Dissertori, co-examiner

2017

ISBN 978-3-906916-05-7
DOI 10.3929/ethz-b-000222412

Abstract

An analysis of proton-proton collision data at a centre-of-mass energy of 8 TeV is presented in this thesis. Data were collected with the Compact Muon Solenoid particle detector in 2012. The Standard Model of Particle Physics is probed by measuring the production cross section of top quark pairs in association with a W boson. To identify this rare process from background contributions, a decay channel with two leptons of same-signed electric charge in the final state is selected. The main background processes, stemming from misidentification of leptons, are estimated using a ratio method. Similarly, the yield of background processes originating from mismeasurements of the lepton's electric charge is estimated. The cross section is measured to be $\sigma_{\mathrm{t\bar{t}W}} = 170\,^{+90}_{-80}\,(\mathrm{stat})\,^{+70}_{-70}\,(\mathrm{syst})\,\mathrm{fb}$ with a significance of 1.6 standard deviations over the background-only hypothesis and found to be in agreement with theoretical predictions.

In the second part of this dissertation, diamond is studied as an alternative to silicon for tracking detectors. The radiation tolerance of diamond strip sensors, manufactured from industrial grown chemical vapour deposition diamond, is characterised. For this purpose, the diamond samples were irradiated with 800 MeV protons, 70 MeV protons, and fast neutrons. Between irradiations, the sensors were tested in a hadron beam with a momentum of 120 GeV/c. The signal response to charged particles, as measured by the observed pulse height, is reconstructed with multiple algorithms. The resulting pulse height as a function of fluence is fitted using a simple model and radiation damage constants of $1.24^{+0.04}_{-0.04}\times10^{-18}\,\mathrm{cm}^2/(\mathrm{p\,\mu m})$, $1.64\,^{+0.25}_{-0.27}\times10^{-18}\,\mathrm{cm}^2/(\mathrm{p\,\mu m})$, and $3.05\,^{+0.27}_{-0.27}\times10^{-18}\,\mathrm{cm}^2/(\mathrm{n\,\mu m})$ are obtained for 800 MeV protons, 70 MeV protons, and fast neutrons, respectively. Furthermore, the fluence dependence of the energy resolution and spatial resolution of the diamond strip detectors are measured.

Zusammenfassung

In dieser Dissertation wird eine Analyse von Proton-Proton-Kollisionen bei einer Schwerpunktsenergie von 8 TeV beschrieben. Die Daten hierfür wurden im Jahr 2012 vom Compact Muon Solenoid Teilchendetektor aufgezeichnet. Durch die Messung des Wirkungsquerschnitts der Produktion von Top-Quark-Paaren in Verbindung mit einem W-Boson, wird das Standardmodell der Teilchenphysik auf seine Richtigkeit im Bezug auf diesen seltenen Prozess geprüft. Um diesen Prozess von Hintergrundprozessen zu unterscheiden, wird ein Zerfallskanal mit zwei Leptonen gleicher elektrischer Ladung im Endzustand gewählt. Der grösste Anteil an Hintergrundereignissen stammt hierbei von fehlerhaft identifizierten Leptonen und wird durch eine Referenzmessung abgeschätzt. Auf ähnliche Weise wird der Hintergrund, verursacht durch Fehlmessung der elektrischen Leptonenladung, abgeschätzt. Ein Wirkungsquerschnitt von $\sigma_{\mathrm{t\bar{t}W}} = 170\,^{+90}_{-80}\,(\mathrm{stat})\,^{+70}_{-70}\,(\mathrm{syst})\,\mathrm{fb}$ mit 1.6 Standardabweichungen über der Hintergrundhypothese wird gemessen und stimmt mit theoretischen Voraussagen überein.

Im zweiten Teil dieser Dissertation wird industriell gefertigter Diamant als Alternative zu Silizium zur Verwendung in Spurdetektoren untersucht. Zu diesem Zweck wird die Strahlenhärte ortsauflösender Streifendetektoren aus Diamant, industriell hergestellt durch chemische Gasphasenabscheidung, charakterisiert. Die Diamanten wurden mit 800 MeV Protonen, 70 MeV Protonen und schnellen Neutronen bestrahlt. Zwischen den Bestrahlungen wurden die Detektoren in einem Hadronenstrahl mit einem Impuls von 120 GeV/c getestet. Aus den gewonnen Daten werden Signale mit mehreren Algorithmen rekonstruiert. Mit den gemessenen Signalen wird mit Hilfe eines einfachen Modells eine Strahlenschadenkonstante von $1.24\,^{+0.04}_{-0.04} \times 10^{-18}\,\mathrm{cm}^2/(\mathrm{p\,\mu m})$ für 800 MeV Protonen, $1.64\,^{+0.25}_{-0.27} \times 10^{-18}\,\mathrm{cm}^2/(\mathrm{p\,\mu m})$ für 70 MeV Protonen und $3.05\,^{+0.27}_{-0.27} \times 10^{-18}\,\mathrm{cm}^2/(\mathrm{n\,\mu m})$ für schnelle Neutronen berechnet. Zudem wird die Energie- und Ortsauflösung der Streifendetektoren in Abhängigkeit der Fluenz gemessen.

Acknowledgements

I wish to express my sincere thanks to Professor Rainer Wallny for giving me the opportunity to work in his research group during these exciting times in high energy physics and for his confidence during these years. I am also thankful to Professor Günther Dissertori for being my co-examiner.

I am very grateful to Professor Harris Kagan for his guidance in becoming an experimental physicist. It was a great pleasure to work with him on beam tests, analysing data and enjoying great barbecues. I am also very thankful for his sincere commitment in reviewing my thesis drafts.

I would like to thank my postdoc Amanda for introducing me to the physics of top quarks. Working with her was always fun. I will keep all the cakes and Yosemite as good memories. Boris is warmly acknowledged for his excellent guidance on a daily basis and his patience. I wish to thank Dmitry for sharing his experience and making the many beam tests a success.

During the beam tests, I was very fortunate to share this time with great colleagues. I am grateful to Joe, Felix, and Matevz for making these tests a fun experience and to Felix for the good times spent working together on the data analysis. Especially, I will keep the diamond related trips with all of you in good memories.

My office mates Marco, Felix, Philipp, Jan, and Gregor are warmly acknowledged. I enjoyed sharing time with them – in the office as well as after work during the many outdoor activities.

While writing this thesis I was lucky to have the support of my colleagues. I am indebted to Felix, Simon, Boris, Dmitry, Gregor, and Harris for proofreading my thesis. The same is true for Marc to whom I am also thankful for his support on the dilepton analysis. I would also like to thank Marco for his help with the detector illustrations.

Last but not least, I am very grateful for the support of my family and friends during this long journey. I am truly thankful to my parents and my brother for encouraging me to follow my ideas and to Anna for always motivating me and keeping my life well balanced.

Contents

Part I

Top Quark Pairs in Association with a W Boson

Chapter 1

Introduction

All currently known particles and the forces mediating their interaction, with the exception of gravity, are described by the Standard Model of Particle Physics (SM). Since its conception in the 1960s, it has been a very successful theory. Today, there are no known experimental deviations from the SM predictions. The latest example is the discovery of the Higgs boson by the ATLAS (A Toroidal LHC ApparatuS) and CMS (Compact Muon Solenoid) collaborations [1, 2] which was necessary to complete the particle content of the SM.

The heaviest known elementary particle, the top quark, was first experimentally observed in 1995 by the CDF (Collider Detector at Fermilab) and DØ (DZero) collaborations [3, 4]. Over the last 20 years the top quark has been studied in great detail. While many of its properties are measured very precisely, such as its mass [5] and the pair production cross section [6, 7], many other attributes have yet to be probed. The production of top quarks in association with a vector boson, W or Z, is one of these. A precise measurement of this cross section would probe SM calculations as well as support searches for new physics with more accurate background estimates. Furthermore, measuring $t\bar{t}Z$ production provides direct information on the coupling of the top quark to the Z boson.

The challenging task in measuring such processes is their small production cross sections. The $t\bar{t}W$ and $t\bar{t}Z$ cross sections are predicted to be 206^{+21}_{-23} fb and 197^{+22}_{-25} fb, respectively, at a centre-of-mass energy of 8 TeV [8]. These cross sections are three orders of magnitude smaller than the $t\bar{t}$ cross section of (241.5 ± 8.5) pb at the same energy [7]. Thus, these events at the Large Hadron Collider (LHC) remain rare and therefore a «simple» measurement of the cross sections of these processes adds new information.

In this dissertation the cross section of the $t\bar{t}W$ process with two leptons of the

same-signed electric charge in the final state is measured. Only electrons and muons are considered which results in a branching fraction of roughly 4 % of this final state. Despite the low branching fraction, this final state benefits from a low level of background from other processes due to the same-sign leptons.

Three sorts of backgrounds are considered. The first and dominant background arises from so-called fake leptons. These leptons do not come directly from the decay of one of the three W bosons of the $t\bar{t}W$ process, but rather from the leptonic decay of a bottom quark or more rarely from particles misidentified as leptons. To estimate this background a «data-driven» method was used. Since the final state requires two same-sign leptons, a second background originates from mismeasurements of the lepton's charge. Processes featuring two opposite-sign leptons have much larger cross sections than the ones from same-signs leptons. Therefore, even a small charge misidentification probability can yield a significant number of background events. Similarly as for the fake lepton background, this background is estimated from data control samples and sidebands. Processes which naturally yield two same-sign leptons in their final state constitute the third background category. Besides multiboson production such processes include the associated production of top quarks with a Higgs boson ($t\bar{t}H$) and $t\bar{t}Z$ production. The latter process is of great interest for this analysis, since the result obtained on the $t\bar{t}W$ process is later combined into one measurement with the $t\bar{t}Z$ process.

In the following chapters the reader is guided through the various steps of this measurement, starting with a brief summary of the underlying theory which is given in chapter 2, followed by a description of the experimental setup at the LHC and the CMS experiment. The data analysis is presented in the subsequent chapters with details on the reconstruction, analysis strategy and the estimation of the backgrounds as well as the description of associated systematic uncertainties. Finally, the results are presented in section 5.4. Concluding remarks and an outlook are given in chapter 6.

Chapter 2

Physics at High Energies

A short introduction into the theoretical principles of particle physics is given in this chapter. It is followed by an overview of the physics involving top quarks and concludes with a section on associated production of vector bosons with top quark pairs.

2.1 The Standard Model

In the field of particle physics, the basic building blocks of nature are studied. The underlying theory is described by the Standard Model of Particle Physics (SM). Elementary particles as well as the forces between them, with the noted exception of gravity, are described. However, the interaction strength of gravity is orders of magnitude lower than the other forces at experimentally probed scales and therefore can be neglected. The most commonly known interaction is electromagnetism. In addition, the *weak* and *strong* forces are present. These three fundamental interactions are formulated as so-called *gauge theories* in the SM.

The basic theory of the SM follows that of references [9–12]. First, the particles of the SM are presented. Matter particles carry half-integer spin and thus are *fermions*. The interactions are mediated by *bosons* which carry integer spin. In the subsequent sections the different interactions are introduced.

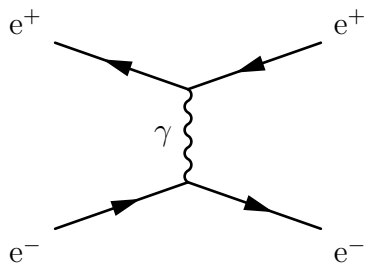

Figure 2.1: Feynman diagram of an electron positron interaction exchanging a photon.

2.1.1 Bosons

In the SM, the forces are realised as exchange of gauge bosons between fermions. A representation of an electron interacting with a positron exchanging a photon is shown in figure 2.1. In electromagnetic interactions, a massless photon is exchanged. The photon itself is chargeless and couples to particles carrying electric charge.

In the case of the weak force, a W or Z boson is exchanged. These were discovered in 1983 experimentally [13–16]. Unlike other gauge bosons, the W and Z bosons are massive. Therefore, the weak force covers only short ranges. A W boson with positive and negative electric charge exists, while the Z boson is neutral. The W boson mediates the charged current interactions between particles carrying weak *isospin*. In neutral current interactions, a Z boson, coupling to particles carrying *hypercharge*, is exchanged. The hypercharge is related to the third component of the isospin, I_3, and the electric charge by

$$Y = 2(Q - I_3). \tag{2.1}$$

Electromagnetic and weak interactions are unified in the electroweak theory.

The quantum number associated with the strong force is colour charge. Gluons are exchanged in interactions of the strong force. They couple to particles carrying colour charge. Since gluons carry colour charge, they interact among themselves. Like the photon, gluons are assumed massless in the SM.

As described in the subsequent sections, these gauge bosons are the field quanta of the gauge fields. Their properties are summarised in table 2.1.

The scalar Higgs boson is the field quantum of the Higgs field. As described later in section 2.1.4, it provides the massive gauge bosons and fermions with mass.

Photon	W boson	Z boson	Gluon
0 γ 1	± 1 $W^{\pm}$ 1	0 Z 1	0 g 1
$<10^{-18}$ eV	80.385 GeV	91.187 6 GeV	0 eV*

* theoretical value

Table 2.1: Properties of gauge bosons [17]. Each boson's charge and spin are quoted to its left and right, respectively. Below each particle, its mass is stated. The photon is predicted massless in the SM. The experimental limit is set by analysing properties of the solar wind in Pluto's orbit [18].

	up	charm	top
	2/3 u 1/2	2/3 c 1/2	2/3 t 1/2
	2.3 MeV	1.275 GeV	173.21 GeV
Quarks	down	strange	bottom
	$-1/3$ d 1/2	$-1/3$ s 1/2	$-1/3$ b 1/2
	4.8 MeV	95 MeV	4.18 GeV
	electron neutrino	muon neutrino	tau neutrino
	0 ν_e 1/2	0 ν_μ 1/2	0 ν_τ 1/2
	<2 eV	<2 eV	<2 eV
Leptons	electron	muon	tau
	-1 e 1/2	-1 μ 1/2	-1 τ 1/2
	511 keV	105.7 MeV	1.777 GeV

Table 2.2: Fermions' properties [17]. The charge and spin of each particle are quoted to its left and right, respectively. Below each particle, its mass is stated.

2.1.2 Fermions

Fermions are split into two families: *quarks* and *leptons*. Both are organised in three generations. The generations have similar properties but increasing mass. Only particles of the first generation are stable and thus matter is formed of particles from this generation. Table 2.2 provides an overview of the fermions' properties. For each particle listed exists a corresponding antiparticle with opposite quantum numbers.

Leptons

The three generations of leptons (ℓ^-, ν) are listed in table 2.2. Their corresponding antiparticles are denoted as ℓ^+ and $\overline{\nu}$, respectively. To each generation a quantum number is assigned: the so-called lepton flavour. It is postulated to be conserved. Furthermore, the leptons have two chirality modes. They are either *left-* or *right-handed*.

Leptons interact electromagnetically and undergo weak interactions depending on their electric and weak charges. The charged leptons interact electromagnetically. Only left-handed leptons carry isospin and thus interact with W bosons. Right-handed neutrinos have not been observed. Consequently, if right-handed neutrinos would exist, they would only interact via gravity or other yet unknown forces.

The observation of neutrino oscillations gives evidence that neutrinos are massive [19–22]. Currently a limit on the neutrino mass of $m_\nu < 2\,\mathrm{eV}$ [17] is set. How the three mass eigenstates relate to each other is known as the neutrino mass hierarchy problem, which represents an active field of research.

Quarks

The six quarks come in three doublets: (u, d), (c, s), and (t, b). The first quark of each doublet carries isospin $I_3 = \frac{1}{2}$ and has electric charge $\frac{2}{3}$. The latter ones carry $I_3 = -\frac{1}{2}$ and have electric charge $-\frac{1}{3}$. Unlike leptons, quarks carry an additional quantum number, so-called colour charge, which is labelled *red*, *blue*, or *green*. The antiquarks carry the corresponding anticolour. As a consequence, quarks are affected by three SM forces. As for the leptons, two chirality states exist, of which only the left-handed quarks carry isospin.

Quarks' weak eigenstates differ from their mass eigenstates. The Cabibbo-Kobayashi-Maskawa (CKM) matrix [23, 24]

$$V = \begin{pmatrix} V_{\mathrm{ud}} & V_{\mathrm{us}} & V_{\mathrm{ub}} \\ V_{\mathrm{cd}} & V_{\mathrm{cs}} & V_{\mathrm{cb}} \\ V_{\mathrm{td}} & V_{\mathrm{ts}} & V_{\mathrm{tb}} \end{pmatrix} \tag{2.2}$$

mixes mass states into weak states and describes the strength of flavour changing charged weak couplings.

Quarks are only observed in bound states. Either a quark antiquark pair forms a so-called *meson* or three quarks build a *baryon*. In both cases quarks are selected such that a colour neutral state results. More precisely these are colour singlet

states. For example the pion π^+ consists of one up quark and one down antiquark: $\mathrm{u}\overline{\mathrm{d}}$. Its colour wave function can be written as [25]

$$\left|\pi^+\right\rangle = \frac{1}{\sqrt{6}} \sum_{ij=1}^{3} \delta_{ij} \left(\left|\mathrm{u}_i \uparrow\right\rangle \left|\overline{\mathrm{d}}_j \downarrow\right\rangle + \left|\mathrm{u}_i \downarrow\right\rangle \left|\overline{\mathrm{d}}_j \uparrow\right\rangle \right) \tag{2.3}$$

where $\uparrow$ and $\downarrow$ indicate the spin direction and the indices i and j denote the colour charge. Like other mesons, this is a superposition of colour anticolour states. Baryons are described by superpositions of different arrangements of the three colours between the constituent quarks, resulting in a colour neutral state. Made of three up quarks: uuu, the Δ^{++} baryon's colour wave function for example is described by the superposition [25]

$$\left|\Delta^{++}; +3/2\right\rangle = \frac{1}{\sqrt{6}} \sum_{ijk=1}^{3} \varepsilon_{ijk} \left|\mathrm{u}_i \uparrow\right\rangle \left|\mathrm{u}_j \uparrow\right\rangle \left|\mathrm{u}_k \uparrow\right\rangle \tag{2.4}$$

where ε_{ijk} is the completely antisymmetric tensor.

2.1.3 Interactions

The SM is formulated in the framework of Quantum Field Theory (QFT). As in other theories, symmetries are a fundamental concept in the SM. The presence of a symmetry implies a conservation law, as Noether's theorem indicates [26]. In the SM, the Lagrangian describing the interactions is required to be invariant under local gauge symmetries. Hereby, a *local* gauge transformation may depend on spacetime, unlike a global gauge transformation. The symmetry group of the SM is

$$SU(3)_C \otimes SU(2)_L \otimes U(1)_Y \tag{2.5}$$

where $SU(3)_C$ is associated with the strong interaction and $SU(2)_L \otimes U(1)_Y$ with the electroweak interaction. Within this framework, the previously introduced leptons are fields, which interact by exchanging field quanta, the gauge bosons.

Strong Interaction

Quantum Chromodynamics (QCD) describes the theory of strong interaction, following a perturbative approach which assumes the interaction strength to be small. Its symmetry group is $SU(3)_C$. As introduced in section 2.1.2, the colour quantum number is the charge of the strong interaction. Gluons, the gauge bosons

which mediate the strong force, carry colour charge as well, a colour and an anticolour each. Thus, they come as an octet and interact among themselves.

The Lagrangian, describing the strong interaction of the quark fields q, needs to be locally gauge invariant under $SU(3)_C$ transformations. It is written as

$$\mathcal{L}_{\mathrm{QCD}} = \overline{q}\left(\mathrm{i}\gamma^{\mu}\partial_{\mu} - g_{\mathrm{s}}\gamma^{\mu}T_a G_{\mu}^{a}\right) q - \frac{1}{4} G_{\mu\nu}^{a} G_{a}^{\mu\nu} \tag{2.6}$$

where g_{s} is the strong coupling constant, T_a are the generators of the $SU(3)_C$ group, G_{μ}^{a} describe the eight gluon fields with $a = 1, \ldots, 8$, and the field strength tensor is

$$G_{\mu\nu}^{a} = \partial_{\mu} G_{\nu}^{a} - \partial_{\nu} G_{\mu}^{a} - g_{\mathrm{s}} f_{abc} G_{\mu}^{b} G_{\nu}^{c}. \tag{2.7}$$

The first part in equation (2.6) includes the kinematic and interaction terms. The term in the second part ensures gauge invariance under $SU(3)_C$.

In the following the strong coupling constant is defined as

$$\alpha_{\mathrm{s}} = \frac{g_{\mathrm{s}}^2}{4\pi}. \tag{2.8}$$

It depends on the scale of the interaction. For high momentum transfer Q or at short distances the coupling constant decreases. In this limit, quarks and gluons may be considered as free particles. This effect is named *asymptotic freedom* [27, 28].

Further, at larger distances or for small momentum transfers the strong force increases and is no longer described by perturbation theory. Thus, quarks are not observed as free particles. This is known as *confinement*.

The probability of a certain hard interaction is described by a so-called matrix element. With a perturbation series, the matrix element can be calculated. Feynman diagrams with the fewest number of interaction vertices are the leading order (LO) diagrams of a process. The LO approximation includes contributions at $\mathcal{O}\left(\alpha_{\mathrm{s}}^{n}\right)$ where n depends on the process, while the next to leading order (NLO) approximation includes the next simplest diagrams which contribute at $\mathcal{O}\left(\alpha_{\mathrm{s}}^{n+1}\right)$.

Electroweak Interaction

The electromagnetic and weak interactions are unified by the Glashow-Salam-Weinberg (GSW) theory [29–32]. In this theory, the symmetry group

$$SU(2)_L \otimes U(1)_Y \tag{2.9}$$

describes the interactions. The group $SU(2)_L$ is associated with the weak isospin I which only left-handed fermions carry, while the hypercharge Y corresponds to the group $U(1)_Y$.

The triplet of fields (W_1, W_2, W_3) fulfils the gauge invariance of $SU(2)_L$ and the field B meets the gauge invariance of $U(1)_Y$. The fields W_i couple to the weak isospin with the coupling constant g, while the field B couples to the hypercharge with the coupling constant g'. With these, the fields of the physical W^+ and W^- bosons, which mediate the charged weak interactions, can be written as linear combinations of W_1 and W_2:

$$\mathrm{W}^{\pm} = \frac{1}{\sqrt{2}} \left(W_1 \pm \mathrm{i} W_2 \right). \tag{2.10}$$

Whereas, the photon and the Z boson, mediating the electromagnetic and neutral weak interactions, are linear combinations of W_3 and B

$$\begin{pmatrix} \mathrm{Z}^0 \\ \gamma \end{pmatrix} = \begin{pmatrix} \cos\theta_W & -\sin\theta_W \\ \sin\theta_W & \cos\theta_W \end{pmatrix} \begin{pmatrix} W_3 \\ B \end{pmatrix} \tag{2.11}$$

where θ_W denotes the weak mixing angle. This mixing angle relates the coupling constants g and g' with the electric charge as

$$g \sin\theta_W = g' \cos\theta_W = q_\mathrm{e} = \sqrt{4\pi\alpha} \tag{2.12}$$

where $\alpha \approx \frac{1}{137}$ is the fine-structure constant.

2.1.4 Higgs Mechanism

An important aspect of the SM is its renormalisability. This prevents the theory from divergences in the calculation of certain processes. As a consequence of the gauge invariance, the gauge bosons are massless, which stands in contrast to what is observed. The Higgs mechanism [33–35] spontaneously breaks the local gauge symmetry. Thereby, it theoretically generates the masses without destroying the renormalisability and gauge invariance.

A potential

$$V(\Phi) = -\mu^2 \Phi^\dagger \Phi + \frac{1}{4} \lambda \left(\Phi^\dagger \Phi \right)^2 \tag{2.13}$$

is introduced for a scalar complex field

$$\Phi = \begin{pmatrix} \phi^+ \\ \phi^0 \end{pmatrix} = \frac{1}{\sqrt{2}} \begin{pmatrix} \phi_1 + \mathrm{i}\phi_2 \\ \phi_3 + \mathrm{i}\phi_4 \end{pmatrix}. \tag{2.14}$$

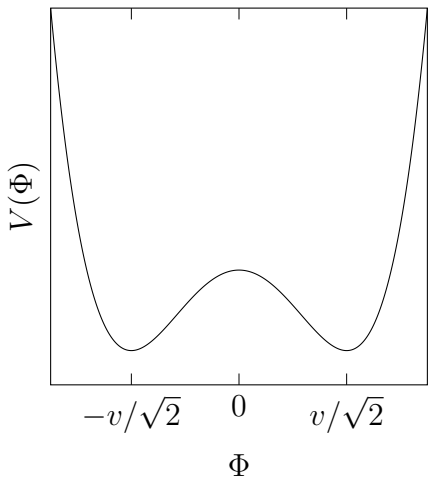

Figure 2.2: Higgs potential $V(\Phi)$.

In the classical case, in which $\mu^2 < 0$, the minimum energy state is $\langle 0|\Phi|0\rangle = 0$ which leaves the symmetry unbroken. On the contrary, the potential in one dimension for $\mu^2 > 0$ is illustrated in figure 2.2. In the minimum energy states the field is

$$\langle 0|\Phi|0\rangle = \frac{1}{\sqrt{2}}\begin{pmatrix}0\\v\end{pmatrix} \tag{2.15}$$

where

$$v = \frac{2\mu}{\sqrt{\lambda}} \tag{2.16}$$

is denoted the vacuum expectation value. This degenerate vacuum state *spontaneously breaks* the symmetry but stays invariant under transformations of $U(1)$ and the third component of $SU(2)$. By adding a field H one can parameterise oscillations around the vacuum state as

$$\Phi = \frac{1}{\sqrt{2}}\begin{pmatrix}0\\v+H\end{pmatrix}. \tag{2.17}$$

With this, the electroweak Lagrangian can be written as

$$\begin{aligned}\mathcal{L} = &\frac{1}{2}\partial_\mu H \partial^\mu H - \mu^2 H^2 \\ &- \sum_{i=1}^{3}\frac{1}{4}\left(\partial_\mu W_{i\nu} - \partial_\nu W_{i\mu}\right)\left(\partial^\mu W_i^\nu - \partial^\nu W_i^\mu\right) \\ &+ \frac{1}{8}g^2v^2 W_{1\mu}W_1^\mu + \frac{1}{8}g^2v^2 W_{2\mu}W_2^\mu \\ &- \frac{1}{4}G_{\mu\nu}G^{\mu\nu} + \frac{1}{8}v^2\left(gW_{3\mu} - g'B_\mu\right)\left(gW_3^\mu - g'B^\mu\right)\end{aligned} \tag{2.18}$$

where $G_{\mu\nu} = \partial_\mu B_\nu - \partial_\nu B_\mu$. Since the B field is coupled to the unbroken symmetry, the photon stays massless. The fields W_1 and W_2 acquire a mass term in the Lagrangian and the associated W boson becomes massive:

$$m_{\mathrm{W}} = \frac{1}{2} g v. \tag{2.19}$$

The mass of the Z boson is

$$m_{\mathrm{Z}} = \frac{1}{2} v \sqrt{g^2 + g'^2} = \frac{m_{\mathrm{W}}}{\cos\theta_W} \tag{2.20}$$

and is related to the mass of the W boson via the weak mixing angle. Finally, the mass of the scalar *Higgs* boson

$$m_{\mathrm{H}} = \sqrt{2}\mu \tag{2.21}$$

is indicated by the mass term in the first line of equation (2.18). Recently, the Higgs boson was discovered experimentally with a mass of 125 GeV [1, 2].

The Higgs mechanism provides not only the vector bosons with masses, it generates masses for the fermions as well. A fermion's mass

$$m_{\mathrm{f}} = g_{\mathrm{f}} v \tag{2.22}$$

is introduced by its Yukawa coupling to the Higgs field. For all quarks, except the top quark, this coupling is small $g_{\mathrm{f}} \ll 1$. This renders top quark physics an interesting topic to study.

2.2 Proton-Proton Collisions

Since hadrons are not point-like particles, like leptons, collisions in a hadron collider are more complicated compared to collisions at an electron-positron collider. Besides the two up and one down quarks, which represent the valence quarks, the proton consists of sea quarks and gluons. These constituents, or so-called partons, carry the fraction x of the proton's momentum. Parton density functions (PDFs) describe the probability densities for finding certain partons with proton momentum fraction x. In figure 2.3 PDFs derived by the MSTW 2008 group are illustrated at different scales Q^2.

Figure 2.4 illustrates a simplified proton-proton collision. The hard scattering vertex of the partons is indicated by the large red dot. Products of the hard interaction split into quarks or radiate gluons. This process, shown in red, is

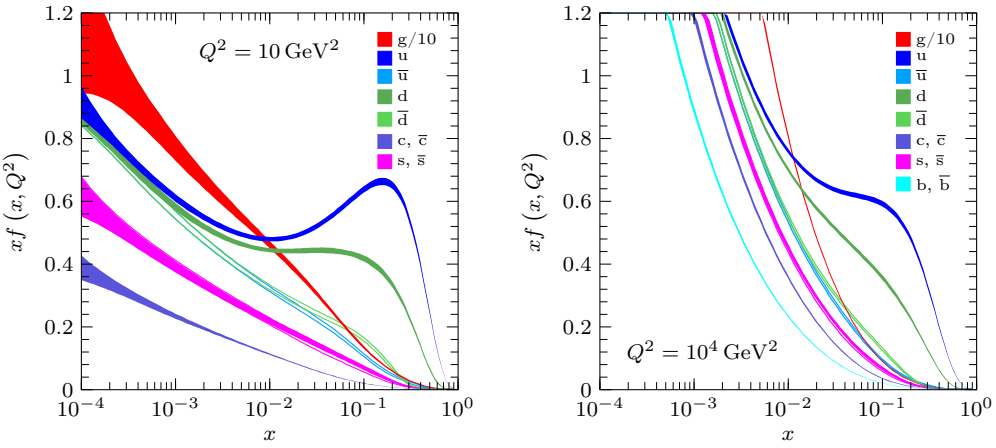

Figure 2.3: MSTW 2008 NLO PDFs (68 % confidence level) at $Q^2 = 10\,\mathrm{GeV}^2$ and $Q^2 = 10^4\,\mathrm{GeV}^2$, derived from reference [36].

known as *parton showering*. After this stage, the strong coupling constant is rather large resulting in quarks and gluons forming colour neutral hadrons due to confinement. This so-called *hadronisation* process is shown in green. Partons can radiate gluons or split into quarks before the actual collision, which is referred to as initial state radiation (ISR), resulting in the hadrons illustrated in green below the hard interaction. Similarly, after the hard interaction this process is called final state radiation (FSR). Apart from ISR, scattering processes of other partons can occur, like multi-parton scattering, shown in purple. This so-called underlying event (UE) is illustrated in the underpart of figure 2.4 below the hard interaction. Along all stages photons can be radiated, depicted in orange.

2.3 Top Quark Physics

By far the heaviest of all known particles is the top quark with a mass of $(173.34 \pm 0.76)\,\mathrm{GeV}$ [5]. It was first observed in 1995 by the CDF and DØ collaborations [3, 4] and completed the third quark generation. Some very interesting possibilities arise from its properties. Due to its large mass, the top quark has a very short lifetime of the order of $10^{-25}\,\mathrm{s}$ [17]. As a consequence, it decays before it can hadronise. This allows the study of properties of the bare top quark, such as the spin. The following brief overview about top quarks' production, decay, and its characteristics follows the description in references [38–40].

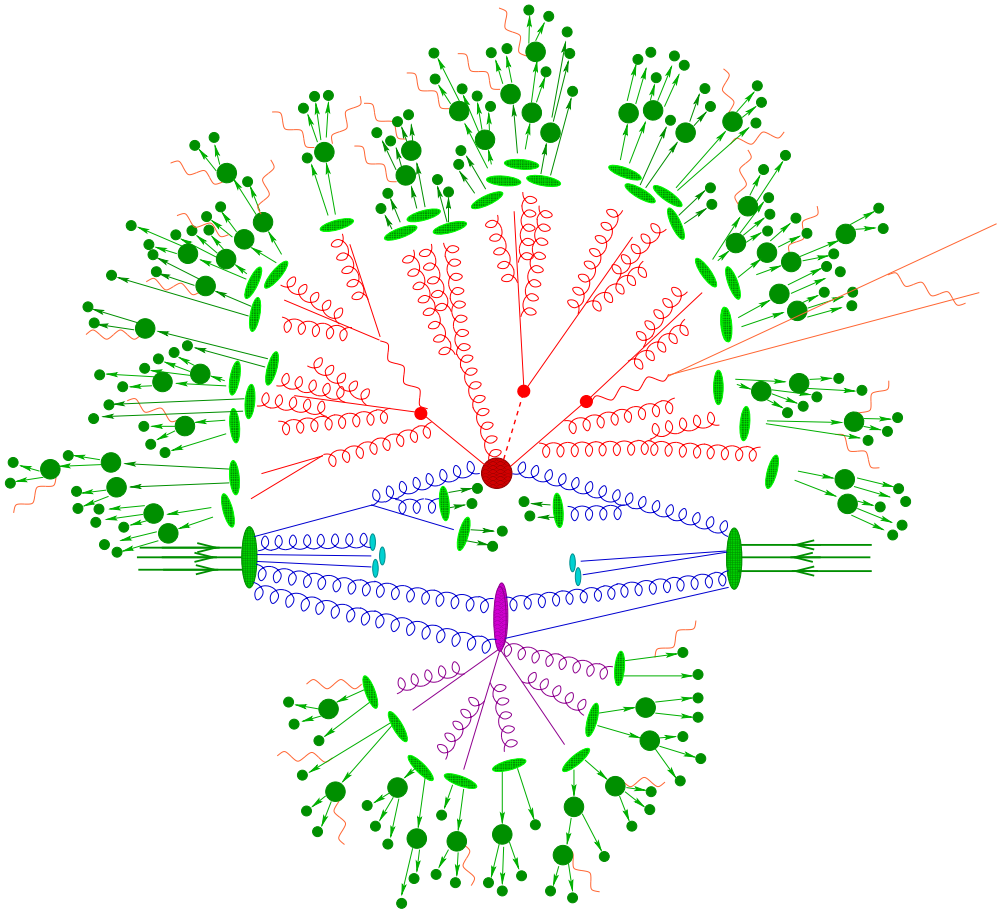

Figure 2.4: Illustration of a proton-proton collision [37]. Incoming partons are marked in blue. The large red dot indicates the hard interaction vertex with resulting parton shower in red. Hadronisation is shown in green and radiated photons in orange. The underpart of the figure shows the underlying event.

2.3.1 Production

In hadron collisions, top quarks are produced through strong or weak interactions. The former and dominant process yields a top quark pair, while the latter results in a single top quark.

Top Quark Pair Production

Pairs of top quark are produced through gluon-gluon fusion or a quark antiquark annihilation at hadron colliders. These strong interactions are described by QCD. With the factorisation theorem, the theoretical cross section can be expressed as [38]

$$\sigma_{\mathrm{pp}\to\mathrm{t\bar{t}}} = \sum_{i,j=\mathrm{q},\bar{\mathrm{q}},\mathrm{g}} \int \mathrm{d}x_i \, \mathrm{d}x_j \, f_i\left(x_i, \mu_f^2\right) f_j\left(x_j, \mu_f^2\right) \times \hat{\sigma}_{ij\to\mathrm{t\bar{t}}}(\hat{s}, m_\mathrm{t}, \mu_f, \mu_r, \alpha_\mathrm{s}) \quad (2.23)$$

where $f_k\left(x_k, \mu_f^2\right)$ are the protons' PDFs and $\hat{\sigma}$ denotes a partonic cross section. The variables x_k are the fractions of the proton momenta, carried by parton k, μ_f and μ_r are the factorisation and renormalisation scales, respectively, m_t is the top quark mass, and α_s is the strong coupling constant. The squared partonic centre-of-mass energy $\hat{s}$ can be written as a fraction of the squared centre-of-mass energy of the proton-proton interaction, s, by $\hat{s} = x_i x_j s$.

To produce a pair of top quarks a centre-of-mass energy of $\hat{s} > 4m_\mathrm{t}^2$ is necessary. Taking the simplification of $x_1 = x_2 = x$, a minimum parton's momentum fraction of $x > 2m_\mathrm{t}/\sqrt{s}$ is required. Thus, at the LHC small values of x are sufficient. At $\sqrt{s} = 8\,\mathrm{TeV}$, the parton's momentum fraction is required to be $x > 0.04$. In this range of small x, the gluon density is high compared to the density of quarks, see figure 2.3. Therefore and due to the absence of antiquarks among the protons' valence quarks, gluon-gluon fusion is the dominating $\mathrm{t\bar{t}}$ production process. Gluon-gluon fusion accounts for approximately 90 % at a centre-of-mass energy of 14 TeV [39]. The remaining 10 % is mostly from quark antiquark scattering. The corresponding LO Feynman diagrams are shown in figure 2.5.

Single Top Quark Production

Single top quarks are produced in weak interactions in three different channels:

- In the t-channel, a virtual W boson scatters off a bottom quark. The bottom quark is either from flavour excitation or produced via gluon splitting $\mathrm{g} \to \mathrm{b\bar{b}}$.

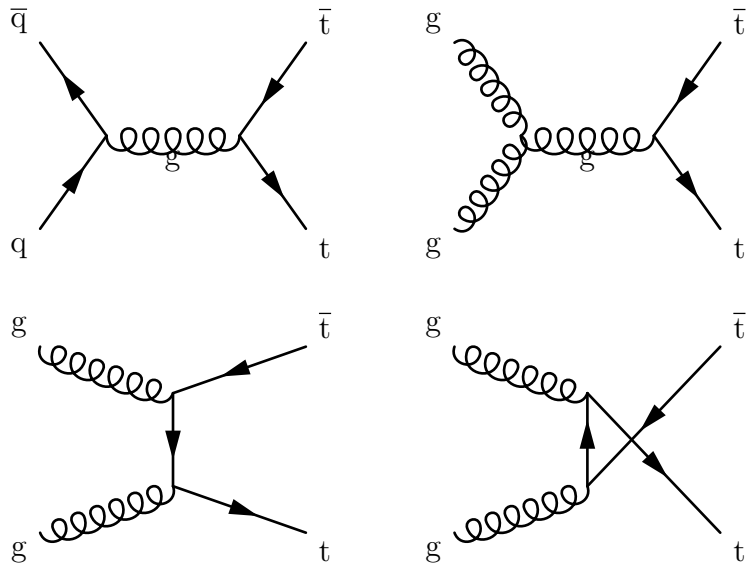

Figure 2.5: Leading order Feynman diagrams for $t\bar{t}$ production in proton-proton collisions via quark antiquark annihilation (first diagram) and gluon fusion (diagrams 2 to 4).

In the former process, the bottom quark is scattered off the initial state by a light quark or gluon. At the LHC, the processes $ub \to dt$ and $d\bar{b} \to u\bar{t}$ indicate the dominant contributions to this channel [39].

- In the *s*-channel, the top quark is produced via a time-like W boson from quark antiquark annihilation. The quark pair is an isospin doublet.
- The third channel is the associated tW production. In this channel, the top quark is produced along with a real W boson.

The Feynman diagrams corresponding to these processes are pictured in figure 2.6.

2.3.2 Top Quark Decays

At lowest order, three two-particle decays of the top quark are possible in the SM: $t \to dW$, $t \to sW$, and $t \to bW$. Their rates are proportional to the square of the corresponding CKM matrix elements, V_{td}, V_{ts}, and V_{tb}. Since $|V_{tb}| \gg |V_{td}|$ and $|V_{tb}| \gg |V_{ts}|$, the top quark decays almost exclusively via the process $t \to bW^+$ and $\bar{t} \to \bar{b}W^-$ in case of its antiparticle. Its lifetime is inversely proportional to

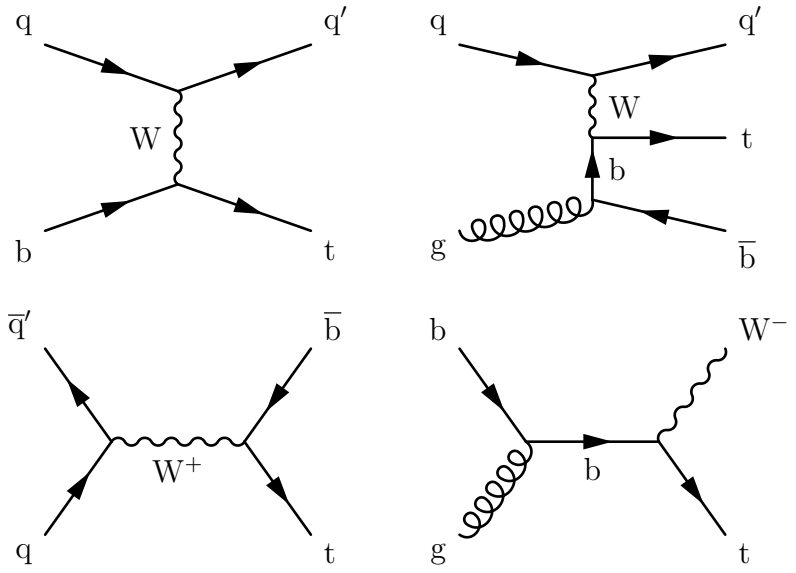

Figure 2.6: Leading order Feynman diagrams for single top quark production. The diagrams in the upper row represent the t-channel. In the bottom row, the s-channel (left) and associated tW production (right) diagrams are shown.

its decay width which is given in NLO QCD by [41]

$$\Gamma_{\mathrm{t}} = \frac{G_{\mathrm{F}} m_{\mathrm{t}}^3}{8\pi\sqrt{2}} |V_{\mathrm{tb}}|^2 \left(1 - \frac{m_{\mathrm{W}}^2}{m_{\mathrm{t}}^2}\right)^2 \left(1 + 2\frac{m_{\mathrm{W}}^2}{m_{\mathrm{t}}^2}\right) \left[1 - \frac{2\alpha_{\mathrm{s}}}{3\pi}\left(\frac{2\pi^2}{3} - \frac{5}{2}\right)\right] \tag{2.24}$$

where G_{F} is the Fermi coupling constant. As $|V_{\mathrm{tb}}| \approx 1$, the Fermi coupling constant $G_{\mathrm{F}} \approx 1.17 \times 10^{-5}/\mathrm{GeV}^2$ [17] and the top quark mass $m_{\mathrm{t}} \approx 173\,\mathrm{GeV}$ [5] are the driving values in equation (2.24) and resulting in a very short lifetime of about $5 \times 10^{-25}\,\mathrm{s}$. As a consequence the top quark does not hadronise and no bound states of toponium ($\mathrm{t\bar{t}}$) exist. These characteristics are interesting from an experimental point of view as well, since the top quark's decay products have a nicely reconstructable signature. To observe this signature requires identification of the bottom quark. It is identified via its relatively long lifetime, as described later in section 4.5.3. If the W boson decays into a lepton and neutrino, the W boson leaves a typical signature in the detector as well.

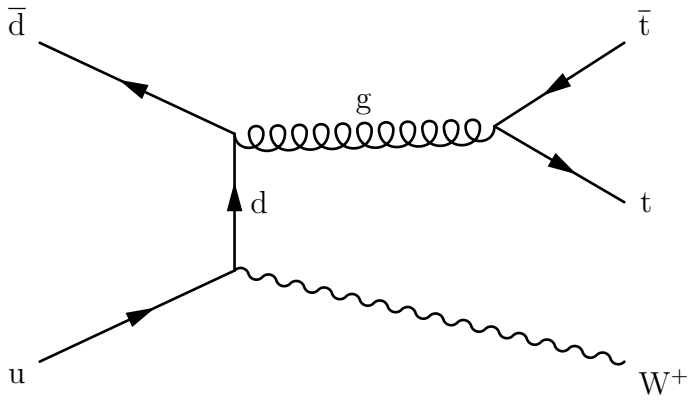

Figure 2.7: Leading order Feynman diagram for $t\bar{t}W^+$ production in proton-proton collisions. The top quark pair is produced via quark antiquark annihilation. One of the incoming quarks radiates a W boson.

2.4 Top Quark Pairs in Association with a Vector Boson

The LHC provides an overwhelming number of top quarks in its proton-proton collisions. Besides measures of single and pair production cross section of top quarks, the large number of top quarks produced allows, for the first time, studies of rarer processes such as the associated production of $t\bar{t}$ pairs with a Higgs, W, or Z boson. This dissertation focuses on the $t\bar{t}W$ production. In the following sections the production mechanism and the studied decay modes are presented.

2.4.1 Production

At LO a W boson can be produced in association with a top quark pair if the $t\bar{t}$ pair is stemming from quark antiquark annihilation. In this case, the associated W is produced through ISR: one of the initial state quarks radiates a W boson. The corresponding Feynman diagram for the $t\bar{t}W^+$ production process is shown in figure 2.7. In contrast, the $t\bar{t}W^-$ process has an up antiquark and a down quark in the initial state. Since the proton PDFs of up and down quarks are different, see figure 2.3, the $t\bar{t}W^+$ process is more likely and its expected cross section larger than the one of the $t\bar{t}W^-$ process. NLO calculations predict a cross section of

$$\sigma_{t\bar{t}W^+} = 161^{+12\,\%}_{-20\,\%}(\text{scale})^{+7\,\%}_{-8\,\%}(\text{pdf}+\alpha_s)\,\text{fb} \tag{2.25}$$

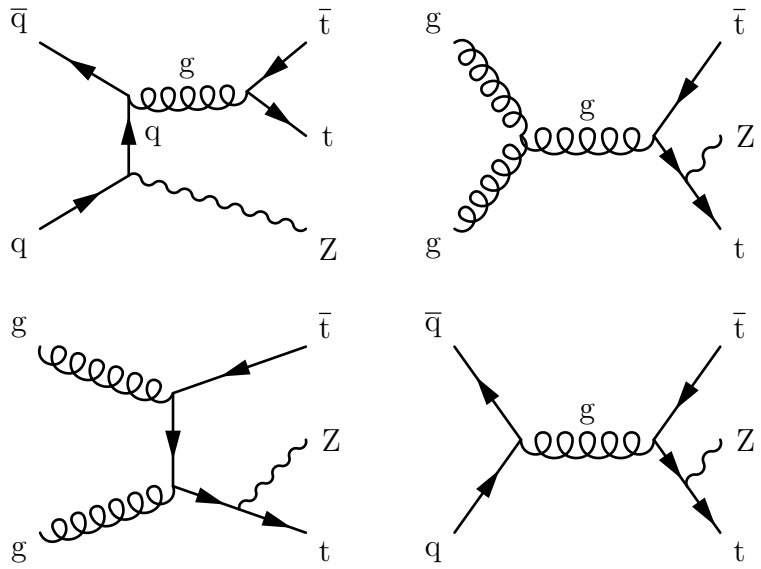

Figure 2.8: Leading order Feynman diagrams for $t\bar{t}Z$ production via initial state radiation (first diagram) and final state radiation (remaining diagrams) in proton-proton collisions.

and

$$\sigma_{t\bar{t}W^-} = 71^{+16\,\%}_{-21\,\%}(\text{scale})^{+6\,\%}_{-8\,\%}(\text{pdf}+\alpha_s)\,\text{fb} \tag{2.26}$$

for the $t\bar{t}W^+$ and $t\bar{t}W^-$ processes at $\sqrt{s} = 8\,\text{TeV}$ [42].

Similarly, a Z boson can be produced in association with a top quark pair through radiation. Unlike the W boson, the Z boson does not change the flavour when coupling to the top quark and therefore a Z boson can be radiated from one of the top quarks as well. The $t\bar{t}$ pair is produced via gluon splitting or quark antiquark annihilation, as described in section 2.3.1, and one of the final state top quarks radiates a Z boson. The corresponding LO Feynman diagrams are shown in figure 2.8.

The predicted cross sections of both processes, $t\bar{t}W$ and $t\bar{t}Z$, are rather small and at the same order of magnitude as the cross section of the $t\bar{t}H$ process. Figure 2.9 shows their predicted cross sections at LO in proton-proton collisions as a function of centre-of-mass energy.

2.4.2 Decay Modes

Since the top quark almost exclusively produces a bottom quark and a W boson when it decays, different decay modes of the $t\bar{t}W$ process are defined by the

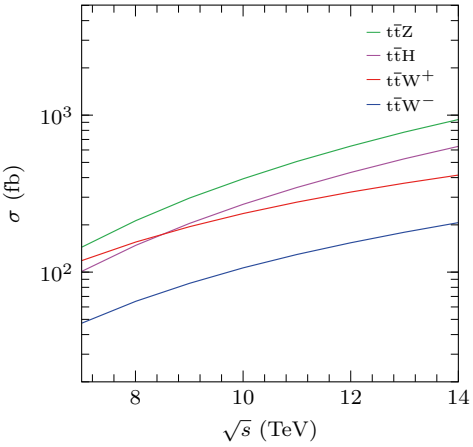

Figure 2.9: Leading order cross sections of associated top quark pair production with a boson (H, $W^{\pm}$, or Z) in proton-proton collisions as functions of the centre-of-mass energy $\sqrt{s}$, derived from reference [42].

disintegration of the three W bosons. These W bosons decays either *hadronically* into a quark antiquark pair or *leptonically* into a lepton and neutrino. In this dissertation the focus lies on final states consisting of two same-sign leptons where only electrons and muons are considered. This results in two possible decay modes: two same-sign W bosons are decaying leptonically and one W boson hadronically

$$t\bar{t}W \to \left(t \to b\ell^{\pm}\nu\right)\left(t \to bq\bar{q}'\right)\left(W \to \ell^{\pm}\nu\right) \tag{2.27}$$

and the second mode

$$t\bar{t}W \to \left(t \to b\ell^{+}\nu\right)\left(\bar{t} \to \bar{b}\ell^{-}\bar{\nu}\right)\left(W \to \ell^{\pm}\nu\right) \tag{2.28}$$

in which all three W bosons decay leptonically. The former mode is illustrated in figure 2.10.

The W boson decays leptonically[1] with a branching fraction of [17]

$$\mathcal{B}\left(W^{+} \to \ell^{+}\nu\right) = (21.72 \pm 0.18)\,\% \tag{2.29}$$

and decays hadronically into a quark antiquark pair with a branching fraction of [17]

$$\mathcal{B}\left(W^{+} \to q\bar{q}'\right) = (67.41 \pm 0.27)\,\%. \tag{2.30}$$

This results in a branching fraction for the mode in equation (2.27) of

$$\mathcal{B}\left(t\bar{t}W \to \left(t \to b\ell^{\pm}\nu\right)\left(t \to bq\bar{q}'\right)\left(W \to \ell^{\pm}\nu\right)\right) = (3.18 \pm 0.04)\,\% \tag{2.31}$$

[1]Here, ℓ indicates the sum over e and μ.

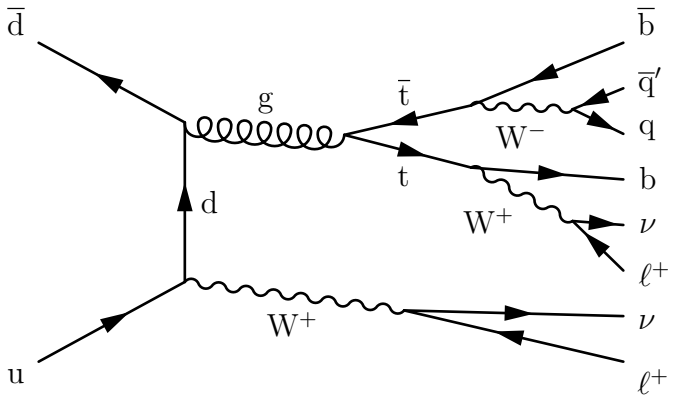

Figure 2.10: Leading order Feynman diagram for $\mathrm{t\bar{t}W}^+$ production with two same-sign leptons in the final state. The top quarks each decay into a bottom quark and W boson. One W boson produces a quark antiquark pair. The remaining two equally charged W bosons are decaying leptonically.

and

$$\mathcal{B}\left(\mathrm{t\bar{t}W} \to \left(\mathrm{t} \to \mathrm{b}\ell^+\nu\right)\left(\overline{\mathrm{t}} \to \overline{\mathrm{b}}\ell^-\overline{\nu}\right)\left(\mathrm{W} \to \ell^\pm\nu\right)\right) = (1.025 \pm 0.015)\,\% \tag{2.32}$$

for the all leptonic mode. In total, a branching fraction of

$$\mathcal{B}\left(\mathrm{t\bar{t}W} \to \ell^\pm\ell^\pm X\right) = (4.20 \pm 0.04)\,\% \tag{2.33}$$

is expected. When taking into account tau leptons, which decay leptonically into an electron or muon, the branching ratio in equation (2.29) gets larger and the total branching fraction becomes

$$\mathcal{B}\left(\mathrm{t\bar{t}W} \to \ell^\pm\ell^\pm X\right) = (6.07 \pm 0.06)\,\%. \tag{2.34}$$

Despite its small branching fraction, the *same-sign dilepton* decay modes have experimental advantages, since very few background processes have similar same-sign lepton signatures, as described later in chapter 5.

The decay modes of the $\mathrm{t\bar{t}Z}$ process are similar when restricting to modes in which the Z boson decays leptonically. As in the case of the $\mathrm{t\bar{t}W}$ process, the modes differ by the decay of the W boson. Figure 2.11 shows the modes with three and four leptons in the final state.

The Z boson decays with a branching fraction of [17]

$$\mathcal{B}\left(\mathrm{Z} \to \ell^+\ell^-\right) = (6.732 \pm 0.005)\,\% \tag{2.35}$$

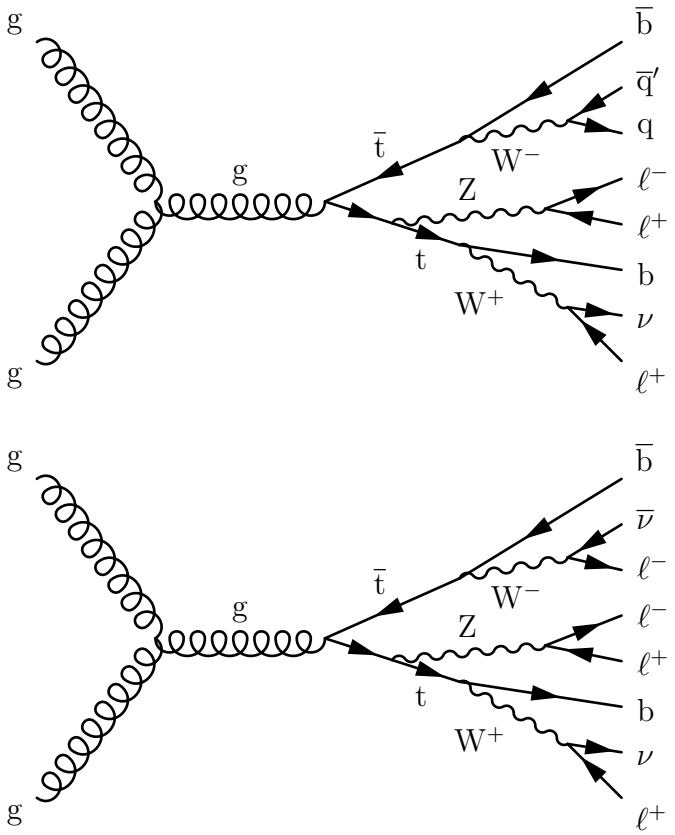

Figure 2.11: Leading order Feynman diagrams for the $t\bar{t}Z$ process with three and four leptons in the final state. The Z boson is radiated from one of the top quarks which are produced via gluon fusion. A W boson is decaying into a quark antiquark pair in the upper diagram while all W bosons are decaying leptonically in the lower diagram.

into a e^+e^- or $\mu^+\mu^-$ pair. This results in a branching fraction of

$$\mathcal{B}\left(t\bar{t}Z \to \ell^{\pm}\ell^{+}\ell^{-}X\right) = (1.971 \pm 0.018)\,\% \tag{2.36}$$

for the decay mode with three leptons in the final state and

$$\mathcal{B}\left(t\bar{t}Z \to \ell^{+}\ell^{-}\ell^{+}\ell^{-}X\right) = (0.318 \pm 0.004)\,\% \tag{2.37}$$

for the all leptonic mode.

Chapter 3

Experimental Environment

3.1 The Large Hadron Collider

The Large Electron-Positron Collider (LEP) was the largest circular collider of its kind, located at the European Organization for Nuclear Research (CERN), near Geneva, Switzerland. It was operated from 1989 till 2000 and achieved a beam energy of 104.5 GeV [17]. To push the energy frontier further, a new accelerator and collider, the Large Hadron Collider (LHC), was developed and installed in the 26.7 km long LEP tunnel. The LHC is designed to collide protons or heavy ions instead of the much lighter electrons and positrons. Thus, it benefits from smaller synchrotron radiation losses which are proportional to the negative fourth power of the particle's mass. This section briefly summarises the design of the LHC machine which is described in detail in reference [43].

The existing injection and acceleration chain of CERN was reused and upgraded to meet the needs of the LHC. An overview of the accelerator complex is given in figure 3.1. Protons are obtained from ionisation of hydrogen by a duoplasmatron source and brought to 50 MeV by the Linear accelerator 2 (Linac2). The Proton Synchrotron Booster (PSB) accelerates them to 1.4 GeV and delivers them to the Proton Synchrotron (PS) which brings the protons to 25 GeV. After injecting into the Super Proton Synchrotron (SPS), the protons are accelerated to 450 GeV. The final acceleration to 4 TeV is done in the LHC ring.[1] For heavy ion runs, particles are accelerated by the Linear accelerator 3 (Linac3) and the Low Energy Ion Ring (LEIR), instead of Linac2 and PSB, before injection into the PS.

Around the ring are eight straight sections and eight arcs. Superconducting dipole

[1] Since 2015, the LHC is operated at a beam energy of 6.5 TeV.

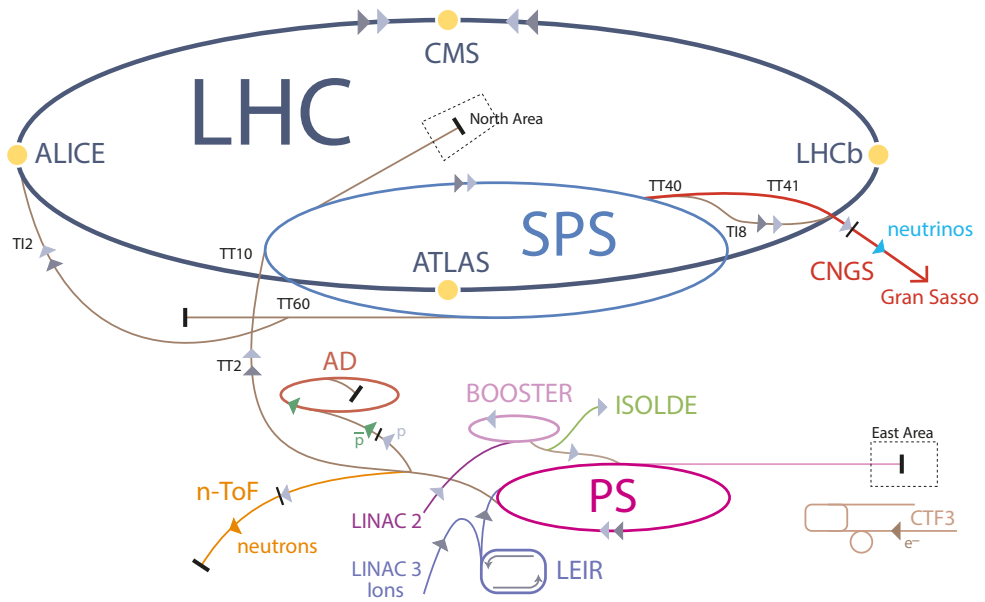

Figure 3.1: CERN accelerator complex [44]. Protons are accelerated by the Linear accelerator 2 (Linac2), the Proton Synchrotron Booster (PSB), the Proton Synchrotron (PS), the Super Proton Synchrotron (SPS), and finally injected into the Large Hadron Collider (LHC). The Linear accelerator 3 (Linac3) and the Low Energy Ion Ring (LEIR) are used for acceleration of heavy ions before injecting them into the PS. The North Area provides beam lines of several different particle species, supplied by the SPS.

Parameter	2012	Design	Unit
Beam energy	4	7	TeV
β-function at collision point	60	55	cm
Bunch spacing	50	25	ns
Number of bunches	1 380	2 808	
Protons per bunch	1.7×10^{11}	1.15×10^{11}	
Normalised emittance	2.5	3.75	mm mrad
Peak luminosity	7.7×10^{33}	10^{34}	$1/(\mathrm{cm}^2\,\mathrm{s})$
Collisions per bunch crossing (av.)	37	19	
Stored beam energy	140	362	MJ

Table 3.1: Overview of the LHC parameters during the 2012 run and their design values [49].

magnets keep the protons on a circular path. For two counter-rotating beams magnetic dipoles in opposite directions are necessary. Thus, the beams are kept in separate beam pipes. Due to the limited amount of space inside the tunnel, with 3.7 m in diameter, twin bore magnets are used. To run at the design beam energy of 7 TeV a magnetic dipole field of 8.33 T is required, which is one of the limiting factors for the centre-of-mass energy. In four of the straight parts the beams are brought to collision at four interaction points where the experiments are located in underground caverns:

- ATLAS (A Toroidal LHC ApparatuS) [45]
- ALICE (A Large Ion Collider Experiment) [46]
- CMS (Compact Muon Solenoid) [47]
- LHCb (Large Hadron Collider beauty) [48]

The particles are accelerated by radiofrequency (RF) cavities which are operated at 400 MHz and arrange the protons in separate *bunches*. The LHC is designed to circulate 2 808 bunches with a bunch spacing of 25 ns and about 1.15×10^{11} protons per bunch. In table 3.1 the basic parameters of the LHC during the 2012 run are summarised and compared to their design values.

To minimise statistical uncertainties on their measurements and observe rare processes, the experiments are interested in collecting as much data as possible. The number of events of a given process is [17]

$$N = \sigma \times \int \mathcal{L}(t)\,\mathrm{d}t = \sigma \times \mathcal{L}_{\mathrm{int}} \tag{3.1}$$

where σ is the cross section of interest and $\mathcal{L}(t)$ the *instantaneous luminosity*. The integral over time in equation (3.1) defines the *integrated luminosity* $\mathcal{L}_{\text{int}}$. For a Gaussian beam distribution in both longitudinal and transversal directions, the luminosity is defined as [43]

$$\mathcal{L} = \frac{n^2 f \gamma_r}{4\pi\varepsilon_n \beta^*} F \tag{3.2}$$

where n is the number of particles in a bunch, f is the bunch crossing frequency, γ_r the relativistic γ-factor, ε_n the normalised transverse beam emittance, β^* the β-function at the collision point, and F denotes the geometric luminosity reduction factor, reflecting the crossing angle of the beams. The luminosity in the LHC is not constant, mainly due to the beam loss from collisions. To maximise the integrated luminosity $\mathcal{L}_{\text{int}}$ in equation (3.1), and thereby the amount of collected data, the beam parameters such as the emittance, the β-function, or the bunch spacing can be optimised. This increases the frequency with which the data needs to be recorded and therefore is limited by the readout capabilities of the experiments. Another option is to enlarge the luminosity by raising the number of protons per bunch or reducing the bunch size. The resulting higher beam intensity raises the number of interactions per bunch crossing which is known as *pileup* (PU). A larger number of proton-proton collisions per bunch crossing naturally complicates the disentangling of the different events which took place. As reported in table 3.1 the number of protons per bunch has already exceeded its design value and the design peak luminosity is almost reached with twice the design bunch spacing.

3.2 The Compact Muon Solenoid

The CMS detector is installed in a cavern at the interaction point 5 of the LHC ring. Interaction point 5 is located in the northern part of the ring, near Cessy, France. It is a general purpose experiment which aims for new physics discoveries and precise measurements of SM processes. If not stated otherwise information in the following sections are taken from reference [47].

3.2.1 General Concept

The design of the CMS detector is driven by the choice of the magnetic field. Thus, a superconducting solenoid is the corner stone of the detector. It is 12.5 m long, 6.3 m in diameter and can produce a nominal magnetic flux density of 3.8 T. The magnetic field is returned by an iron yoke, weighing roughly 10 000 t. Charged particles are deflected on their path through the magnetic field. By measuring the

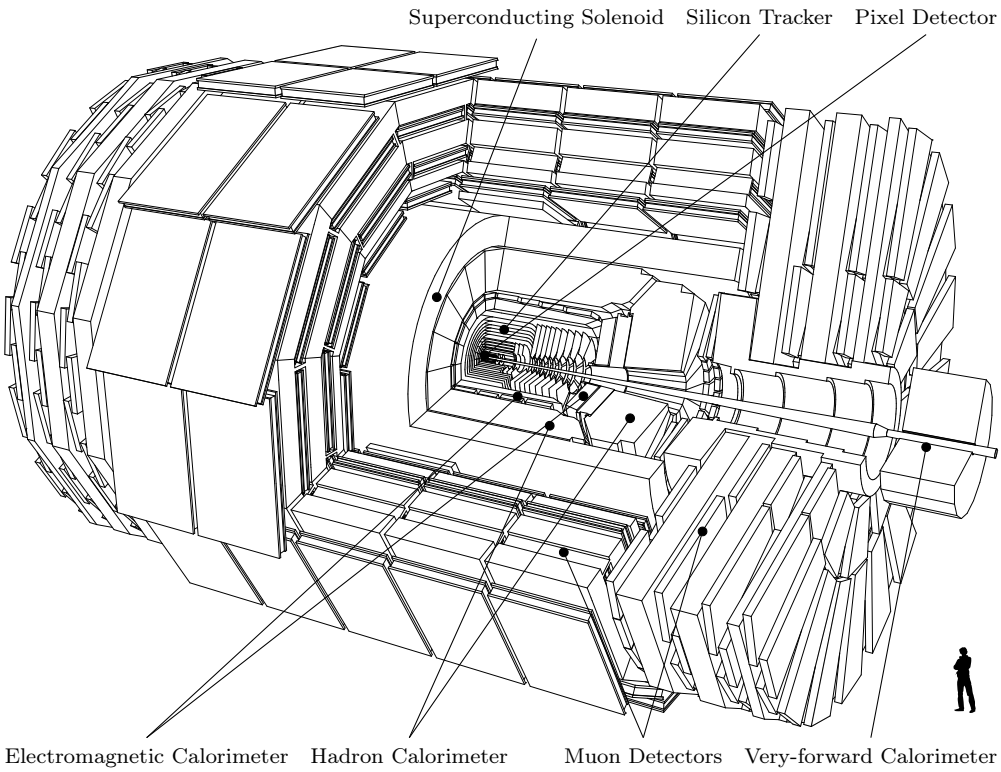

Figure 3.2: Schematic view of the CMS detector and its sub-detectors, derived from references [50, 51].

trajectory the particle's momentum can be calculated from the curvature of the path. The direction of the magnetic deflection indicates the electrical charge of the particle and the radius its momentum. A stronger magnetic field increases the deflection and therefore enhances the resolution on the momentum measurement. Figure 3.2 shows a schematic view of the detector. It is divided into two main sections: the *barrel* in the centre and an *endcap* at both sides. The barrel consists of five wheels which can be separated for maintenance and upgrades of the detector. Each wheel carries a part of the iron yoke in which the muon system is embedded. On the central wheel the solenoid, which houses the inner sub-detectors, is mounted. The endcaps complete the yoke and hold the sub-detectors in the forward region.

3.2.2 Coordinate System and Conventions

The origin of the coordinate system is chosen at the nominal interaction point, with the x-axis pointing radially inwards to the centre of the LHC ring, the y-axis

pointing vertically upwards, and the z-axis pointing tangentially along the ring in a north-westward direction. The azimuthal angle ϕ is defined from the x-axis in the x-y plane. From the z-axis the polar angle θ is measured. A more useful quantity than the polar angle is the rapidity

$$y = \ln\left(\frac{E + |\vec{p}|\cos\theta}{E - |\vec{p}|\cos\theta}\right) \tag{3.3}$$

which is dimensionless. Differences in rapidity have the advantage that they are invariant under Lorentz boosts along the z axis. The pseudorapidity is defined as

$$\eta = -\ln\left(\tan\left(\frac{\theta}{2}\right)\right). \tag{3.4}$$

Furthermore, the number of particles produced per unit of pseudorapidity is roughly equal. The pseudorapidity is independent of the particle's energy and momentum. For small masses ($m \ll p$), it offers a good approximation of the rapidity. To measure angular distances the variable

$$\Delta R = \sqrt{\Delta\phi^2 + \Delta\eta^2} \tag{3.5}$$

is defined, which is Lorentz invariant along the z axis as well. In this coordinate system the momentum transverse to the beam, $p_\perp$, is calculated from the x and y components. The sum of all particles' transverse momenta in an event should equalise due to momentum conservation. A possible imbalance gives indication for particles which are not detected and is called missing transverse energy $\not{E}_\perp$.

As common in high energy physics, the velocity of light c and the reduced Planck constant $\hbar$ are both set equal to one. With these conventions, energies and momenta can both be quoted in electronvolts (eV).

3.2.3 Tracking System

As mentioned before, for high momentum resolution a precise measurement of the particles' trajectories is necessary. The precise measurement of the trajectories is also necessary to reconstruct not only primary vertices (PVs), which describe the location of the hard scattering along the beam spot, but also secondary vertices (SVs) along the decay chain of produced particles. To achieve this, as many measuring points as possible along the trajectories are required and therefore as many detector layers as possible. Furthermore, the detector material needs to be as minimal as possible to reduce multiple scattering, bremsstrahlung, photon conversion, and nuclear interactions on the particle's path through the detector

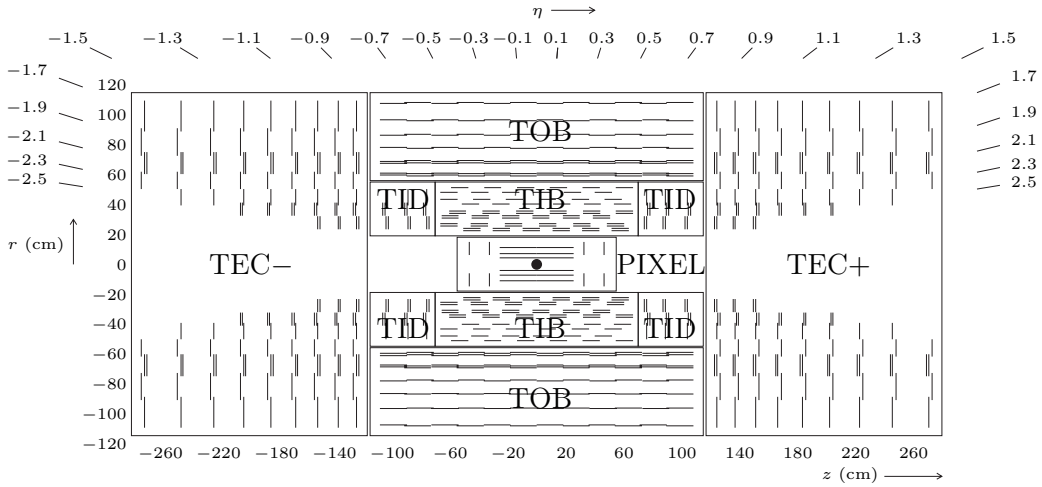

Figure 3.3: Schematic view of the CMS tracking system, derived from reference [47]. The silicon pixel detector is located close to the interaction point at the centre. It is surrounded by the Tracker Inner Barrel (TIB) and Tracker Outer Barrel (TOB). The forward region is covered by the Tracker Inner Disks (TID) and Tracker Endcaps (TECs).

material. On the other hand a detector with fast response is needed which requires on-detector electronics. Due to its location close to the interaction point the particle flux is very high. Thus, special care must be taken on the radiation hardness of the tracking system. In CMS, the tracking system is designed with silicon detector technology. Figure 3.3 shows a longitudinal cross section in the r-z plane through the CMS tracking system.

The tracking system is built in the core of CMS. In its centre and closest to the interaction point lies the *pixel detector*[2]. It consists of three layers of pixel modules in the barrel region at radii 4.4 cm, 7.3 cm, and 10.2 cm. In the forward region two disks of pixel modules at $z = \pm 34.5$ cm and $z = \pm 46.5$ cm complete the pixel detector. Together, the barrel and endcap detectors hold 66 million pixels with a size of 100 µm × 150 µm each.

The *silicon strip tracker* covers the radial range between $r = 20$ cm and $r = 116$ cm. In the area up to $r = 55$ cm the Tracker Inner Barrel (TIB), consisting of strip detectors in four layers, is placed and framed by three disks of the Tracker Inner Disks (TID) on each side. The sensors are 320 µm thick. TIB and TID are surrounded by six layers of 500 µm thick strip sensors in the Tracker Outer Barrel (TOB). Along

[2]In 2017, the described pixel detector was replaced to maintain a high tracking performance at increased instantaneous luminosities of up to $2 \times 10^{34}/(\mathrm{cm}^2\,\mathrm{s})$ [52]. The upgraded pixel detector consists of four barrel layers and three endcap disks on each side.

the beam line the range $124\,\text{cm} < |z| < 282\,\text{cm}$ is covered by nine disks of the Tracker Endcaps (TECs). In total the silicon strip tracker consists of 9.3 million strips and has an active area of $198\,\text{m}^2$.

In the barrel, at a pseudorapidity of $|\eta| < 1.6$, the resolution on the transverse momentum is about 1 % to 2 % for tracks with a momentum of the order of 100 GeV. In addition to the high momentum resolution, the tracking system provides an efficiency of about 99 % in tracking muons over most of the phase space. In the forward direction the efficiency decreases due to the reduced coverage of the pixel detector in this area.

3.2.4 Electromagnetic Calorimeter

After reconstructing a particle's momentum, its energy may be measured in the calorimeter. With these quantities in hand, a complete four-vector can be constructed. The CMS detector has two different calorimeters. The Electromagnetic Calorimeter (ECAL) aims for the electromagnetically interacting particles. It is surrounded by the Hadron Calorimeter (HCAL) which is designed to measure the strongly interacting particles.

In the ECAL, lead tungstate ($PbWO_4$) crystals are used as scintillator material. Photons deposit their energy via e^+e^- pair production, while electrons deposit their energy as bremsstrahlung. These two processes lead to cascades of particle showers in the crystal. $PbWO_4$ has a high density of $8.28\,\text{g/cm}^3$ and a short radiation length[3] of 0.89 cm which makes it the optimal choice for a compact calorimeter. Its scintillation decay time is comparable to the LHC bunch crossing time of 25 ns.

The ECAL in CMS is composed of the ECAL barrel (EB) and the ECAL endcap (EE). The EB covers a range in pseudorapidity of $|\eta| < 1.479$ and holds 61 200 $PbWO_4$ crystals pointing to the interaction point. The front face of the 230 mm long crystals measures 22 mm × 22 mm and the rear face 26 mm × 26 mm. In the EB they add up to a total volume of $8.14\,\text{m}^3$ and weigh 67.4 t. At the rear face of each crystal the emitted scintillation light is collected by an avalanche photodiode (APD). On each side of the EB, two half disks, the EE, cover the pseudorapidity range $1.479 < |\eta| < 3.0$. In it, the 220 mm long crystals are arranged in a rectangular x-y grid. They are 30 mm × 30 mm at their rear face and 28.62 mm × 28.62 mm at their front face. In the EE the crystals take a volume of $2.90\,\text{m}^3$ and weigh 24.0 t.

[3]The radiation length is defined as the mean distance over which an electron has lost all but $\frac{1}{e}$ of its energy due to bremsstrahlung and $\frac{7}{9}$ of the mean distance after which pair production of high-energy photon occurs [17].

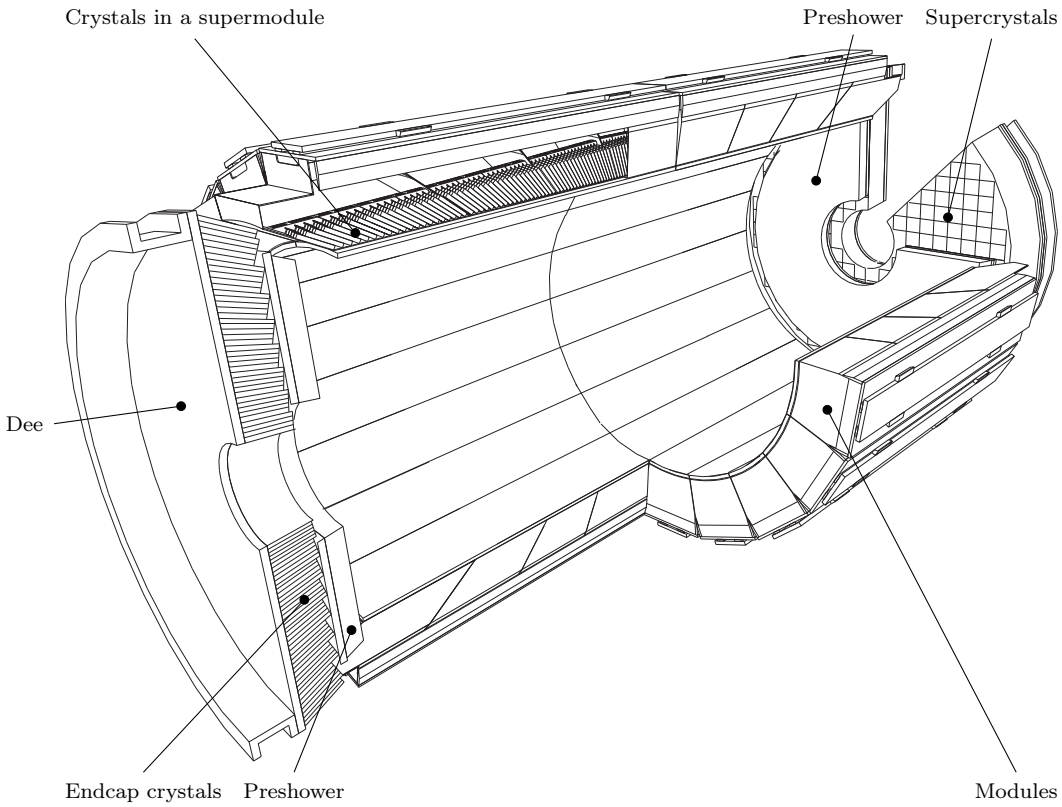

Figure 3.4: Schematic view of the Electromagnetic Calorimeter layout [47].

At the end of the crystals, vacuum phototriodes (VPTs) are used as photodetectors. The ECAL layout is shown in figure 3.4.

The temperature of the crystals has to be very stable since the number of emitted scintillation photons and the amplification of the APD are both temperature dependent. With a water cooling system the crystals are kept at $(18.00 \pm 0.05)\,^{\circ}\mathrm{C}$.

When studying the performance of a calorimeter, the energy resolution is parameterised as

$$\left(\frac{\sigma}{E}\right)^2 = \left(\frac{S}{\sqrt{E}}\right)^2 + \left(\frac{N}{E}\right)^2 + C^2 \tag{3.6}$$

where S stand for the stochastic term, N the noise term, and C the constant term. The contributions to the stochastic term are: photostatistics and fluctuations in the deposited energy. It was measured to be $S = 0.028\,\mathrm{GeV}^{1/2}$. The noise term includes noise due to electronics, digitisation, and PU. It is at the order of $0.12\,\mathrm{GeV}$. The non-uniformity of the light collection, intercalibration errors, and the energy leakage at the back of the crystal enter the constant term C which is

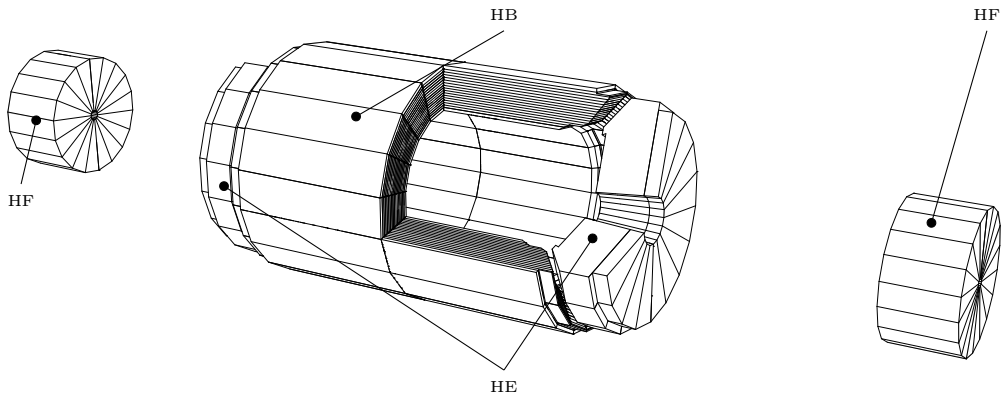

Figure 3.5: Schematic view of the Hadron Calorimeter, derived from reference [51]. The sub-detectors HCAL endcap (HE), HCAL barrel (HB), and HCAL forward (HF) are shown.

about 0.3 %. For a 120 GeV electron, this translates into an energy resolution of 0.5 %.

3.2.5 Hadron Calorimeter

While the ECAL absorbs electromagnetically interacting particles almost completely, it does not provide enough material to stop hadrons. Hence, hadronic particles reach the area beyond the ECAL and are detected in the HCAL. It is an important component of the detector to measure hadronic jets and missing transverse energy. The HCAL is divided into four main parts, illustrated in figure 3.5. Between the EB and the solenoid lies the HCAL barrel (HB). It is built of layers of brass absorbers and 3.7 mm thick plastic scintillators to collect the signal. The brass absorber has a nuclear interaction length[4] λ_I of 16.42 cm and a density of 8.53 g/cm^3. This results in a absorber thickness of $5.82\lambda_I$ at 90° to the beam pipe and $10.6\lambda_I$ at $|\eta| = 1.3$. The ECAL adds about $1.1\lambda_I$.

At each end an HCAL endcap (HE) covers a range in pseudorapidity of $1.3 < |\eta| < 3$. The HE is mounted on the endcap yoke. Brass plates with a thickness of 79 mm are used as absorber and scintillators are placed in between.

Due to the limited space, the calorimeters inside the solenoid are not sufficient to contain the full hadronic shower. Thus, the HCAL outer barrel (HO) is mounted outside the solenoid. It covers the central region with pseudorapidity $|\eta| < 1.3$ and is divided into five rings along the z-axis. The central ring consists of two

[4]The nuclear interaction length is defined as the mean distance a hadronic particle covers in a material until it interacts.

layers of scintillators while the other rings have only one layer. The solenoid coil acts as an absorber and provides additional $\frac{1.4}{\sin\theta}\lambda_I$. With the HO the total length is at least $11.8\lambda_I$ in the barrel region.

On the outside of the detector, 11.2 m away from interaction point, the very forward direction ($3 < |\eta| < 5$) is covered by the HCAL forward (HF). At the maximum covered pseudorapidity a radiation dose of about 10 MGy is expected during ten years of LHC operation. To resist these harsh conditions, steel absorber plates along with quartz fibres as active material are used. The emitted Cherenkov light is measured by photomultipliers.

3.2.6 Muon System

Muons are an important signature to identify interesting processes. Thus, a reliable muon identification is crucial. Unlike electrons, muons do not radiate much of their energy through bremsstrahlung when passing the ECAL. Since they do not undergo strong interactions they pass the HCAL as well. The yoke works as hadron absorber too and makes muons the only detectable particles left in the outer part of CMS. Therefore detectors in this area can be used to identify muons' trajectories. In figure 3.2 the muon system is illustrated radially outside the HO and HE.

In total the muon system consists of 25 000 m^2 of detection planes which are enclosed by the yoke. The barrel part, which covers the pseudorapidity range $|\eta| < 1.2$, is divided into four stations of muon chambers. Each station is a rectangular Drift Tube (DT). The three inner stations each hold eight chambers to measure the r-ϕ coordinate, and four chambers for z position. The fourth station has only eight chambers to detect the r-ϕ position. In the barrel region the magnetic field is uniform and mostly inside the steel yoke. Furthermore, a low muon rate is expected here. The rectangular DTs are placed with an offset of half the cell width with respect to the cells in the adjacent layers. Due to the resulting overlap, dead spots in the efficiency are avoided. This provides a well prepared arrangement to link muon hits together and reject background. Figure 3.6 shows a cross section through the muon detectors in the barrel region.

In the forward region, the muon rates are higher and the magnetic field is non-uniform. The muon system in the endcaps is built of Cathode Strip Chambers (CSCs) which provide a fast response time and adequate radiation resistance. The CSCs cover $0.9 < |\eta| < 2.4$ with a high granularity and are arranged in four stations. In each chamber the cathode strips are arranged radially and measure the r-ϕ coordinates. Perpendicular to the strips are the anode wires which provide the η position. The solid pattern recognition of the CSCs ensures an efficient matching

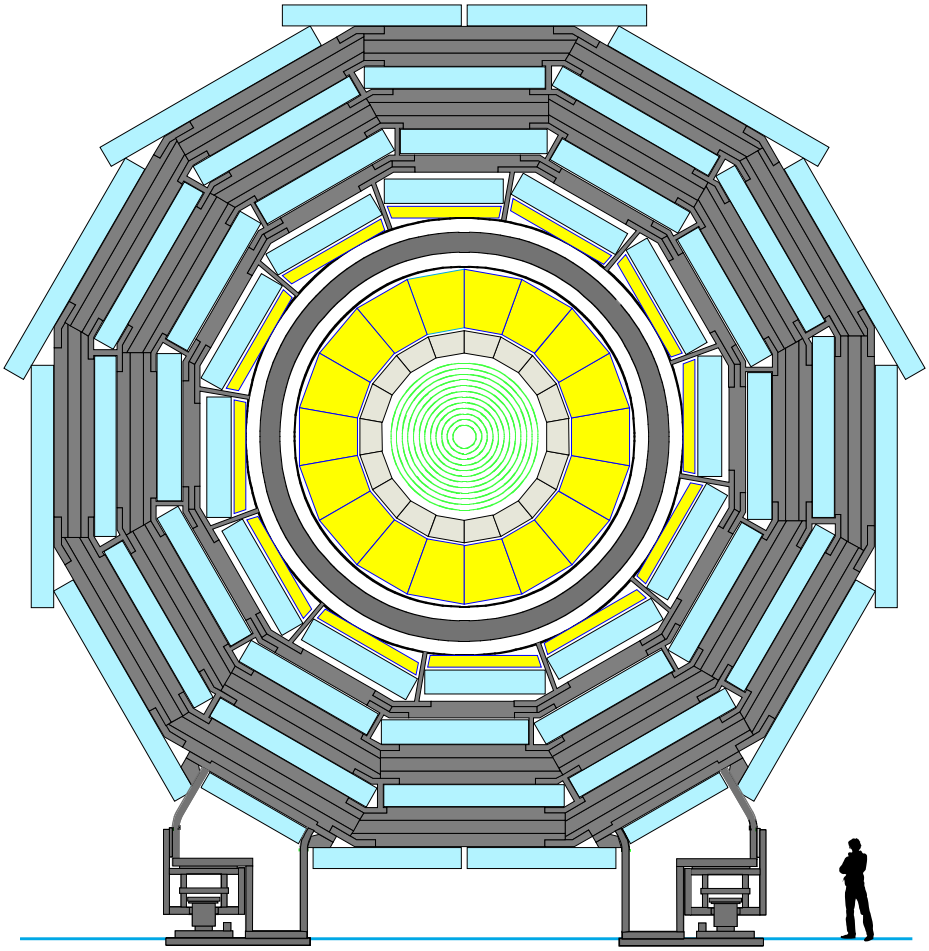

Figure 3.6: Cross section through one of the CMS barrel wheels showing the muon DT chambers in cyan, derived from reference [47].

of hits in several stations and to the inner tracker.

The muon system is completed by Resistive Plate Chambers (RPCs) which are attached to the DTs and CSCs and cover the range of $|\eta| < 1.6$. The RPCs are part of the trigger decision of the muon system, since they feature a fast response and high time resolution, but a less precise position resolution compared to the rest of the muon system. Furthermore, the RPCs help to solve ambiguities in the reconstruction of muon tracks. Six RPC layers are mounted among the barrel muon system. In the endcaps each of the first three stations is equipped with an RPC plane.

The muon system finds its main applications in selecting interesting events for physics analyses, by identifying muons, and improving muons' trajectory measurements, by exploiting their magnetic deflection over the full range of the detector. Combining the information of the tracker and the muon system in a momentum fit improves the momentum resolution. This results in a momentum resolution of approximately 5 % for momenta of 1 TeV.

3.2.7 Trigger System

The bunch crossing rate of the LHC at nominal beam conditions is 40 MHz. Since it is not possible to record data at such a high rate, a dedicated system is necessary to select events of possible interest. The decision to read out and store an event is made by the *trigger* system.

At the first stage stands the Level-1 (L1) trigger. It is based on programmable electronics. Part of the system is mounted on the detector itself to meet a maximum latency of 3.2 µs. During this time the signals of all sub-detectors are stored in buffers on the detectors. The logic recognises local hit patterns in the calorimetry and muon system which are used to provide trigger objects, such as muon or electron candidates. At this stage no tracking information is available. The objects are further processed by the *global calorimeter* and *global muon* triggers. They evaluate if a certain event is rejected or passed to next stage, the High-Level Trigger (HLT). The L1 trigger has a maximum output rate of 100 kHz. A flow chart of the L1 trigger is shown in figure 3.7.

Other than the L1 trigger the HLT is based on software which is run in a filter farm outside the detector cavern. More complex combinations and decisions are possible since all read out data are accessible, including tracking information. The HLT provides various trigger *paths*, depending on the needs of different physics analyses. A path stands for an algorithm aiming for specific particles passing defined thresholds. `HLT_Mu17_Mu8` is such a path which is used in this dissertation.

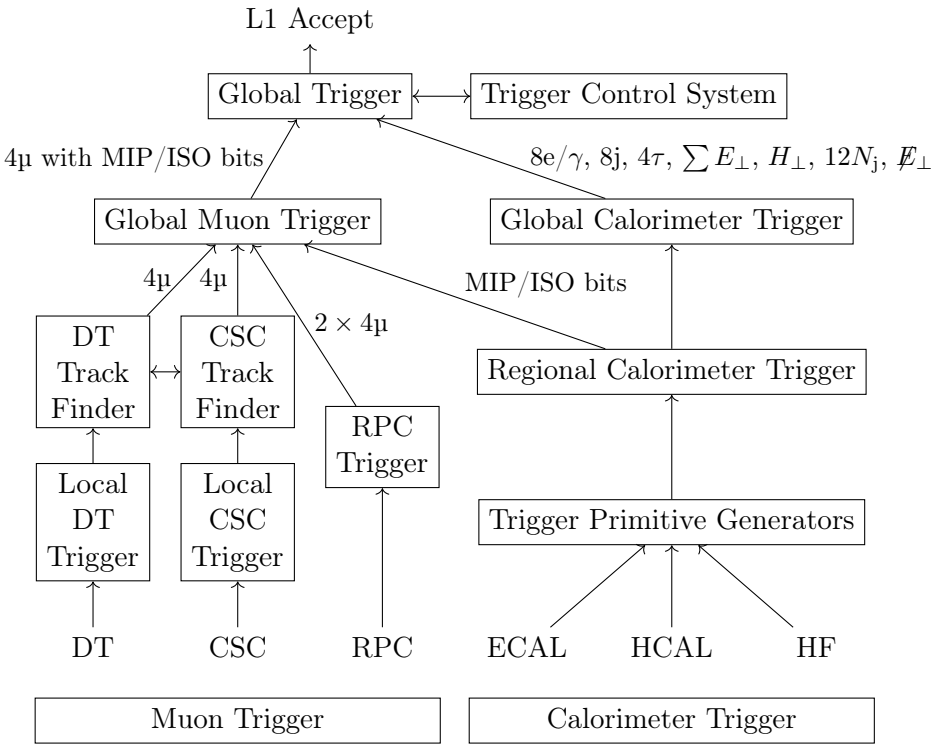

Figure 3.7: Decision tree of Level-1 trigger, derived from reference [47].

It selects events with two muons which fulfil transverse momentum thresholds of $p_\perp^{\mu_1} > 17\,\text{GeV}$ and $p_\perp^{\mu_2} > 8\,\text{GeV}$. Furthermore, an HLT path can be *pre-scaled*. This means only a defined fraction of the selected events are further processed and stored. Together, the L1 trigger and the HLT reduce the rate by a factor of 10^6.

3.2.8 Data Acquisition

The signals of the CMS sub-detectors are collected by the Data Acquisition (DAQ) system. It is designed to handle the nominal bunch spacing of the LHC and reads out the detector electronics for events passing the L1 trigger, see section 3.2.7. Therefore, the DAQ system has to manage an input rate of 100 kHz which corresponds to a data flow from the sub-detectors of about 100 GB/s. The data stream is transmitted to the HLT farm where the event rate is further reduced to about 1 kHz and recorded for later physics analyses. In parallel, the Data Quality Monitoring (DQM) controls the quality of the taken data.

Chapter 4

Event Reconstruction

For each recorded event the raw signals of the sub-detectors, describing position and energy, are translated into physics objects, like photons, leptons, or hadronic jets. In this *reconstruction* process the particles' type, direction, and energy are identified. First, the position hits in the tracker and muon system are used to form tracks. In a second step, the tracks are combined with energy deposits in the calorimeters.

4.1 Particle-Flow

To measure rare processes it is crucial to reconstruct and identify as many final state particles as possible. This is true even for particles with a low transverse momentum since they contribute to the missing transverse energy measurement or can stem from decays of particles of interest. For this purpose, information from all CMS sub-detectors are combined with the particle-flow (PF) algorithm [53, 54]. Namely, the inputs to select PF candidates are tracks found by the tracker, tracks reconstructed in the muon system, and clusters of energy deposits in the calorimeters. By linking these inputs, the algorithm's goal is to provide a full picture of all particles produced in an event.

The algorithm starts by reconstructing global muons, followed by the reconstruction of electrons, as described in the following sections. The particles found are added to the list of PF candidates and their associated tracks are removed from the collection of tracks. In the next step, tracks are combined with energy deposits in the HCAL to identify charged hadrons. The remaining energy clusters in the ECAL and HCAL give rise to photons and neutral hadrons.

4.2 Tracking

The trajectories which charged particles cover in the detector are a fundamental component in the determination of particles' properties, such as their momenta, charge, and origin. The tracks are reconstructed using the tracking detector alone, and in case of muons, in combination with the muon system.

In a first step, local signals in the pixel and strip tracker, which are above defined thresholds, specify so-called *hits*. From these hits the particles' individual tracks are reconstructed by the Combinatorial Track Finder (CTF), which is an adapted Kalman filter [55]. A tracking efficiency close to 100 % is necessary, since charged hadrons missed by the tracking algorithm would be reconstructed (if at all) by the calorimeters with an inferior energy resolution. Furthermore, the tracking fake rate must be small to avoid large energy excesses. To obtain both a high efficiency and a low fake rate, an *iterative tracking* algorithm is applied. First, tight criteria on the trajectory seeds are applied which reduce the tracking efficiency, but provides a negligible fake rate. This step targets tracks with high transverse momenta and tracks originating close to the interaction point. These tracks are relatively easy to identify. All hits associated with tracks found are removed before subsequent tracking iterations are run. This reduces the complexity of pattern recognition in following iterations. The seeding criteria are loosened from one iteration to the next. This increases the efficiency step by step while the fake rate is kept low. Tracks with low transverse momenta and tracks stemming from outside the beam spot are found in following iterations. More detailed informations on the track reconstruction can be found in reference [56].

From the collection of tracks, vertices are reconstructed. A PV is associated with a hard scatter. The PVs in an event include the signal vertex and vertices from PU collisions.

4.3 Muon Reconstruction

The muon system and tracks found by the silicon tracker are used to reconstruct muons. Several categories of muon candidates are defined in reference [57]. First, *standalone muon* tracks are reconstructed by using hits in the DTs and CSCs. Candidates which can be combined with a tracker track by a Kalman filter [55] define *global muons*. In case multiple tracker tracks can be fitted with a muon track, only the combination with the best fit result is kept. This exploits the magnetic deflection over the full range of the detector. Therefore, the resolution

of global muons with transverse momentum above 200 GeV is enhanced compared to the momentum measurement of the tracker.

4.4 Electron Reconstruction

Electrons are identified combining their energy deposits in the ECAL with a track reconstructed in the tracker. Along their trajectory through the detector material, electrons face a high probability of loosing a significant part of their energy through bremsstrahlung. This can lead to secondary energy deposits from the radiated photons which need to be taken into account to accurately reconstruct the electron's energy. This characteristic is considered when so-called *superclusters* are formed in the ECAL. A supercluster is a group of dedicated energy deposit clusters. The algorithm accounts for the different spreads in η and ϕ coming from the magnetic deflection of the electron. Electron tracks are found by matching superclusters to track seeds in the inner tracker layers. A Gaussian Sum Filter (GSF) [58], which accounts for energy losses through bremsstrahlung, is used to fit a trajectory from a supercluster to such a track.

4.5 Jet Reconstruction and Identification

Quarks and gluons do not exist freely due to colour confinement. When produced in collisions they form immediately colour neutral states in a process called hadronisation, as described in section 2.2. This leads to jets of hadrons which are measured by the detector and known as *hadronic jets*. The clustering algorithm used is briefly described.

4.5.1 Clustering Algorithm

To reconstruct jets from the PF candidates the anti-k_t jet clustering algorithm [59] is used. The algorithm defines the distance between two entities[1] i and j as

$$d_{ij} = \min\left(k_{ti}^{-2}, k_{tj}^{-2}\right) \frac{\Delta_{ij}^2}{R^2} \tag{4.1}$$

where k_{ti} is the transverse momentum of entity i, R specifies the radius parameter, and Δ_{ij}^2 is defined as

$$\Delta_{ij}^2 = (y_i - y_j)^2 + (\phi_i - \phi_j)^2 \tag{4.2}$$

[1] An entity is either a particle candidate or a pseudojet.

using the rapidity y_i and azimuth ϕ_i of entity i. Between entity i and the beam B the quantity

$$d_{iB} = k_{ti}^{-2} \tag{4.3}$$

specifies the distance. In each step of the clustering process the smallest distance is identified. If it is d_{ij} the entities i and j are combined to a pseudojet. If d_{iB} is the smallest distance, entity i is called a jet.

All associated particle momenta are summed to derive the jet momentum and direction. The jet properties are corrected for various effects as described below.

4.5.2 Jet Energy Correction

The measured energy of jets is calibrated to match on average the true energy of the jet. A detailed description is given in reference [60] on which this section is based. Each component μ of the raw four-momentum vector of a jet is corrected with a factor $\mathcal{C}$,

$$p_\mu^{\text{cor}} = \mathcal{C} \times p_\mu^{\text{raw}}. \tag{4.4}$$

The factor $\mathcal{C}$ contains corrections for noise $\mathcal{C}_{\text{offset}}$, the Monte Carlo (MC) calibration $\mathcal{C}_{\text{MC}}$ and the relative and absolute energy scales calibrations, $\mathcal{C}_{\text{rel}}$ and $\mathcal{C}_{\text{abs}}$. The corrections are applied sequentially

$$\mathcal{C} = \mathcal{C}_{\text{offset}}(p_\perp^{\text{raw}}) \times \mathcal{C}_{\text{MC}}(p'_\perp, \eta) \times \mathcal{C}_{\text{rel}}(\eta) \times \mathcal{C}_{\text{abs}}(p''_\perp) \tag{4.5}$$

where $p'_\perp$ refers to the transverse momentum after applying the offset correction and $p''_\perp$ to the transverse momentum after all previous corrections.

With rising luminosity, the number of PU interactions increases. Thus, the probability that signals of particles originating from PU overlap with signals of particles associated with the PV rises. Consequently these PU particles can deposit their energy in the same area of the detector and can be caught by the jet clustering algorithm. The first applied factor $\mathcal{C}_{\text{offset}}$ corrects for those contributions by using the concept of jet areas [61, 62]. The second correction uses studies on MC simulation to account for the difference of the actual jet transverse momentum and the reconstructed transverse momentum. To correct for the non-uniform energy response of the detector in pseudorapidity η, the factor $\mathcal{C}_{\text{rel}}$ is applied. It is evaluated from data by selecting dijet events. Similarly, the absolute energy correction $\mathcal{C}_{\text{abs}}$ addresses such effects for different jet transverse momenta. It is derived by the missing transverse energy projection fraction (MPF) method [63] on γ/Z+jets events.

4.5.3 Bottom Quark Jets

Hadrons composed of bottom quarks have a relatively large mass and long lifetime compared to lighter ones such as J/ψ or D mesons. The precise tracking information of CMS is the key to distinguishing bottom quark jets (b-jets) from light-parton and gluon jets.

SVs are reconstructed as an indication of a long-lived particle. This is exploited to identify («tag») b-jets. Various SV variables (e.g. flight distance, vertex mass) are used as discriminators. The Combined Secondary Vertex (CSV) algorithm [64] uses in addition track-based lifetime information. This makes it possible to identify b-jets even if no SV was reconstructed and increases the efficiency compared to algorithms using SV information only. The CSV algorithm provides multiple working points which correspond to different misidentification probabilities for light-flavoured jets. In this analysis the medium working point is chosen with a misidentification probability of 1 % at an average jet transverse momentum of $p_\perp \approx 80\,\text{GeV}$. With these settings the algorithm identifies b-jets with an efficiency of roughly 70 %.

4.6 Missing Transverse Energy

Events with an imbalance in the momenta transverse to the beam direction imply the production of particles which could not be detected, such as neutrinos. These particles are quantified with the missing transverse energy variable $\not{\vec{E}}_\perp$ [65], derived from the vectorial sum of all reconstructed PF particles' transverse momenta

$$\not{\vec{E}}_\perp \equiv -\sum_i \vec{p_\perp}^{\,i}. \tag{4.6}$$

In this thesis mostly its magnitude

$$\not{E}_\perp = \left|\not{\vec{E}}_\perp\right| \tag{4.7}$$

is used.

4.7 Simulation

An important aspect in analysing proton-proton collision data is to compare measured data to expectations. For this, expected processes and their interaction

with the detector are simulated. The various tools, which are used for this purpose, apply MC techniques, which are based on random sampling of distributions. These simulations are done for a number of reasons. The response of the detector is studied, meaning the final observables in the detector are compared to the initially simulated quantities of the particles, like momentum or energy. Background processes can be analysed and the expected behaviour of the signal can be probed. This section summarises the production of MC simulated samples, which are centrally processed by the CMS collaboration, and an overview of the corrections applied is given.

4.7.1 Event Generation and Detector Response

The simulation of the various processes happening in proton-proton collisions is carried out in multiple steps by MC generators. First, the matrix elements, which describe the probabilities of certain processes to occur in the hard interaction of two partons, are calculated. This is followed by simulating the decay of produced particles. For most of the processes MadGraph5 [66] is used for these steps. As described in section 2.2, after the hard interaction the partons split into quarks in the parton shower. This process includes ISR and FSR as well. Due to colour confinement, quarks produced hadronise and form colour neutral states. For these processes, the generator is interfaced with Pythia [67]. Pythia estimates the hadronisation and adds the parton showering.

In the next step, the interactions of the particles generated with the detector are simulated. The CMS detector is modelled in great detail with Geant4 [68]. This software framework takes care of all particle-matter interactions, such as energy deposits or scattering processes. In its output, the CMS detector simulation based on Geant4 provides the same sort of signals as the actual collision data.

Finally, the simulated detector signals are handled in the same way as described in the previous sections for real data.

4.7.2 Event Weights

The simulated MC samples vary from processes with large cross sections to processes with very small cross sections. All MC samples are normalised to the integrated luminosity $\mathcal{L}_{\text{int}}$ recorded in data by applying an event weight

$$w = \frac{\sigma_{\text{MC}} \times \mathcal{L}_{\text{int}}}{N_{\text{gen}}} \tag{4.8}$$

where σ_{MC} is the theoretical cross section and N_{gen} the number of generated events. Since high event weights would lead to large statistical uncertainties on the final yields, the number of simulated events N_{gen} needs to be sufficiently large. On the other side, the full simulation of an event takes about 1 min and therefore the number of simulated events N_{gen} is constrained by the available computing facilities.

4.7.3 Corrections

The production of MC simulated samples is a computationally intense process. Aside the underlying theory, a number of assumptions are taken on the conditions during actual collisions, such as the PU scenario or particles' reconstruction efficiencies. Thus, the simulations are corrected to best fit the actual conditions as described below.

Lepton Trigger and Selection Efficiencies

The trigger menu used in the later analysis has changed during the run period. For this reason no trigger requirement was set on simulated events. Instead, simulated events are corrected to represent the trigger efficiencies of actual data. The presented analysis applies dilepton triggers, as described later in section 5.1.1. Their efficiencies are measured on events selected by orthogonal triggers, as described in reference [69], and applied as a weight on each simulated event.

As described later in section 5.1.2 further selection criteria are required on the leptons. The corresponding selection efficiencies are compared between data and MC simulation. With a tag-and-probe algorithm [70], the efficiencies are measured on prompt leptons originating from Z boson decays [71]. This algorithm uses one lepton from the $\mathrm{Z} \to \ell^+\ell^-$ decay as the *tag* to select events. From the second *probe* lepton the efficiency is measured. Similarly as for the trigger efficiency, the resulting scale factors are applied as modifications to the event weights.

Bottom Quark Jets

Among the hadronic jets, jets originating from bottom quarks can be identified as described in section 4.5.3. The corresponding tagging and misidentification efficiencies, which depend on the quark flavour, might differ between MC simulation and actual data. Instead of applying additional event weights, the CSV discriminator of each jet is corrected [64]. In this way, the b-tagging status of a jet can change

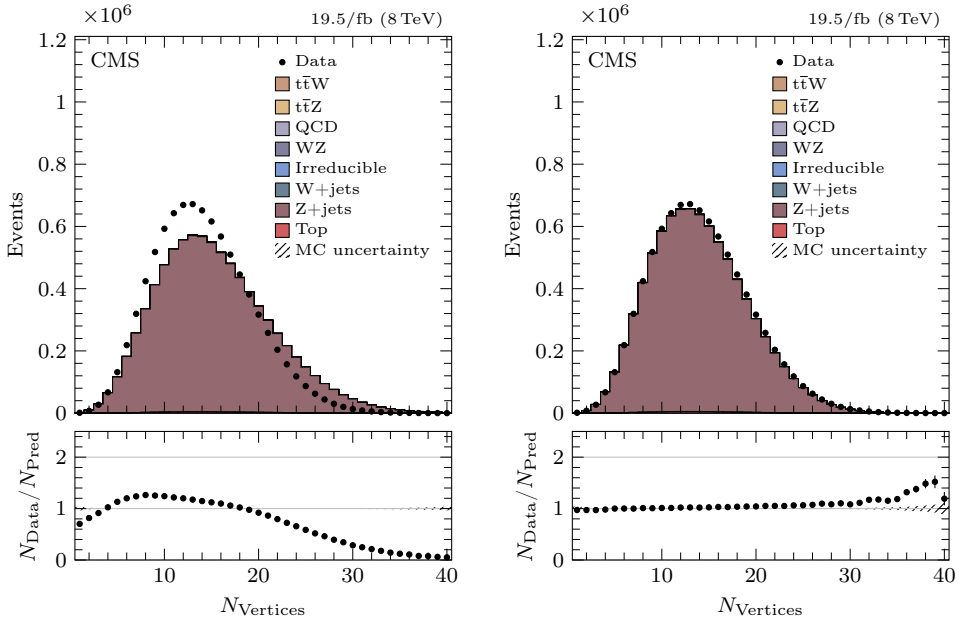

Figure 4.1: Number of primary vertices N_{Vertices} distributions before (left) and after (right) pileup reweighting for events which contain an opposite-sign lepton pair passing the tight selection criteria.

and thereby the number of b-tagged jets in an event, but the overall event weight stays the same.

Pileup

Multiple proton-proton collisions can take place in a bunch crossing, depending on the instantaneous luminosity. This leads to multiple reconstructed PVs. When generating MC simulations a certain PU scenario is assumed. Naturally, this does not reflect the conditions when data is recorded. Simulated events are reweighted so that the number of true PU interactions distributions match. In data, the number of true interactions is not known, but estimated using the instantaneous luminosity and the total proton-proton inelastic cross section. Compared to reweighting by the number of reconstructed vertices, this avoids biases by event selection criteria or differences between data and simulation in the UE and the reconstruction of the PV. Figure 4.1 shows the number of vertices distribution before and after reweighting simulated events for correct PU conditions. Since the correction is based on the number of true interactions, the distributions of this observable quantity N_{Vertices} disagree slightly.

Chapter 5

Cross Section Measurement

After recording 19.5/fb of proton-proton collision data at a centre-of-mass energy of 8 TeV and reconstructing physics objects from the detected signals, the data were further processed for individual physics analyses. With the theoretical principles of chapter 2 in place, the goal of this analysis is to study the $t\bar{t}W$ process and measure its cross section. The analysis uses an updated procedure of the analysis carried out at a centre-of-mass energy of 7 TeV, published in 2013 [72]. This chapter presents the strategy to find the signal, the different methods of estimating the background processes and the systematic uncertainties arising during the analysis. Using the updated analysis, the cross section is derived from the observed and predicted yields.

The analysis was performed in cooperation with analysis efforts targeting the $t\bar{t}Z$ process. The groups involved in the $t\bar{t}Z$ analysis are from University of California, Santa Barbara (UCSB), University of California, San Diego (UCSD), Fermi National Accelerator Laboratory (FNAL), and Rutgers University. The $t\bar{t}W$ and $t\bar{t}Z$ collaborative effort produced a combined measurement of the $t\bar{t}W$ and $t\bar{t}Z$ cross sections [8].

5.1 Object and Event Selection

A sketch of the $t\bar{t}W$ process with two leptons in the final state is shown in figure 5.1. Along with the two leptons, two hadronic jets originating from a W boson decay and two jets from bottom quark hadronisation are expected. Since the signal has an expected cross section of only a few hundred femtobarns, the event selection is very challenging. Events from background processes which are much more frequent,

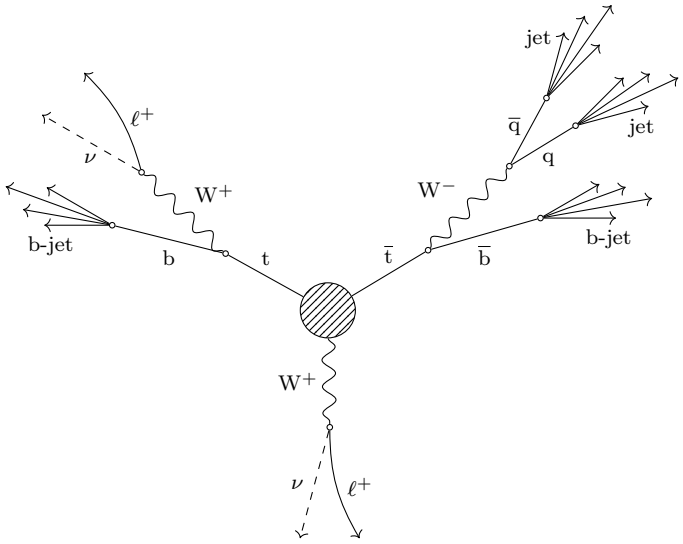

Figure 5.1: $t\bar{t}W$ topology with two same-sign leptons in the final state. The central circle represents the production mechanism discussed in section 2.4. Two W bosons of equal charge decay leptonically, resulting in two same-sign leptons. Four jets are present in the final state. Two of them originate from bottom quarks while the remaining are light-flavour jets from a hadronic W boson decay.

such as $t\bar{t}$ production, can give rise to a similar signature in the detector. The $t\bar{t}$ production cross section is $(241.5 \pm 8.5)\,\text{pb}$ [7], three orders of magnitude larger than the $t\bar{t}W$ cross section. Thus, effective handles are necessary to identify the signal and reduce background contributions.

The basic approach of the event selection is to target $t\bar{t}W$ events by selecting events with a lepton pair of same-signed electric charge which are both prompt and isolated. A lepton is prompt if its track is compatible with the signal PV. As a lepton only electrons and muons are considered in this dissertation. Taus are only included if they decay leptonically into an electron or muon, which has a probability of the order of 35 % [17]. Such a lepton pair is produced if the promptly generated W boson, as well as the equally charged W boson stemming from one of the top quarks, both decay via the process $W \to \ell\nu$. The same-sign criterion suppresses events from processes such as $t\bar{t}$ or Z+jets production since these feature opposite charged lepton pairs. The Z+jets process has a four orders of magnitude larger cross section than the $t\bar{t}W$ cross section. Thus, this requirement improves effectively the signal-to-background ratio. Requiring prompt isolated leptons aims to reject non-signal-like leptons such as leptons produced within hadronic jets. Events with lepton pairs having an invariant mass compatible with the mass of a Z boson are rejected. This further reduces contributions from processes

including the production of Z bosons, like WZ production, which has an order of magnitude larger cross section than the $t\bar{t}W$ signal. Furthermore, the invariant mass requirement ensures that the $t\bar{t}W$ and $t\bar{t}Z$ cross section measurements are statistically independent.

After these basic requirements, $t\bar{t}$ production remains the dominant background process. Its events can leave a signal-like signature in the detector if a lepton, which is not stemming promptly from the $t\bar{t}$ decay, carries the same charge as a prompt lepton. Thus, the identification of prompt leptons is crucial when selecting leptons to further reduce this sort of background. A second type of background is caused by mismeasurements of leptons' charge. Hence events with an opposite-sign lepton pair, which are much more frequent, can enter the signal selection if one of these leptons has a wrongly determined charge. Finally, processes which naturally result in two equally charged leptons are irreducible and contribute as background.

The analysis strategy includes splitting events into lepton flavour channels, to profit from the flavour dependence of some of the backgrounds, such as background stemming from non-prompt leptons or from mismeasurements of leptons' charge. Further, the yields are split by the charge of the lepton pair, since the $t\bar{t}W^+$ process has roughly a twice as large cross section as the $t\bar{t}W^-$ process [42] due to the abundance of up quarks compared to down quarks in proton-proton collisions.

In the following sections physics objects are defined. The challenge in defining these objects is to have a high signal purity, i.e. reject background as effectively as possible. On the other hand the efficiency should not suffer from too tight a selection, since the targeted signal is very rare.

5.1.1 Triggers

Since the analysis requires the presence of a same-sign lepton pair, events are selected by the HLT, requiring two leptons. In particular a dimuon, a dielectron and two cross-flavour triggers are applied. They apply thresholds on the transverse momenta $p_\perp^{\ell_1} > 17\,\text{GeV}$ and $p_\perp^{\ell_2} > 8\,\text{GeV}$ of the leading and subleading lepton, respectively.

5.1.2 Object Definitions

Based on the event reconstruction, shown in chapter 4, physics objects are defined in this section.

Electrons

After reconstructing electrons, as described in section 4.4, further thresholds are set to target signal-like electrons. As a baseline, electrons are required to have a transverse momentum of $p_\perp > 20\,\text{GeV}$ and a pseudorapidity of $|\eta| < 2.4$. Electrons in the region of the gap between EB and EE ($1.444\,2 < |\eta| < 1.566\,0$) are excluded. The increased requirement on the momentum with respect to the trigger threshold is to avoid inefficiencies.[1] Thresholds on the transverse and longitudinal impact parameters, $|d_0| < 0.1\,\text{mm}$ and $|d_z| < 2\,\text{mm}$, are set respectively. These select mostly prompt electrons and reject electrons originating from bottom quark decays. Since an accurate identification of the electron's charge is of fundamental importance for the analysis, it is measured in three ways, by the GSF, the CTF, and with the super cluster [56]. Only if their results are consistent, is the electron accepted.

On top of these general definitions, the PF relative isolation

$$I_{\text{rel}} = \frac{1}{p_\perp^\ell} \left(\sum_{\gamma,\, \Delta R<0.3} p_\perp^i + \sum_{\text{Hadrons},\, \Delta R<0.3} p_\perp^i \right) \tag{5.1}$$

offers a powerful handle to distinguish signal leptons and leptons from other sources. It measures the hadronic activity around the lepton. The parenthesised term in equation (5.1) is the sum of transverse momenta of all photons and hadrons in a cone of $\Delta R < 0.3$ around the lepton's direction and is divided by the lepton's transverse momentum. A signal lepton stemming from a prompt W boson is not expected to feature a lot of hadronic activity, unlike electrons from processes such as decays of B mesons into leptons. In figure 5.2 the relative isolation spectra of electrons are shown for simulated $\text{t}\bar{\text{t}}$ and QCD processes. Electrons from $\text{t}\bar{\text{t}}$ production peak towards zero, indicating their origin from a prompt W boson, whereas non-signal type electrons stemming from QCD processes are distributed more broadly with a maximum at around 0.2. A threshold of $I_{\text{rel}} < 0.05$ shows suitable separation and defines a *tight* signal electron.

To estimate the background contribution to the tight signal electrons, a second category is defined, so-called *loose* electrons, which are meant to include electrons not stemming from prompt W bosons. Their threshold on the relative isolation is $I_{\text{rel}} < 0.6$. The background contribution to the tight signal electrons is estimated using the event ratio between these two categories, as described later in section 5.2.1.

[1] The transverse momentum used by the trigger might differ from the final reconstructed momentum utilised in the analysis. This effect results in inefficiencies close to the trigger threshold.

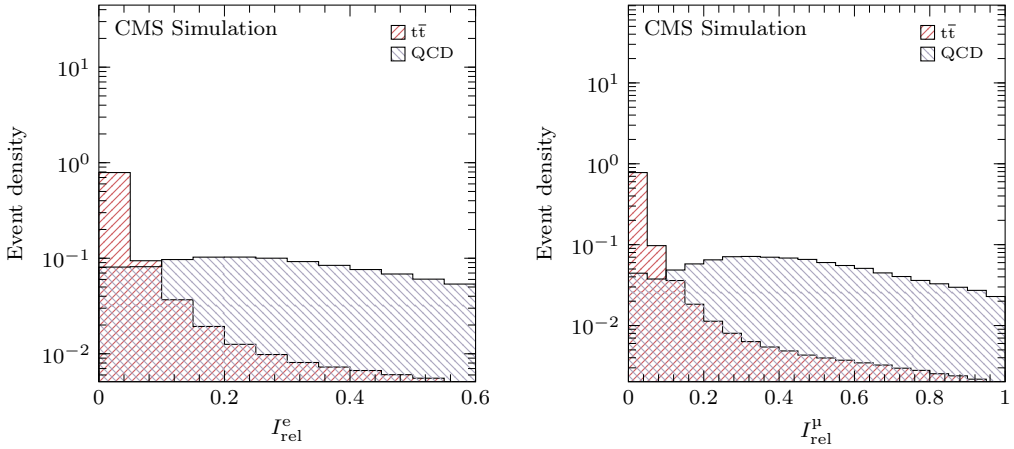

Figure 5.2: Relative isolation distribution for loose electrons (left) and loose muons (right) from $t\bar{t}$ and QCD processes. The spectra are normalised to unity.

A third category of electrons is defined to reject events including leptonic Z decays. These *veto* electrons have very loose definitions. A threshold of $p_\perp > 10\,\text{GeV}$ is set on their transverse momentum and a relative isolation of $I_{\text{rel}} < 0.2$ is required. This ensures a more inclusive collection of electrons and renders the Z veto more efficient.

Muons

A similar baseline is chosen for muons, as for electrons. Reconstructed muons, as described in section 4.3, are required to pass a transverse momentum threshold of 20 GeV and a pseudorapidity threshold of $|\eta| < 2.4$. Furthermore, thresholds on the transverse and longitudinal impact parameters, $|d_0| < 0.05\,\text{mm}$ and $|d_z| < 1\,\text{mm}$, are applied respectively. Due to the higher precision of the muon's momentum measurement, its charge is measured precisely enough and no further requirements are necessary. Likewise for electrons, three muon categories are defined using the relative isolation. Tight muons require a relative isolation of $I_{\text{rel}} < 0.05$, whereas the threshold is released to $I_{\text{rel}} < 1.0$ for loose muons. Simulated shapes of the muon relative isolation spectra from $t\bar{t}$ and QCD processes are illustrated in figure 5.2, representing a similar situation as in the case of electrons. The third category, veto muons, are defined by a lower threshold on their transverse momentum of $p_\perp > 10\,\text{GeV}$ and a relative isolation of $I_{\text{rel}} < 0.2$.

Jets

Jets reconstructed from PF candidates by the anti-k_t algorithm with a radius parameter of 0.5, see section 4.5, are selected for the analysis. A transverse momentum threshold of $p_\perp > 30\,\text{GeV}$ is applied to the reconstructed jets and a pseudorapidity of $|\eta| < 2.4$ is accepted. Further, jets are rejected if a tight signal lepton is within a cone of $\Delta R < 0.4$ around the direction of the jet. This is to avoid possible double counting of objects, since leptons are among the PF candidates used by the jet clustering algorithm.

When selecting jets with low transverse momentum, jets originating from PU are likely instead of the decay of interest. To characterise the probability that a jet comes from PU the β^* variable is used. It is defined as [73]

$$\beta^* = \frac{\sum_{i \in C'} p_\perp^i}{\sum_{i \in C} p_\perp^i} \tag{5.2}$$

where C is the set of all charged PF candidates in a jet and C' its subset with candidates associated to another PV. A value close to zero indicates that the jet is originating from the same PV, whereas values close to one refer to PU jets. To reject PU jets a threshold of $\beta^* < 0.2 \times \log\left(N_{\text{Vertices}} - 0.67\right)$ is applied.

The decay chain of the targeted signal process in this dissertation involves the production of bottom quarks, see section 2.4.2. Therefore, the identification of b-jets is an important handle to reject background events. As described in section 4.5.3, the CSV algorithm is used for this purpose. The algorithm offers multiple working points with different misidentification probabilities. On the selected jets, a threshold on the CSV discriminator is applied which corresponds to the medium working point.

5.1.3 Signal Region

In figure 5.1 a sketch of the targeted $\text{t}\bar{\text{t}}\text{W}$ decay topology is shown. The two equally charged W bosons both decay leptonically in the chosen decay mode, as described in section 2.4.2. This leaves two leptons of same charge and two neutrinos leading to missing transverse energy in the detector. The four quarks manifest themselves as hadronic jets.

The analysis is performed on different event selections. First, a rather basic *loose selection* is defined. This region is enriched in backgrounds and is meant to verify the background prediction methods. The *preselection* signal region targets signal

events. It is used as a baseline for the optimisation of tighter thresholds, which finally define the *signal region*.

Loose Selection

In this first selection only basic thresholds are applied together with the same-sign signal lepton criteria. Selected events are required to have two leptons of same-signed charge which pass the tight lepton criteria. Events which feature a combination of a lepton and a veto lepton with an invariant mass close to the mass of the Z boson $|m_{\ell\ell} - m_{\mathrm{Z}}| < 15\,\mathrm{GeV}$ are rejected to minimise the contribution of events which involve the production of a Z boson, such as the WZ process. Moreover, this ensures that the selection in this analysis is orthogonal to the selection used in the $\mathrm{t\bar{t}Z}$ cross section measurement, which is important for a later combination of the two measurements. Furthermore, two jets are required.

Table 5.1 provides an overview of the contributing processes in this region. Over all three channels, the WZ process represents the dominant background yield. Its events can naturally feature two prompt and isolated leptons. The second largest yield stems from Z+jets production. It contributes mainly with $\mathrm{Z} \to \mathrm{e^+e^-}$ events in which the charge of an electron is mismeasured. The charge measurement of muons is more accurate and therefore contributions to these channels are suppressed. W+jets production has a larger cross section, but yields only one prompt lepton and therefore results in a minor contribution.

About 10 % of the total yield originates from $\mathrm{t\bar{t}}$ events. This process can contribute either through charge mismeasurements if both top quarks decay leptonically or, more likely, if a top quark decays leptonically and a second lepton of same charge is produced within one of the b-jets. Events from single top quark production add to the total yield in a similar manner, but more rarely due to the smaller cross section.

At the same level as the yield from $\mathrm{t\bar{t}}$ production are the signal yield and contributions from $\mathrm{W^{\pm}W^{\pm}}$ production. This process yields two equally signed leptons and involves the associated production of a quark pair resulting in two jets. Production of oppositely charged W pairs contributes only via charge mismeasurements. Thus, the expected yields are very small. Yields from ZZ production are low due to the small cross section. Other diboson and triboson processes can yield lepton pairs of same-sign charge but have generally very small cross sections.

A small fraction of events at this stage originate from $\mathrm{t\bar{t}}$ pairs produced in association with a Z or H boson. The yield of associated production of top pairs with a photon or W boson pair is very low. The latter has a predicted cross section two

Process	μμ		eμ		ee	
$t\bar{t}$	7.4	± 1.3	25.0	± 2.1	17.2	± 1.8
Single t	0.5	± 1.4	3.1	± 2.1	0.5	± 1.4
W+jets	0	± 18	1	± 26	9	± 22
Wbb+jets	1.0	± 0.8	1.2	± 0.9	1.2	± 0.8
Z+jets	0	± 6	11	± 9	57	± 16
γ+jets	0.0	± 0.6	0.4	± 0.8	0.8	± 0.9
WW	0.00	± 0.11	0.12	± 0.15	0.05	± 0.13
WZ	24.1	± 0.6	54.6	± 0.8	26.7	± 0.6
ZZ	2.04	± 0.04	5.54	± 0.07	3.31	± 0.05
$W^{\pm}W^{\pm}$	12.8	± 0.8	23.3	± 1.1	9.0	± 0.7
$W\gamma^{*}$	1.6	± 0.7	1.2	± 0.6	0.00	± 0.33
Triboson	3.16	± 0.19	6.12	± 0.27	2.88	± 0.21
WW (DPS)	0.44	± 0.10	0.48	± 0.10	0.22	± 0.08
$t\bar{t}Z$	3.11	± 0.28	6.1	± 0.4	2.86	± 0.26
$t\bar{t}\gamma$	0.07	± 0.09	1.91	± 0.26	1.43	± 0.23
$t\bar{t}H$	3.93	± 0.34	7.5	± 0.4	3.67	± 0.33
$t\bar{t}WW$	0.268	± 0.008	0.471	± 0.010	0.197	± 0.007
tZ	0.397	± 0.028	0.98	± 0.04	0.530	± 0.031
Sum	61	± 19	150	± 27	137	± 28
$t\bar{t}W$	12.6	± 0.6	23.2	± 0.8	9.4	± 0.5

Table 5.1: Overview of contributing processes in the three lepton flavour channels, normalised to an integrated luminosity of 19.5/fb. All processes are taken from MC simulation, requiring their events to pass loose selection criteria. Errors indicate statistical uncertainties arising from the number of simulated events.

orders of magnitude smaller than the $t\bar{t}W$ cross section. In case of the $t\bar{t}\gamma$ process, electrons are produced in photon conversions. This can result in a same-sign lepton pair with a lepton from the $t\bar{t}$ decay.

Background processes clearly dominate the loose selection. It is used to check if the background prediction methods work well when comparing to data.

Preselection Signal Region

The preselection signal region is a subset of the previously defined loose selection. By increasing the thresholds on the jets, the $t\bar{t}W$ signal is enhanced and diboson background is suppressed. The preselection requires three jets out of which at least one is identified as a b-jet. Requiring a b-jet targets events including the production of a top quark, since these quarks decay via the process $t \to bW$. The jet thresholds are chosen this way to account for possible inefficiencies in the reconstruction of the used objects. Event yields from MC simulation are listed in table 5.2. Signal events represents the largest fraction with about 35 % while $t\bar{t}$ production is the dominant background and contributes with about 25 % to the total yield.

Signal Region Optimisation

To further isolate the signal, tighter threshold cuts are investigated. In a first step, signal properties are compared to the main background at this stage, which is stemming from $t\bar{t}$ production. The kinematic variables studied are:

- leading lepton transverse momentum $p_{\perp}^{\ell_1}$
- subleading lepton transverse momentum $p_{\perp}^{\ell_2}$
- sum of jet transverse momenta $H_{\perp} = \sum_i p_{\perp}^{\mathrm{j}_i}$
- missing transverse energy $\not{E}_{\perp}$
- number of jets N_{j}
- number of b-jets N_{b}

An optimal variable should have different distribution shapes for signal and background which allows suppressing the background contribution without loosing much signal efficiency. To quantify this ability the separation $\langle S^2 \rangle$ is used. It is

Process	μμ	eμ	ee
$t\bar{t}$	2.8 ± 0.9	9.6 ± 1.4	6.6 ± 1.2
Single t	0.0 ± 1.1	0.6 ± 1.4	0.5 ± 1.3
Wbb+jets	0.4 ± 0.6	0.0 ± 0.5	0.0 ± 0.5
Z+jets	0 ± 4	0 ± 4	8 ± 7
γ+jets	0.00 ± 0.10	0.00 ± 0.10	0.05 ± 0.12
WZ	0.70 ± 0.10	1.73 ± 0.15	0.73 ± 0.10
ZZ	0.059 ± 0.008	0.153 ± 0.012	0.096 ± 0.010
$W^{\pm}W^{\pm}$	0.44 ± 0.20	0.93 ± 0.25	0.34 ± 0.19
Triboson	0.16 ± 0.10	0.38 ± 0.12	0.16 ± 0.10
WW (DPS)	0.000 ± 0.025	0.000 ± 0.025	0.012 ± 0.031
$t\bar{t}Z$	1.89 ± 0.22	3.76 ± 0.31	2.05 ± 0.23
$t\bar{t}\gamma$	0.04 ± 0.08	1.21 ± 0.21	0.87 ± 0.19
$t\bar{t}H$	1.65 ± 0.24	3.01 ± 0.30	1.79 ± 0.24
$t\bar{t}WW$	0.188 ± 0.007	0.330 ± 0.008	0.141 ± 0.006
tZ	0.122 ± 0.016	0.337 ± 0.025	0.192 ± 0.019
Sum	8 ± 5	22 ± 5	21 ± 7
$t\bar{t}W$	7.3 ± 0.4	14.0 ± 0.6	5.7 ± 0.4

Table 5.2: Expected event yields from different processes after applying preselection criteria, normalised to an integrated luminosity of 19.5/fb. All yields are derived from MC simulation. Errors indicate the statistical uncertainties arising from the number of simulated events.

Rank	Variable	Separation
1	$p_{\perp}^{\ell_2}$	1.84×10^{-1}
2	$p_{\perp}^{\ell_1}$	1.54×10^{-1}
3	N_{b}	8.70×10^{-2}
4	$H_{\perp}$	8.22×10^{-2}
5	$\not{E}_{\perp}$	8.00×10^{-2}
6	N_{j}	1.82×10^{-2}

Table 5.3: Separation power of different variables determined with the TMVA package [75] of ROOT.

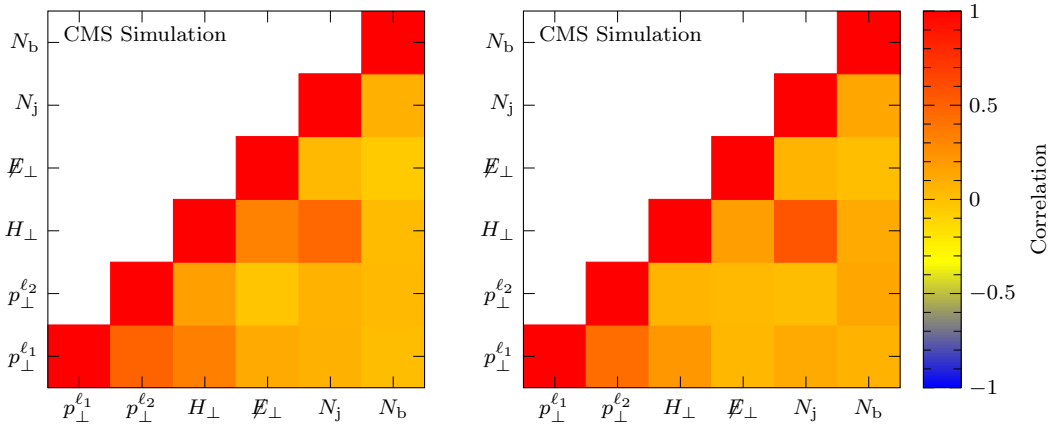

Figure 5.3: Correlation matrices of the $\mathrm{t\bar{t}W}$ signal (left) and $\mathrm{t\bar{t}}$ background (right).

defined as [74]

$$\left\langle S^2 \right\rangle = \frac{1}{2} \int \frac{\left(\hat{x}_S(x) - \hat{x}_B(x)\right)^2}{\hat{x}_S(x) + \hat{x}_B(x)} \, \mathrm{d}x \tag{5.3}$$

where $\hat{x}_S$ and $\hat{x}_B$ are the signal and background distributions of the variable x. Table 5.3 lists the separation power of the studied variables. In figure 5.3 the correlations between the studied variables are shown. For the further steps the variables $H_{\perp}$ and $p_{\perp}^{\ell_2}$ which have a low correlation of 0.16 and show a high separation power are selected to optimise their thresholds. The number of b-jets is not considered further since a higher threshold would reduce the signal efficiency dramatically. In figure 5.4 the expected shapes from MC simulation are shown for the $p_{\perp}^{\ell_2}$ and $H_{\perp}$ spectra in the preselection signal region. Events from $\mathrm{t\bar{t}}$ production contribute mainly to the phase space with low lepton transverse momenta or smaller values of $H_{\perp}$. The signal spectra are generally harder. Thus, higher thresholds on these variables are expected to improve the signal-to-background

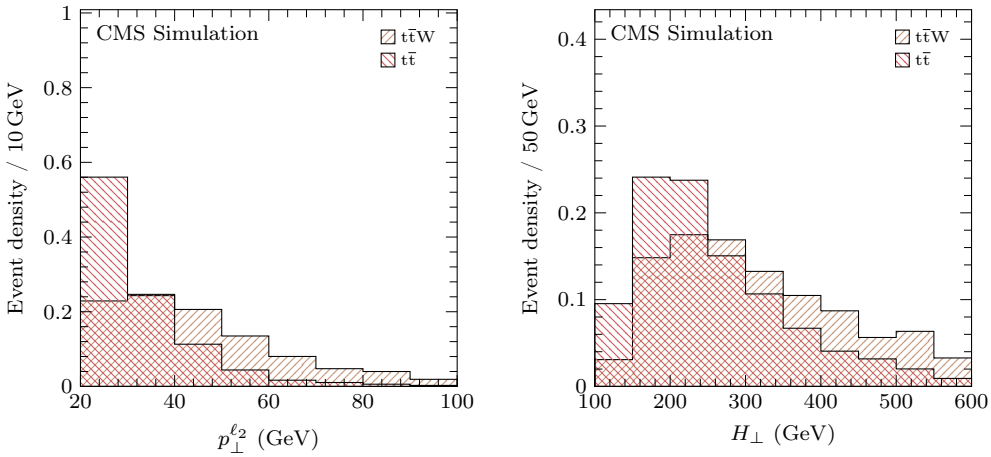

Figure 5.4: Expected shapes of subleading lepton transverse momentum (left) and $H_\perp$ variable (right) in MC simulation. The $t\bar{t}W$ signal is compared to $t\bar{t}$ background in the preselection signal region, see section 5.1.3. In case of the $t\bar{t}$ process, the leptons' relative isolation thresholds are released to $I_{\text{rel}} < 0.35$ to reduce statistical uncertainties, as described in the text. Each spectrum is normalised to unity.

ratio.

To optimise the thresholds the TMVA package [75] of ROOT [76] was used. A two-dimensional scan was performed by the TMVA package to find the pair of thresholds on the selected variables which maximises the background rejection at a given signal efficiency. This scan was performed for signal efficiencies from 25 % to 100 % in steps of 5 %. Only the dominant $t\bar{t}$ background was considered. This avoids biasing the results by optimising on simulated datasets which have high event weights. To further reduce the statistical uncertainties, the tight threshold on the lepton isolation was released to $I_{\text{rel}} < 0.35$. The resulting sets of thresholds are reported in table 5.4.

The next step is to predict the signal and background rates for each set of thresholds, using the background estimation techniques, and evaluate the associated systematic uncertainties. Selected events are further split according to the flavour and the charge of the lepton pair, exploiting the signal charge asymmetry. A profile likelihood method, as described in section 5.3.3, is used to compute the expected significance. The method is performed in three different ways: using the integrated yields, using the yields split by lepton flavour, and after dividing into six lepton charge flavour channels. The point which maximises the expected significance is chosen and the thresholds on the subleading lepton transverse momentum of $p_\perp > 40\,\text{GeV}$ and the hadronic activity of $H_\perp > 155\,\text{GeV}$ are added on top of the preselection to define the final *signal region*. This selection yields a signal efficiency

$H_{\perp}^{\min}$ (GeV)	$p_{\perp}^{\min}$ (GeV)	ε (%)	Z_{exp}
162	58	23.9 ± 1.1	1.5
139	54	29.6 ± 1.2	1.7
141	51	33.4 ± 1.2	1.7
151	47	40.3 ± 1.3	1.8
154	44	44.2 ± 1.3	1.8
158	41	50.9 ± 1.3	1.8
153	39	55.1 ± 1.3	1.7
172	35	61.0 ± 1.3	1.6
173	33	64.8 ± 1.2	1.6
155	32	70.0 ± 1.2	1.6
161	29	74.8 ± 1.1	1.4
125	29	79.7 ± 1.0	1.3
141	26	85.6 ± 0.9	1.3
125	24	90.3 ± 0.8	1.2
161	20	93.4 ± 0.6	1.2
125	20	99.0 ± 0.3	1.1

Table 5.4: Optimised selection thresholds at different signal efficiencies ε and resulting expected significances Z_{exp}.

of 50 %. As a cross check the expected uncertainty on the $t\bar{t}W$ cross section is quantified for each point as well. The chosen selection corresponds to the minimal cross section uncertainty. Figure 5.5 shows the expected significance and expected uncertainty on the cross section. The distributions display further the benefit in significance and uncertainty when splitting by the charge of the lepton pair.

5.2 Background and Signal Estimation Methods

The background processes contributing to the selected event yields vary from rare SM processes to processes with rather large cross sections. An overview of the contributing processes is given in table 5.1. Three distinctly different sources of backgrounds contribute after the final selection requirements. Two are related to the limited information from the detector. The third background originates from processes which naturally yield same-sign dileptons in the final state. The methods to estimate these background rates are discussed in the following sections.

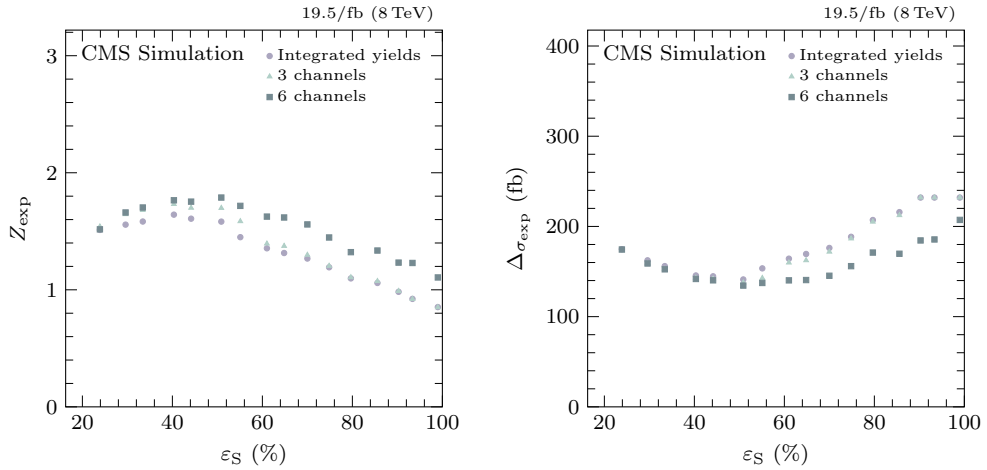

Figure 5.5: Expected significance (left) and cross section uncertainty (right) for the optimised selections at different signal efficiencies. The three series of points correspond to the methods how the yields are split into lepton flavour and charge channels.

5.2.1 Fake Leptons

The fake lepton background consists of events in which at least one of the same-sign leptons does not originate from the prompt W bosons. These leptons are real leptons which mostly originate from bottom quark decays in which the bottom quark decays into a lighter quark by emitting a W boson which decays semi-leptonically. Another less dominating source of this background arises in the electron reconstruction. A pion can be misidentified as a lepton by processes like $\pi^0 \to \gamma\gamma$ giving an ECAL deposit within a jet and a charged track then being mismatched with this energy deposit or a charge exchange reaction $\pi^+ \to \pi^0 e^+ \nu_e$ where the track of the π^+ is matched to the ECAL deposit.

Overall, the dominant physical process contributing to this background is top pair production in which one lepton originates from leptonic W boson decay at the PV, and the bottom quark from the other top quark decays leptonically by producing an electron or muon with the same electric charge.

A well established technique [3, 4, 77, 78] is applied to estimate this type of background. It relies on measurements on actual proton-proton collision data, rather than on pure MC simulation.

Method

Both processes described above, which produce fake leptons, have in common that the leptons are surrounded by hadronic activity from either an associated jet or a light-flavoured quark of the bottom quark decay. On the other hand, prompt leptons, i.e. leptons originating from a prompt $W \to \ell\nu$ decay, do not generally feature a lot of hadronic activity in their proximity. This means the lepton relative isolation variable, defined in equation (5.1), is a powerful discriminator to distinguish real, prompt signal leptons from fake leptons.

The goal of the background estimation method is to calculate the probability for non-isolated fake leptons to «leak» into the signal selection region of prompt, isolated leptons. Since hadronisation processes are difficult to simulate very precisely and fake leptons are mostly produced in such processes, their isolation variable is believed to be not very well modelled in MC simulation. For this reason the implementation of a data-driven method, the fake-rate method, was chosen [79]. It relies on measurements performed in orthogonal regions of phase space and extrapolates from the sidebands of the isolation variable in the signal region to estimate the fake lepton background. Another reason to rely on a data-driven method rather than on simulation is the large statistical uncertainties on the MC simulations of contributing processes such as W+jets and QCD, see table 5.1.

By loosening the isolation threshold on the *tight* signal leptons, *loose* leptons are defined. The method's basic concept is to relate the number of fake and prompt leptons with the observable number of loose and tight leptons. The assumption is taken that the probability for a fake lepton to pass the tight selection, the fake ratio f, is universal. This implies that this ratio can be measured in the isolation spectrum of a region enriched in fake leptons and the same ratio may be applied to the isolation sidebands of the final signal region. Thus, the fake ratio

$$f = \frac{N_{\mathrm{t}}}{N_{\mathrm{t}} + N_{\mathrm{l}}} \tag{5.4}$$

can be measured on a control sample in which all leptons are assumed to be fake leptons. N_{t} describes the number of events with a lepton passing the tight lepton requirements and N_{l} is defined to be the number of events with a lepton fulfilling the loose, but not the tight criteria. When making the simplification of single lepton events the contribution due to fake leptons to the signal region

$$N_{\text{Fake lepton}} = \frac{f}{1-f} \times N_{\mathrm{l}} \tag{5.5}$$

can be estimated from the sideband yield in the signal region, N_{l}.

Since not all prompt leptons pass the tight requirements, the prompt ratio

$$p = \frac{N_{\mathrm{t}}}{N_{\mathrm{t}} + N_{\mathrm{l}}} \tag{5.6}$$

is derived from a control region with mostly prompt signal type leptons, the analogue of the fake ratio f. It describes the probability that a prompt lepton passes the tight selection thresholds.

When taking into account that the signal consists of two leptons and the lepton ratios actually depend on the lepton's flavour, transverse momentum, and pseudorapidity, this calculation becomes a little more complex. Events are divided into four categories which classify if the leptons pass the loose (l) or tight (t) selection criteria. This defines the corresponding yields N_{tt}, N_{tl}, N_{lt}, and N_{ll}, where the indices refer to the two leptons. Similarly, N_{pp}, N_{pf}, N_{fp}, and N_{ff} define the yields of the four combinations in which the two leptons are prompt (p) or fake (f). The sum of the four categories

$$\begin{aligned} N &= N_{\mathrm{pp}} + N_{\mathrm{pf}} + N_{\mathrm{fp}} + N_{\mathrm{ff}} && (5.7)\\ &= N_{\mathrm{tt}} + N_{\mathrm{tl}} + N_{\mathrm{lt}} + N_{\mathrm{ll}} && (5.8) \end{aligned}$$

defines the total yield. Using the two lepton probabilities $p_i = p(\ell_i)$ and $f_i = f(\ell_i)$ the contribution to the tight-loose categories can be written as a function of the yields N_{pp}, N_{pf}, N_{fp}, and N_{ff}

$$\begin{pmatrix} N_{\mathrm{tt}} \\ N_{\mathrm{tl}} \\ N_{\mathrm{lt}} \\ N_{\mathrm{ll}} \end{pmatrix} = \begin{pmatrix} p_1 p_2 & p_1 f_2 & f_1 p_2 & f_1 f_2 \\ p_1 \bar{p}_2 & p_1 \bar{f}_2 & f_1 \bar{p}_2 & f_1 \bar{f}_2 \\ \bar{p}_1 p_2 & \bar{p}_1 f_2 & \bar{f}_1 p_2 & \bar{f}_1 f_2 \\ \bar{p}_1 \bar{p}_2 & \bar{p}_1 \bar{f}_2 & \bar{f}_1 \bar{p}_2 & \bar{f}_1 \bar{f}_2 \end{pmatrix} \begin{pmatrix} N_{\mathrm{pp}} \\ N_{\mathrm{pf}} \\ N_{\mathrm{fp}} \\ N_{\mathrm{ff}} \end{pmatrix} \tag{5.9}$$

where $\bar{p}_i = 1 - p_i$ and $\bar{f}_i = 1 - f_i$. As in reference [79] the matrix is inverted and the prompt and fake lepton contribution

$$\begin{pmatrix} N_{\mathrm{pp}} \\ N_{\mathrm{pf}} \\ N_{\mathrm{fp}} \\ N_{\mathrm{ff}} \end{pmatrix} = \frac{1}{(p_1 - f_1)(p_2 - f_2)} \begin{pmatrix} \bar{f}_1 \bar{f}_2 & -\bar{f}_1 f_2 & -f_1 \bar{f}_2 & f_1 f_2 \\ -\bar{f}_1 \bar{p}_2 & \bar{f}_1 p_2 & f_1 \bar{p}_2 & -f_1 p_2 \\ -\bar{p}_1 \bar{f}_2 & \bar{p}_1 f_2 & p_1 \bar{f}_2 & -p_1 f_2 \\ \bar{p}_1 \bar{p}_2 & -\bar{p}_1 p_2 & -p_1 \bar{p}_2 & p_1 p_2 \end{pmatrix} \begin{pmatrix} N_{\mathrm{tt}} \\ N_{\mathrm{tl}} \\ N_{\mathrm{lt}} \\ N_{\mathrm{ll}} \end{pmatrix} \tag{5.10}$$

can be predicted using the measurable quantities on the right side of the equation. Finally, the background yield in the tight signal region due to fake leptons

$$N_{\text{Fake lepton}} = p_1 f_2 N_{\mathrm{pf}} + f_1 p_2 N_{\mathrm{fp}} + f_1 f_2 N_{\mathrm{ff}} \tag{5.11}$$

can be predicted.

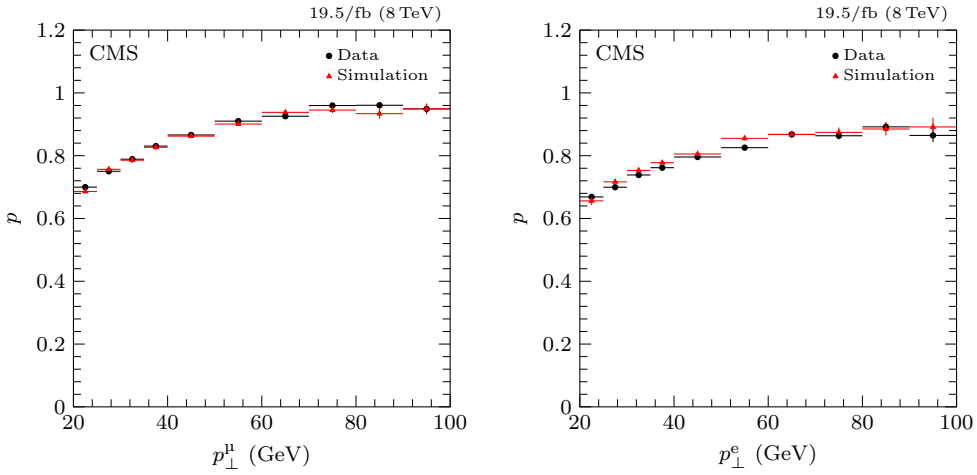

Figure 5.6: Prompt ratios for muons (left) and electrons (right) as functions of their transverse momentum $p_\perp$.

Prompt Ratio Measurement

To measure the prompt ratio, a region in which all leptons are expected to be prompt is defined. The prompt lepton control region uses $Z \to \ell^+\ell^-$ events. It requires two loose opposite-sign, same-flavour leptons with $|m_{\ell\ell} - m_Z| < 15\,\text{GeV}$ and no missing transverse energy ($\not{E}_\perp < 20\,\text{GeV}$). Furthermore, at least two jets with $p_\perp^j > 20\,\text{GeV}$ are required to select events with an overall similar hadronic activity as the signal. The prompt ratio

$$p = \frac{N_t}{N_t + N_l} \tag{5.12}$$

is measured in bins of the softer lepton's transverse momentum. In figure 5.6 the measured ratio as a function of the lepton's transverse momentum is compared to simulation. The measured ratios are found in agreement for both muons and electrons. On average, a prompt ratio of $0.803\,7 \pm 0.001\,2$ and $0.750\,0 \pm 0.001\,5$ is found for muons and electrons, respectively.

Fake Ratio Measurement

To measure the fake ratio, a region with mostly fake leptons is required. QCD events fulfil this requirement since they are expected to have only hadronic jets and no prompt leptons in the final state. Therefore, the control region targets QCD dijet events in which a fake lepton originates from one of the jets.

Events are selected from prescaled single lepton triggers and are required to include a loose lepton and a second jet. The single electron trigger sets a threshold on the electron's transverse momentum of $p_{\perp}^{\mathrm{e}} > 17\,\mathrm{GeV}$ and requires a jet with transverse momentum $p_{\perp}^{\mathrm{j}} > 30\,\mathrm{GeV}$. Two triggers are used to select muons. The first one selects events comprising a muon with transverse momentum $p_{\perp}^{\mu} > 24\,\mathrm{GeV}$ and pseudorapidity $\eta < 2$. A second trigger with a transverse momentum threshold of $p_{\perp}^{\mu} > 17\,\mathrm{GeV}$ is chosen for the phase space not covered by the first trigger. The second trigger is not used exclusively since it has a higher prescale and would therefore increase the statistical uncertainty of the lepton ratio measurement. Triggers are usually not fully efficient close to their threshold. Thus, the selected lepton's transverse momentum is required to be $p_{\perp}^{\ell} > 20\,\mathrm{GeV}$ to avoid possible inefficiencies.

Final states with one lepton and one jet can also originate directly from W+jets events. Also, in Z+jets events, if one of the leptons from the Z boson decay is not measured, such a process can contaminate the QCD region in which the fake ratio is measured. Since such events contain a prompt lepton, this contamination artificially increases the fake ratio by introducing isolated leptons into the QCD region. Since the leptonic W boson decay includes the production of a neutrino, the W+jets contribution is reduced by an upper threshold on the missing transverse energy of $\not{E}_{\perp} < 20\,\mathrm{GeV}$, as well as a cut on the electron transverse mass of $m_{\perp}^{\mathrm{e}} < 20\,\mathrm{GeV}$ or $m_{\perp}^{\mu} < 15\,\mathrm{GeV}$ for muons respectively. The transverse mass $m_{\perp}$ is defined as

$$m_{\perp} = \sqrt{2 p_{\perp}^{\ell} \not{E}_{\perp} (1 - \cos\phi)} \tag{5.13}$$

where ϕ is the angle between the directions of the lepton and missing momentum. In QCD dijet events which pass these thresholds, the jet faking a lepton is expected to have opposite direction of the second jet. For this reason, events containing exactly one jet with $p_{\perp}^{\mathrm{j}} > 40\,\mathrm{GeV}$ which is $|\Delta\phi| > 2$ away from the lepton are selected. This requirement on the second jet further reduces the contributions from W+jets and Z+jets events.

Figure 5.7 shows the missing transverse energy and transverse mass spectra in the control region with released threshold on the variable itself, respectively, for electrons passing loose and tight selection thresholds. The expected contributions from QCD, W+jets, and Z+jets processes are taken from MC simulation. Their yields are normalised to the data by a template fit which determines an individual normalisation factor for each process. In the selected events with an electron passing the tight criteria a non-negligible contribution from electroweak processes is observed.

From figure 5.7 one can see that the contributions from W+jets and Z+jets processes is not sufficiently suppressed by the requirements on $\not{E}_{\perp}$ and $m_{\perp}$. Therefore,

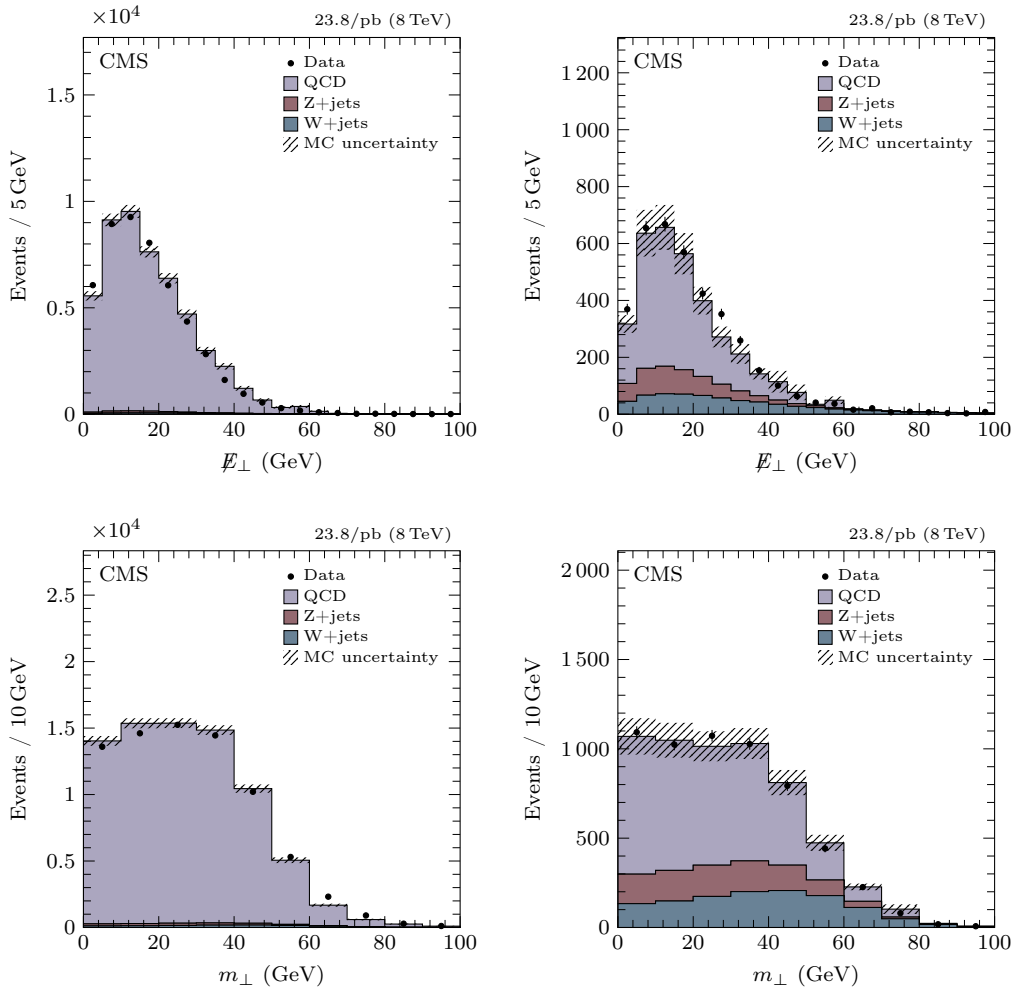

Figure 5.7: Missing transverse energy $\not\!\!E_\perp$ (top row) and transverse mass $m_\perp$ (bottom row) distributions for events selected by the fake control region, in which the electron passes the loose (left) and tight (right) criteria. The threshold on the plotted variable is released, respectively. The predictions of QCD events and electroweak processes are taken from MC simulations and fitted to data in a template fit.

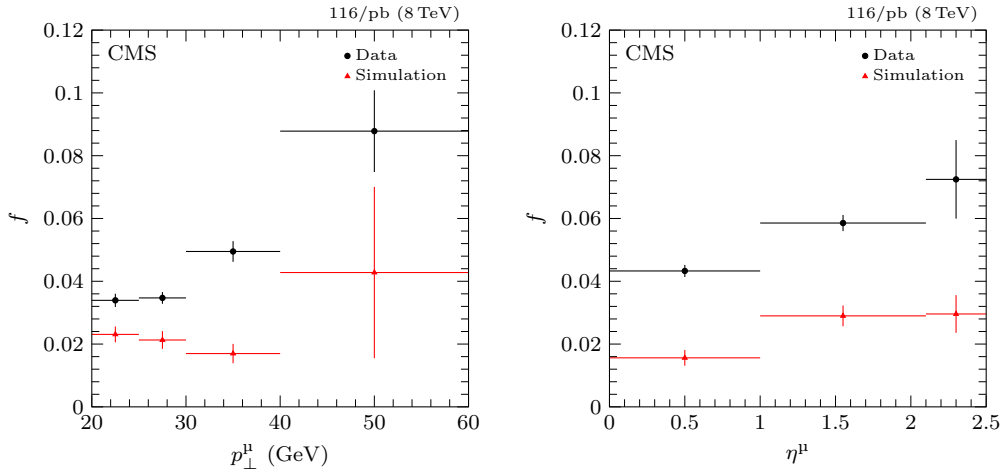

Figure 5.8: Misidentified muon ratios as a function of muon transverse momentum $p_\perp$ (left) and pseudorapidity η (right) after correcting for contributions from electroweak processes.

their MC yields are subtracted from the data measurement to correct for this electroweak contamination. The lepton fake ratio

$$f = \frac{N_\mathrm{t}^\mathrm{Data} - N_\mathrm{t}^\mathrm{W+jets} - N_\mathrm{t}^\mathrm{Z+jets}}{N_\mathrm{t}^\mathrm{Data} + N_\mathrm{l}^\mathrm{Data} - \left(N_\mathrm{t}^\mathrm{W+jets} + N_\mathrm{l}^\mathrm{W+jets}\right) - \left(N_\mathrm{t}^\mathrm{Z+jets} + N_\mathrm{l}^\mathrm{Z+jets}\right)} \tag{5.14}$$

is derived from the corrected yields. The corrected ratios are shown in figure 5.8 for muons and for electrons in figure 5.9 as functions of lepton's transverse momentum and pseudorapidity. As a comparison, the plots include the fake ratios derived from MC simulation. The simulation includes all processes listed in table 5.1, as well as QCD processes. The latter have rather large event weights which lead to the large uncertainties in the simulated fake ratios. This fact together with the assumption that the isolation variable might not accurately be modelled in simulation can explain the disagreement between the data and simulation. Pure QCD events, which are targeted by the fake ratio measurement, predict a nearly flat ratio as a function of the lepton's transverse momentum in MC simulation. Therefore, the fake ratio distribution is assumed flat for lepton's transverse momentum $p_\perp^\ell > 40\,\mathrm{GeV}$.

Systematic Uncertainty

The method's assumption of a fake rate depending only on the lepton's transverse momentum and pseudorapidity is only true at first order. The fake ratio also depends on the underlying parton's flavour and momentum, an effect which is not

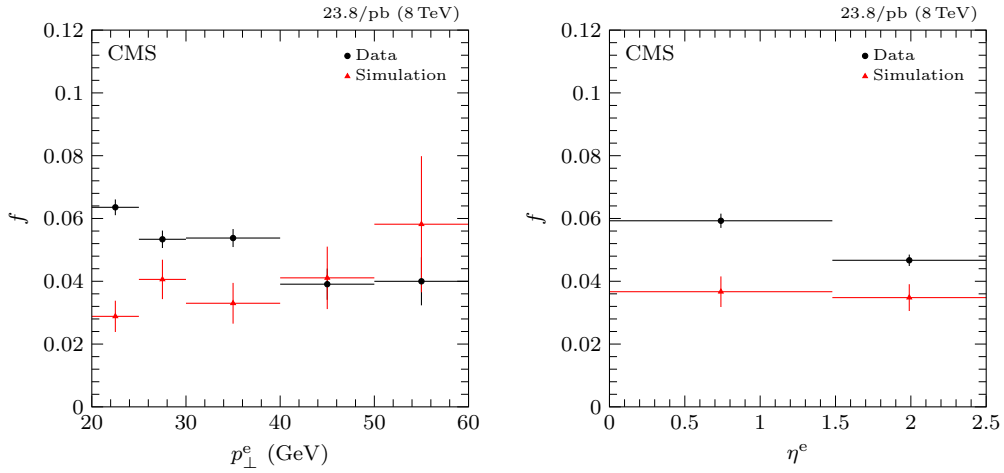

Figure 5.9: Misidentified electron ratios as a function of electron transverse momentum $p_\perp$ (left) and pseudorapidity η (right) after correcting for contributions from electroweak processes.

considered here. Thus, a large systematic uncertainty is assigned to the method. To quantify how well the method performs, a consistency check is carried out on MC simulation where the entire estimation method is performed on MC simulation. The method is tested on simulated $t\bar{t}$ events, which contribute to signal region mostly due to the described fake lepton mechanism. Thus, their yield in the signal region, N_{tt}, can be compared to the predicted fake contribution, $N_{\text{Fake lepton}}$, estimated from the yields in the loose sideband signal region, N_{tl}, N_{lt}, and N_{ll}. Due to the observed over-prediction, shown in table 5.5, a conservative systematic uncertainty of 50 % is assigned on the predicted fake lepton yield. Statistical uncertainties arising from the lepton ratio measurements itself are considered as systematic uncertainty as well, but the former uncertainty clearly dominates.

5.2.2 Charge Mis-Reconstruction

The charge of a particle is identified using the curvature of its trajectory. As the analysis selects events by the charge of the leptons, the charge measurement is fundamental. A mismeasurement of the charge leads to a background contribution of opposite-sign lepton events in the signal region. The muons' charge is considered more accurate than electrons and its contribution to this type of background is neglected. This is a valid assumption since muon detection is spread over the full size of the detector, unlike electrons which are stopped by the ECAL. The longer lever arm yields a more precise measurement of the track curvature and thus a

	μμ	eμ	ee
$N_{\text{Fake lepton}}$	7.16 ± 0.16	17.78 ± 0.30	9.67 ± 0.24
N_{tt}	4.5 ± 0.9	11.6 ± 1.4	8.0 ± 1.2
$N_{\text{Fake lepton}}/N_{\text{tt}}$	1.60 ± 0.32	1.53 ± 0.18	1.20 ± 0.18

Table 5.5: Consistency test of the estimated background contribution from fake leptons after applying preselection criteria on MC simulated $\mathrm{t\bar{t}}$ events. The number of predicted fake lepton events, $N_{\text{Fake lepton}}$, is compared to the number of events in the signal region, N_{tt}, using prompt and fake ratios which are derived from the full collection of MC samples. If the prediction reproduces the MC simulated yield in the signal region, the ratio would be one. The quoted uncertainties include only a statistical component.

more accurate charge measurement. Furthermore, electrons are more affected by bremsstrahlung which can lead to kinks in their tracks.

In the same-flavour channels, events with opposite-sign leptons from $\mathrm{Z} \to \ell^+\ell^-$ decays are much more frequent than the signal and therefore a charge mismeasurement may produce a background to the same-sign final state. The top quark pair production process, in which both top quarks decay leptonically, contributes as well. In both cases the charge of an electron is mismeasured and the lepton pair is reconstructed with same-signed charge.

Method

A similar approach is chosen as for the fake lepton background. The probability that the lepton's charge is misidentified is measured using a control sample in data. It targets $\mathrm{Z} \to \ell^+\ell^-$ events. The lepton pair in all events under the Z peak are considered to originate from a Z boson and carry therefore opposite-signed charge. Thus, the ratio of opposite-sign N^{OS} and same-sign N^{SS} lepton events under the Z peak in the dilepton invariant mass distribution

$$p_{\text{CM}} = \frac{N^{\text{SS}}}{N^{\text{OS}}} \tag{5.15}$$

indicates the probability of mismeasuring the lepton's charge. Since the accuracy with which the trajectory is measured differs in the barrel and endcap region of the detector, the probability p_{CM} is evaluated in two bins of lepton pseudorapidity η. The contributions to the same-sign signal yield

$$N^{\text{SS}} = \left(p_{\text{CM}}^{\ell_1} + p_{\text{CM}}^{\ell_2}\right) \times N^{\text{OS}} \tag{5.16}$$

can be estimated by applying the probability to the opposite-sign yield in the sideband of any signal region.

Charge Misidentification Probability Measurement

A control region in which nearly all lepton pairs are expected to carry opposite-signed charges is required for an accurate estimate of the leptons' charge misidentification probability. Using $Z \to e^+e^-$ events, events with a signal electron pair are selected. Further, an upper threshold on missing transverse energy of $\not{E}_\perp < 30\,\text{GeV}$ is set. The transverse mass is required to be $m_\perp < 25\,\text{GeV}$ and at least one jet is required. In this selection the charge misidentification probability p_{CM} is derived from the number of same-sign and opposite-sign events. It is measured to be $(7.1 \pm 1.2) \times 10^{-5}$ and $(5.8 \pm 1.3) \times 10^{-4}$ in the barrel and endcap of the detector, respectively. Similarly the probability p_{CM} for muons is measured to be $(1.49 \pm 0.34) \times 10^{-5}$.

Since the charge is derived from the track's curvature, the charge misidentification probability depends on the curvature and thereby on the transverse momentum. The electrons' transverse momentum spectra of $Z \to e^+e^-$ events in the control region might be different than the transverse momentum spectra of electrons contributing to the charge misidentification background in the signal region. The fact that the thresholds on the number of jets are different between the two regions supports this assumption since the electrons are expected to balance the transverse momentum of the jets. To correct for this, the predicted contribution due to charge misidentification is studied for different thresholds on the number of jets N_{j}. It is carried out using two event selections, both are background enriched and orthogonal in phase space to the signal region. The first selection requires a same-sign signal electron pair, at least one jet and rejects events with any b-jets. The second selection is a subset of the first with an increased threshold on number of jets of $N_{\text{j}} \geq 2$. In figure 5.10 the invariant mass distribution of the electron pair is shown for both selections. It clearly indicates an underestimation under the Z peak where most of the misidentified charge background is expected. Therefore, the probability p_{CM} needs to be corrected to better account for the electrons' kinematic properties in the signal region. A scale factor is calculated in the $m_{\ell\ell}$ spectrum only from the 80 GeV to 100 GeV bin. Other backgrounds are subtracted from the data yields and the scale factor is found to be

$$f_{\text{CM}} = \frac{N_{\text{Data}} - N_{\text{Fake lepton}} - N_{\text{Irreducible}} - N_{\text{WZ}} - N_{\text{t}\bar{\text{t}}\text{Z}} - N_{\text{t}\bar{\text{t}}\text{W}}}{\left(p_{\text{CM}}^{\ell_1} + p_{\text{CM}}^{\ell_2}\right) \times N^{\text{OS}}} = 1.60 \pm 0.11. \tag{5.17}$$

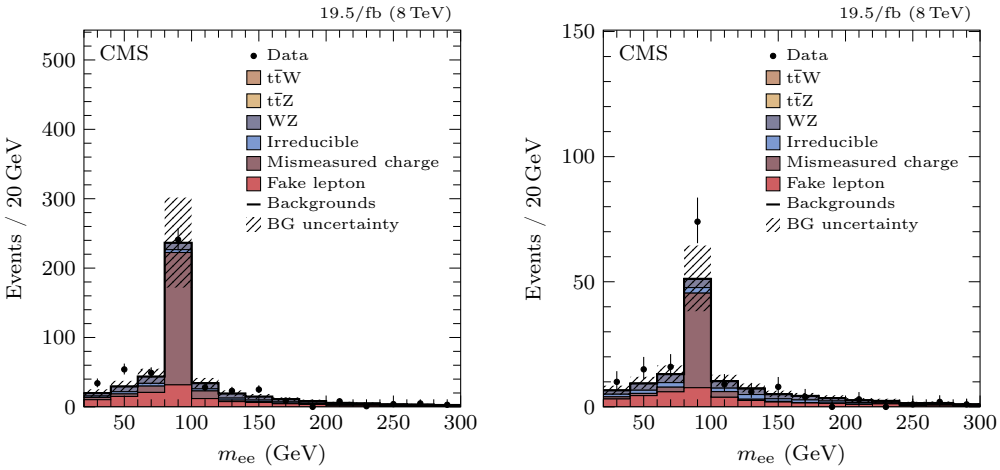

Figure 5.10: Spectra of invariant mass of electron pairs, m_{ee}. Observations are compared to the full background estimations, but without corrections on the charge misidentification probability. Events containing a same-sign tight electron pair with $p_\perp > 20\,\text{GeV}$, at least one jet, and no b-jets are selected for the left plot. The event selection used in the right plot is a subsection of the one used in the left plot and requires at least two jets.

From the opposite-sign yields the estimated background contributions to the same-sign yields

$$N_{ee}^{SS} = f_{CM} \times 2p_{CM} \times N_{ee}^{OS} \tag{5.18}$$

$$N_{e\mu}^{SS} = f_{CM} \times p_{CM} \times N_{e\mu}^{OS} \tag{5.19}$$

can be calculated.

Systematic Uncertainty

The discovered difference in charge misidentification probability between the control and signal region is assumed to come from the different lepton's transverse momentum spectra. To account for these and the uncertainty of the correction factor, a conservative approach is chosen and a systematic uncertainty of 15 % per lepton is applied.

5.2.3 Irreducible Backgrounds

Prompt same-sign lepton pairs can arise from rare SM processes. This includes processes such as the $t\bar{t}W$ signal and also backgrounds such as $t\bar{t}Z$, $t\bar{t}H$, multiboson

	μμ	eμ	ee
ZZ	0.059 ± 0.008	0.153 ± 0.012	0.096 ± 0.010
$W^{\pm}W^{\pm}$	0.44 ± 0.20	0.93 ± 0.25	0.34 ± 0.19
$t\bar{t}\gamma$	0.04 ± 0.08	1.21 ± 0.21	0.87 ± 0.19
$t\bar{t}H$	1.65 ± 0.24	3.01 ± 0.30	1.79 ± 0.24
$t\bar{t}WW$	0.188 ± 0.007	0.330 ± 0.008	0.141 ± 0.006
tZ	0.122 ± 0.016	0.337 ± 0.025	0.192 ± 0.019
Triboson	0.16 ± 0.10	0.38 ± 0.12	0.16 ± 0.10
WW (DPS)	0.000 ± 0.025	0.000 ± 0.025	0.012 ± 0.031
Irreducible (sum)	2.67 ± 0.34	6.4 ± 0.5	3.6 ± 0.4
WZ	0.70 ± 0.10	1.73 ± 0.15	0.73 ± 0.10
$t\bar{t}Z$	1.89 ± 0.22	3.76 ± 0.31	2.05 ± 0.23

Table 5.6: Predicted background yields in the three lepton-flavour channels due to irreducible processes, after requiring preselection thresholds and normalised to an integrated luminosity of 19.5/fb. The quoted uncertainties include only a statistical component.

production such as WZ, and other processes with even smaller cross sections like $t\bar{t}WW$, triboson production or same-sign dileptons from double parton scattering (DPS) processes. These processes have generally a very small cross section. Since, with few exceptions, none of these processes have been experimentally observed with the cross section measured, this background is estimated from MC simulation. The WZ process is treated separately since its cross section has been measured [80–82] and a smaller systematic uncertainty of 15 % could be applied. Since the analysis aims for a later combined $t\bar{t}W$ and $t\bar{t}Z$ cross section measurement, the $t\bar{t}Z$ yields are treated separately as well. For most other rare SM backgrounds LO cross section calculations are used. In the extreme phase space region in which the signal is expected, large NLO to LO k-factors are predicted [42]. For this reason, a flat systematic uncertainty of 50 % is assigned in a conservative approach.

The resulting yields after applying preselection requirements are listed in table 5.6. As mentioned, in the further analysis only $t\bar{t}Z$ and WZ are handled separately, while for the remaining processes the sum of their yields is used. For illustration reasons, the contributing processes are split up in the upper part of the table. In this selection the main contributions are coming from the processes $t\bar{t}Z$ and $t\bar{t}H$.

Source of uncertainty	Uncertainty (%)		
	Signal efficiency	WZ	Irreducible
Lepton scale factor	4	4	4
Muon scale factor	0.3	0.3	0.3
Electron scale factor	1.5	1.5	1.5
Lepton trigger	3	3	3
Jet energy scale	3	8	4
Jet energy resolution	1	0.8	0.6
Bottom quark jet identification	2	7	5
Luminosity		2.6	2.6
Pileup	0.5	0.3	0.6
Top quark mass	2		
Renormalisation and factorisation scales	3		
Generator	5		
Parton density function	1.5		

Table 5.7: Summary of studied systematic uncertainties on signal selection efficiency and background yields estimated from simulation.

5.2.4 Signal and Background Modelling

Several components contribute in a cross section measurement, besides the observed yields. Background predictions, the signal acceptance, and the integrated luminosity measurement enter the cross section calculation. The signal acceptance and the irreducible background prediction rely on MC simulated samples. Each of these has a statistical uncertainty based on the number of simulated events and an associated systematic uncertainty. The systematic uncertainty depends on the models used when producing a specific MC sample. In the following sections, these systematic effects are studied for the $t\bar{t}W$ signal and the irreducible background.

Table 5.7 summarises the found results. In the case of the irreducible background, the found systematic uncertainty is added in quadrature to the background prediction uncertainty quoted in section 5.2.3. The uncertainties on the signal acceptance are at the 1 % to 5 % level and add up to a total systematic uncertainty of 8 % on the signal acceptance.

Lepton Selection

As described in section 4.7.3, the lepton efficiencies for identification, isolation, and trigger in MC simulation are corrected to match the corresponding efficiencies in data. These efficiencies were measured using a tag-and-probe algorithm [70] on $Z \to \ell^+\ell^-$ events.

To estimate the systematic uncertainty, this measurement was performed in two ways on a $Z \to \ell^+\ell^-$ sample [71]. As default, the scale factors were measured with lepton identification and isolation requirements applied. Next, two separate scale factors were measured for lepton identification and isolation, respectively, by applying either of the two requirements. The scale factors were multiplied together and compared to the scale factor derived in the default procedure. The difference between the two methods was found to be 1.5 % on the electron scale factors and 0.3 % on the muon scale factors [71]. The two uncertainties are considered to be not correlated and translate into two separate systematic uncertainties on the simulated MC yields when varying either the electron or muon scale factors within their uncertainty.

In general, the hadronic activity in signal events is expected to be different than a $Z \to \ell^+\ell^-$ event. Thus, the actual lepton efficiencies might differ as well. With an uncertainty of 2 % on the scale factors these differences are reflected. This uncertainty was estimated in a study on MC simulation which compared the lepton efficiencies of $Z \to \ell^+\ell^-$ and $t\bar{t} \to \ell^+\nu b\ell^-\overline{\nu}\overline{b}$ events [71]. The uncertainty is considered fully correlated between electrons and muons and translates into a 4 % systematic uncertainty on the MC simulated yields.

The lepton trigger efficiencies were measured using orthogonal triggers. The uncertainty of these measurements is addressed with a systematic uncertainty of 3 % on the simulated MC yields.

Jet Energy Scale

As described in section 4.5 jet energies are corrected. Among other corrections, the differences between measured and predicted energy scale are corrected. The uncertainty of the measured correction factors are binned in transverse momentum and pseudorapidity of the jet, as documented in reference [60]. This correction may lead to an uncertainty in the reconstructed jet transverse momentum.

This analysis uses in the event selection thresholds on N_j and $H_\perp$. Hence, it is affected by the uncertainty on the reconstructed jet momenta. To study its effect the reconstructed jet momenta were varied up and down within their uncertainties.

This translates into a systematic uncertainty of 3 % in signal efficiency and 4 % to 8 % for the background yields.

Jet Energy Resolution

To match the jet energy resolution in data, the reconstructed jet transverse momenta in simulated MC samples were smeared with a Gaussian of width $\sqrt{c_i^2 - 1} \times \sigma_{\mathrm{MC}}$, where σ_{MC} is the resolution in MC simulation and i denotes the jet pseudorapidity bin. The factors c_i were measured in bins of jet pseudorapidity on a dijet data sample by using a method based on momentum conservation in the transverse plane [60].

As mentioned before the analysis event selection is sensitive to the jet $p_\perp$. To determine a systematic uncertainty the scale factors c are varied up and down by one sigma. The background yields vary by 0.6 % to 0.8 % and the signal efficiency by 1 % compared to the nominal value.

Bottom Quark Jet Identification

Section 4.5.3 describes the method used to identify jets as b-jets. In MC simulation a certain probability is assumed that a jet passes the identification criteria. The probability depends on the actual flavour of the jet. Jets stemming from charm quarks have a larger misidentification probability than the light-flavour jets. The identification efficiency in MC simulations is corrected on a jet-by-jet basis. The correction is applied by changing the CSV discriminator of each jet, such that overall the simulation represents the situation in data. In order to study the systematic effect of the correction on the signal and background yields the scale factors used and efficiencies in simulation are scaled up and down by one sigma of their uncertainty. After full selection an effect of 2 % on the signal yield and 5 % to 7 % on the background yields is observed.

Luminosity

Yields derived from MC simulations are scaled to the recorded integrated luminosity. The collected luminosity is measured using the silicon pixel detector, described in section 3.2.3. It is calculated offline by counting the average number of pixel clusters in a zero-bias event[2] and using the Van der Meer scan technique [83].

[2]The only requirement for a zero-bias event is that two bunches cross at the interaction point.

The measurement quotes a total uncertainty of 2.6 % [84] which is assigned as a systematic uncertainty on the yields estimated from MC simulation.

Pileup

To address the correct PU conditions during data taking simulated MC events are reweighted, see section 4.7.3. To study systematic effects of this correction the total cross section for minimum bias processes is varied up and down by 5 % when reweighting the MC samples. The effect on the background yields after final event selection is found to be at the order of 0.3 % to 0.6 %. The signal efficiency is observed to vary by 0.5 %.

Top Quark Mass

MC simulations which involve the production of a top quark depend on the assumed top mass m_t in the event generation. This affects the background yields of the $t\bar{t}Z$ process as well as the $t\bar{t}W$ signal efficiency. To assign a systematic uncertainty on the ambiguity of the exact top mass the effect is studied when varying this parameter up and down by 3 GeV. In dedicated $t\bar{t}$ samples lepton plus jets events are selected to create a signal-like topology without the prompt W boson. The selection corresponds to the final analysis selection without the requirements on the lepton originating from the prompt W boson decay, namely it requires one tight lepton with $p_\perp > 40\,\text{GeV}$, $H_\perp > 155\,\text{GeV}$, at least three jets and one of them needs to be b-tagged. The effect on the selection efficiency is found to be 4 %.

A top quark mass of $m_t = (173.29 \pm 0.95)\,\text{GeV}$ is stated by the combined LHC measurement [85]. This is three times more precise than the variation used in this study. It is assumed that the effect due to a deviation of the top mass used in the MC sample production from the true top mass is linear. Thus, half of the effect found is assigned as a systematic uncertainty in a conservative approach, namely 2 %.

Renormalisation and Factorisation Scales

When generating MC events the renormalisation and factorisation scales are free parameters. The renormalisation and factorisation scales are varied up and down by a factor of four to study the systematic effect of their choice on the analysis. Variations in ISR and FSR are covered as well, since the variation is done simultaneously in the matrix element and the showering [86]. The systematic effect

on the yields is studied on dedicated $t\bar{t}$ samples with these variations. Similar to the study of the top quark mass variation events with a signal-like topology are selected. A variation of the $t\bar{t}$ yield of 3 % is observed.

Generator

The signal sample has been generated in MadGraph 5 [66] and the parton shower and hadronisation has been simulated by Pythia 6 [67]. This generator was chosen since the available sample included the simulation of FSR photons. But MadGraph is only an LO generator. As shown in reference [42], NLO to LO k-factors for the signal rise with a higher threshold in $H_{\perp}$. Hence one likes to study possible biases in the signal efficiency compared to an NLO generator.

In order to evaluate this, MadGraph samples are compared to aMC@NLO [87] samples. The aMC@NLO samples include NLO corrections. Between the two $t\bar{t}W$ samples the number of additional partons at the matrix element level is different. The $t\bar{t}Z$ MadGraph and aMC@NLO samples both are generated with only one extra parton at the matrix element level. Therefore, the study is carried out using the two $t\bar{t}Z$ samples. The $t\bar{t}Z$ process is expected to show a similar behaviour as the $t\bar{t}W$ process. To study the differences in the hadronic part of the decay and avoid picking up discrepancies due to the missing FSR photons, the comparison is done after the selection on the reconstructed lepton. As a baseline the Z boson is required to decay leptonically, as well as the W boson from a top quark decay. In addition the W boson needs to be matched to a reconstructed lepton passing the tight analysis selection requirements and with transverse momentum $p_{\perp} > 40\,\text{GeV}$. On top of this selection the final analysis thresholds, namely $H_{\perp} > 155\,\text{GeV}$, at least three jets, and one or more of the jets identified as b-jet, are applied and its efficiency is calculated. The efficiencies differ by 5 % which is assigned as systematic uncertainty on the signal efficiency.

Parton Distribution Function

PDFs are an important ingredient in simulating the theoretical event yield. PDFs describe the structure of the colliding protons and are derived by various collaborations. Since the signal efficiency and part of the background prediction relies on simulation, it is important to quantify the uncertainty of the prediction coming from PDFs. The described procedure follows the description in the Les Houches Accord PDF (LHAPDF) [88].

The Hessian Method [89] is used which provides an eigenvector basis for the PDFs

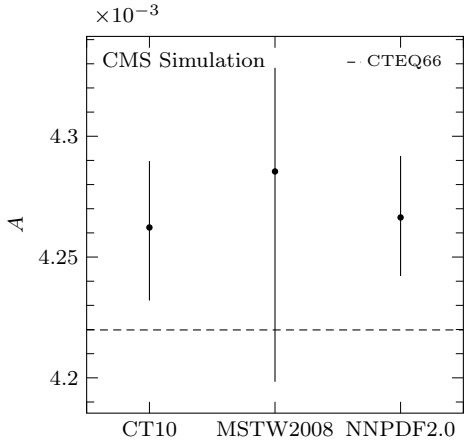

Figure 5.11: $t\bar{t}W$ signal acceptances when reweighting the $t\bar{t}W$ signal sample to CT10, MSTW 2008, and NNPDF2.0 PDF sets. The nominal acceptance of the sample is shown by a dashed line.

and a technique to calculate uncertainties on observables by varying up and down the eigenvectors. For the three PDF sets CT10, MSTW 2008, and NNPDF2.0, the $t\bar{t}W$ signal acceptance and the uncertainty on it is evaluated. The uncertainties of the PDF sets are propagated to the signal acceptance. Figure 5.11 shows the resulting acceptances. These acceptances with their uncertainties are used to define an envelope. Half of this envelope is assigned as systematic uncertainty to account for the uncertainty in the choice of PDF set. For the $t\bar{t}W$ signal this results in a systematic uncertainty of 1.5 %.

5.2.5 Comparison to Data

To verify the background prediction methods, comparisons to data are performed in the loose background dominated region, described in section 5.1.3. The backgrounds are calculated using the procedures described in the previous sections and the $t\bar{t}W$ signal is estimated using MC simulation. Distributions of variables used in selection thresholds are studied. In general, a high level of agreement within the uncertainties is achieved between the data points and the total prediction. The leptons' transverse momenta, see figure 5.12, show that the background prediction is under control. The jet multiplicity plots in figure 5.13 indicate the potential of increasing the signal to background ratio when setting threshold cuts on these variables. In figure 5.14, the dilepton invariant mass distribution proves that the background due to charge mismeasurement is under control and its correction works well. Since this sort of background is stemming mostly from $Z \to e^+e^-$

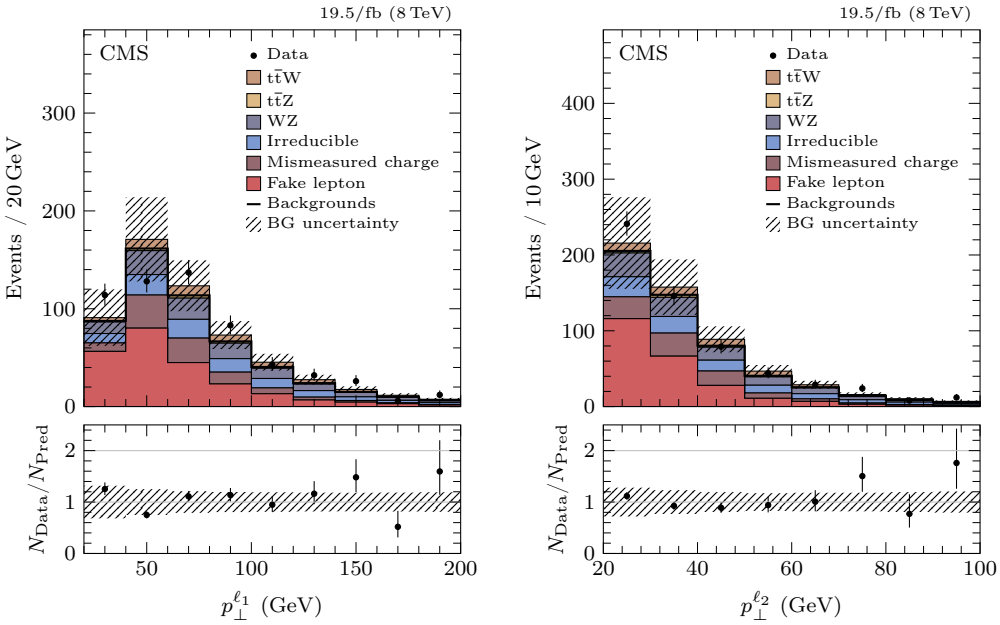

Figure 5.12: Transverse momentum of leading (left) and subleading (right) lepton after loose event selection requirements, as defined in section 5.1.3.

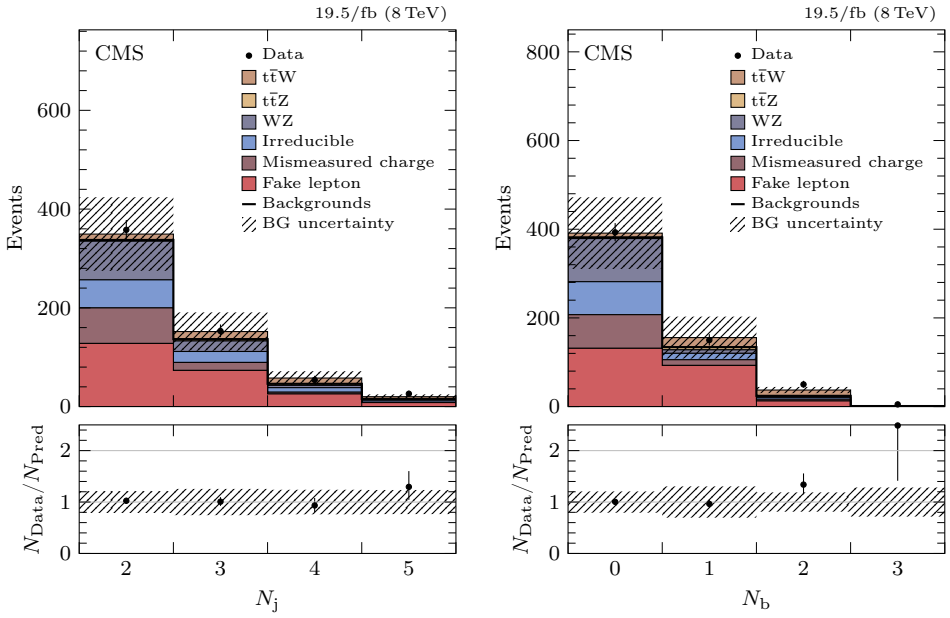

Figure 5.13: Jet multiplicity (left) and multiplicity of jets identified as b-jets (right) distributions after loose event selection requirements, as defined in section 5.1.3.

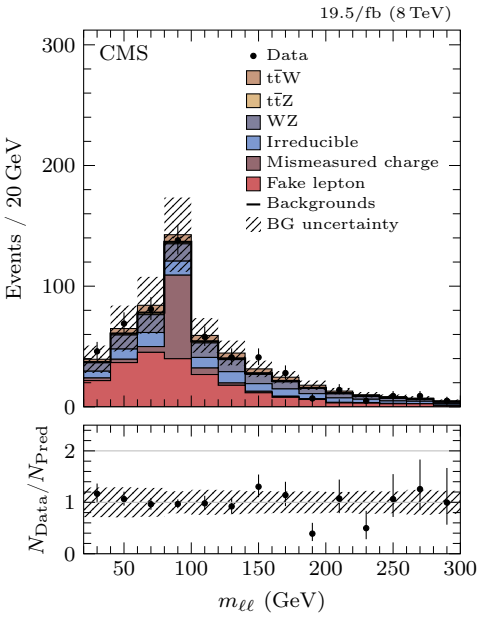

Figure 5.14: Invariant mass distribution of the two leptons after applying loose selection criteria, as defined in section 5.1.3.

decays, it is expected to contribute mainly around the Z mass in the $m_{\ell\ell}$ spectrum.

5.3 Statistical Methods

To quantify the significance of the signal and extract the $t\bar{t}W$ cross section from the signal and background yields similar statistical methods were used as for the observation of the Higgs boson candidate [90, 91].

5.3.1 Definitions

The signal cross section is derived by fitting the predictions to the observed data yield. For this purpose, the theoretical signal cross section is modified allowing the predictions to fit the data. A signal strength modifier μ is defined as

$$\mu = \frac{\sigma}{\sigma_{\text{MC}}} \tag{5.20}$$

to adjust the assumed signal cross section σ_{MC} in MC simulation. Hence, a signal strength modifier of $\mu = 1$ represents a perfect description of the signal cross

section in MC simulation. Further, the signal strength modifier is used to scale the number of predicted signal events s.

For each systematic uncertainty, see section 5.2.4, a nuisance parameter θ_i and a corresponding probability density function (pdf) $p_i(\tilde{\theta}_i|\theta_i)$ are allocated. The pdf $p_i(\tilde{\theta}_i|\theta_i)$ characterises the probability for the nuisance parameter to take the value $\tilde{\theta}_i$, given the true value θ_i. Since some of the systematic uncertainties are fairly large, the log-normal pdf

$$p_i(\tilde{\theta}_i|\theta_i) = \frac{1}{\sqrt{2\pi}\ln\kappa_i}\exp\left(-\frac{\left(\ln\theta_i - \ln\tilde{\theta}_i\right)^2}{2(\ln\kappa_i)^2}\right)\frac{1}{\theta_i} \tag{5.21}$$

is the appropriate choice [90]. The parameter κ_i stands for the width of the pdf and is given by the systematic uncertainties ε_i from table 5.7 with $\kappa_i = 1 + \varepsilon_i$. Using the nuisance parameters, the expected signal and background yields can be written as functions: $\mu \times s(\theta)$ and $b(\theta)$. With these, the likelihood is introduced as

$$\mathcal{L}(\text{Data}\,|\,\mu s(\theta) + b(\theta)) = \mathcal{P}(\text{Data}\,|\,\mu s(\theta) + b(\theta)) \times p(\tilde{\theta}|\theta) \tag{5.22}$$

where $\mathcal{P}(\text{Data}\,|\,\mu s(\theta) + b(\theta))$ is a product of Poisson probabilities to observe N_i events in bins i

$$\mathcal{P}(\text{Data}\,|\,\mu s(\theta) + b(\theta)) = \prod_i \frac{(\mu s_i + b_i)^{N_i}}{N_i!}\exp\left(-\mu s_i - b_i\right) \tag{5.23}$$

and $p(\tilde{\theta}|\theta)$ is the pdf for all nuisance parameters, given by a product of pdfs for the individual nuisance parameters.

5.3.2 Signal Cross Section

From the yields in the different channels after applying all final selection criteria the signal cross section is extracted with the *maximum likelihood method*. The method finds the signal strength modifier $\mu = \hat{\mu}$ and parameters $\theta_i = \hat{\theta}_i$ which maximise the likelihood in equation (5.22).

As described in section 5.1, an improvement of the cross section measurement is expected from splitting the data into subchannels depending on the leptons' flavour and charge. To verify this gain, the procedure is performed in two different ways. First, the likelihood using the integrated yields is maximised. Next, the yields are split into three lepton flavour channels. This step benefits from the non-uniformly distributed background processes among the lepton channels. To

exploit the charge asymmetry of the signal the channels are further split according to the charge of the lepton pair. The likelihoods of the six channels are multiplied and the signal strength modifier is extracted as before.

Resulting cross sections are quantified, as described in the following section, by their significance. By splitting into subchannels an increase in significance is expected, ultimately resulting in the highest significance when splitting into six lepton charge flavour channels.

5.3.3 Quantification

To quantify the significance of the signal a scan of the profile likelihood

$$q_\mu = -2 \ln \frac{\mathcal{L}(\mu, \hat{\theta}_\mu)}{\mathcal{L}(\hat{\mu}, \hat{\theta})} \tag{5.24}$$

is performed. In equation (5.24) $\hat{\mu}$ and $\hat{\theta}$ are the maximum likelihood estimators while the value $\hat{\theta}_\mu$ maximises the likelihood in the numerator for a given μ. Lower values of q_μ stand for a better agreement with the data. To quantify the disagreement the p-value

$$p_\mu = \int_{q_{\mu,\text{obs}}}^{\infty} f(q_\mu|\mu)\, \mathrm{d}q_\mu \tag{5.25}$$

is used where $f(q_\mu|\mu)$ is the pdf describing q_μ.[3] Via the Gaussian integral

$$p_\mu = \int_Z^{\infty} \frac{1}{\sqrt{2\pi}} \exp\left(-\frac{x^2}{2}\right) \mathrm{d}x \tag{5.26}$$

the significance Z is defined. The *observed significance* of the $t\bar{t}W$ signal is calculated by comparing to the background-only hypothesis ($\mu = 0$). The *expected significance* is derived in a similar way by fixing the signal strength modifier in the maximum likelihood fit to $\hat{\mu} = 1$.

5.4 Results

Events fulfilling signal region thresholds are used to derive the $t\bar{t}W$ production cross section in a standalone measurement. In a second step, the channels are combined with the analyses targeting the $t\bar{t}Z$ process [8, 71].

[3] Approximations of the probability density function $f(q_\mu|\mu)$ can be found in reference [92].

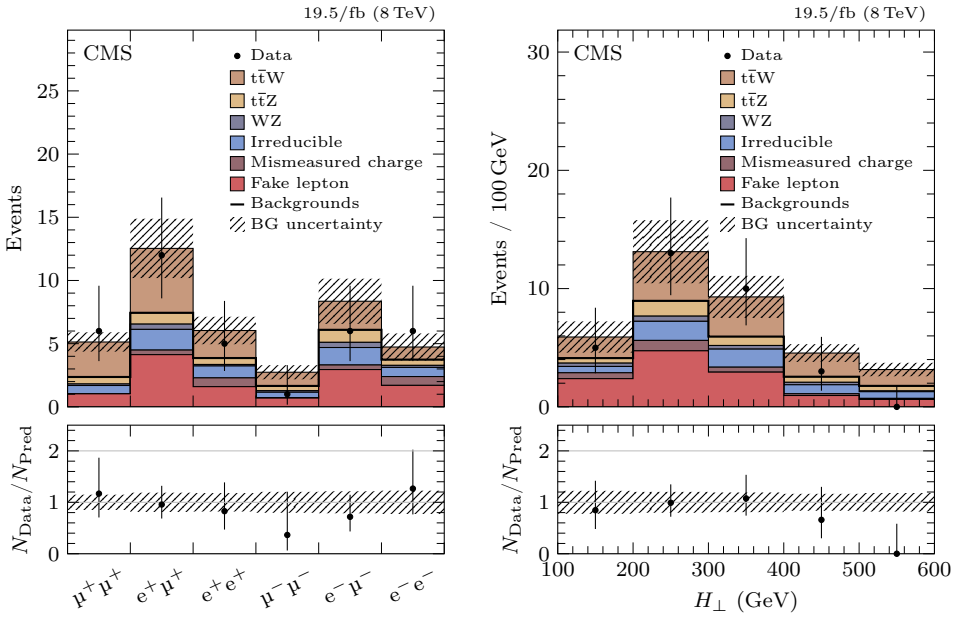

Figure 5.15: Comparison between event yields in data and estimates after final event selection requirements. The event yields of the six lepton charge flavour channels (left) and the distribution of the $H_\perp$ variable (right) are shown. The statistical and systematic uncertainties of the background estimates are depicted by the shaded area.

5.4.1 Cross Section Measurements

The signal region requirements are applied to the data and the resulting yield is compared to the background and signal prediction. An integrated yield of 36 events is observed, which is in agreement with 40 ± 8 predicted events. The background processes are estimated to contribute with 25 ± 7 events.

The resulting yields of the six charge flavour channels are listed in table 5.8 and pictured in figure 5.15. The signal clearly sticks out above the background uncertainty in most of the channels. Furthermore, the charge asymmetry of the signal is visible. The distribution of the $H_\perp$ variable after final event selection requirements is shown in the right plot of figure 5.15. In figure 5.16, the transverse momentum spectra of the leading and subleading lepton are depicted. The jet multiplicity and b-jet multiplicity distributions are shown in figure 5.17. Overall, a high level of agreement is achieved between data and the combined prediction.

The cross section can be calculated as

$$\sigma = \frac{N_{\text{Data}} - N_{\text{BG}}}{\mathcal{L}_{\text{int}} \times \mathcal{B} \times A \times \varepsilon} \tag{5.27}$$

	$\mu^+\mu^+$	$e^+\mu^+$	e^+e^+	$\mu^-\mu^-$	$e^-\mu^-$	e^-e^-
Fake lepton	1.0 ± 0.6	4.1 ± 2.1	1.6 ± 0.9	0.7 ± 0.4	3.0 ± 1.5	1.7 ± 0.9
Mismeasured charge	–	0.36 ± 0.10	0.70 ± 0.23	–	0.36 ± 0.10	0.70 ± 0.23
Irreducible	0.7 ± 0.4	1.6 ± 0.9	0.9 ± 0.5	0.46 ± 0.30	1.4 ± 0.7	0.7 ± 0.4
WZ	0.12 ± 0.05	0.42 ± 0.10	0.12 ± 0.05	0.13 ± 0.06	0.41 ± 0.10	0.16 ± 0.06
$t\bar{t}Z$	0.55 ± 0.30	0.9 ± 0.5	0.51 ± 0.28	0.37 ± 0.22	1.0 ± 0.5	0.45 ± 0.26
Total background	2.4 ± 0.7	7.4 ± 2.3	3.9 ± 1.1	1.7 ± 0.5	6.1 ± 1.8	3.7 ± 1.1
$t\bar{t}W$ (expected)	2.8 ± 0.4	5.1 ± 0.5	2.18 ± 0.30	1.08 ± 0.20	2.26 ± 0.32	1.00 ± 0.20
Total expected	5.1 ± 0.8	12.5 ± 2.4	6.0 ± 1.1	2.7 ± 0.6	8.4 ± 1.8	4.7 ± 1.1
Data	6	12	5	1	6	6

Table 5.8: Estimated backgrounds, observed number of events and expected signal events for the $\mu^\pm\mu^\pm$, $e^\pm\mu^\pm$ and $e^\pm e^\pm$ channels. The stated errors include statistical and systematic uncertainties.

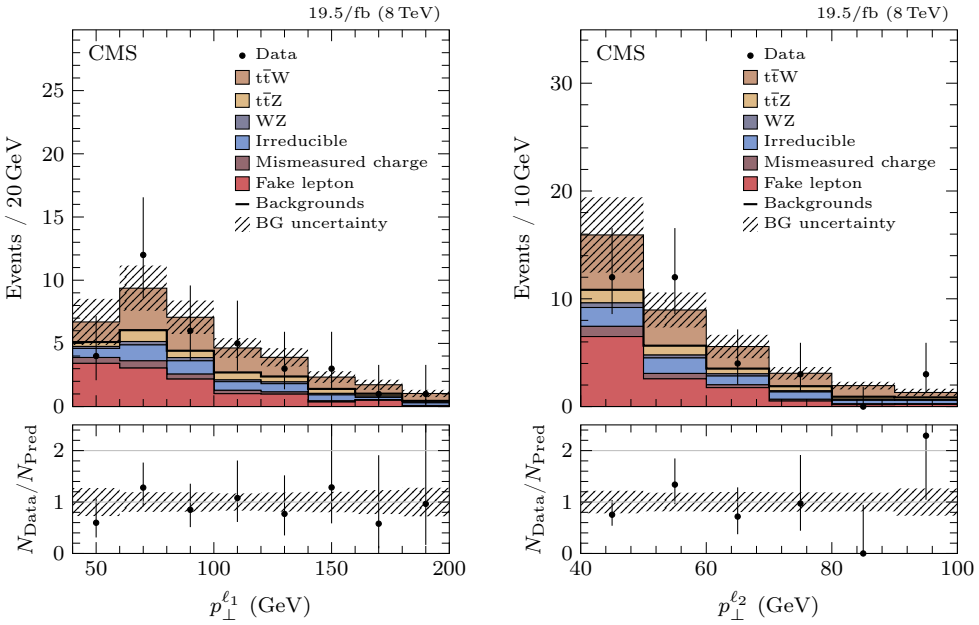

Figure 5.16: Transverse momentum distribution of the leading (left) and subleading (right) lepton after final event selection requirements.

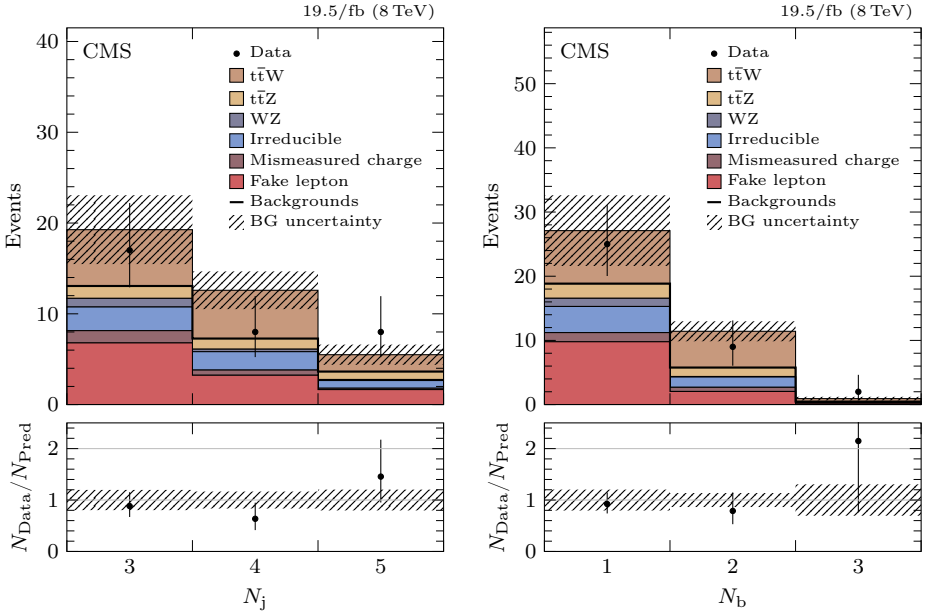

Figure 5.17: Jet multiplicity (left) and multiplicity of jets identified as b-jets (right) distributions after final event selection requirements.

where N_{Data} is the observed event yield, N_{BG} the predicted background contribution, $\mathcal{B}$ the branching ratio, and A and ε are the acceptance and efficiency of the selection, respectively. The product $\mathcal{B} \times A \times \varepsilon$ is calculated using the MC simulated $\mathrm{t\bar{t}W}$ sample by

$$\mathcal{B} \times A \times \varepsilon = \frac{N_{\text{pass}}}{N_{\text{gen}}} = (4.1 \pm 0.4) \times 10^{-3} \tag{5.28}$$

where N_{pass} is the number of events passing the final event selection and N_{gen} is the number of simulated events. Based on the observed yield and background estimates, the $\mathrm{t\bar{t}W}$ cross section is measured to be

$$\sigma_{\mathrm{t\bar{t}W}} = (140 \pm 120)\,\text{fb} \tag{5.29}$$

where the error includes statistical and systematic uncertainties.

A more thorough approach is to calculate the cross section with the maximum likelihood method, described in section 5.3. The method finds the signal strength modifier and the nuisance parameters which maximise the likelihood, defined in equation (5.22). Using equation (5.20), one can derive the cross section from the signal strength modifier. Based on the integrated data yield and background estimates, a $\mathrm{t\bar{t}W}$ cross section of

$$\sigma_{\mathrm{t\bar{t}W}} = 160\,^{+90}_{-80}\,(\text{stat})\,^{+80}_{-90}\,(\text{syst})\,\text{fb} \tag{5.30}$$

is derived with a significance of 1.2 standard deviations over the background-only hypothesis.

To benefit from the charge asymmetry of the $\mathrm{t\bar{t}W}$ signal, the yields are split into six channels according to the charge and flavour of the lepton pair. The likelihoods of the six channels are multiplied and a $\mathrm{t\bar{t}W}$ cross section of

$$\sigma_{\mathrm{t\bar{t}W}} = 170\,^{+90}_{-80}\,(\text{stat})\,^{+70}_{-70}\,(\text{syst})\,\text{fb} \tag{5.31}$$

is observed with a significance of 1.6 standard deviations over the background-only hypothesis. The main uncertainties are of statistical nature, due to the low signal yields, and from the systematic uncertainty of 50 % on the fake lepton background estimation.

5.4.2 Combined Cross Section Measurement

To measure the combined $\mathrm{t\bar{t}W}$ and $\mathrm{t\bar{t}Z}$ cross sections, three exclusive analyses were performed, aiming for three different final states. First, the *dilepton* analysis, presented in this dissertation, targets final states of the $\mathrm{t\bar{t}W}$ and $\mathrm{t\bar{t}Z}$ processes

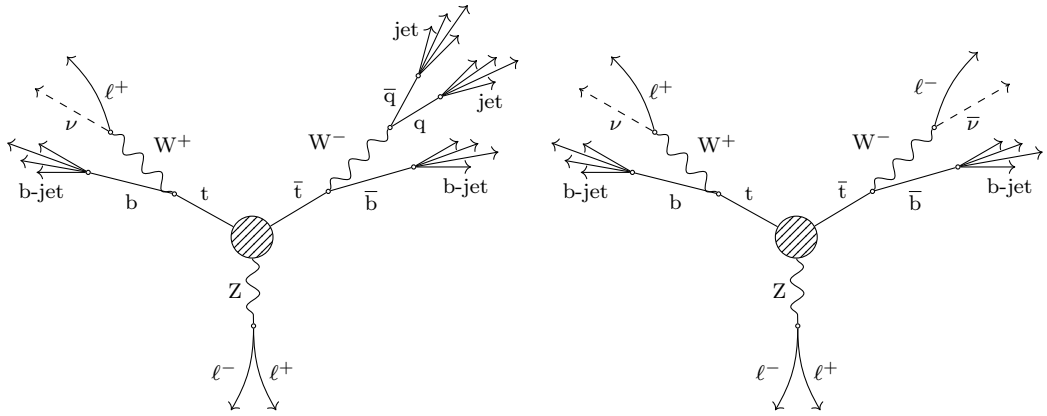

Figure 5.18: $t\bar{t}Z$ topologies with three (left) and four (right) leptons in the final state. The shaded circles represent the production mechanisms shown in section 2.4. In the case of the former a W boson decays hadronically resulting in two light-flavour jets. Both processes yield two jets originating from bottom quark hadronisation and an opposite-sign lepton pair of same flavour.

with two same-sign leptons. Secondly, the so-called *trilepton* analysis aims for $t\bar{t}Z$ events in which exactly three leptons are present in the final state [8, 71]. This is the case if the Z boson decays into a lepton pair, one of the two W bosons decays leptonically, and the other hadronically. The *four-lepton* analysis focuses on events in which the second W boson decays leptonically too [8]. In figure 5.18, the topologies of the $t\bar{t}Z$ process with three and four leptons in the final state are illustrated.

The results of the three exclusive analyses were used as input for a combined measurement of the $t\bar{t}W$ and $t\bar{t}Z$ cross sections [8, 71]. This combined measurement was performed in cooperation with groups from UCSB, UCSD, FNAL, and Rutgers University. Special care is given to the orthogonality of the selections of the three analyses, achieved by event vetoes on the leptons. The dilepton analysis rejects events in which the invariant mass of the lepton pair is compatible with the mass of a Z boson. Such events are selected by the tri- and four-lepton analyses. The event selections of the tri- and four-lepton analyses are exclusive due to an event veto on a fourth lepton in the trilepton event selection. Like the dilepton analysis, the $t\bar{t}Z$ four-lepton final state was measured in two subchannels to maximise the significance. Since no gain is expected by splitting the trilepton final state into subchannels, the total yield was used. This results in nine channels used as input for the combined measurement.

First, the $t\bar{t}W$ and $t\bar{t}Z$ cross sections are derived individually with one-dimensional fits. In these one-dimensional fits, the cross section of one process is constrained

to the SM prediction and the other is determined by the fit. The one-dimensional fit of the dilepton channels results in the $t\bar{t}W$ cross section given in equation (5.31) and represents the result of this dissertation. Similarly, the $t\bar{t}Z$ cross section is measured individually with an one-dimensional fit of the tri- and four-lepton channels. The likelihood fit results in a $t\bar{t}Z$ cross section of [8, 71]

$$\sigma_{t\bar{t}Z} = 200\,^{+80}_{-70}\,(\text{stat})\,^{+40}_{-30}\,(\text{syst})\,\text{fb} \tag{5.32}$$

with a significance of 3.1 standard deviations over the background-only hypothesis.

In a next step, all three analyses are combined and the $t\bar{t}W$ and $t\bar{t}Z$ cross sections are derived simultaneously in a two-dimensional maximum likelihood fit. For this purpose, $t\bar{t}W$ and $t\bar{t}Z$ are both treated as signals in all channels and are attached with individual signal strength modifiers $\mu_{t\bar{t}W}$ and $\mu_{t\bar{t}Z}$ in the likelihood function, see equation (5.22). This offers the benefit that no assumption on the $t\bar{t}Z$ cross section is taken when measuring the $t\bar{t}W$ cross section and vice versa. The fit chooses the best values of both cross sections simultaneously. The $t\bar{t}W$ cross section is evaluated by the collaborative effort [8, 71] with

$$\sigma_{t\bar{t}W} = 170\,^{+110}_{-100}\ \text{fb} \tag{5.33}$$

and the $t\bar{t}Z$ cross section is found to be

$$\sigma_{t\bar{t}Z} = (200 \pm 90)\,\text{fb} \tag{5.34}$$

where the quoted errors include statistical and systematic uncertainties. The results of this combined measurement agree with individual measurements of the $t\bar{t}W$ and $t\bar{t}Z$ cross sections.

In figure 5.19 the results of the two-dimensional fit, with its 68 % and 95 % confidence level contours, are illustrated. The results of the one-dimensional fits are shown by solid lines with coloured uncertainty bands. Further, the theoretical predictions are indicated by dashed lines. Within their uncertainties, the measured cross sections are found in agreement with the NLO prediction [42, 93].

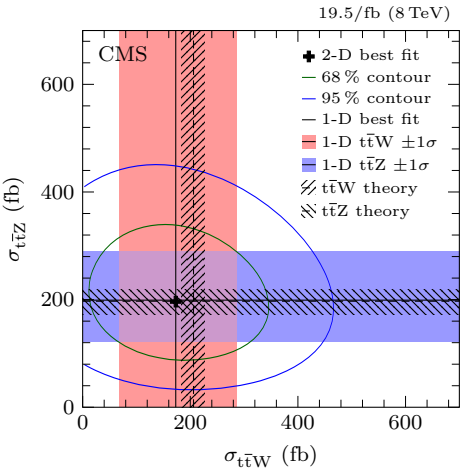

Figure 5.19: Result of the simultaneous fit of $t\bar{t}W$ and $t\bar{t}Z$ cross sections (2-D best fit) with 68 % and 95 % confidence level contours [8]. The result is compared to the individual $t\bar{t}W$ and $t\bar{t}Z$ cross section fits (1-D best fit). Theoretical predictions are indicated by dashed lines.

Chapter 6

Conclusion

An analysis of proton-proton collisions at a centre-of-mass energy of 8 TeV was presented. The data were collected by the CMS collaboration in 2012. The underlying theoretical framework was introduced and the experimental environment described.

The analysis focused on a rare SM process by measuring the $t\bar{t}W$ production cross section with two leptons of same-signed electric charge in the final state. The main contributing background processes were estimated with methods relying on proton-proton collision data instead of simulation. On a sample of background events obtained using loose selection criteria, the prediction methods were checked and found to work well. A selection, driven by the final state of the signal, was chosen as a result of an optimisation to increase sensitivity on the final cross section measurement. From the event yields passing the final selection requirements, the cross section was measured and found in agreement with NLO predictions. Finally, the result of this work was used as input for a combined measurement of the $t\bar{t}W$ and $t\bar{t}Z$ cross sections [8].

The investigated processes remain very interesting for further analyses of the LHC Run 2 data at a centre-of-mass energy of 13 TeV. At this energy, the production cross sections are expected to increase by factors up to four. The processes are expected to be measured with higher sensitivity. Furthermore, they will be an important background on measurements such as $t\bar{t}H$ or searches for new physics with similar final states.

Part II

Radiation Tolerance of Diamond Sensors

Chapter 7

Introduction

Most phenomena of interest in particle physics take place at very short distance scales and hence very high energies. This makes the LHC at CERN the ideal place to search for interesting phenomena. Although the total proton-proton cross section at a centre-of-mass energy of 8 TeV was measured to be (101.7 ± 2.9) mb [94], recent measurements at CERN investigate processes which have a cross section typically twelve orders of magnitude smaller. Such rare processes are usually statistically dominated by large numbers of background events. To observe a signal in such circumstances, it is therefore necessary to analyse a large number of interactions. Thus, the highest peak luminosity possible ($7.7 \times 10^{33}/(\mathrm{cm}^2\,\mathrm{s})$) was used for data recording in 2012, resulting in up to 37 collisions per bunch crossing [49]. Individual vertices resulting from these collisions are reconstructed by measuring trajectories of the particles produced. This implies the need for high precision tracking detectors. Furthermore, analyses of many processes, such as the one studied in chapter 5, rely on the reconstruction of secondary vertices to identify hadronic jets originating from bottom quarks. This technique is crucial for suppressing backgrounds and depends on the precise reconstruction of particle tracks.

To attain precise information on trajectories, tracking detectors are usually positioned at a central region of the detector, close to the interaction point, as described in section 3.2.3 for the CMS experiment. At this position, tracking detectors are exposed to high radiation doses. After an integrated luminosity of 500/fb, which roughly corresponds to ten years of LHC operation, the inner most layer of the CMS tracker will accumulate a 1 MeV neutron equivalent fluence in silicon of about $3.2 \times 10^{15}/\mathrm{cm}^2$ [47]. An upgrade of the LHC is planned in the mid-2020s. Its successor, the High Luminosity LHC (HL-LHC), is foreseen to deliver data with an instantaneous luminosity up to $5 \times 10^{34}/(\mathrm{cm}^2\,\mathrm{s})$ [95]. The innermost

layer of the CMS tracker is expected to accumulate a 1 MeV neutron equivalent fluence in silicon of the order of $2 \times 10^{16}/\text{cm}^2$ after an integrated luminosity of 3 000/fb [96]. Tracking detectors which will be capable of tolerating such a harsh radiation environment are necessary. The CMS tracking detector is based on silicon technology. While silicon represents a well established material used in particle tracking detectors, current silicon detectors are not expected to be able to sustain the fluence foreseen at the HL-LHC.

Diamond offers a promising alternative to silicon for position sensitive sensors. Diamond is operated as ionisation chamber. The large band gap of diamond results in low leakage currents. Diamond's large displacement energy (compared to silicon) means a more radiation tolerant material due to less lattice defects induced through radiation. Unlike silicon, a diamond sensor can be operated at ambient temperature due to its higher band gap. These are just a few of the characteristics which render diamond capable of operating in such harsh conditions [97].

Natural diamond proved to be a suitable detector material for charged particle tracking and detection [98, 99]. However, its low purity and high cost limited the application of natural diamond in high energy physics experiments. Alternatively, industrial grown diamond is available at lower cost and the higher purity necessary by such applications. Industrial grown diamond has been used successfully in past and present experiments for beam monitoring systems. These devices survey beam status, perform luminosity measurements, and protect the experiment from adverse beam conditions. The systems in the BaBar ($\text{B}\overline{\text{B}}$) [100], CDF [101], ATLAS [102, 103], CMS [104], and LHCb [105] experiments are just a few examples.

The RD42 (CVD Diamond Radiation Detector Development) collaboration has studied and developed applications of industrial grown diamond for the last 20 years [106–111]. As part of the RD42 programme, beam tests are performed at CERN. These involve performance analyses, reference measurements, as well as tests of new geometries, such as 3D diamond detectors [112, 113]. To verify the suitability of diamond for future high energy physics experiments, the radiation tolerance of industrial grown chemical vapour deposition diamond was analysed in this dissertation. For this purpose, position sensitive diamond sensors were manufactured and tested in hadron beams after different radiation doses of 800 MeV, 70 MeV protons and approximately 1 MeV neutrons. The evolution of resulting signals was studied as a function of irradiation dose.

Chapter 8

Diamond Physics

Diamond is a material with outstanding properties. Some of its characteristics render it interesting for detector applications. In particular, its radiation tolerance turns diamond into a promising alternative to silicon tracking detectors for future high energy experiments. This chapter presents an overview of the characteristics of diamond, describes how particles interact with matter, and provides an introduction on the application of diamond as particle detector.

8.1 Properties

Diamond is composed of carbon atoms organised in a tetrahedral lattice. Carbon atoms have a $1s^2$, $2s^2$, $2p^2$ electron configuration in their ground state. In a process called sp^3 hybridisation, a linear combination of the $2s$ and $2p$ orbitals forms four sp^3 hybrid orbitals [114]. The energy levels of the ground state and after hybridisation are illustrated in figure 8.1. Each sp^3 orbital is filled with one electron. A carbon atom in this configuration can bond to four other carbon atoms in a tetrahedral formation. The energy released when forming such bonds surpasses the energy necessary for the hybridisation. Thus, this represents an

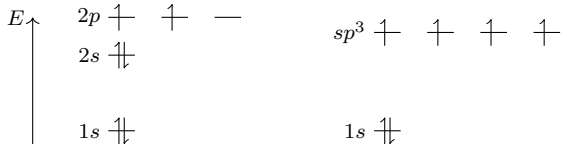

Figure 8.1: Orbitals of a carbon atom in its ground state (left) and after sp^3 hybridisation (right).

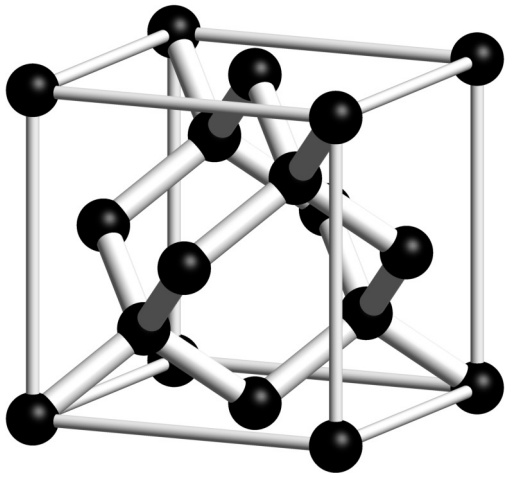

Figure 8.2: Unit cell of the diamond lattice.

energetically favourable state. Assembling carbon atoms in this way results in the diamond lattice, shown in figure 8.2. The diamond lattice has a face-centred cubic (fcc) structure with a primitive unit cell of two carbon atoms: one carbon atom at $(0, 0, 0)$ and one at $(1/4, 1/4, 1/4)$.

Diamond is a material of extremes in many ways. Being the hardest natural material on earth is just one example. A selection of diamond's properties are compared to silicon in table 8.1. Carbon has a low atomic number and is an element of group 14 in the periodic table. Silicon is an element of this group as well. Silicon has the same lattice structure as diamond but with a lower band gap ($E_g = 1.12\,\text{eV}$) and thus represents a semiconductor. Diamond is categorised as an insulator due to its large intrinsic resistivity ($>10^{40}\,\Omega\,\text{m}$). However, since many of its characteristics are better described by the theory of semiconductors, diamond is often referred as a large band gap semiconductor with a band gap of 5.48 eV. Thus, very small leakage currents are expected in a detector application and operation at ambient temperature without cooling is possible. The large band gap results in a 2.5 times smaller average number of electron-hole pairs created per length of material per charged particle compared to silicon and thus yields smaller signals. The large charge carrier mobility of around $2\,000\,\text{cm}^2/(\text{V s})$, for both electrons and holes, renders fast signal responses. This is further enhanced by the high break down field of $100\,\text{V}/\mu\text{m}$ to $1\,000\,\text{V}/\mu\text{m}$. The larger displacement energy (37.5 eV to 47.6 eV) compared to silicon augments resistance against any radiation since it takes more energy to displace atoms from their lattice position, the result of which is unwanted defects in the lattice structure. The low dielectric constant of 5.7 leads to a small capacitance and is reflected in a low electronic noise level on readout signals. Diamond has a large thermal conductivity of $6\,\text{W}/(\text{cm K})$ to $22\,\text{W}/(\text{cm K})$,

	Silicon	Diamond	Unit	Reference
Element symbol	Si	C		
Atomic number	14	6		
Atomic weight	28.085	12.011		[115]
Mass density	2.329	3.520	g/cm^3	[17]
Lattice constant	5.431	3.567	Å	[116]
Dielectric constant	11.7	5.7		[116, 117]
Thermal conductivity	1.3	6 to 22	$W/(cm\,K)$	[116, 117]
Band gap	1.12	5.48	eV	[118]
Electron mobility	1 450	2 000	$cm^2/(V\,s)$	[119]
Hole mobility	370	2 100	$cm^2/(V\,s)$	[119]
Mean excitation energy	173	89.4	eV	[120–122]
Breakdown field	30	100 to 1 000	V/µm	[116]
Intrinsic resistivity	3 200	$>10^{40}$	$\Omega\,m$	[116]
Displacement energy	15 to 20	37.5 to 47.6	eV	[123, 124]
Radiation length	9.370	12.13	cm	[17]
Nuclear interaction length	46.52	24.38	cm	[17]
e-h pair creation energy	3.62	13.19	eV	[99, 125]
e-h pairs per MIP (av.)	90	36	1/µm	[126, 127]

Table 8.1: Properties of silicon and diamond.

which facilitates cooling of attached electronics. These properties promote diamond as a suitable material for detection of charged particles in environments with a high particle flux and high radiation dose.

8.2 Synthesis

The formation of diamond in nature is a very slow process. It happens under high pressure mostly in the lithospheric mantle at depths of more than 140 km [128]. The lithospheric mantle is the outermost mantle. Fluids percolating through the lithospheric mantle are assumed to provide the carbon atoms for the formation of the diamond lattice [128]. Ascending magma from the deeper mantle can bring formed diamonds to the surface.

Two methods for artificial production of diamond are known. As in nature, diamond can be formed by high pressure and high temperature. Temperatures above 1 500 °C and pressure higher than 5 GPa are necessary [129]. This high-pressure high-temperature (HPHT) technique uses graphite as a base material. Such diamonds are not suitable for detector applications due to a generally large impurity level. Diamond synthesised in a chemical vapour deposition (CVD) procedure instead is available in higher purity. Rather than applying high pressure to graphite, diamond is grown on a substrate by adding carbon atoms one by one. Carbon atoms are provided in a gas phase chemical reaction above the substrate. The procedure is performed at relatively low substrate temperatures around 700 °C to 1 200 °C [129]. Diamond samples analysed in this dissertation were produced by CVD.

Several CVD growth techniques have been established over the years [130]. Figure 8.3 shows a schematic drawing of a widely used microwave plasma CVD reactor. Gases containing carbon, hydrogen, and oxygen atoms are injected and mixed in the chamber. In the next stage, microwaves are used to heat up and activate the gas mixture via electric discharge. Molecules split into free radicals, atoms, ions, and electrons, forming a plasma. The resulting constituents experience a number of chemical interactions until they reach the surface of the substrate or the growing diamond. Other CVD techniques mainly differ in the method of activating the gas phase and the reactive species used. Hot filament, arc jet, and combustion flame are examples of such methods [130].

For successful diamond growth, the ratio of carbon, hydrogen, and oxygen atoms is important. The diagram in figure 8.4 illustrates for which concentrations diamond growth is observed. Around the carbon monoxide line a region of

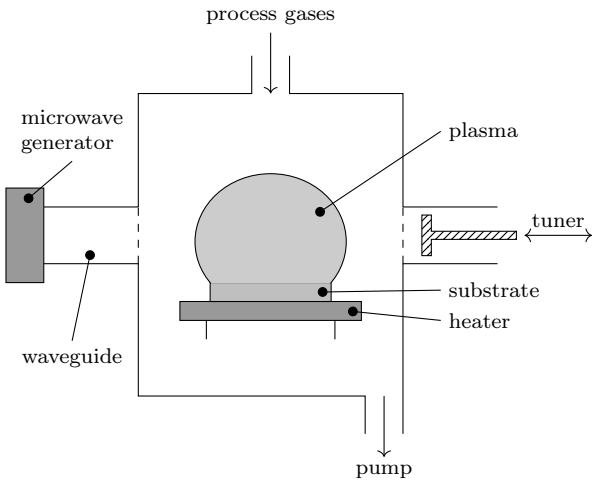

Figure 8.3: Schematic drawing of microwave plasma CVD reactor, derived from reference [130]. A vacuum pump is connected at the bottom. Process gases are supplied at the top of the reactor. Microwaves, which heat the gas mixture and form a plasma above the substrate, are induced through a dielectric window into the reactor. A tuner is used to adjust the position of the plasma.

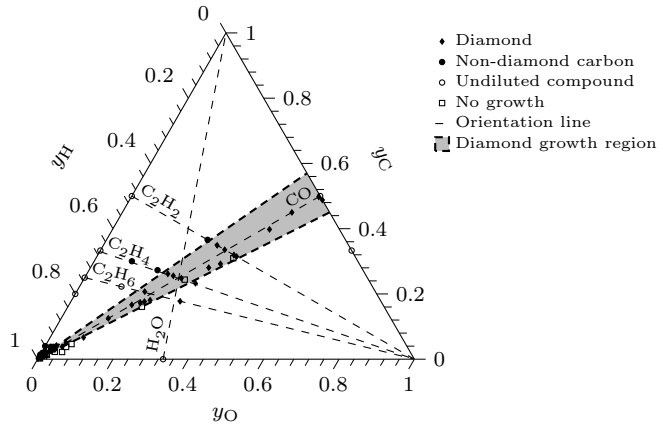

Figure 8.4: Atomic carbon hydrogen oxygen phase diagram for the CVD process, derived from reference [131]. The axes describe the carbon, hydrogen, and oxygen amount fractions of the gas mixture, respectively. Diamond growth is observed between the thick dashed lines.

diamond growth is found. On the carbon-rich side of the diamond growth region, only non-diamond carbon is formed, while no growth is found for lower carbon concentrations. Successful diamond growth is observed over the full range of hydrogen concentrations. However, the majority of successful mixtures features a fraction of hydrogen above 90 %.

A couple of different reactions take place at the surface during growth of the diamond. Hydrogen plays a key role here and is therefore kept at a high concentration. It temporarily terminates the diamond lattice at the surface. Such hydrogen terminations are continuously displaced and refilled by other hydrogen radicals, retaining the surface in a metastable state. A resulting free lattice point can be filled with a growth species such as methyl (CH_3). Hereby, the diamond lattice grows by a carbon atom. Hydrogen has additional important functions. It etches graphite and other non-diamond structures from the surface and splits long hydrocarbon chains into smaller segments which are required by the growth process.

The final crystal structure depends on the choice of substrate. Single-crystalline CVD (sCVD) diamond can be grown on an HPHT diamond substrate. An HPHT diamond consists of a single crystal. During the growth process this single-crystalline structure is copied and a sample consisting of a single crystal is produced. Currently sCVD diamond samples are limited in size to less than 8 mm × 8 mm [132] by the availability of large diamond substrates. If silicon or a carbide forming metal, such as tungsten or titanium, is used as a substrate, polycrystalline CVD (pCVD) diamond is produced. Its lattice grows from multiple seeds. Resulting grains can vary in size and are arranged like columns pointing from the substrate to the growth side. Grain boundaries represent defects in the lattice structure. However, pCVD diamond can be grown in larger sizes than sCVD diamond. Additional details on the production procedure can be found in references [97, 129, 130].

8.3 Particle Detection

The fundamental requirement for particle detection is interaction of incident particles with the detector. Different processes occur depending on the particle's species, the energy scale and the detector material. In all processes, the particle's energy is deposited partially or entirely in the detector medium. This section provides a brief introduction to the physics processes involved in detector technology of diamond sensors, following the descriptions in references [17, 133].

8.3.1 Charged Particle Propagation through Matter

Charged particles passing through matter interact mainly electromagnetically with electrons and nuclei, resulting in phenomena such as bremsstrahlung, particle scattering, ionisation, Cherenkov radiation, or excitation of atoms. Ionisation is the dominant process for a relativistic particle of velocity $v = \beta c$ in the range of $0.1 < \beta\gamma < 1\,000$ where γ is the Lorentz factor and can be written as

$$\gamma = \frac{E}{mc^2}. \tag{8.1}$$

When interacting with an electron on its passage through matter, the particle either transfers energy to the electron placing it in an excited state or removing it from its shell, creating an electron-hole pair and thereby ionises the atom. The mean energy a charged particle loses through ionisation when passing through matter is described by the Bethe-Bloch equation [134–136]

$$\left\langle -\frac{\mathrm{d}E}{\mathrm{d}x} \right\rangle = 4\pi N_\mathrm{A} r_\mathrm{e}^2 m_\mathrm{e} c^2 z^2 \frac{Z}{A}\frac{1}{\beta^2}\left(\frac{1}{2}\ln\frac{2m_\mathrm{e}c^2\beta^2\gamma^2 W_\mathrm{max}}{I^2} - \beta^2 - \frac{\delta(\beta\gamma)}{2}\right) \tag{8.2}$$

where I denotes the mean excitation energy, Z the atomic number of the absorber, A the atomic mass of the absorber, N_A the Avogadro constant, r_e and m_e the electron's radius and mass, z the charge number of the incident particle, W_max the maximum energy transfer in a collision of the projectile with an electron, and $\delta(\beta\gamma)$ the density effect correction, which considers medium polarisation. The maximum energy transfer W_max is given by [17]

$$W_\mathrm{max} = \frac{2m_\mathrm{e}c^2\beta^2\gamma^2}{1 + 2\gamma\frac{m_\mathrm{e}}{M} + \left(\frac{m_\mathrm{e}}{M}\right)^2} \tag{8.3}$$

where M is the incident particle's mass. At very high energies, the density effect correction in equation (8.2) becomes [17, 133]

$$\frac{\delta(\beta\gamma)}{2} \to \ln\frac{\hbar\omega_\mathrm{p}}{I} + \ln\beta\gamma - \frac{1}{2} \tag{8.4}$$

where $\hbar\omega_\mathrm{p}$ is the plasma energy. The density effect correction can be estimated using the Sternheimer's parametrisation [137, 138]

$$\delta(\beta\gamma) = \begin{cases} 2\ln\beta\gamma + C & \log\beta\gamma \geq x_1 \\ 2\ln\beta\gamma + C + a(x_1 - \log\beta\gamma)^m & x_0 \leq \log\beta\gamma < x_1 \\ 0 & \log\beta\gamma < x_0 \end{cases} \tag{8.5}$$

in which the parameters C, a, m, x_0, and x_1 depend on the material traversed.

In figure 8.5, the mean energy loss function is plotted for protons passing through diamond. It has a broad minimum. Most relativistic particles feature energy losses around this minimum and are thus denoted minimum ionising particles (MIPs). Their ionisation losses are in all materials, with the exception of hydrogen, in the range of about $1\,\mathrm{MeV\,cm^2/g}$ to $2\,\mathrm{MeV\,cm^2/g}$ [133].

After the density effect correction, equation (8.2) grows as $\ln\beta\gamma$ caused by the $\beta^2\gamma^2$ term of the maximum energy transfer $W_{\max}$. The relativistic rise in equation (8.3) is due to rare large energy transfers [17]. Equation (8.2) describes the energy loss in an infinite material. In case of tracking detectors, thin sensor material is used to keep interactions with incident particles at a low level and avoid biasing particle trajectories. In thin material, secondary particles may leave the material and carry off energy. Thus, the energy transfer may be restricted. Limiting the energy transfer to $T \leq W_{\mathrm{cut}} \leq W_{\max}$ results in the Restricted Energy Loss rate given by [17]

$$\left\langle -\frac{\mathrm{d}E}{\mathrm{d}x} \right\rangle_{T<W_{\mathrm{cut}}} = Kz^2 \frac{Z}{A}\frac{1}{\beta^2}\left(\frac{1}{2}\ln\frac{2m_\mathrm{e}c^2\beta^2\gamma^2 W_{\mathrm{cut}}}{I^2} - \frac{\beta^2}{2}\left(1+\frac{W_{\mathrm{cut}}}{W_{\max}}\right) - \frac{\delta(\beta\gamma)}{2}\right) \tag{8.6}$$

where K is defined as

$$K = 4\pi N_\mathrm{A} r_\mathrm{e}^2 m_\mathrm{e} c^2. \tag{8.7}$$

Unlike the relativistic rise in the Bethe-Bloch equation, the Restricted Energy Loss reaches the constant Fermi plateau, as shown in figure 8.5.

When the thickness of the material is limited, the interaction of a particle with matter is a statistical process and therefore fluctuations in effective energy loss are observed. For relativistic particles passing through thin layers of material, the energy loss fluctuates around the mean value. The pdf of the particle's energy loss is described by the Landau-Vavilov distribution [139, 140]

$$f(x,E) = \frac{1}{\xi}\omega(\lambda) \tag{8.8}$$

where x is the thickness of the material, E is the energy loss, and

$$\xi = 2\pi N_\mathrm{A} r_\mathrm{e}^2 m_\mathrm{e} c^2 \frac{Z}{A}\frac{x}{\beta^2}. \tag{8.9}$$

The term $\omega(\lambda)$ can be approximated by [141, 142]

$$\omega(\lambda) \approx \frac{1}{\sqrt{2\pi}}\exp\left(-\frac{\lambda+\exp(-\lambda)}{2}\right) \tag{8.10}$$

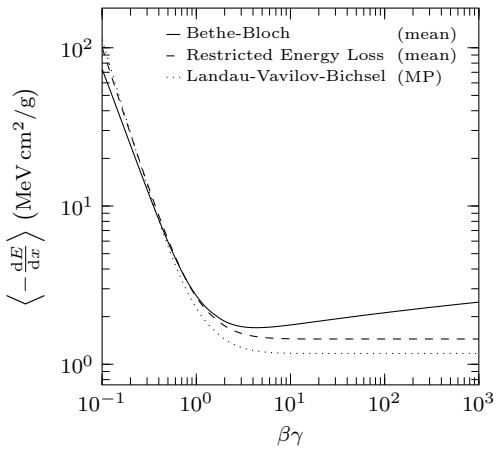

Figure 8.5: Mean ionisation loss as a function of $\beta\gamma = \frac{p}{mc}$ for protons in 500 µm thick diamond calculated with the Bethe-Bloch equation and Restricted Energy Loss. $W_{\mathrm{cut}} = 585\,\mathrm{keV}$ was used for the Restricted Energy Loss. The most probable energy loss per unit thickness using Landau-Vavilov-Bichsel is plotted with a dotted line. The density effect correction is estimated using Sternheimer's parametrisation [137, 138].

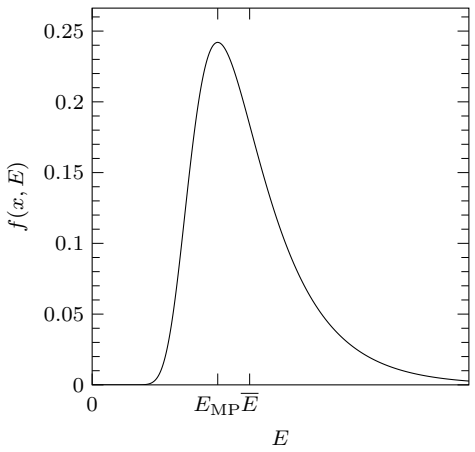

Figure 8.6: Probability density function of energy loss E in thin material of thickness x described by the Landau distribution. The most probable value E_{MP} and an approximation of the mean value $\overline{E}$ are indicated.

where

$$\lambda = \frac{E - E_{\mathrm{MP}}}{\xi}. \tag{8.11}$$

The distribution's most probable (MP) value, including later corrections, is given by [143]

$$E_{\mathrm{MP}} = \xi \left(\ln \frac{2mc^2\beta^2\gamma^2}{I} + \ln \frac{\xi}{I} + j - \beta^2 - \delta(\beta\gamma) \right) \tag{8.12}$$

where $j = 0.20$. The MP energy loss is compared to the mean energy loss and the Restricted Energy Loss in figure 8.5. For a MIP, it is found about 1.2 times smaller compared to the latter. Figure 8.6 shows the Landau-Vavilov distribution. It is strongly asymmetric and has a long tail at high energies. Therefore, its MP value is below the mean value.

For higher energetic particles, at $\beta\gamma > 1\,000$, radiative effects get more significant. Besides loosing energy through ionisation, particles in this regime are decelerated by the Coulomb field of the nuclei and radiate photons. These losses due to

bremsstrahlung are expressed as

$$-\frac{\mathrm{d}E}{\mathrm{d}x} = \frac{E}{X_0} \tag{8.13}$$

where X_0 is the radiation length.

8.3.2 Signal Formation

As discussed in the previous section, the main process for MIPs interacting with diamond is ionisation. Electron-hole pairs created during ionisation can be collected and converted into a signal. This section gives a short overview of the processes involved in signal formation.

The conduction band (CB) denotes the highest energy band for electrons in a lattice, separated by a band gap from the valence band (VB). At ambient temperature, electrons may be excited from the VB to the CB due to thermal excitation, generating electron-hole pairs. These electron-hole pairs have a probability to recombine. These two processes keep the lattice in a state of thermal equilibrium with a number of free carriers. The number of free carriers depends on the band gap [144]

$$n_{\text{intrinsic}} = \sqrt{N_{\mathrm{C}} N_{\mathrm{V}}} \exp\left(-\frac{E_{\mathrm{g}}}{2k_{\mathrm{B}}T}\right) \tag{8.14}$$

where N_{C} and N_{V} are the effective density of states in the CB and VB, respectively, k_{B} denotes the Boltzmann constant, and T the thermodynamic temperature. At ambient temperature, the intrinsic carrier concentration in diamond ($E_{\mathrm{g}} = 5.48\,\mathrm{eV}$) is about $10^{-27}/\mathrm{cm}^3$ [116], while the intrinsic carrier concentration in silicon with a given band gap ($E_{\mathrm{g}} = 1.12\,\mathrm{eV}$) is $1.02 \times 10^{10}/\mathrm{cm}^3$ [119].

A particle which propagates through the diamond bulk generates additional electron-hole pairs, leading to excess charge carriers. The number of such excess charge carriers generally depends on the incident particle's species and energy. On average, a MIP is found to create 36 electron-hole pairs per micrometre of path length traversed [127]. In diamond, in the presence of these excess charge carriers, the charge carrier density due to thermal excitation is negligible. As the excess carriers drift through the material they may recombine or get trapped. The charge carrier density can then be described by a rate equation of electrons and holes [127]

$$\frac{\mathrm{d}n_i}{\mathrm{d}t} = -\frac{n_i}{\tau_i} \tag{8.15}$$

where τ_i is the excess carrier lifetime of electrons and holes, respectively.

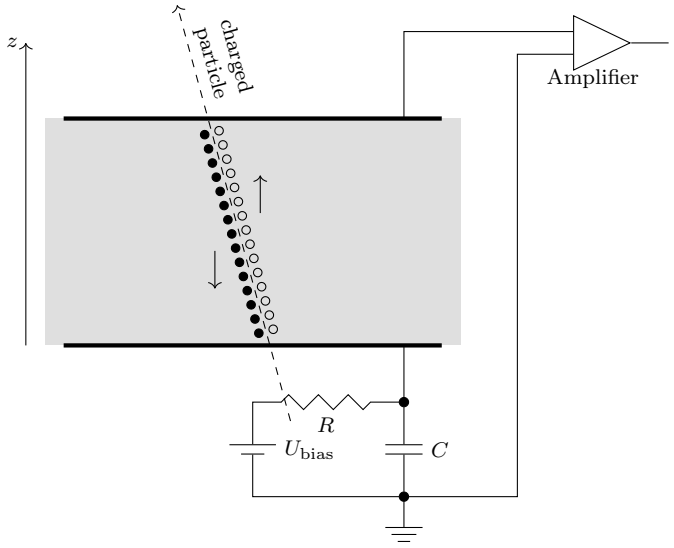

Figure 8.7: A schematic drawing of a diamond detector. A high voltage is applied at the electrodes on the surface of the diamond through a resistor R and capacitor C. The time constant $\tau = RC$ is chosen to stabilise the applied voltage. On their passage through the diamond bulk, charged particles create electron-hole pairs which drift in the applied electric field towards the electrodes. The moving charge is amplified and read out.

A diamond detector is operated as an ionisation chamber to collect these excess charge carriers. After the growth process, the diamond is polished to remove the remains of the substrate and planarise the surfaces. In the case of pCVD diamond, samples are thinned to retain only the material of highest growth quality. Both sides are metallised. The electrodes can be realised in different shapes such as single pads, strips, or pixels, depending on the application's needs. A high voltage is applied to the electrodes to introduce an electric field in the diamond bulk of typically $1\,\mathrm{V/\mu m}$ to $2\,\mathrm{V/\mu m}$. The resulting free charge carriers move under the influence of the external electric field and produce a signal proportional to the distance they drift. Since the number of electron-hole pairs created is related to the incident particle's species and energy, the measured signal depends on these properties as well.

A schematic of a diamond detector layout is shown in figure 8.7. The bottom electrode is connected to high voltage (positive or negative) through a resistor R and a capacitor C, while the top electrode is biased by the readout electronics and is near or at ground potential. The capacitor and resistor are chosen to obtain a time constant $\tau = RC$ which stabilises the applied voltage.

The mean distance an electron or hole drifts before being trapped in an infinite material under the influence of an electric field E is given by the mean free path

(MFP), λ_i,

$$\lambda_i = \tau_i \times v_i = \tau_i \times \mu_i E \tag{8.16}$$

where $i = \mathrm{e},\ \mathrm{h}$, $v_i = \mu_i E$ is its drift speed, τ_i the trapping time, and μ_i the charge carrier mobility. The sum of drift lengths

$$\lambda = \lambda_\mathrm{e} + \lambda_\mathrm{h} \tag{8.17}$$

defines the total MFP. Introducing the mobility weighted lifetime

$$\tau = \frac{\tau_\mathrm{e}\mu_\mathrm{e} + \tau_\mathrm{h}\mu_\mathrm{h}}{\mu_\mathrm{e} + \mu_\mathrm{h}}, \tag{8.18}$$

the MFP can be written as

$$\lambda = \tau \times (v_\mathrm{e} + v_\mathrm{h}). \tag{8.19}$$

For an electric field pointing in the z direction, the drift velocities of electrons and holes are

$$v_\mathrm{e} = -\frac{\mathrm{d}z}{\mathrm{d}t} \qquad\qquad v_\mathrm{h} = \frac{\mathrm{d}z}{\mathrm{d}t}. \tag{8.20}$$

Thereby, equation (8.15) can be written as

$$\frac{\mathrm{d}n_\mathrm{e}}{\mathrm{d}z} = \frac{n_\mathrm{e}}{\tau_\mathrm{e} v_\mathrm{e}} = \frac{n_\mathrm{e}}{\lambda_\mathrm{e}} \tag{8.21}$$

and

$$\frac{\mathrm{d}n_\mathrm{h}}{\mathrm{d}z} = -\frac{n_\mathrm{h}}{\tau_\mathrm{h} v_\mathrm{h}} = -\frac{n_\mathrm{h}}{\lambda_\mathrm{h}}, \tag{8.22}$$

describing the linear charge carrier density of electrons and holes, respectively. The MFP is constant in single-crystalline diamond once a minimum external electric field is introduced. For an initial charge carrier density n_0 at $z = z'$, the corresponding solutions of equation (8.21) and equation (8.22) are

$$n_\mathrm{e}(z, z') = n_0 \exp\left(\frac{z - z'}{\lambda_\mathrm{e}}\right) \tag{8.23}$$

where $z < z'$ and

$$n_\mathrm{h}(z, z') = n_0 \exp\left(-\frac{z - z'}{\lambda_\mathrm{h}}\right) \tag{8.24}$$

where $z > z'$.

The induced charge on the plates of a detector of thickness d is derived by [127]

$$Q_{\mathrm{ind}} = \int_0^d \int_{z'}^0 \frac{-q}{d} n_{\mathrm{e}}(z, z')\,\mathrm{d}z\,\mathrm{d}z' + \int_0^d \int_{z'}^0 \frac{q}{d} n_{\mathrm{h}}(z, z')\,\mathrm{d}z\,\mathrm{d}z' \tag{8.25}$$

where q denotes the elementary charge. After integration, the induced charge results in [127]

$$Q_{\mathrm{ind}} = \sum_{\mathrm{e,\ h}} q n_0 \lambda_i \left(1 - \frac{\lambda_i}{d}\left(1 - \exp\left(-\frac{d}{\lambda_i}\right)\right)\right) \tag{8.26}$$

where n_0 is the average linear charge carrier density induced by a MIP. The charge collection distance (CCD) is defined as the average distance the electron-hole pair moved apart and is related to the average measured charge, $\overline{Q}_{\mathrm{ind}}$, by

$$\mathrm{CCD} \equiv \overline{r} = \frac{\overline{Q}_{\mathrm{ind}}}{n_0 q}. \tag{8.27}$$

As the CCD is proportional to the collected charge, it is used as a measure to characterise and compare diamond detectors. If the CCD equals the sample's thickness, the diamond is said to collect full charge, as the CCD is limited (in the absence of internal gain) to a maximum value of the sample's thickness. Unlike the CCD, the MFP denotes a measure which is independent of the sample's thickness.

8.4 Defects

Similar to other crystal structures, the diamond lattice can have defects or impurities. Such defects result in a variety of effects. While pure diamond is colourless in visible light, natural diamonds often come in various colours, such as brown, yellow, blue, green, and others [129] caused by impurities in the lattice structure.

A wide range of defects is possible. An overview of possible defects is shown in figure 8.8. The defects where carbon atoms are missing or displaced in the lattice structure constitute so-called *intrinsic defects* [129]. Two types of intrinsic defects are distinguished, point defects and edge dislocations. If a single atom is misplaced, it denotes a point defect. An empty lattice point or an additional carbon atom between lattice points, a so-called interstitial atom, are this type of defect. An edge dislocation adds an additional chain or layer to the lattice. Such edge dislocations are observed in pCVD diamond at grain boundaries. In *extrinsic defects* foreign atoms are enclosed in the lattice or replace carbon atoms [129]. Such impurities may be incorporated during the growth process. Many elements can

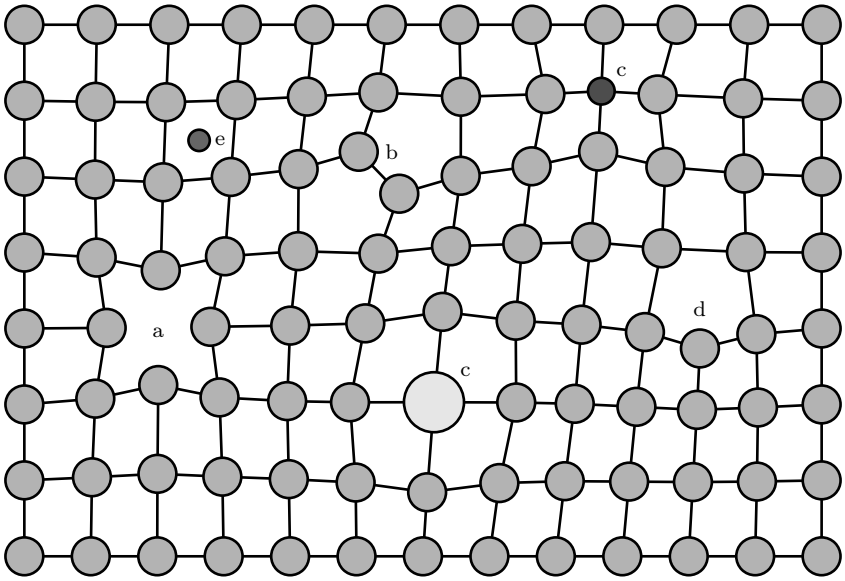

Figure 8.8: Schematic of different lattice defects in diamond [129]: vacancy (a), interstitial carbon atom (b), foreign interstitial atom (e), foreign substitutional atom (c), and edge dislocation (d).

cause impurities, but the most common one is nitrogen [129]. Therefore, diamonds are commonly classified by their nitrogen content.

Defects affect the electrical properties of all materials. They can add energy levels in the band gap. Depending on the position of the additional energy level, see figure 8.9, a defect may lead to charge trapping, recombination, or generation. Defects with an energy level close to the VB or CB represent traps for free holes or electrons, respectively. Once a trap is filled, no further charge carriers are captured. Thus, these kinds of defects influence the detector performance only on a minor basis. As shown in figure 8.9, defects with an energy level in the middle of the band gap can trap both electrons and holes. In this way, free electron-hole pairs are recombined and the CCD is consequently reduced. These kinds of defects can generate free charge carriers as well. If an electron from the VB is promoted to the defect level and further to the CB, a new electron-hole pair is available. In a detector application, such additional charge carriers increase the noise level on the signal.

For these reasons, control of defects is important in the production and selection of diamond samples for detector applications.

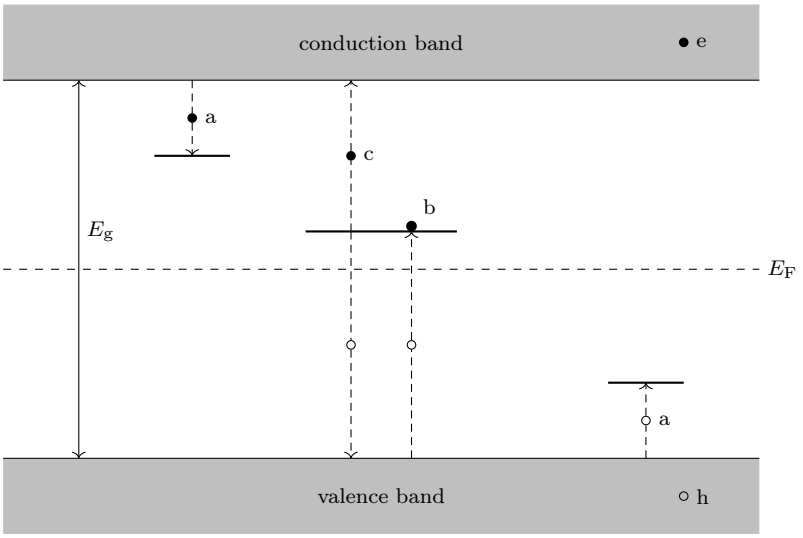

Figure 8.9: Energy levels of defects in band gap E_g of diamond, derived from reference [145]. The processes of charge trapping (a), recombination (b), and generation (c) are illustrated. The dashed line represents the Fermi level E_F.

8.5 Radiation Damage

When a charged particle passes through a medium, it deposits energy as discussed in section 8.3.1. This process of generating electron-hole pairs, creates reversible effects on the lattice. Non-ionising energy loss (NIEL) is more important when considering bulk damage to the lattice. In NIEL, charged and neutral particles can interact with nuclei. A high-energetic incident particle can kick an atom from its lattice site and leave a vacancy behind. Before the recoil and the dislocated lattice atom from the elastic scattering come to rest and cause interstitials, they can create subsequent displacements on their path, leading to a cascade of defects in the lattice. In the case of inelastic scattering, nuclear reactions can occur, leading to foreign substitutional atom defects. As in the case of elastic scattering, the products from nuclear reactions can lead to subsequent displacements or result in new interstitials.

These additional defects may change the electrical properties and affect the sensor performance as described previously. Defects, which create additional charge carriers, give rise to leakage currents. These so-called dark currents lead to higher noise levels and if excessive may necessitate cooling the device to prevent it from thermal runaway. Unlike silicon detectors, in diamond dark currents stay small even after irradiation [123]. Thus, diamond detectors can operate at room temperature. On the other hand, defects can cause signals to decrease since the probability

for a charge to get trapped is increased due to the extra traps which results in a shorter trapping time and hence reduced MFP. The trapping time τ is reciprocally proportional to the number of defects per unit area induced by radiation [146]

$$\frac{1}{\tau} \propto N_{\text{Defects}} \tag{8.28}$$

which is proportional to the particle fluence ϕ

$$N_{\text{Defects}} \propto \phi. \tag{8.29}$$

The *fluence* is defined as the integrated particle flux over time. Thus, in the simplest radiation damage model the reciprocal trapping time is described by a linear relation with the fluence

$$\frac{1}{\tau} = \frac{1}{\tau_0} + k'\phi \tag{8.30}$$

where τ_0 is the initial trapping time and k' depends on incident particle species and energy. Using equation (8.19), the MFP is related to the particle fluence by

$$\frac{1}{\lambda} = \frac{1}{\lambda_0} + k\phi \tag{8.31}$$

with λ_0 the initial MFP before irradiation and k the *damage constant* given by

$$k = \frac{k'}{v_{\text{e}} + v_{\text{h}}}. \tag{8.32}$$

The MFP in sCVD and pCVD diamond follows the same radiation damage mechanism [147–149]. Due to its grain boundaries, pCVD diamond has more initial traps than sCVD diamond and therefore has a smaller MFP in the unirradiated state. This characteristic may be regarded as a fluence offset of pCVD diamond, ϕ_0. Namely, unirradiated pCVD diamond functions as though it has the same number of trapping centres as sCVD diamond irradiated with a fluence $\phi = \phi_0$.

Equation (8.31) describes the damage law in MFP space. It can be transformed into CCD space using equation (8.26) and equation (8.27)

$$\overline{r} = \sum_{\text{e, h}} \frac{f_i\lambda_0}{1+\lambda_0 k\phi}\left(1 - \frac{f_i\lambda_0}{d(1+\lambda_0 k\phi)}\left(1 - e^{-d\frac{1+\lambda_0 k\phi}{f_i\lambda_0}}\right)\right) \tag{8.33}$$

where the factor

$$f_i = \frac{v_i}{v_{\text{e}} + v_{\text{h}}} = \frac{\lambda_i}{\lambda} \tag{8.34}$$

defines the relation between the drift velocities of electrons and holes.

The damage mechanisms, described above, generally depend on the incident particle's species and energy. They are related to NIEL. The NIEL scaling hypothesis provides a handle to compare damage from particles of different species and energies. It predicts the signal decrease to be proportional to the NIEL [150]. The NIEL can be expressed by the displacement damage cross section $D(E)$, which can be calculated from the possible interactions in the bulk of the material.

For damage in silicon, fluences are commonly stated in 1 MeV neutron equivalent fluence in silicon. A fluence of a specific particle species and energy can be converted into 1 MeV neutron fluence by

$$\phi_{\mathrm{eq}}^{\mathrm{Si}} = \kappa_{\mathrm{Si}} \phi \tag{8.35}$$

where κ_{Si} is the hardness factor. The hardness factor is given by

$$\kappa_{\mathrm{Si}} = \frac{D^{\mathrm{Si}}(E)}{D_{\mathrm{n}}^{\mathrm{Si}}(1\,\mathrm{MeV})} \tag{8.36}$$

for a monoenergetic particle flux [150], where $D^{\mathrm{Si}}(E)$ is the displacement damage cross section in silicon. In diamond, similar relations are expected and have to be experimentally verified.

Chapter 9

Experimental Data

The main radiation damage in CVD diamond in high energy physics applications close to the interaction region is expected to come from charged hadrons, mostly pions with an energy spectrum from thermal energies up to the GeV region [95]. The expected number of particles after ten years of LHC operation is $10^{16}/\text{cm}^2$. Pion irradiation facilities meeting these parameters are not regularly available.[1] However, proton irradiation facilities are available at the Los Alamos Neutron Science Center (LANSCE) [152], the Cyclotron and Radioisotope Center of Tohoku University (CYRIC) [153], CERN [154], the Paul Scherrer Institute (PSI) [155], and the Tri-University Meson Facility (TRIUMF) [156, 157]. Neutron irradiation facilities are available at the ISIS neutron and muon source at the Rutherford Appleton Laboratory [158] or at research reactors such as the TRIGA (Training, Research, Isotopes, General Atomics) nuclear reactor of the Jožef Stefan Institute (JSI) [159]. The NIEL theory, discussed in section 8.5, allows one to relate irradiations with different particle species. Thus, diamond sensors after several stages of proton and neutron irradiations were examined. Studying irradiations with different particle species and energies provides an important ingredient to predict radiation damage of diamond in future high energy physics experiments and allows to probe the NIEL theory for diamond.

Position sensitive strip detectors were manufactured from the diamond samples. After each irradiation, the devices under test (DUTs) were tested in a particle beam at CERN. Beam tests were conducted in cooperation with groups from the Ohio State University (OSU), which was responsible for detector assembly and calibration, and Institut Pluridisciplinaire Hubert Curien, Strasbourg (IPHC), which provided the telescope described in section 9.2.2.

[1] The main pion irradiation facility is at the Paul Scherrer Institute, which provides a pion beam momentum of 300 MeV [151].

Particle species	Diamond	Type	Size (mm^2)	Thickness (µm)
800 MeV protons	PW205B	sCVD	5×5	466
	L107-10	pCVD	10×10	466
	L107-11	pCVD	10×10	510
	L114-13	pCVD	10×10	516
70 MeV protons	T15-33	pCVD	10×10	518
	T15-43	pCVD	10×10	506
Fast neutrons	L107-9	pCVD	5×5	512

Table 9.1: Properties of the tested diamond samples.

9.1 Diamond Samples

This dissertation focuses on seven particular diamond samples which were characterised after several irradiations. All samples are electronic grade CVD diamond and were produced by Element Six [160]. Electronic grade sCVD diamond from Element Six typically features a nitrogen impurity fraction below 5×10^{-9}, while for pCVD diamond this fraction is typically below 5×10^{-8} [132]. Table 9.1 shows an overview of the samples with their basic properties.

The first sample, referred to as PW205B, is an sCVD diamond with a thickness of 466 µm and measures 5 mm × 5 mm. In 2011 and 2012, this sample was operated in four beam tests. Between these tests, the diamond was irradiated with 800 MeV protons in multiple steps up to a fluence of $(3.05 \pm 0.19) \times 10^{15}\,\mathrm{p/cm^2}$. Three pCVD diamond samples, L107-10, L107-11, and L114-13, were irradiated with 800 MeV protons as well. These samples measure 10 mm × 10 mm and have a thickness of 466 µm (L107-10), 510 µm (L107-11), and 516 µm (L114-13).

The samples, T15-33 and T15-43, are pCVD diamond samples with a thickness of 518 µm and 506 µm, respectively. Both samples measure 10 mm × 10 mm. They were irradiated with 70 MeV protons to fluences of $(8.8 \pm 0.9) \times 10^{15}\,\mathrm{p/cm^2}$ and $(1.96 \pm 0.14) \times 10^{15}\,\mathrm{p/cm^2}$, respectively. After each irradiation the samples were probed in multiple beam test campaigns.

The seventh sample, L107-9, is a pCVD diamond. It measures 5 mm × 5 mm and is 512 µm thick. This sample was irradiated with fast neutrons ($E > 1\,\mathrm{keV}$) up to a dose of $(1.30 \pm 0.13) \times 10^{16}\,\mathrm{n/cm^2}$ and characterised in two beam test campaigns.

9.2 Beam Tests

A high resolution tracking telescope was operated in a particle beam to measure the fully assembled detectors. This section describes procedures and the experimental environment of these tests.

9.2.1 Beam Line

The sensors were tested in the H6 beam line [161] which is located within the North Area at CERN, see figure 3.1. Up to the SPS, this beam line uses the same accelerator chain as the LHC, described in section 3.1. Protons with a momentum of 450 GeV are supplied by the SPS and directed on a beryllium target. Beam particles interact with the target and the products of these interactions result in a secondary beam. A set of magnets, installed before and after the target, allow the secondary beam to be separated by momentum. Downstream a thick dump collimator separates the H6 and two other beam lines. It allows passage in three different angles where the individual beam lines follow and thereby absorbs particles with undesired momentum. This target facility has the capability to adjust the particle species and momentum of the individual beam lines. However, particle momenta and polarities are strongly correlated among the three beam lines.

Along the H6 beam line the facility is equipped with several magnet types to adjust the beam profile and position. Dipole magnets are used to bend the beam and thus shift the beam spot depending on the orientation horizontally or vertically. Quadrupole magnets can focus and defocus the beam. They act like optical lenses and are used to adjust the beam spot size. Several collimators are positioned along the beam line to regulate intensity and momentum spread of the beam. Furthermore, the beam line features removable absorbers. These are used to remove electrons and obtain a pure hadron beam or to spread the beam. To monitor beam profiles, several wire chambers are installed along the beam line.

The beam line facilities in H6 were adjusted to obtain a hadron beam with a momentum of 120 GeV. The beam was tuned to a profile which is approximately flat in x and y to cover the detector tested. Figure 9.1 shows typical beam profiles, recorded by the wire chambers just behind the experimental setup. A broad horizontal profile with a standard deviation of about 9.7 mm was chosen. The vertical profile had a narrow peak with a standard deviation of about 5.9 mm. These profiles ensure that the detector tested has equal illumination across the detector and avoids effects arising from different intensities in different areas of

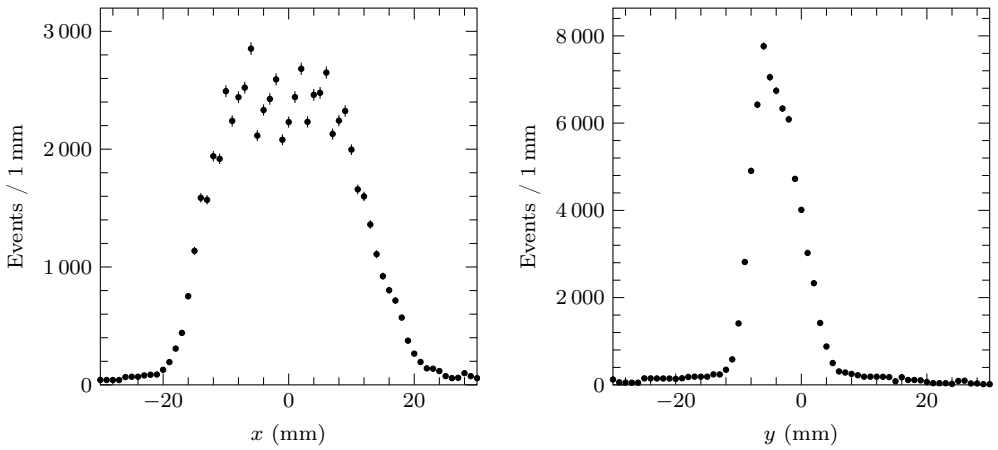

Figure 9.1: Beam profiles in horizontal (left) and vertical (right) directions. The spectra shown were measured by wire chambers during a spill of the beam test in July 2011 and represent the typical beam conditions.

the sensor. The beam intensity was adjusted to avoid recording multiple hits in a detector plane with the selected readout settings. Since the SPS supplies other facilities with protons as well, the protons come in spills every 40 s. Such a spill is typically 4 s to 10 s long.

9.2.2 Telescope

In order to analyse the behaviour and performance of the diamond detectors, precise position information of the ionising particle which passes through the detector is necessary. For this reason the diamond sensor was tested within a telescope. A telescope is a tracking system which is used to reconstruct particle trajectories. Thereby, it provides reference information about the particles passing through the DUT. It typically has a higher resolution than the DUT.

The diamond sensors were tested with the «Strasbourg telescope» consisting of eight planes of silicon strip detectors [162]. The silicon strip detectors measure 12.8 mm × 12.8 mm. A telescope module consists of a pair of planes. Each of the four modules has a pair of detectors with strips orientated horizontally and vertically, respectively. Two modules were located in front of the DUT and two behind it. A plastic scintillator, measuring 7 mm × 7 mm, was installed behind for triggering purposes. Figure 9.2 shows a schematic drawing of the telescope. 256 strips are read out in each plane. The readout pitch of the strips is 50 µm. In

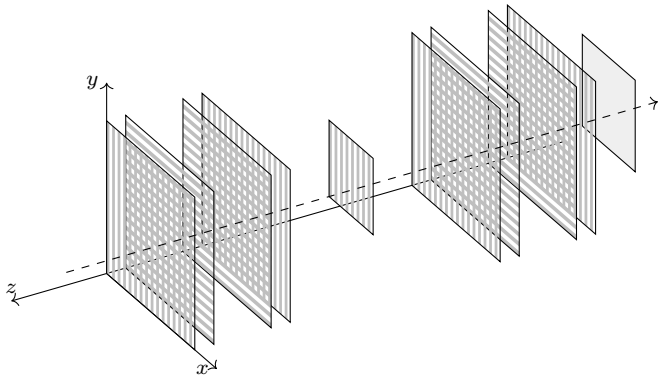

Figure 9.2: Schematic view of the reference telescope. The DUT is mounted in the centre. Two modules are placed in the front of the DUT and two behind it. The modules are orientated in such a way that an x plane is followed by two y planes and another x plane. A plastic scintillator at the end completes the telescope. The dashed line illustrates a particle of the beam propagating trough the telescope.

between readout strips lie one or two floating intermediate strips[2], depending on the module. As described later in section 10.3.2, an uncertainty on the predicted track position of 1.3 µm was observed in the plane of the DUT.

Readout strips were wire bonded to application-specific integrated circuits (ASICs). Low-noise charge sensitive VA2 chips [164] with 128 channels were used for this purpose. Each channel consists of a charge sensitive preamplifier followed by a *CR-RC* signal shaper. Since signals can be rather small, a preamplifier is used. The shaper aims to improve the signal-to-noise ratio (SNR) by exploiting different frequency spectra of signal and noise. It consists of a CR high-pass filter which sets the decay time of the resulting pulse. An RC low-pass filter follows which defines the signal's rise time and tailors the upper frequency band. The resulting pulse's amplitude is proportional to the signal charge. Limiting the frequency band width influences the time response as well and pulses get longer. Thus, the expected signal rate needed to be limited to avoid overlap of subsequent pulses. An analog buffer follows the signal shaper and stores the signal until they are read out. Buffered signals from different channels are multiplexed. The signal of each channel is digitised sequentially with a SIROCCO (silicon strip read out CAMAC controller) analog-to-digital converter (ADC) [165]. Each telescope plane uses two VA2 chips to read out 256 strips. The signal rise time was set to 1 µs for the silicon detectors.

[2]Generally, the required space of readout electronics is restricting the granularity of readout strips and thereby limiting the resolution of a strip detector. Intermediate strips can increase the resolution of the sensor while keeping the number of readout strips fixed [163].

Two photomultipliers were attached to the scintillator behind the telescope. If their signals were in coincidence, the telescope readout was triggered. About 10 000 to 50 000 events were triggered per spill with the chosen beam intensities. Out of these, about 3 600 events were stored. Typically, 10^6 events are recorded in a run, which took 4 h to 5 h.

As depicted in figure 9.2, a cartesian coordinate system was defined with x and y pointing in horizontal and vertical directions, respectively, both perpendicular to the beam. The z direction was defined by the beam. Rotation around the z axis is described by ϕ. The first module's corner specifies the origin.

9.2.3 Device Assembly and Preparation

Assembly

For a beam test campaign, DUTs holding one or two diamond samples were assembled at OSU. The diamond was cleaned with hot acids and etched with an oxygen plasma. After cleaning, both sides were metallised using a photolithographic lift-off process. On one side, the strip pattern was manufactured. The strips have a width of 25 µm and are separated by 25 µm resulting in a strip layout with a pitch of 50 µm to match the readout electronics. A guard ring enclosed the strip pattern. Similarly, a single pad structure was fabricated on the second side of the diamond. Both sides were metallised with a chromium layer of 50 nm followed by a gold layer of 200 nm. After the pattern on both sides was formed, the sample was annealed in a nitrogen atmosphere at 400 °C.

Similar to the telescope planes, described in section 9.2.2, the diamond sensor was connected to the readout electronics. A single VA2.2 chip with a signal rise time set to 2 µs was used to read out 128 strips. The guard ring was connected to the same potential as the strips using a VA channel and protected them from edge currents. Figure 9.3 shows a photograph of an assembled diamond detector connected to the readout electronics. To facilitate handling of the DUT and avoid light exposure, the sensor was mounted in an aluminium box. These boxes are lightproof and feature connectors for readout and high voltage supply.

Preparation

As described in section 8.4, the diamond lattice can feature charge traps. These may result in initial inefficiencies of the collected charge. During long-term operation of a detector in a high energy physics experiment, such traps would be filled. Once a

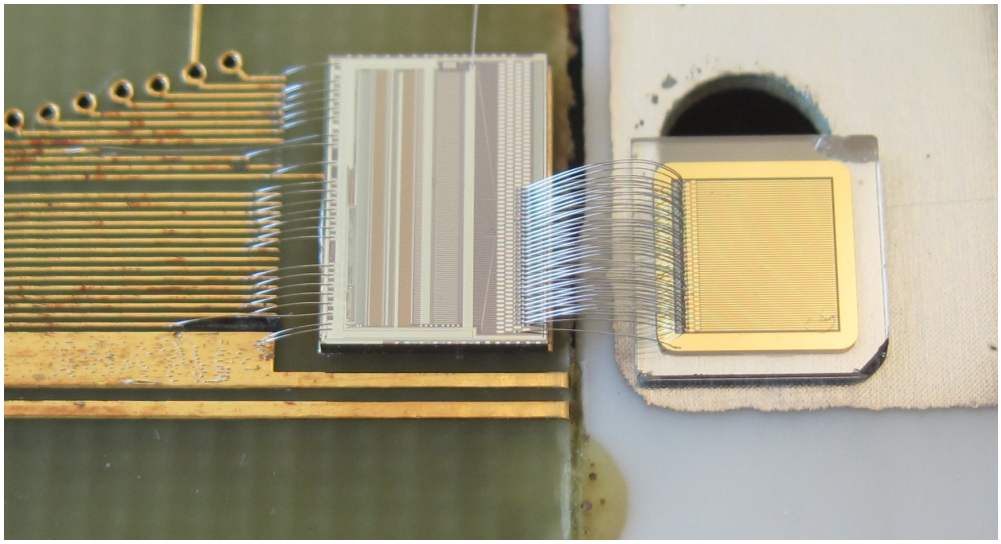

Figure 9.3: Photograph of a diamond sensor [166]. The diamond sample PW205B on the right is mounted and wire bonded to the VA2.2 readout ASIC on the left. Each strip was wire bonded to an individual readout channel as shown.

charge trap is filled, it cannot catch further charges. For this reason, the sensor was exposed to a ^{90}Sr source before testing. This so-called *pumping* procedure aims to fill the traps [108] and set the DUT into a stable state as it would be during operation in an experiment. Energy is mostly deposited via ionisation and the resulting charges can fill the traps. The device was exposed to a high activity source (54 MBq) for 4 h before each beam test and in between runs with opposite polarity. During this time, the DUT was exposed to a MIP fluence of about $10^{10}/\mathrm{cm}^2$ which is sufficient to saturate the charge traps [167]. In between runs with equal polarity, the diamond detector was exposed to a low activity source (23 MBq) for 20 min. Since exposure to light could reset the sensor to its initial state, the sensor was kept in the sealed aluminium box.

After pumping, the DUT was mounted in the middle of the telescope and connected to the readout system. The high voltage source was connected and turned up slowly to the desired bias potential such that the leakage current was kept below 100 nA at all times. To start a beam test, the leakage current was required to be below 10 nA. The total currents measured before and after the beam test are listed in table 9.2. A decrease of the detector leakage current is usually observed during the beam tests.

Beam test	Diamond	Run	$I_{\text{total}}^{\text{initial}}$ (nA)	$I_{\text{total}}^{\text{final}}$ (nA)
August 2008	T15-33	13 003	*	*
		13 004	*	*
		13 008	<30	*
		13 009	*	<1
	L107-9	13 026	< 1	<1
June 2009	T15-43	14 022	<15	*
		14 024	<19	*
September 2009	T15-43	14 102	< 2	*
		14 103	< 2	*
		14 107	< 3	*
		14 108	< 2	*
	T15-33	14 111	< 1	*
		14 114	< 1	*
June 2010	L107-10/L114-13	15 004	<16	*
		15 005	< 9	*
		15 011	<25	*
		15 012	<25	*
August 2010	L107-11	15 104	<13	*
July 2011	PW205B	16 001	< 9	*
		16 005	< 8	*
	T15-43	16 003	< 2	*
		16 007	< 2	*
	L107-10/L107-11	16 009	< 2	*
		16 011	< 2	*
October 2011	PW205B/L107-9	16 303	< 1	0.1
		16 307	< 1	0.1
August 2012	PW205B	17 101	< 4	4
		17 104	< 7	6
October 2012	PW205B	17 208	< 3	1.4
		17 211	< 4	1.5

* Not measured

Table 9.2: Total current in the detector system measured before and after beam test runs. At the beginning of a run the current is dropping very rapidly and hence an upper limit of the initial value is quoted.

Beam test	Diamond	c (ADC/e)	Method
August 2008	T15-33	$7.00 \pm 0.35 \times 10^{-2}$	‡
	L107-9	$6.90 \pm 0.35 \times 10^{-2}$	‡
June 2009	T15-43	$6.80 \pm 0.34 \times 10^{-2}$	‡
September 2009	T15-33	$5.50 \pm 0.23 \times 10^{-2}$	‡
	T15-43	$7.5 \pm 0.4 \times 10^{-2}$	‡
June 2010	L107-10/L114-13	$7.60 \pm 0.12 \times 10^{-2}$	‡
August 2010	L107-11	$8.72 \pm 0.12 \times 10^{-2}$	‡
July 2011	PW205B	$8.62 \pm 0.17 \times 10^{-2}$	*†‡
	T15-43	$7.40 \pm 0.37 \times 10^{-2}$	‡
	L107-10/L107-11	$8.72 \pm 0.12 \times 10^{-2}$	*†
October 2011	PW205B/L107-9	$7.80 \pm 0.12 \times 10^{-2}$	†
August 2012	PW205B	$7.80 \pm 0.12 \times 10^{-2}$	†‡
October 2012	PW205B	$7.60 \pm 0.12 \times 10^{-2}$	†‡

* Reference diamond
† Precision capacitor
‡ Noise reference

Table 9.3: Overview of calibration constants of individual diamond samples for different beam tests.

9.2.4 Signal Calibration

Read out signals were stored as integer ADC values. The amplified signals digitised into integer ADC values require a calibration to be converted into the collected charge. Since the output signals of the ADC depend on settings and characteristics of the readout electronics which can vary between beam test campaigns, an individual calibration for each device and beam test campaign was obtained. Three different methods were employed to calculate the calibration constant

$$c = \frac{Q_{\text{meas}}}{Q_{\text{ind}}} \tag{9.1}$$

where Q_{meas} is the measured charge of the ADC and Q_{ind} the induced charge on the electrode. The obtained calibration constants are summarised in table 9.3. Overall, an uncertainty of about 1 % to 2 % was achieved. The calibration methods are briefly described below.

Reference Diamond

The first method uses a reference diamond on the same readout chip as the DUT. This exploits unirradiated sCVD diamond samples with CCD equal to the thickness of the material. With equation (8.27), the mean induced charge in the reference diamond

$$\overline{Q}_{\text{ind}} = n_0 dq \tag{9.2}$$

can be computed. Combining with equation (9.1), the calibration constant is derived as

$$c = \frac{\overline{Q}_{\text{meas}}}{n_0 dq}. \tag{9.3}$$

Since the DUT is mounted on the same ASIC, the gain, noise, and thus calibration constant should be the same.

Precision Capacitor

In the second method, a well defined input charge on a well defined capacitor was used. A 1 V square wave pulse was formed and then divided by 1 000, resulting in a input pulse of 1 mV to charge a precision capacitor. The capacitance was $C = 1.8\,\text{pF}$ with a tolerance of 1 %. This resulted in an input charge of

$$Q = CU = 11\,230\,\text{e} \tag{9.4}$$

which is comparable to the signal response of an sCVD or a pCVD diamond sensor. The calibration constant can be calculated by relating to the output signal

$$c = \frac{Q_{\text{meas}}}{CU}. \tag{9.5}$$

Noise Reference

The noise measurement of each beam test run may be used as consistency check for the calibration. Suppressing physical signal charges, the raw noise charge of a strip i is

$$q_i^{\text{raw noise}} = q_i^{\text{raw}} - p_i \tag{9.6}$$

where q_i^{raw} is the raw output signal of the ADC with a pedestal p_i. The raw noise consists of two components, the random noise charge, q_i^{noise}, originating from the amplifier and a common shift among all channels, q^{CMN}. Thus, the random noise charge or common mode corrected (CMC) noise charge is given by

$$q_i^{\text{noise}} = q_i^{\text{raw}} - p_i - q^{\text{CMN}}. \tag{9.7}$$

The noise charge depends on the settings of the electronics used and the capacitances connected. Therefore, it is expected to be consistent between beam tests with the same setup.

A theoretical prediction of the expected noise charge was derived, following the description in reference [126]. The noise charge of a single amplifier channel with the signal rise time set to 2 µs is $60\,\mathrm{e} + 11\,\mathrm{e/pF} \times C_\mathrm{d}$ [164]. It depends on the connected detector capacitance C_d. Figure 9.4 shows a schematic of a strip detector and its capacitances. The detector capacitance C_d can be estimated by

$$C_\mathrm{d} = 2C_\mathrm{s} + C_\mathrm{b} + C_\mathrm{stray} \tag{9.8}$$

where C_s is the interstrip capacitance, C_b the strip to backplane capacitance, and C_stray is the stray capacitance associated with the wire bonds and the hybrid board. In equation (9.8), only the capacitance between adjacent strips is considered, capacitive coupling to farther strips are neglected. Approximating the electrodes by cylindric wires embedded in the diamond, the capacitance between two strips is given by [168]

$$C_\mathrm{s} = \frac{2\pi\varepsilon_0\varepsilon_r l}{\ln\left(\frac{2p^2-w^2}{w^2} + \sqrt{\left(\frac{2p^2-w^2}{w^2}\right)^2 - 1}\right)} \tag{9.9}$$

where l is the length of a strip, w its width, and p the pitch width. The relative permittivity ε_r in this geometry with two dielectrics of dielectric constants 1 and ε is $\varepsilon_r = (\varepsilon + 1)/2$ [126, 169]. The capacitance between a strip and the backplane electrode, C_b, for a detector of thickness d was estimated by a simple plate capacitor

$$C_\mathrm{b} = \varepsilon_0\varepsilon\frac{pl}{d}. \tag{9.10}$$

The stray capacitance was approximated to be 1.0 pF to 1.5 pF. For the DUT used which has a thickness of 466 µm, 25 µm wide and 4 mm long strips, and a strip pitch of 50 µm, the interstrip capacitance and the strip to backplane capacitance were calculated to be 0.28 pF and 0.02 pF, respectively, resulting in a noise charge of 77 e to 83 e.

The raw and CMC noise values were reconstructed for each beam test run from the width of the raw and CMC charge distribution of non-hit events as described later in section 10.1.1. Table 9.4 lists the measured raw and CMC noise values. The raw noise was observed to be (101.1 ± 3.5) e, while the CMC noise was observed to be (79 ± 4) e. It should be noted that the typical raw noise spread is approximately 13 e with individual runs having noise values as high as 139.9 e [149]. The small spread in the raw noise is therefore an artefact of this two year running period. In all runs, the CMC noise value was found in agreement with the theoretical prediction.

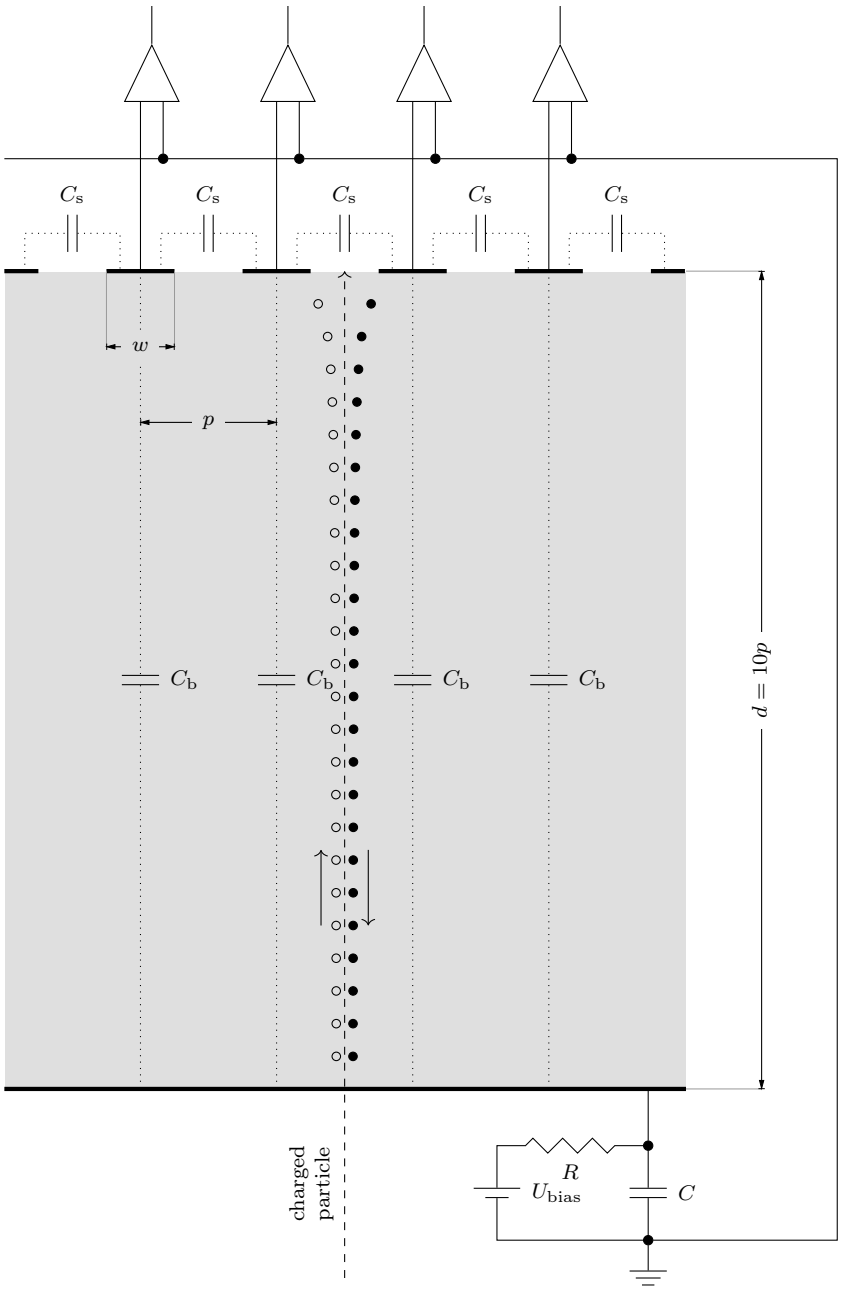

Figure 9.4: Schematic drawing of a strip detector, derived from reference [126]. The capacitances between strips and from the strips to the backplane electrode, C_s and C_b, are indicated. Each strip of width w is connected to an amplifier channel. The pitch width between readout strips, p, is labelled, which is 50 µm for this thesis, and d is the thickness of the detector material. The high voltage U_{bias} is applied to the backplane electrode via a resistor R. A capacitor C connects the backplane electrode to ground to stabilise the applied voltage.

Run	$\sigma_{\text{raw}}^{\text{noise}}$ (e)	$\sigma_{\text{CMC}}^{\text{noise}}$ (e)
16 001	103.9	83.1
16 005	102.7	82.1
16 303	94.7	71.4
16 307	95.8	72.5
17 101	102.0	80.3
17 104	102.0	79.7
17 208	103.3	79.6
17 211	104.4	83.1

Table 9.4: Raw and common mode corrected (CMC) noise measured with the sCVD diamond sample `PW205B`.

The slightly larger spread of CMC values may originate from a larger statistical uncertainty in the common mode noise (CMN) calculation. After calibration, the noise values were required to differ less than two standard deviations from the mean value for the run to be included in this analysis.

9.3 Irradiations

In between beam test campaigns, the samples were irradiated. The sCVD diamond sample, `PW205B`, and three pCVD diamond samples, `L107-10`, `L107-11`, and `L114-13`, were irradiated with 800 MeV protons. Two of the pCVD diamond samples, `T15-33` and `T15-43`, were exposed to a 70 MeV proton beam and one pCVD diamond sample, `L107-9`, was irradiated with neutrons. Since the readout electronics used was not radiation hard, the sensors were disassembled for each irradiation. Furthermore, cool down times due to activation of the metallisation were avoided by only irradiating the bare diamond.

9.3.1 Proton Irradiations

A proton beam with a momentum of 800 MeV at LANSCE [152] was used to irradiate the diamond samples. Aluminium foils were used for the dosimetry and placed in front or behind the diamond sample. Incident protons interact with aluminium atoms and ^{22}Na isotopes are produced. This nuclide has a half-life of 2.603 y [17]. A given time after irradiation, the activity of the aluminium was

Diamond	Date	$\Delta\phi$ (p/cm^2)	ϕ (p/cm^2)
PW205B	June 2011	0×10^{15}	0×10^{15}
	August 2011	$0.78 \pm 0.07 \times 10^{15}$	$0.78 \pm 0.07 \times 10^{15}$
	December 2011	$1.61 \pm 0.16 \times 10^{15}$	$2.39 \pm 0.18 \times 10^{15}$
	September 2012	$0.66 \pm 0.07 \times 10^{15}$	$3.05 \pm 0.19 \times 10^{15}$
L107-10	December 2009	$5.5 \pm 0.6 \times 10^{15}$	$5.5 \pm 0.6 \times 10^{15}$
	August 2010	$4.8 \pm 0.5 \times 10^{15}$	$10.3 \pm 0.7 \times 10^{15}$
L107-11	November 2009	0×10^{15}	0×10^{15}
	August 2010	$3.50 \pm 0.35 \times 10^{15}$	$3.50 \pm 0.35 \times 10^{15}$
L114-13	December 2009	$12.6 \pm 1.3 \times 10^{15}$	$12.6 \pm 1.3 \times 10^{15}$

Table 9.5: Irradiations with 800 MeV protons at LANSCE. The fluences of each irradiation, $\Delta\phi$, have an uncertainty of $\pm 9\,\%$ to $\pm 10\,\%$. The error of the integrated fluence ϕ was calculated by propagating the uncertainty of each individual irradiation.

Diamond	Date	$\Delta\phi$ (p/cm^2)	ϕ (p/cm^2)
T15-33	March 2008	$8.8 \pm 0.9 \times 10^{15}$	$8.8 \pm 0.9 \times 10^{15}$
T15-43	March 2008	$0.96 \pm 0.10 \times 10^{15}$	$0.96 \pm 0.10 \times 10^{15}$
	July 2010	$1.00 \pm 0.10 \times 10^{15}$	$1.96 \pm 0.14 \times 10^{15}$

Table 9.6: Irradiations with 70 MeV protons at CYRIC. The uncertainty of each fluence measurement is 10 %. The error on the individual irradiations is propagated to calculate the uncertainty of the integrated dose.

measured. The fluence was determined by applying the total cross section of proton-aluminium interactions. The method achieves an uncertainty of about 9 % to 10 % on the fluence measurement. More details can be found in reference [170]. The diamond sample PW205B acquired a total dose of $(3.05 \pm 0.19) \times 10^{15}\,\mathrm{p/cm^2}$ in three irradiations. The highest dose was accumulated by the pCVD diamond sample L114-13. A summary of the irradiation campaigns and doses is given in table 9.5.

Two pCVD diamond samples, T15-33 and T15-43, were irradiated at CYRIC [153] with 70 MeV protons. Aluminium foil activation was used for dosimetry. The proton fluences of both samples are summarised in table 9.6. In two irradiation campaigns, the samples accumulated fluences of $(8.8 \pm 0.9) \times 10^{15}\,\mathrm{p/cm^2}$ and $(1.96 \pm 0.14) \times 10^{15}\,\mathrm{p/cm^2}$, respectively.

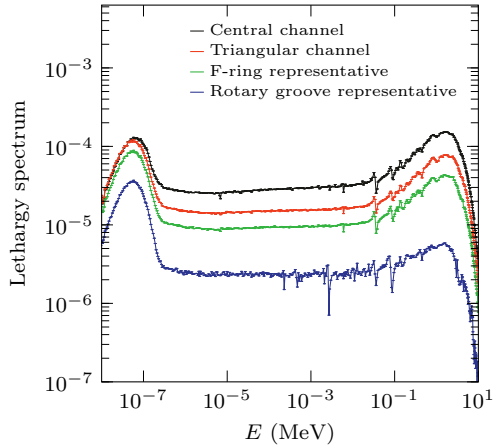

Figure 9.5: Lethargy neutron spectrum in representative irradiation channels of the TRIGA reactor at JSI, derived from reference [159].

9.3.2 Neutron Irradiations

The neutron irradiations were performed at the TRIGA nuclear reactor of JSI in Ljubljana, Slovenia. In the irradiation channel used, the neutron energy spectrum ranged from thermal neutrons with an energy of 10^{-8} MeV to fast neutrons of 7 MeV [171]. Figure 9.5 shows the neutron spectrum of the reactor in the lethargy[3] representation.

Gold activation was used to determine the fluence of fast neutrons above 0.1 MeV [173]. In several irradiations, the sample `L107-9` was irradiated to a fast neutron fluence of $(1.30 \pm 0.13) \times 10^{16}\,\mathrm{n/cm^2}$.

[3]The lethargy spectrum relates to the energy spectrum by [172]

$$\varphi(u) = E\varphi(E) \tag{9.11}$$

where the lethargy u is defined by [172]

$$\mathrm{d}u = -\frac{\mathrm{d}E}{E}. \tag{9.12}$$

Chapter 10

Signal Reconstruction

Pedestal and noise values were obtained from raw signals. In each detector plane, hit positions were determined which were afterwards combined into reconstructed tracks. Trajectories meeting the analysis requirements were extrapolated into the DUT plane and the signal of the corresponding channels was analysed. These reconstructed signals were converted into CCDs which are presented in chapter 11.

10.1 Signal Determination

As described in section 9.2.2, measured signals were amplified and digitised for each strip in an individual channel. The raw recorded signal q_i^{raw} of an ADC channel i is composed of multiple quantities

$$q_i^{\text{raw}} = q_i^{\text{signal}} + q_i^{\text{noise}} + p_i + q^{\text{CMN}}. \tag{10.1}$$

The physical signal q_i^{signal} is caused by the crossing of a charged particle, resulting in a so-called hit. The random noise in the electronics is denoted by q_i^{noise}. It is expected to be white noise and therefore Gaussian distributed. The analog electronics provides the signals with a pedestal p_i which must be subtracted. Furthermore, a common mode (CM) shift of this pedestal value among all channels is considered in the CMN charge, q^{CMN}.

10.1.1 Pedestal Reconstruction Algorithm

To obtain the physical signal which is proportional to the collected charge, a reliable reconstruction of pedestal and noise is essential. An algorithm, which

estimates a pedestal and noise value for each channel and event from the past N events, was used. The procedure was carried out for each individual strip channel separately.

In the first step, initial values for pedestal and noise are iteratively derived. A set $\mathcal{E}$ of the first $N = 500$ events is chosen. During usual beam conditions, this set corresponds to a data recording time of about 1 s. Ideally, pedestal and noise values are calculated from the raw ADC signal q_i^{raw} of events in which channel i has no physical signal. These events define a subset $\mathcal{E}' \subset \mathcal{E}$. Neglecting CMN, the raw ADC signal of non-hit channels has a Gaussian distribution around the pedestal value. Mean and width of the raw ADC signal distribution define pedestal

$$p_i^{\text{init}} = \overline{p}_i = \frac{1}{N - N_{\text{signal}}} \sum_{n \in \mathcal{E}'} q_i^{\text{raw}}(n) \tag{10.2}$$

and noise

$$\sigma_i^{\text{init}} = \sqrt{\frac{1}{N - N_{\text{signal}} - 1} \sum_{n \in \mathcal{E}'} \left(q_i^{\text{raw}}(n) - p_i^{\text{init}}\right)^2} \tag{10.3}$$

where N_{signal} is the number of identified signal events. Since signal events are not known initially, all events of set $\mathcal{E}$ are considered in the first iteration. Afterwards, a threshold is set to define events with physical signal within $\mathcal{E}$. Since physical signals are always positive[1], events with a raw signal $q_i^{\text{raw}} > p_i + 5\sigma_i$ are considered hits and ignored in subsequent iterations. Pedestal and noise are recalculated. This iteration is repeated seven times letting initial pedestal and noise values converge. The first N events are associated with the initial pedestal p_i^{init} and noise σ_i^{init} values, respectively.

For each following event the collection window moves with event number. Event $n - N$ is removed from set $\mathcal{E}$ and event n is added. Applying equation (10.2) and equation (10.3) the pedestal $p_i(n)$ and $\sigma_i(n)$ are calculated for the current event n.

CMN is a common pedestal shift among all channels. However, to avoid a bias from inoperable or disconnected channels, such channels are excluded from the CMN estimation. Channels selected for the analysis, as described later in section 10.1.2, define a set $\mathcal{S}$. The CMN contribution is calculated from a subset $\mathcal{S}' \subset \mathcal{S}$ which excludes channels whose signal exceeds $p_i + 5\sigma_i$. It is the average difference of raw signal and pedestal value

$$q^{\text{CMN}} = \frac{1}{S'} \sum_{i \in \mathcal{S}'} \left(q_i^{\text{raw}} - p_i\right) \tag{10.4}$$

[1]Normally the sign of the signal depends on the applied voltage. In this case, jumpers were used on the output amplifier to make all signals positive irrespective of the voltage.

where S' is the number of channels in subset $\mathcal{S}'$. Since the random noise component is similarly distributed in selected channels, its contribution to the raw signal is averaged out in equation (10.4). A noticeable contribution of CMN is observed in the DUT only [149, 174]. This is explained by a finer granularity of the ADC in the readout of the DUT compared to the telescope planes. After estimating the CM shift, a correction is applied in equation (10.2) and equation (10.3), resulting in a CMC pedestal of

$$\overline{p}_i(n) = \frac{1}{N - N_{\text{signal}}} \sum_{n' \in \mathcal{E}'} q_i^{\text{raw}}(n') - q^{\text{CMN}}(n') \tag{10.5}$$

and a CMC noise of

$$\sigma_i(n) = \sqrt{\frac{1}{N - N_{\text{signal}} - 1} \sum_{n' \in \mathcal{E}'} \left(q_i^{\text{raw}}(n') - q^{\text{CMN}}(n') - \overline{p}_i(n)\right)^2} \tag{10.6}$$

for event n.

This iterative algorithm ensures that fluctuations and other temporary changes such as electronic noise are not biasing the signal. In figure 10.1 pedestal subtracted and CMC signal are shown for strips in $\mathcal{S}'$. This noise distribution is centred around zero which verifies a good pedestal estimation. The Gaussian fit results in a width of about 83 e.

10.1.2 Selection

In the next step, the functionality of all channels was verified. Non-hit channels were studied to monitor noise behaviour and hit events were investigated to test strip connections. Channels not connected to the sensor or not working properly were excluded, as described below. Remaining channels define a set $\mathcal{S}$ good for the analysis.

CMC pedestal mean and standard deviation of all events are shown in figure 10.2 for individual channels. Mean pedestal values are in the range 6×10^3 e to 2×10^4 e. A periodic structure along the strips is observed which is associated with the readout chip. The majority of channels yield a standard deviation around 83 e and reflect a well working algorithm. Channels indicating a noisy behaviour by a larger spread of the pedestal distribution, such as channel 64 in figure 10.2, were excluded from the further analysis.

Figure 10.3 shows a histogram of the largest signal position. Due to the settings of the beam profile, a uniform distribution is expected. Single channels which

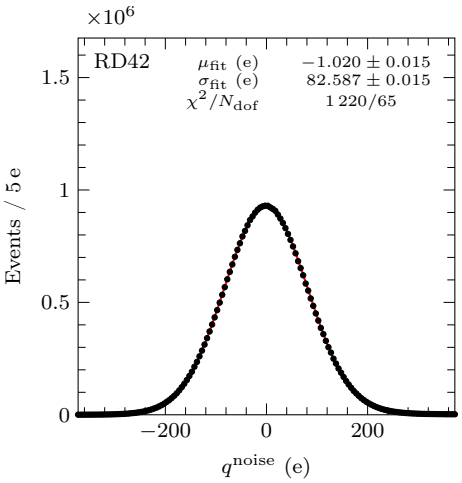

Figure 10.1: Pedestal subtracted and CMN corrected signal distribution of non-hit events including strips all selected for the analysis. A Gaussian fit is drawn in red.

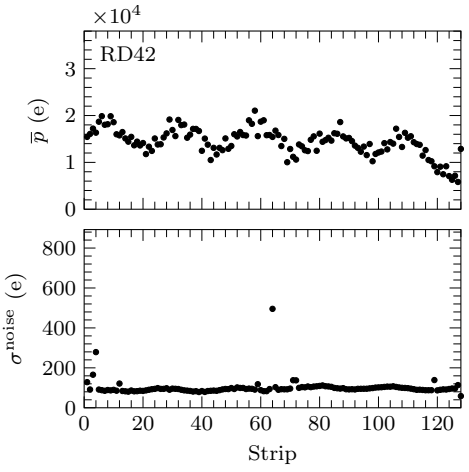

Figure 10.2: CMN corrected pedestal mean (top) and standard deviation (bottom) for each channel. Channels indicating significantly higher noise are excluded in the further analysis.

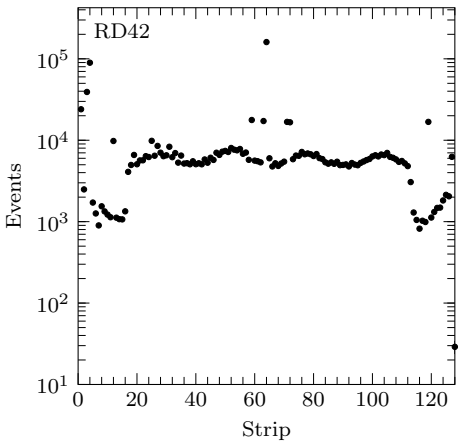

Figure 10.3: Spectrum of the largest signal position in all readout channels. Channels 2 to 64 are connected to the diamond sample under test and channels 66 to 128 connect a second sample. The guard rings are connected to channels 1 and 65, respectively.

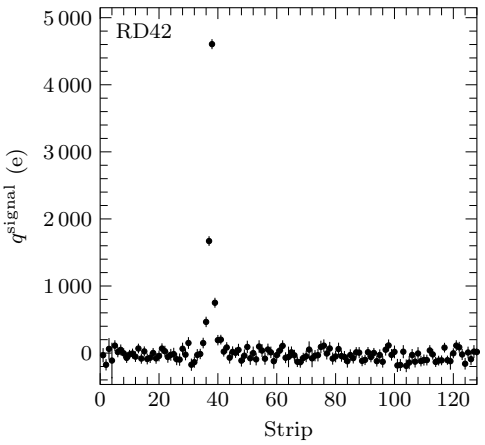

Figure 10.4: Pedestal subtracted and CMN corrected signals of a single event in the diamond plane. Error bars denote the random noise quantities. Channels 36 to 39 feature signals associated with a particle hit.

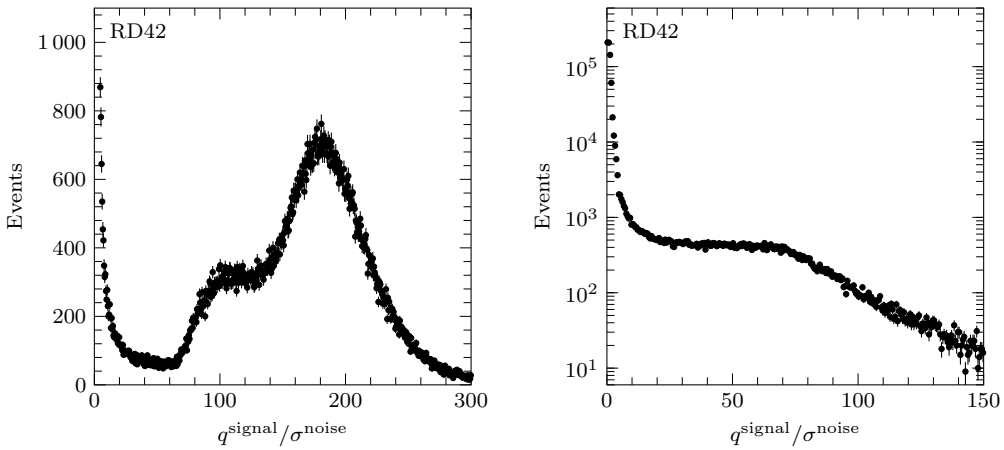

Figure 10.5: CMN corrected signal-to-noise ratio distribution of the strip with the highest signal (left) and of its adjacent strip (right) in the diamond detector plane. A signal-to-noise ratio around 180 corresponds to full charge collection in a strip.

deviate significantly from this were marked and excluded in the further steps. These channels can either be dead channels due to a broken wire bond or noisy because of a problem in the readout chip. In the case of figure 10.3, channels 17 to 55 are selected for the further analysis and define the set $\mathcal{S}$.

10.2 Clustering

Induced charges in the bulk of a diamond sensor spread while they drift towards the surface due to diffusion. Thus, the signal of a single particle can be collected by more than one strip. This effect is called *charge sharing*. Figure 10.4 shows the reconstructed signals per strip in an event. After pedestal subtraction, signals of all strips are distributed around zero. Four strips represent large signals caused by a particle hit. Thus, multiple adjacent strips are associated with one particle hit. A so-called *cluster* was built to combine this collection of strips and reconstruct a particle's hit position and deposited charge.

10.2.1 Clustering Algorithm

To distinguish hits belonging to a cluster from background noise, thresholds on the SNR are used. In figure 10.5, the SNR distributions in the diamond plane are shown. The left spectrum represents the strip with the highest signal of each event. At low SNRs, the Gaussian noise tail is visible. The particle which triggered the

scintillator does not pass through the area of the detector in these events. A peak at around 180 represents signal events in which most of the charge is collected by this single strip. The plateau at its lower tail originates from events in which multiple strips collect the deposited charge (charge sharing). In the second plot of figure 10.5, the SNR distribution of the largest adjacent signal strip is shown. It has a high Gaussian noise peak at zero which originates from pure background events and events in which the charge is collected only by the primary strip. Events sharing deposited charge with two or more strips are found in the SNR region around 10 to 100.

Based on the shape difference in the SNR spectra of the primary and adjacent strip, two types of thresholds on the SNR were defined. In the primary strip, events associated with a particle hit are clearly separated from the noise tail by a minimum in the SNR spectrum. The adjacent strip's SNR spectrum is continuously decreasing. For this reason, a smaller threshold was chosen to identify adjacent strips belonging to a cluster. A channel with an SNR

$$\frac{q_i^{\text{signal}}(n)}{\sigma_i(n)} > t_{\text{seed}} \tag{10.7}$$

is labelled as *seed* and associated with the primary strip. Such channels with

$$\frac{q_i^{\text{signal}}(n)}{\sigma_i(n)} > t_{\text{hit}} \tag{10.8}$$

are called *hits* and identify remaining strips belonging to a cluster. Since the characteristics of the readout electronics can vary, thresholds were defined individually for each detector and beam test campaign. A threshold of $t_{\text{seed}} = 16$ was chosen to identify a seed in the case shown in figure 10.5. This choice of seed threshold provides good separation from background events without loosing much signal. Additional hit strips were selected by a threshold of $t_{\text{hit}} = 6$ in this case. Similarly, thresholds were chosen for the silicon telescope planes.

For each event, all channels were scanned for hits and seeds. Groups of adjacent hits which contained at least one seed form a cluster. A cluster was further required not to include saturated or masked channels nor be located next to a masked channel. In figure 10.6, the cluster size distribution is shown for different accumulated 800 MeV proton fluences. On average in $(45 \pm 12)\,\%$ of the events 1-strip clusters are reconstructed and about $(41 \pm 5)\,\%$ of the events the cluster includes two strips. Together, the reconstruction efficiency of one and two strip clusters was observed to be $(87 \pm 7)\,\%$. $(7 \pm 5)\,\%$ of the events feature a cluster consisting of three strips and $(2.8 \pm 2.0)\,\%$ a 4-strip cluster. Clusters including five or more strips were reconstructed in $(2.7 \pm 1.5)\,\%$ of the events. These reconstruction efficiencies depend on the choice of cluster thresholds.

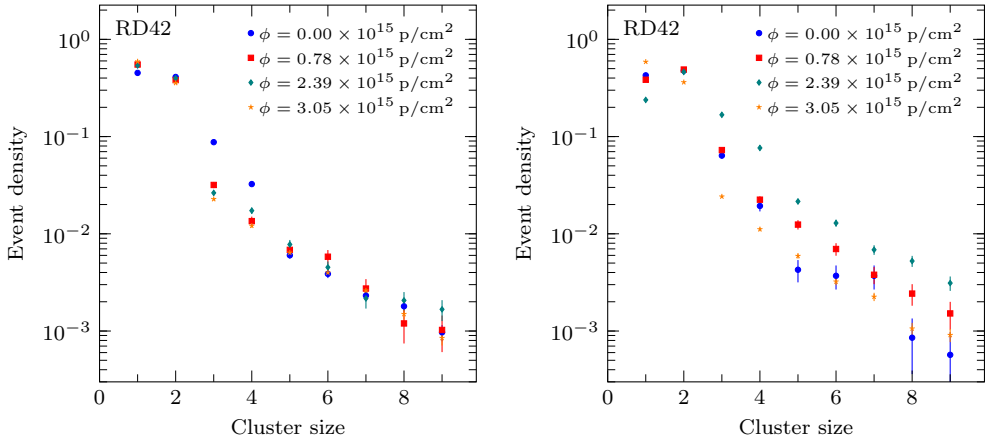

Figure 10.6: Cluster size distribution of reconstructed clusters in diamond plane for different accumulated 800 MeV proton fluences in case of an electric bias field of +2 V/µm (left) and −2 V/µm (right).

Clusters of three or more strips were possibly caused by energetic knock-on electrons [17, 143, 175]. Knock-on electrons or δ rays are produced if the incident particle transfers a sufficient amount of energy to an atomic electron to displace the electron from the atom and form a secondary track. Hence δ rays deposit energy over a larger area away from the primary track resulting in large clusters.

10.2.2 Cluster Charge

The cluster's signal charge or pulse height is defined as the sum of pedestal subtracted signals in all channels associated with the cluster

$$q^{\text{signal}} = \sum_{i \in \mathcal{C}} q_i^{\text{signal}} \tag{10.9}$$

where $\mathcal{C}$ denotes the set of strips belonging to the cluster. Pulse height distributions collected by clusters of size 1, 2, 3, and 4 with the unirradiated diamond sample are shown in the left plot of figure 10.7. The spectra were normalised by their integral and are Landau distributed. All distributions start at around 11 000 e. The cluster size depends on the signal charge. Signals of 4-strip clusters are significantly higher compared to smaller clusters, but overall these clusters are much rarer. This implies that larger clusters are most likely caused by higher charge depositions as expected from δ rays. 2-strip clusters yield a slightly smaller mean signal than 1-strip clusters. The reason for this was found to be a loss of charge in the case of charge sharing between two adjacent strips, as described later in section 10.4.2.

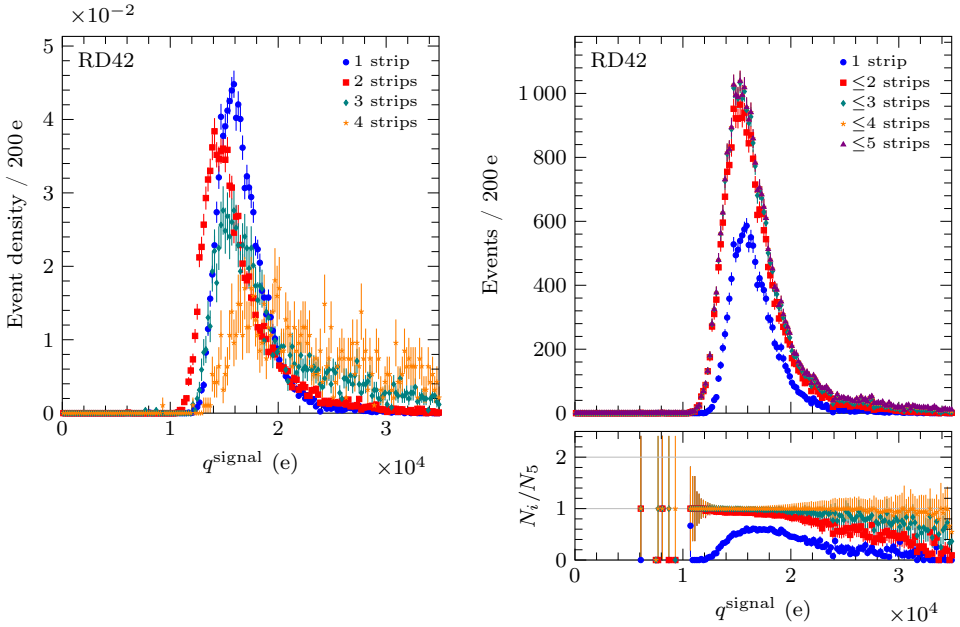

Figure 10.7: Signal charge collected by clusters of different size in the diamond plane before irradiation. In the left plot the pulse height distributions of clusters including 1, 2, 3, and 4 strips are drawn. The distributions in the right plot shows the pulse heights of cluster with a size of 1, ≤2, ≤3, ≤4, and ≤5 strips.

The individual pulse height distributions are summed up in the right plot of figure 10.7. The spectra shown represent the pulse height collected by clusters of 1, ≤2, ≤3, ≤4, and ≤5 strips. All spectra have Landau shapes. The distribution of 1-strip clusters features less events over the full spectrum. Remaining spectra only differ slightly in the higher tail. The signal distribution including 1- and 2-strip clusters is chosen as the reference. It has a mean of 16 400 e which corresponds to a CCD of about 456 µm. Including all cluster sizes would increase the mean signal by less than 3 %.

10.2.3 Cluster Position

A variety of methods is available to reconstruct hit positions in a tracking detector. They differ in complexity and are characterised by the uncertainty on the reconstructed position, the *spatial resolution*. It is defined by the standard deviation of the residual, which is the difference between measured and true hit position. Since the true hit position is usually unknown, the predicted hit position is used instead. Four commonly used algorithms are described below [176].

Digital Position

This method associates the position of highest signal strip's centre with the particle's hit position. The seed strip marks the so-called *digital* position of a cluster

$$x = x_{\text{seed}}. \tag{10.10}$$

A uniform residual distribution as wide as a strip's width is expected. Thus it can be described by a rectangular function of width equals the pitch width. The spatial resolution of a rectangular distribution equals [163]

$$\sigma_x = \frac{p}{\sqrt{12}} \tag{10.11}$$

where p is the pitch width. This results in a theoretical spatial resolution of about 14.4 µm for a strip pitch of 50 µm.

Charge Weighted Position

When reconstructing an incident particle's hit position, charge sharing can be exploited to improve the spatial resolution. The *charge weighted* average strip position of a cluster is defined as

$$x = \frac{1}{Q} \sum_{i \in \mathcal{C}} q_i^{\text{signal}} x_i \tag{10.12}$$

where Q is the reconstructed cluster charge and x_i the position of the centre of strip i. This method uses the charge fractions in the cluster's strips as weights.

Highest Strip Pair Position

The charge is collected mostly by two strips which will be elaborated later in section 10.4.2. About 87 % of reconstructed clusters comprise one or two strips, as seen in section 10.2.1. This *highest pair* method defines the cluster position as the charge weighted position of the two adjacent strips with the highest signal

$$x = x_{\text{left}} + \eta p \tag{10.13}$$

where x_{left} is the position of the left strip's centre, p is the strip pitch, and the variable η, defined as [177]

$$\eta = \frac{q_{\text{right}}}{q_{\text{left}} + q_{\text{right}}}, \tag{10.14}$$

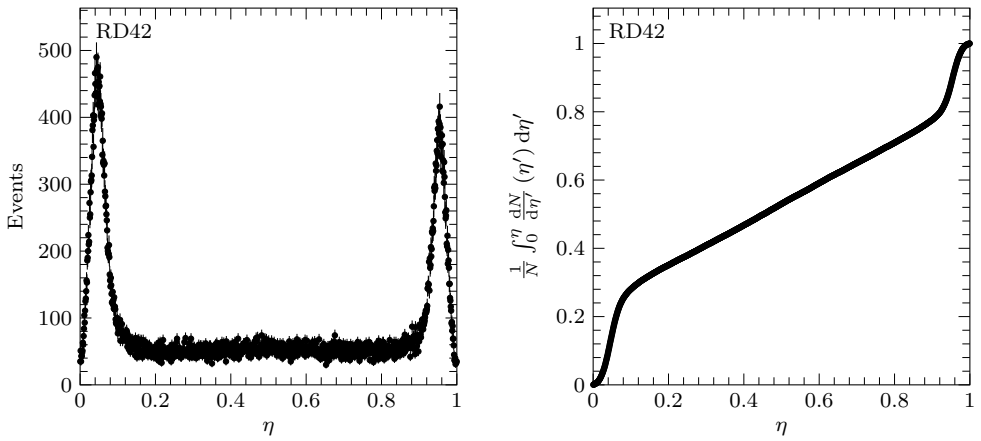

Figure 10.8: Spectrum of the variable η (left) and integrated spectrum as a function of the upper limit η (right).

describes the charge fraction of the right strip.

An equally illuminated detector has a hit position distribution $\frac{\mathrm{d}N}{\mathrm{d}x}$ which is constant. Thus, the method assumes the variable η uniformly distributed versus x. This is not the case, as can be seen in the left plot of figure 10.8 where the η spectrum in the diamond plane is shown. The non-uniform distribution has two peaks at 0.04 and 0.95. Thus, the charge is collected preferentially by the primary strip. Charge sharing occurs in the region between the peaks. In the range 0.2 to 0.8 a linear dependancy between collected charge and hit position is observed. Since a uniform spectrum is assumed, this attaches a systematic uncertainty to the method.

These non-linearities can be corrected [177]. The mapping

$$f : \eta \mapsto f(\eta) = \frac{1}{N} \int_0^{\eta} \frac{\mathrm{d}N}{\mathrm{d}\eta'} (\eta') \, \mathrm{d}\eta' \tag{10.15}$$

is defined and drawn in the right plot of figure 10.8. It maps the distribution of η onto the constant distribution [126]

$$\frac{\mathrm{d}N}{\mathrm{d}f}(f) = \frac{\mathrm{d}N}{\mathrm{d}\eta}(\eta) \times \left(\frac{\mathrm{d}f}{\mathrm{d}\eta} \right)^{-1} = N. \tag{10.16}$$

Therewith, the η *corrected* position is reconstructed with

$$x = x_{\mathrm{left}} + f(\eta) p. \tag{10.17}$$

10.3 Tracking

Particle trajectories were reconstructed from the individual hit positions in the telescope's detector planes. For this purpose precise knowledge of relative detector plane positions is crucial. Therefore, the planes were aligned in a first step using a subset of each run's data set. In a second step, reconstructed tracks for the further analysis were selected.

10.3.1 Telescope Alignment

The telescope's coordinate system (x, y, z) is defined in section 9.2.2. Its z axis points in the sense of the beam to which x and y axes are perpendicular in horizontal and vertical directions, respectively. Each telescope module has its own coordinate system $(x^{\text{det}}, y^{\text{det}}, z^{\text{det}})$ where x^{det} and y^{det} are the positions measured by the plane with vertical and horizontal strips, respectively. Thus, the x^{det} axis is perpendicular to the vertical strips and y^{det} is perpendicular to the horizontal strips. The z^{det} axis is pointing parallel to the beam direction. The origin is defined by the intersection of first strips of the two planes. To consider possible positioning errors during mounting of the telescope planes, linear and angular offsets are assigned to each plane. The plane with vertical strips is shifted by x^{off} and rotated by the angle ϕ_x^{off}. Analogue, the offsets y^{off} and ϕ_y^{off} are applied to the second plane. Since particle tracks are assumed to be perpendicular to the planes, misalignment along the beam axis has only very minor effects and is not further considered. Likewise, rotations of the detector planes around the x and y axes are neglected. The module's mounting point defines the offset z^{off}. Figure 10.9 shows the coordinate system of a module relative to the telescope's coordinate system. The transformation from a detector system into the telescope coordinate system is given by

$$\begin{pmatrix} x \\ y \\ z \end{pmatrix} = \frac{1}{\cos\left(\phi_x^{\text{off}} - \phi_y^{\text{off}}\right)} \begin{pmatrix} \cos\phi_y^{\text{off}} & \sin\phi_x^{\text{off}} & 0 \\ -\sin\phi_y^{\text{off}} & \cos\phi_x^{\text{off}} & 0 \\ 0 & 0 & 1 \end{pmatrix} \begin{pmatrix} x^{\text{det}} + x^{\text{off}}\cos\phi_x^{\text{off}} \\ y^{\text{det}} + y^{\text{off}}\cos\phi_y^{\text{off}} \\ z^{\text{det}} + z^{\text{off}} \end{pmatrix}. \quad (10.18)$$

Equation (10.18) describes an affine map $\vec{x} \mapsto A\vec{x} + \vec{b}$, where $\vec{b}$ specifies the translation of the origin and the matrix A defines the rotations of the x and y axes.

With the exception of z^{off}, the offsets are unknown previous to a run. These are derived in an iterative alignment algorithm. The algorithm finds the offsets which minimise the residuals.

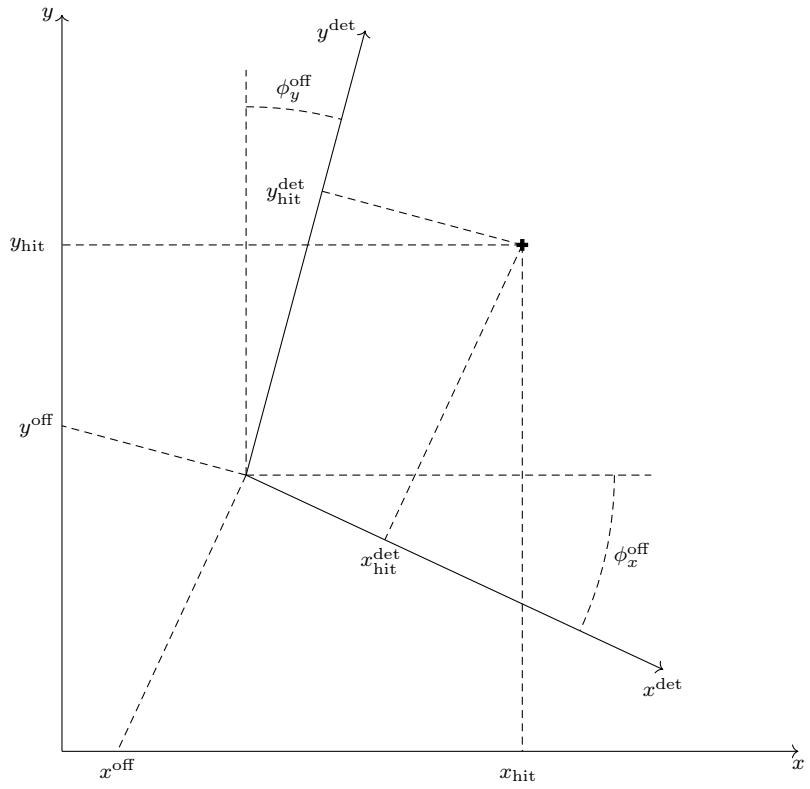

Figure 10.9: Coordinate system of a telescope module. The x and y axes are shifted by x^{off} and y^{off}, respectively. Both planes are rotated individually by the angular offsets ϕ_x^{off} and ϕ_y^{off}. The intersection of the first strips in vertical and horizontal planes defines the origin. A particle hit with its coordinates in the module and telescope coordinate system is illustrated.

Since no magnetic field was applied, particles can be assumed to follow straight trajectories. This allows a prediction in any plane using hit positions of two other modules. A subset of 100 000 events from each run was used to align the individual detector planes. This subset was excluded in the further analysis. To reduce combinatorial errors, only events with exactly one cluster in each plane were used.

The algorithm proceeds as follows. In a first step, basic offset corrections are applied in the x and y directions. Afterwards, planes are aligned one by one using the hit position predicted by two other planes. Hereby, an x plane is shifted along the x axis until the mean residual agrees with zero. Subsequently, the plane is rotated around the z axis to minimise the width of its residual distribution. These steps are iterated five times to obtain the offsets, x^{off} and ϕ_x^{off}. Figure 10.10 shows the residuals as a function of predicted y position before and after alignment. Before alignment, the rotation of the detector plane as well as a shift of about

230 µm is visible. Due to the rotation, the projection of the residual shows a wide distribution. After applying the offsets, the distribution is centred around zero and presents a narrow projection. Similarly, the offsets, y^{off} and ϕ_y^{off}, are determined. In figure 10.11 the corresponding residuals are shown as a function of predicted x position.

The workflow to align all planes is as follows. In a first step, the last plane is shifted and rotated to match the projection of the first plane's hit positions. This is valid since particles can be assumed to propagate perpendicular to the planes. The planes in between are aligned in the following steps using the first and last plane as reference. In the final step the DUT is aligned.

10.3.2 Track Selection

After aligning the setup, tracks to study the DUT were reconstructed and selected. To simplify combinatorics in the reconstruction, events with multiple clusters in a plane were rejected. After this basic requirement, the selection aimed for tracks crossing the region of interest of the DUT. Since trajectories were assumed perpendicular to the detector planes, the average x and y positions of the telescope planes provided a first approximation of the track position in the DUT plane. The left scatter plot in figure 10.12 shows the average hit position of the telescope planes. Since the readout was triggered by a scintillator which is smaller than the silicon planes, tracks are visible in the area covered by the scintillator only. The beam profile is observed flat in x direction and decreases for $y^{\text{pred}} > 8\,\text{mm}$. In the right plot of figure 10.12, the same average positions are drawn with additionally requiring a cluster in the DUT plane. The active area of the DUT is visible. For the beam test shown, the two diamond samples `PW205B` and `L107-9` were wire bonded to the same ASIC. The further analysis was restricted to a single diamond sample by defining a region of interest. The main part of the sample is uniformly illuminated by the beam and defines the region of interest. From this a fiducial region was chosen, restricting the average hit position to the region of interest.

A track was fitted as a straight line through the hit positions in the silicon planes. The fitted tracks were used to determine the average intrinsic resolution of the telescope planes. For this purpose, the intrinsic resolution used as input in the calculation of the goodness of fit χ^2 was varied until the measured χ^2 distribution matched the theoretical χ^2 distribution for two degrees of freedom best. For both fits the final χ^2 distribution is shown in figure 10.13. Observed deviations may be due to the assumption that all telescope planes have the same intrinsic resolution. The average intrinsic resolution of the telescope planes was measured to be 1.8 µm.

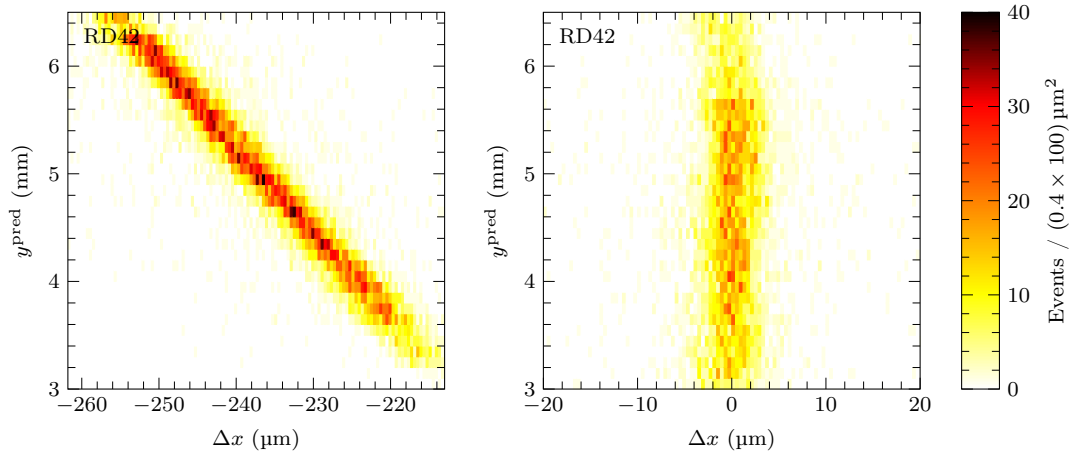

Figure 10.10: Residual of x position as a function of predicted y position before (left) and after (right) alignment in the third telescope module. The predicted position is calculated using the first and fourth telescope module.

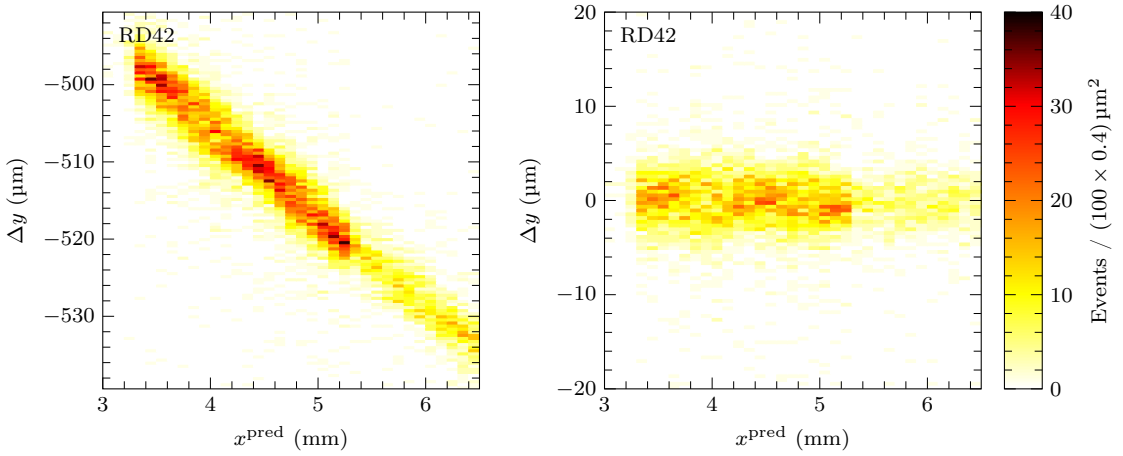

Figure 10.11: Residual of y position as a function of predicted x position before (left) and after (right) alignment in the third telescope module. The predicted position is calculated using the first and fourth telescope module.

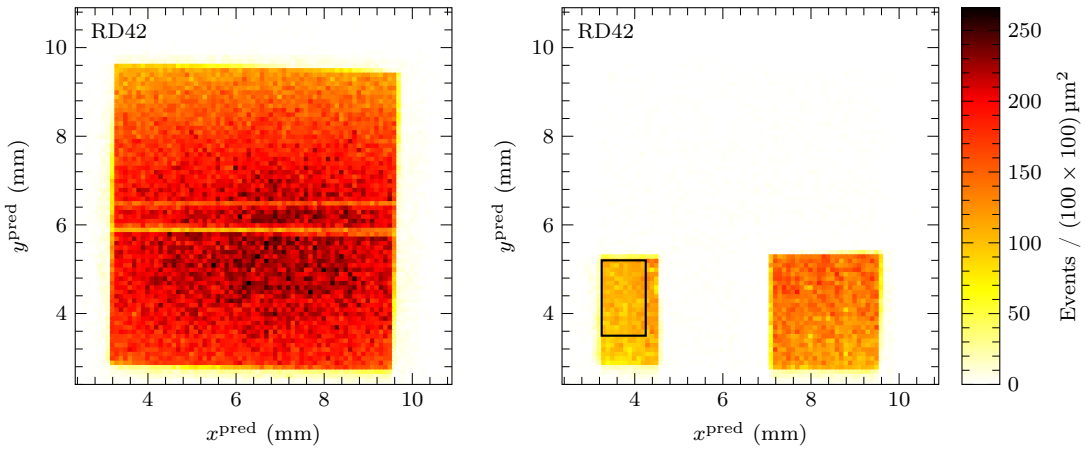

Figure 10.12: Average hit position of telescope planes. Events with exactly one hit in each telescope plane are required in the left plot. The right map shows the diamond plane shadow in the silicon telescope space by also requiring a hit in the diamond plane. The shadows of the two diamond samples `PW205B` and `L107-9` are visible. The fiducial area to select only the sample `PW205B` for the further analysis is indicated by a rectangle.

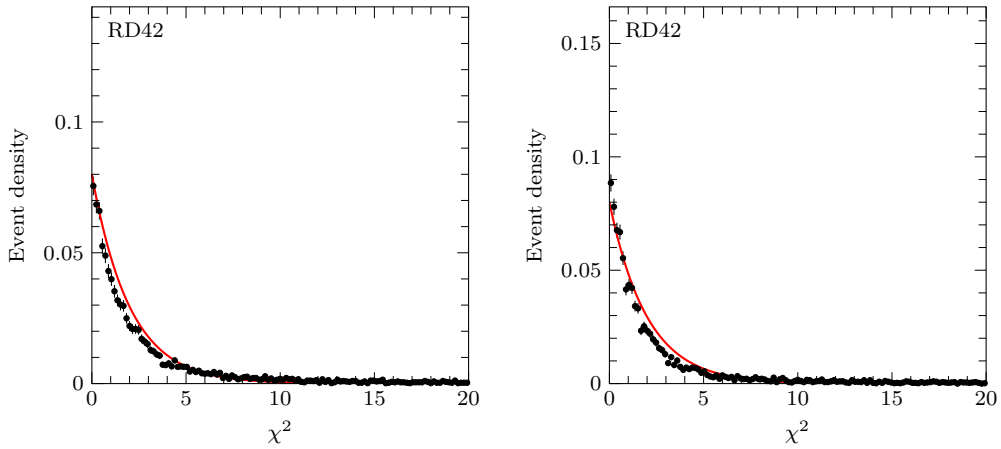

Figure 10.13: χ^2 distributions of tracks fitting x (left) and y (right) positions with a telescope resolution of 1.8 µm per plane. The theoretical χ^2 distribution for two degrees of freedom is indicated by a red line.

This resolution results in an uncertainty on the predicted hit position in the DUT of 1.3 µm.

Since a beam of high energy particles (120 GeV) was used, only a minor contribution of multiple scattering effects is expected. However, to the further reduce multiple scattering events and tracking errors, tracks are required to pass a threshold on the goodness of fit of $\chi^2 < 4$. This eliminates any large angle scatter events in the telescope. On average $(46.3 \pm 2.5)\,\%$ of the tracks were rejected by the χ^2 requirement. From the remaining set of tracks, only tracks which are located in the fiducial area, as indicated in figure 10.12, were used in the further analysis.

10.4 Transparent Analysis

Signals reconstructed with the clustering algorithm, as described in section 10.2, are biased by the choice of thresholds t_{hit} and t_{seed}. As seen, the choice of threshold influences the cluster's size and the hit detection efficiency. Subsequently, the cluster's reconstructed charge and position are affected. The so-called transparent analysis aims to avoid this by making use of the telescope predictions. Reconstructed telescope tracks were used to predict the position in the diamond plane and signals of surrounding strips were studied.

10.4.1 Transparent Clustering Algorithm

From reconstructed and selected tracks, as described in section 10.3, the track position in the DUT is interpolated. N strips whose centroids are closest to this *true* hit position are selected to form a *transparent cluster*. Like the clustering algorithm, clusters which feature masked or saturated strips in their proximity are dropped. Furthermore, all N strips are required to lie within the fiducial region.

10.4.2 Charge Reconstruction

Signals of up to ten adjacent strips were studied. For each selected track, clusters of 1 to 10 strips were formed. From these clusters, two different algorithms were elaborated to reconstruct the signal charge.

The first algorithm equals the one used previously. A cluster's signal is calculated from the sum of strips' signals, as in equation (10.9). Their pedestal subtracted signals are added and result in the cluster's signal. The pulse height distributions

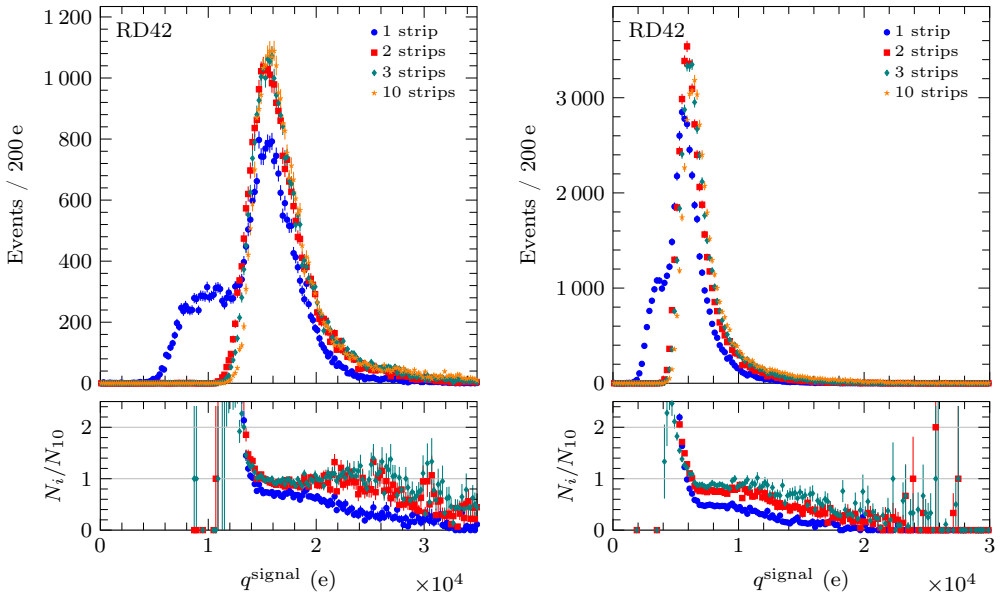

Figure 10.14: Signal charge collected in 1, 2, 3, and 10 strips around predicted track position before (left) and after (right) an 800 MeV proton fluence of $(3.05 \pm 0.19) \times 10^{15}\,\mathrm{p/cm^2}$.

of 1, 2, 3, and 10 strips are shown in figure 10.14 before and after irradiation. Considering only one strip, a bump in the lower tail is observed. In these events the charge is spread and collected by more than one strip. This results in a smaller upper tail with respect to the other distributions. The distributions of two and more strips are Landau distributed which implies full charge collection. However, a disagreement of the spectra, which decreases as more strips are added to the cluster, is observed in the lower tail. In the upper tail, the spectra start to disagree at around twice the MP value. The mean value of the 2-strip cluster distribution is about 5 % lower compared to the average charge collection of ten strips in the unirradiated state. After an 800 MeV proton fluence of $(3.05 \pm 0.19) \times 10^{15}\,\mathrm{p/cm^2}$, two strips collect on average about 10 % less charge than ten strips.

To investigate the effect of charge sharing, the charge collected by single strips was studied as a function of the predicted hit position. In the left plot of figure 10.15, the average strip pulse height is plotted as a function of the predicted hit position for the closest strip, its left and right adjacent strip. For the closest strip, a plateau was observed for tracks hitting the centre of the strip between $\pm 12\,\mu\mathrm{m}$. Towards the edge of the strip the distribution is falling. In these regions the charge is shared with the adjacent strip. In the region $-25\,\mu\mathrm{m}$ to $-12\,\mu\mathrm{m}$ of the left strip's distribution, a slope was observed which confirms the charge sharing model. A flat distribution, close to zero, was observed for $\Delta x > -12\,\mu\mathrm{m}$. A similar behaviour

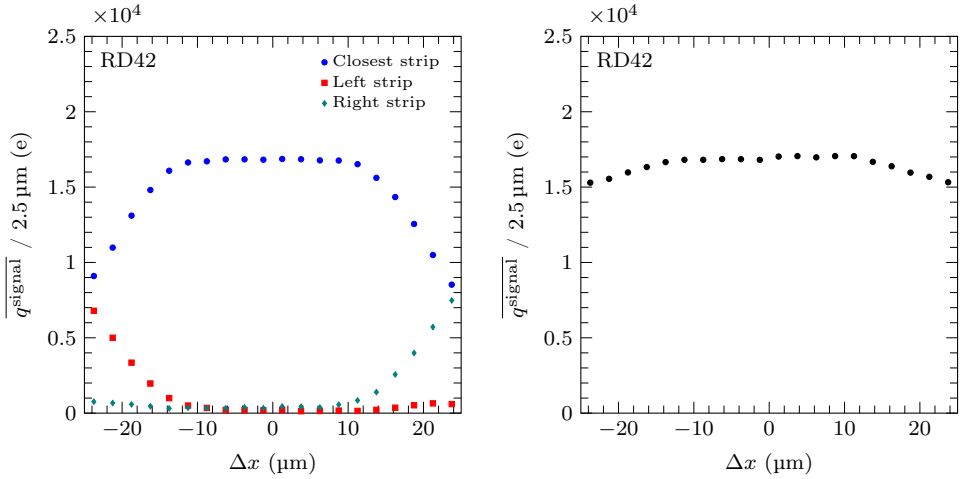

Figure 10.15: Average pulse height as a function of the predicted position relative to the closest strip centre before irradiation for the sCVD diamond sample `PW205B` with an applied electric bias field of $+2\,\mathrm{V/\mu m}$. The left plot shows the average strip pulse height of the strip closest to the predicted position, its left and right adjacent strip. In the right distribution, the mean pulse height sum of closest and second closest strip is plotted.

was observed for the right strip. In the region $\pm 12\,\mu\mathrm{m}$ the charge was observed to be collected solely by the closest strip. This region is directly under the strip metallisation ($\pm 12.5\,\mu\mathrm{m}$). Based on these observations, it was concluded to use the pulse heights of two strips to reconstruct the signal response. The right plot of figure 10.15 shows the pulse height sum of the closest two strips as a function of predicted position. The distribution is flat in the absence of charge sharing. A slope was observed at the edge of the strip indicating a loss of charge for tracks hitting this region.

Considering more than two strips does not significantly increase the average cluster signal. Adding more non-signal strips adds random noise charges. Therefore, the second method uses only the two highest adjacent strips out of N strips. This avoids adding noise to the cluster signal. Furthermore, this method has the advantage, that for an imprecise hit prediction still the full charge is reconstructed. Thereby, the method is less biased by the predicted hit position. Finally, δ rays can distort the position calculation by adding large amounts of charge displaced from the track [178, 179]. For these reasons, the charge of the two highest adjacent strips out of $N = 10$ was selected as reference cluster signal and the latter as cross check.

Chapter 11

Radiation Damage Analysis

The DUTs were measured in multiple beam tests, as described in chapter 9. CCDs were derived from the observed signal responses and corresponding systematic uncertainties were estimated. A simple radiation damage model was used to extract the damage constant from the data. Furthermore, the energy resolution and spatial resolution of the DUTs were studied.

11.1 Radiation Damage Constant Measurements

11.1.1 Procedure

After each proton irradiation a beam test was performed. Two individual algorithms were used to reconstruct an average pulse height. The procedure used to analyse the data is described below for the sCVD diamond sample `PW205B`.

The transparent method uses a particle track, reconstructed by the telescope, to predict a hit position in the DUT. Within ten strips around the predicted position, the algorithm selects the two adjacent strips with the highest signal. The signal response is defined as the pulse height of these two strips and is independent of any threshold. In figure 11.1 the pulse height distributions are shown for different 800 MeV proton irradiation doses. The integral of each spectrum is normalised to unity. At each fluence the pulse height spectrum can be described by a Landau distribution convoluted with a Gaussian due to electronic noise. A decrease in pulse height as function of fluence is observed for both polarities of bias voltage. The mean pulse height decreases while the spectrum becomes narrower with rising fluence. For each pulse height spectrum, the ratio of full width at half maximum

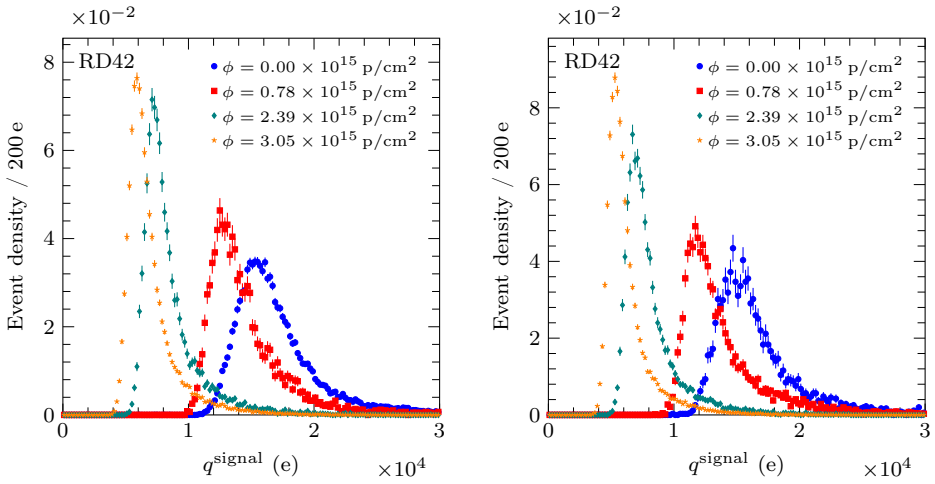

Figure 11.1: Evolution of signal pulse height distribution, reconstructed with the transparent algorithm. The distribution is shown after different accumulated 800 MeV proton fluences, observed with the sCVD diamond sample `PW205B` in the case of an electric bias field of +2 V/µm (left) and −2 V/µm (right). Each distribution's integral is normalised to unity.

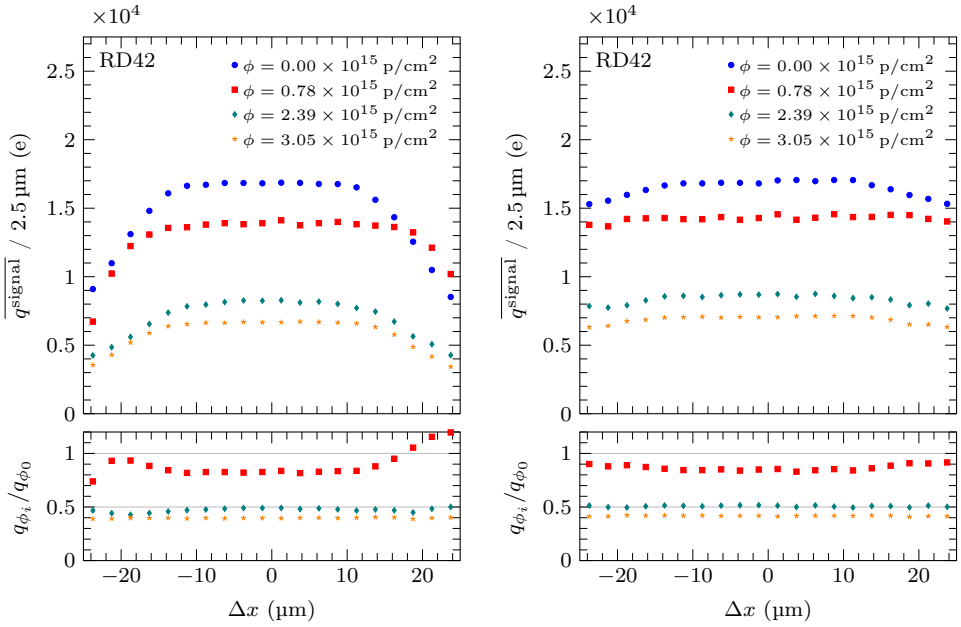

Figure 11.2: Average pulse height as a function of predicted hit position relative to the closest strip centre. In the left plot, the mean pulse height of the strip closest to the predicted position is used. The right plot shows the average pulse height sum of the closest and second closest strip. Both distributions are shown at different 800 MeV proton fluences observed with the sample `PW205B` at an electric bias field of +2 V/µm.

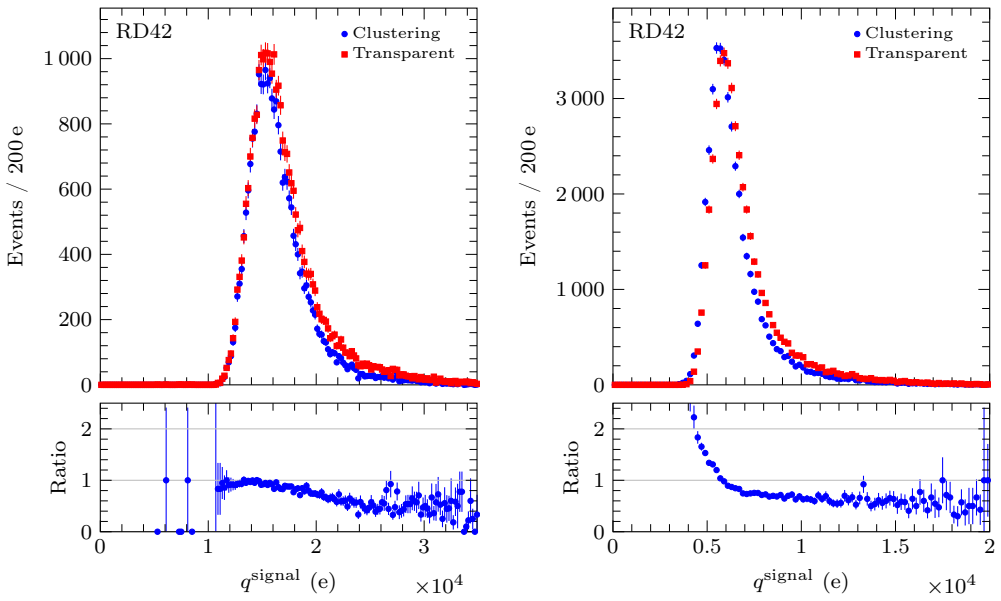

Figure 11.3: Signal charge distributions reconstructed with clustering and transparent algorithms before (left) and after (right) an 800 MeV proton fluence of $(3.05 \pm 0.19) \times 10^{15}\,\mathrm{p/cm^2}$ for the sCVD diamond sample PW205B.

(FWHM) to the MP value, f, was derived. On average a ratio of 0.309 ± 0.005 was observed.

Figure 11.2 shows the mean pulse height as a function of predicted hit position relative to the closest strip centre, Δx, after different 800 MeV proton fluences. The pulse height of the strip closest to the track was used for the left plot, while the sum of the two closest strips was used for the right plot. At all fluence levels, the charge is shared among two strips for $\Delta x < -12\,\mu\mathrm{m}$ and $\Delta x > 12\,\mu\mathrm{m}$. In this region, a slope of the mean pulse height of two strips was observed, indicating an inefficiency in charge collection. Since the radiation damage is constant along the strip, observable by the flat ratio distributions, the observed charge loss may be an effect of the strip geometry.

In the clustering analysis, clusters are searched for independent of the telescope. Strips belonging to a cluster are identified by thresholds on their individual pulse heights. For the chosen thresholds, a cluster reconstruction efficiency of $(99.15 \pm 0.30)\,\%$ was observed. The pulse height of exclusive clusters with a size of one or two strips is chosen as figure of merit for the signal response. Considering only such clusters, the efficiency decreases to $(87 \pm 7)\,\%$.

In figure 11.3 the signal distribution evaluated by the transparent analysis is compared to the signal reconstructed with the clustering algorithm. The signal

ϕ ($\mathrm{p/cm^2}$)	E_{bias} (V/µm)	f_{tr}	$\overline{r}_{\mathrm{tr}}$ (µm)	$\overline{r}_{\mathrm{cl}}$ (µm)	$\overline{r}'_{\mathrm{cl}}$ (µm)
0×10^{15}	+2	0.31 ± 0.04	474 ± 14	460 ± 15	464 ± 15
	−2	0.25 ± 0.04	458 ± 14	444 ± 15	448 ± 14
$0.78 \pm 0.07 \times 10^{15}$	+2	0.29 ± 0.04	404 ± 13	387 ± 14	391 ± 13
	−2	0.27 ± 0.05	383 ± 11	357 ± 12	361 ± 11
$2.39 \pm 0.18 \times 10^{15}$	+2	0.30 ± 0.04	235 ± 12	222 ± 13	225 ± 12
	−2	0.33 ± 0.05	225 ± 8	207 ± 9	211 ± 9
$3.05 \pm 0.19 \times 10^{15}$	+2	0.36 ± 0.06	193 ± 16	181 ± 15	185 ± 14
	−2	0.34 ± 0.05	174 ± 10	162 ± 10	166 ± 9

Table 11.1: An overview of the beam test results at different 800 MeV proton fluence levels for the sCVD diamond sample `PW205B`. The ratio of the FWHM to the MP value of the pulse height distribution, f_{tr}, is listed for the results of the transparent method. Clustered CCDs after correcting for missing charge and missing events, $\overline{r}'_{\mathrm{cl}}$, are compared to uncorrected values, $\overline{r}_{\mathrm{cl}}$, and CCDs obtained with the transparent analysis, $\overline{r}_{\mathrm{tr}}$. The errors include statistical and systematic uncertainties.

response reconstructed by the clustering algorithm was observed to be smaller compared to the transparent analysis before and after irradiation. On average the mean pulse height is $(95.3 \pm 1.7)\,\%$ of the value reconstructed with the transparent method. Both methods use signals collected with two strips. While the transparent method measures the signal response of two strips for every selected track, the clustering algorithm obtains signals only if a one or two strip cluster is found. However, only strips with a charge above the hit threshold contribute to the cluster charge. Therefore, the pulse height of a cluster with a size of $\leq$2 strips misses the charge collected by the second strip if it is below the hit threshold. The missing charge was observed to be on average $(130 \pm 50)\,\mathrm{e}$. Since the signal response reconstructed with the clustering algorithm was observed smaller than the result of the transparent method after all probed fluences, the signal response obtained by the clustering algorithm was increased by 130 e to correct for the missing charge.

The observed signal response measured during each beam test was converted into CCD using equation (8.27). Table 11.1 summarises the beam test results. The signal responses reconstructed by the clustering and transparent algorithms were found in good agreement at all fluences. The outcome of the transparent analysis denotes the reference result which is not biased by thresholds. The clustering algorithm is independent of the telescope and can be applied in a genuine detector application. However, since the clustering method is corrected using the results of

the transparent algorithm, the results are highly correlated.

For the pCVD diamond samples, source tests were performed. The signal response to a ^{90}Sr source was used to obtain their initial CCDs. These measurements were performed at OSU using pad electrodes [171, 180, 181]. Besides the geometry of the electrodes, the setup to apply the bias voltage and read out the signals was different from the setup used during the beam tests. One electrode was connected to ground and a positive potential was applied on the opposite electrode. The readout circuit was always connected to the same electrode as the positive potential. A relatively weak source (37 MBq), with a resulting particle flux through the detector, triggering the scintillator, of the order of 100 Hz, was used. A single measurement cycle includes pumping the diamond for 4 h and taking data for additional 8 h with the same source. During a measurement cycle each diamond is probed on one side for different bias potentials from 0 V to 1 000 V. After each cycle the diamond was flipped, to obtain an electric field of opposite direction in the diamond, and the procedure was repeated. Like in the beam tests, the signal response at a bias potential of 1 000 V was used for the further analyses.

The method used has an average offset of (1.9 ± 0.1) µm. At zero potential, a CCD offset of up to 15 µm was observed with the samples `T15-33` and `T15-43` before irradiation. This deviation from the average offset may be due to a surface effect. The initial surface mechanical planarisation of the diamond may cause additional surface states which are later removed due to irradiation. Since a power supply, designed to operate at high voltage, was used, the observed variation in CCD at zero potential may also be due to an offset in the applied voltage. To avoid a bias from a surface effect, the observed difference in CCD offset was subtracted from the CCD measured before irradiation.

11.1.2 Systematic Uncertainties

Besides the statistical uncertainties, the reconstructed signals and CCDs are attached with systematic uncertainties arising from systematic effects occurring during the measurements and analysis. These effects are studied and quantified below.

Calibration

Calibration constants to convert the ADC output into a signal charge were derived as described in section 9.2.4. In two of the calibrations an unirradiated reference

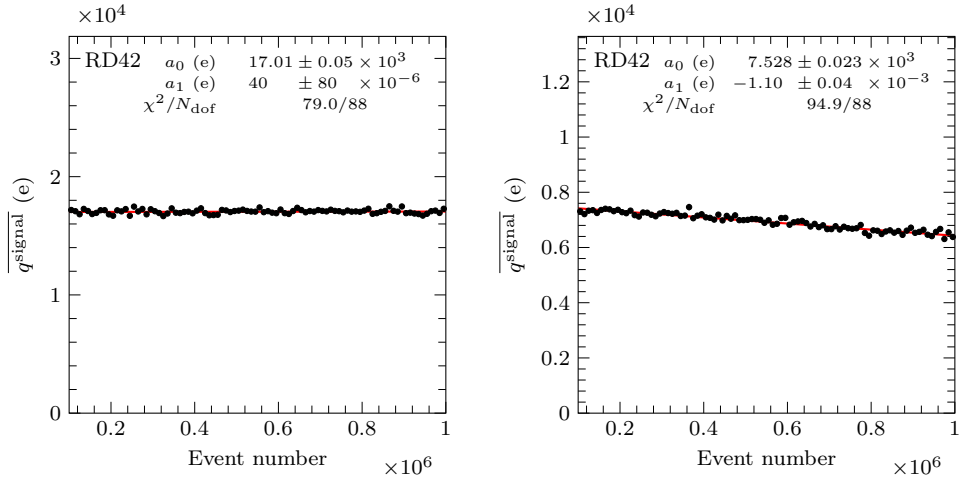

Figure 11.4: Average pulse height of 10 000 events as a function of event number before (left) and after (right) a fluence of $(3.05 \pm 0.19) \times 10^{15}\,\mathrm{p/cm^2}$. A linear fit of the data points is indicated in red.

diamond was analysed and the signals were calibrated to obtain full charge collection. Hence, these calibration constants rely on the analysis method. Another measurement of these calibration constants [149] deviates by about 2 %. The found difference was assigned as uncertainty on the measured CCDs to reflect systematic effects in the signal calibration.

Signal Stability

A pulse height dependence on time was observed after irradiation of the diamond sample `PW205B` [149]. The observed effect appeared to increase with fluence. Since the problem was later discovered to be a surface effect, it was concluded to be a systematic error on the signal response [149].

In the present analysis this effect causes a possible underestimation of the measured pulse height and thus CCD. Therefore, the pulse height as a function of event number is studied for each beam test. Since no time stamps were recorded, the event number is used as indicator of time. In figure 11.4 the mean pulse height of 10 000 events is plotted as a function of event number. In the unirradiated state a flat distribution is observed. After an 800 MeV proton fluence of $(3.05 \pm 0.19) \times 10^{15}\,\mathrm{p/cm^2}$ a small decreasing trend is visible. The trend is evaluated with a linear fit for each beam test run. In the case of the two runs shown in figure 11.4 a slope of $(4 \pm 8) \times 10^{-5}\,\mathrm{e}$ is found in the unirradiated state of the sample and a slope of $(-1.10 \pm 0.04) \times 10^{-3}\,\mathrm{e}$ is observed after a fluence of

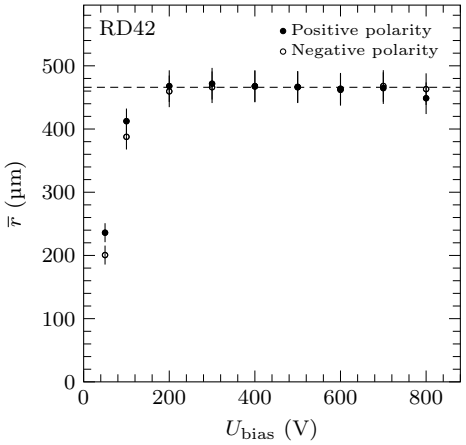

Figure 11.5: Charge collection distance as a function of bias voltage. The signal response to a ^{90}Sr source is measured for different bias voltages using pad electrodes [182]. Full charge collection is observed for a bias voltage above 200 V. The sample's thickness is indicated by the dashed line.

$(3.05 \pm 0.19) \times 10^{15}\,\mathrm{p/cm^2}$. Studying the pulse height behaviour in all beam test runs confirms the trend with fluence. From the resulting slope, the difference in pulse height between beginning and end of a beam test run is evaluated. Half of the found difference is assigned as systematic uncertainty on the reconstructed mean pulse height to cover a possible underestimation. This effect was later cured by proper cleaning of the sample before metallisation and thus concluded not to be a property of the diamond [149].

Electric Field

In each beam test campaign the DUTs were tested in two runs with different polarity of the electric bias field. Previous to a beam test the device's signal response to a ^{90}Sr source was probed at OSU using pad electrodes. The measured CCD is plotted as a function of applied bias voltage in figure 11.5 for the sample `PW205B` in its unirradiated state. At a bias voltage around 200 V, corresponding to an electric field of 0.43 V/µm, the CCD converges and full charge collection is achieved. The measurement indicates the signal response independent of the applied polarity in the region of full charge collection. However, in beam tests a difference in signal response was observed, depending on the applied polarity of the electric field. For the sample `PW205B`, data points obtained with negative bias voltage represent slightly lower CCDs at all fluences compared to corresponding points with positive bias potential. However, with the 70 MeV proton irradiated samples, larger CCD values were observed with negative bias polarity than with

positive bias potential. This discrepancy between bias polarities may originate from the different mobilities of electrons and holes or from a variation in gain in the readout electronics between collection of positive and negative charge carriers. On average a difference of $(10 \pm 7)\,\mu m$ in CCD was observed for the 800 MeV proton irradiated samples with the transparent method. Using the clustering algorithm results in a difference of $(13 \pm 9)\,\mu m$. Half of the observed difference was assigned as systematic uncertainty on the reconstructed CCD.

Cluster Thresholds

As discussed earlier, the choice of cluster thresholds influences the signal response of the clustering analysis and thus causes a systematic error. A correction for this effect was applied. To account for the missing charge of strips below threshold, the pulse height was increased by 130 e. The corresponding uncertainty of 50 e was assigned as systematic uncertainty on the corrected signal response of the clustering algorithm and a systematic uncertainty of 130 e was assigned to the uncorrected values. This correction implies a systematic uncertainty of 1.4 %.

Source Measurements

As described above, an offset correction was applied to the CCD derived from the signal response to a ^{90}Sr source. In a conservative approach, a 100 % uncertainty was assigned to this correction. The uncertainty was propagated to the measured CCDs, resulting in a systematic uncertainty of 4 %. The effect on the final radiation damage constant was evaluated by comparing the nominal result to the value obtained from the uncorrected CCDs.

Between the measurements with different polarities of the electric bias field an average difference of $(8 \pm 4)\,\mu m$ was observed. Similar to the beam test results, a systematic uncertainty 4 µm was assigned to account the observed effect. To reflect uncertainties in the calibration, a systematic uncertainty of 5 % to 10 %, depending on the sample, was assigned.

Summary

The systematic uncertainties are summarised in table 11.2. Individual systematic uncertainties were added in quadrature. In the case of the transparent algorithm, this results on average in a systematic uncertainty of 6.3 %. For the clustering

Source of uncertainty	Uncertainty (%)		
	Transparent	Clustering	Source
Calibration	2	2	5 to 10
Signal stability	1.5	1.4	–
Polarity	5.2	7	1.9
Cluster thresholds	–	1.4	–
Offset correction	–	–	4

Table 11.2: Overview of systematic uncertainties on the signal response. The individual uncertainties of the two algorithms used to reconstruct the beam test signal response and the uncertainties on the source measurements are listed.

method a systematic uncertainty of 7.4 % was assigned on average. On average, the systematic uncertainty on the source measurement is 6.5 %.

11.1.3 Proton Radiation Damage Model Fit

An sCVD diamond sample and three pCVD diamond samples were irradiated with 800 MeV protons. Two pCVD diamond samples were irradiated with 70 MeV protons. In both cases, the radiation tolerance was probed by fitting the radiation damage model to the obtained data. Two methods were used to derive the radiation damage constant. The first method uses the inverse of the MFP to linearise the radiation damage model and fits the model to the data of each sample separately [111, 149]. In the second approach, fluence offsets were applied and a single fit to the MFP data was performed [183, 184].

800 MeV Proton Radiation Damage

The CCD of the sCVD diamond sample `PW205B` after several accumulated 800 MeV proton fluences is listed in table 11.1. For the three pCVD diamond samples `L107-10`, `L107-11`, and `L114-13`, the CCD measured in beam tests after different irradiations with 800 MeV protons is shown in table 11.3. The CCD reconstructed with the clustering algorithm was observed smaller than the value obtained with the transparent method at all stages, confirming the observation with the sCVD diamond sample. After correcting for the missing charge of the second strip, the two methods are in agreement. The initial CCDs were obtained from the signal response to a ^{90}Sr source [180]. To fit the radiation damage model to the data, the CCDs measured were converted into MFPs using equation (8.26) and equation (8.27).

ϕ (p/cm^2)	E_{bias} (V/µm)	f_{tr}	$\overline{r}_{\text{tr}}$ (µm)	$\overline{r}_{\text{cl}}$ (µm)	$\overline{r}'_{\text{cl}}$ (µm)
$3.50 \pm 0.35 \times 10^{15}$	+2	0.96 ± 0.06	118 ± 6	110 ± 8	114 ± 7
	−2	0.98 ± 0.05	123 ± 6	116 ± 8	120 ± 7
$5.5 \pm 0.6 \times 10^{15}$	+2	0.85 ± 0.05	90 ± 5	84 ± 7	88 ± 7
	−2	0.86 ± 0.05	100 ± 5	96 ± 7	99 ± 7
$10.3 \pm 0.7 \times 10^{15}$	+2	0.60 ± 0.12	51 ± 5	47 ± 8	51 ± 7
	−2	0.64 ± 0.08	52 ± 5	49 ± 8	53 ± 7
$12.6 \pm 1.3 \times 10^{15}$	+2	0.58 ± 0.06	52 ± 5	48 ± 7	52 ± 6
	−2	0.58 ± 0.08	54 ± 5	50 ± 7	54 ± 6

Table 11.3: Overview of the beam test results of the pCVD diamond samples. The relative width of the pulse height distribution reconstructed with the transparent algorithm, f_{tr}, is listed. CCDs obtained with the transparent method, $\overline{r}_{\text{tr}}$, are compared to uncorrected clustering CCDs, $\overline{r}_{\text{cl}}$, and the corrected values, $\overline{r}'_{\text{cl}}$. The sample `L107-11` was probed at the lowest fluence. The two intermediate fluences correspond to the sample `L107-10`, while the data after the highest fluence was measured with the sample `L114-13`. The quoted uncertainties include statistical and systematic uncertainties, added in quadrature.

In the unirradiated state of the sCVD diamond sample, an MFP of $10.0\,^{+40}_{-6.5} \times 10^3$ µm was assumed.

In figure 11.6, the inverse of the MFP is plotted as a function of 800 MeV proton fluence for the sCVD diamond sample and the three pCVD diamond samples. As described in section 8.5, the increase of the inverse MFP with fluence can be described by the linear relation of equation (8.31). The initial MFP of individual samples may be different due to their characteristics, such as their initial number of trapping centres. Therefore, the radiation damage model was fitted individually to the data points of each sample. Similar slopes were observed, indicating an equal damage mechanism among the samples. The intercepts of the pCVD diamond samples are shifted with respect to the sCVD diamond sample due to the presence of traps in the unirradiated sample and hence their lower initial MFP. In figure 11.7, the resulting radiation damage constants are shown. By fitting a constant to these individual results, a radiation damage constant of

$$k = 1.206\,^{+0.029}_{-0.029}\,(\text{stat})\,^{+0.04}_{-0.05}\,(\text{syst}) \times 10^{-18}\,\text{cm}^2/(\text{p}\,\mu\text{m}). \tag{11.1}$$

was observed which is shown by a dashed line. The corresponding goodness of fit of $\chi^2/N_{\text{dof}} = 3.33/3$ shows consistency among the samples tested. The statistical uncertainty was estimated by repeating the fit procedure using only the statistical

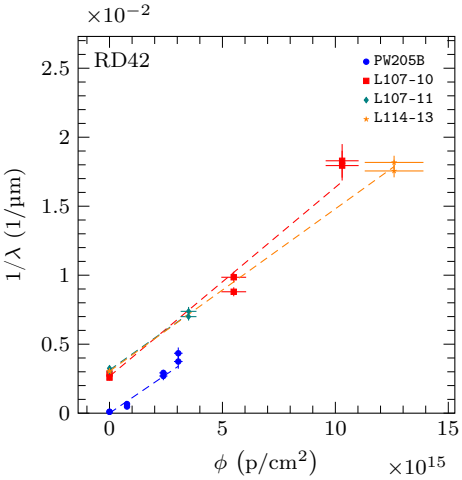

Figure 11.6: Inverse MFP as a function of 800 MeV proton fluence. The data points indicate the MFP obtained from the measured CCD with positive and negative bias potential, respectively. The damage model is fitted separately for each sample.

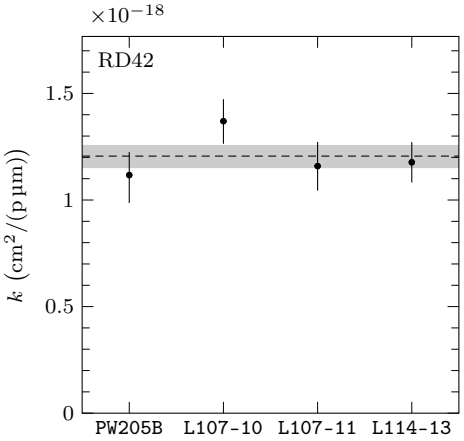

Figure 11.7: Radiation damage constants of 800 MeV protons measured with the sCVD diamond sample `PW205B` and the three pCVD diamond samples `L107-10`, `L107-11`, and `L114-13`. The dashed line represents a fit of a constant to the individual data points resulting in a goodness of fit of $\chi^2/N_{\text{dof}} = 3.33/3$.

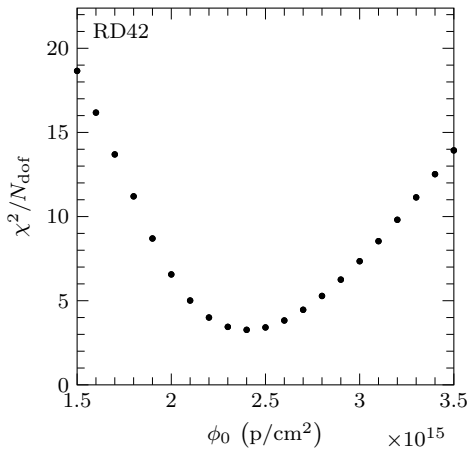

Figure 11.8: Goodness of fit of the radiation damage model fit as a function of fluence offset. The fluence offset of the pCVD diamond sample `L114-13` is varied from $1.5 \times 10^{15}\,\mathrm{p/cm^2}$ to $3.5 \times 10^{15}\,\mathrm{p/cm^2}$.

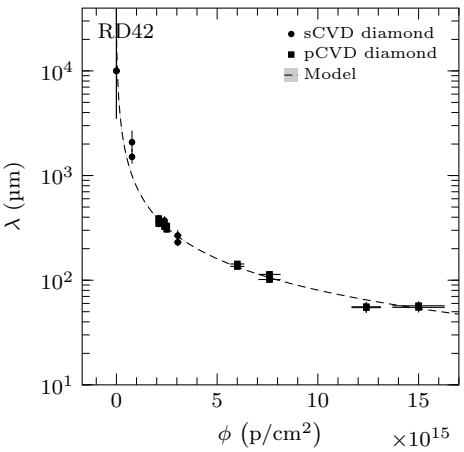

Figure 11.9: MFP as a function of 800 MeV proton fluence. A fluence offset of $2.2 \times 10^{15}\,\mathrm{p/cm^2}$, $2.5 \times 10^{15}\,\mathrm{p/cm^2}$, and $2.4 \times 10^{15}\,\mathrm{p/cm^2}$ is applied to the pCVD diamond samples `L107-10`, `L107-11`, and `L114-13`, respectively. The radiation damage model is fitted to the data points resulting in a goodness of fit of $\chi^2/N_{\mathrm{dof}} = 21.4/20$. A grey uncertainty band indicates the variation of the fit parameters by one standard deviation.

uncertainty on the CCD. To estimate how much the observed difference between bias polarities influences the damage constant, the procedure was repeated twice, including only MFP data points obtained with one bias polarity. The observed deviation from the nominal damage constant was added in quadrature to the systematic uncertainty. In figure 11.7, these uncertainties are depicted by a grey band.

Due to the consistency of the individual results, the samples were combined in a single fit of the radiation damage model. For this purpose, fluence offsets were applied to the pCVD diamond samples to account for their initial MFP. In an iterative algorithm, the offset of each sample was varied from $1.5 \times 10^{15}\,\mathrm{p/cm^2}$ to $3.5 \times 10^{15}\,\mathrm{p/cm^2}$ and the value yielding the minimum goodness of fit when fitting the radiation damage model was chosen. For the pCVD diamond sample `L114-13`, the resulting goodness of fit as a function of fluence offset is depicted in figure 11.8. A minimum, $\chi^2_{\mathrm{min}}/N_{\mathrm{dof}}$, was observed at $2.4\,^{+0.4}_{-0.3} \times 10^{15}\,\mathrm{p/cm^2}$. The up and down variation resulting in a goodness of fit of $\chi^2_{\mathrm{min}}/N_{\mathrm{dof}} + 1$ were averaged between the samples and propagated to the systematic uncertainty of the radiation

damage constant measurement. The combined curve is shown in figure 11.9 where the fit is indicated by a dashed line. A variation of the fit parameters by one standard deviation is reflected in the grey uncertainty band. The fitted model agrees with the data points within their uncertainties and results in a goodness of fit of $\chi^2/N_{\mathrm{dof}} = 21.4/20$. A radiation damage constant of

$$k = 1.240\,^{+0.014}_{-0.014}\,(\mathrm{stat})\,^{+0.04}_{-0.04}\,(\mathrm{syst}) \times 10^{-18}\,\mathrm{cm}^2/(\mathrm{p}\,\mu\mathrm{m}) \tag{11.2}$$

which was observed in agreement with the result in equation (11.1) and a previous measurement [149]. However, the latter method results in a smaller uncertainty and thus is defined as reference.

As a cross check, the damage constant was derived from the signal response reconstructed with the clustering algorithm. Using the values corrected for the missing charge of the second strip results in a radiation damage constant of

$$k = 1.242\,^{+0.014}_{-0.014}\,(\mathrm{stat})\,^{+0.032}_{-0.027}\,(\mathrm{syst}) \times 10^{-18}\,\mathrm{cm}^2/(\mathrm{p}\,\mu\mathrm{m}) \tag{11.3}$$

with a goodness of fit of $\chi^2/N_{\mathrm{dof}} = 16.5/20$. The result was found to be in agreement with the radiation damage constant of the transparent method.

70 MeV Proton Radiation Damage

Since the number of defects induced depends on the incident particle's energy, it is important to study the radiation damage for different energies. Thus, two pCVD diamond samples were irradiated with 70 MeV protons, as described in section 9.3.1. Three beam test campaigns were performed. These included a beam test after each irradiation as well as retests with constant fluence. The measurements of the signal response to a ^{90}Sr source were used to obtain the initial CCDs of the two samples. As described above, an offset correction was applied on the observed values.

The signal response to the particle beam was reconstructed with the clustering and transparent methods. In figure 11.10, the pulse height distribution obtained with the latter method is shown after different fluences. The signal response of the sample `T15-33` was measured after a fluence of $(8.8 \pm 0.9) \times 10^{15}\,\mathrm{p/cm}^2$, while the sample `T15-43` was probed after fluences of $(0.96 \pm 0.10) \times 10^{15}\,\mathrm{p/cm}^2$ and $(1.96 \pm 0.14) \times 10^{15}\,\mathrm{p/cm}^2$. After each fluence, the pulse height spectrum was described by a Landau distribution convoluted with a Gaussian. The relative width of the spectrum was observed to decrease with fluence, as studied below in section 11.2.

An overview of the observed CCDs is shown in table 11.4. The clustering algorithm

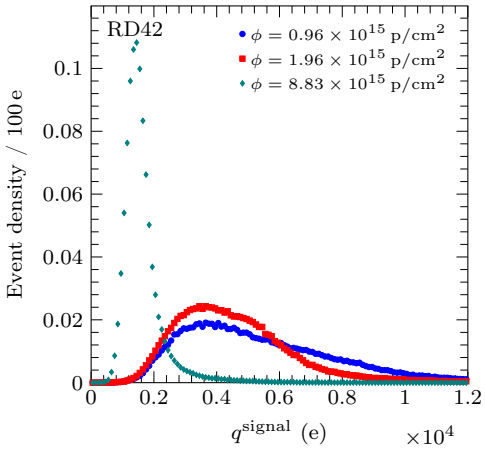

Figure 11.10: Pulse height distribution after different accumulated 70 MeV proton fluences. The electric bias field of the runs shown was set to +2 V/µm. The pulse height at the highest fluence was measured with the sample `T15-33`. The other two distributions were obtained with the sample `T15-43`. Each distribution's integral is scaled to unity.

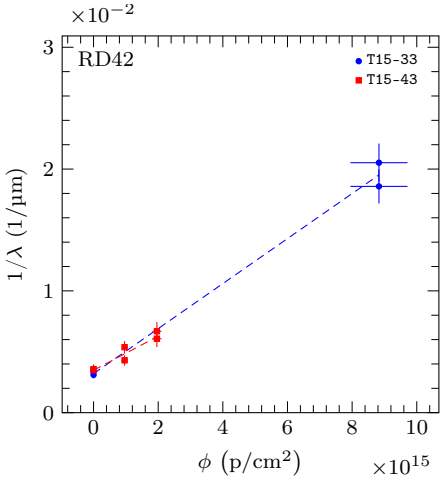

Figure 11.11: Inverse MFP of pCVD diamond as a function of 70 MeV proton fluence. Separate data points indicate the MFP obtained with positive and negative bias potential. The damage law is fitted separately to the data points of each sample.

ϕ (p/cm^2)	E_{bias} (V/µm)	f_{tr}	$\overline{r}_{\text{tr}}$ (µm)	$\overline{r}_{\text{cl}}$ (µm)	$\overline{r}'_{\text{cl}}$ (µm)
$0.96 \pm 0.10 \times 10^{15}$	+2	1.34 ± 0.05	152 ± 9	143 ± 10	147 ± 9
	−2	1.14 ± 0.04	180 ± 11	168 ± 12	172 ± 12
$1.96 \pm 0.14 \times 10^{15}$	+2	1.05 ± 0.06	128 ± 10	119 ± 11	123 ± 10
	−2	1.15 ± 0.06	138 ± 11	133 ± 12	137 ± 11
$8.8 \pm 0.9 \times 10^{15}$	+2	0.54 ± 0.07	46 ± 8	43 ± 9	47 ± 8
	−2	0.56 ± 0.05	51 ± 8	48 ± 9	52 ± 8

Table 11.4: Overview of the beam test results of pCVD diamond samples after different fluences of 70 MeV protons. The results at the two lower fluences correspond to the sample `T15-43`, while the highest fluence results correspond to the sample `T15-33`. If multiple measurements were taken at the same fluence and bias polarity, the average weighted by the number of recorded events is quoted. The uncertainty on the CCD is calculated by propagating the statistical and systematic uncertainties. For the transparent method, the relative width of the pulse height distribution, f_{tr}, is listed.

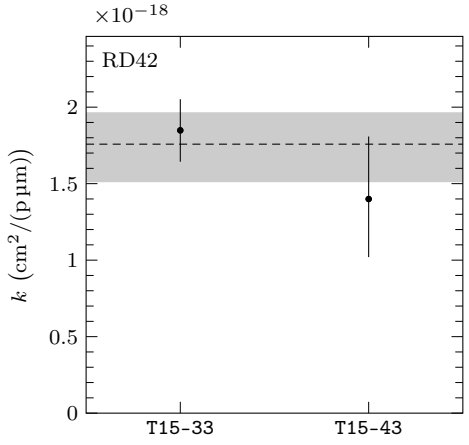

Figure 11.12: Radiation damage constants of 70 MeV protons measured with the pCVD diamond samples `T15-33` and `T15-43`. A constant is fitted to the individual data points, resulting in a goodness of fit of $\chi^2/N_{\mathrm{dof}} = 0.963/1$.

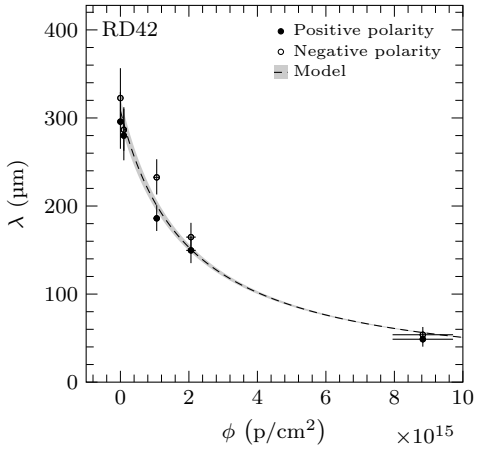

Figure 11.13: Mean free path of pCVD diamond as a function of 70 MeV proton fluence. Separate data points indicate the MFP obtained with positive and negative bias potential. The damage law is fitted to the data points, resulting in a goodness of fit of $\chi^2/N_{\mathrm{dof}} = 5.26/8$. The grey band represents the variation of the fit parameters by a standard deviation.

results in smaller CCDs than the transparent method for both samples. This is in agreement to what was observed in the case of the sCVD diamond sample. The systematic uncertainty of the CCD measurement was estimated as described in section 11.1.2 and added in quadrature to the statistical uncertainty.

The measured CCDs were converted into MFPs. For both samples, the inverse MFP as a function of 70 MeV proton fluence is shown in figure 11.11. The radiation damage model is fitted individually to the data points of both samples, resulting in the radiation damage constants depicted in figure 11.12. A combined radiation damage constant of

$$k = 1.76\,^{+0.10}_{-0.10}\,(\mathrm{stat})\,^{+0.18}_{-0.23}\,(\mathrm{syst}) \times 10^{-18}\,\mathrm{cm}^2/(\mathrm{p\,\mu m}) \tag{11.4}$$

was derived from these individual results with a goodness of fit of $\chi^2/N_{\mathrm{dof}} = 0.963/1$.

In the second approach, the model was fitted to the data points of both samples. The fluence offset due to the initial trapping centres may be different for the two pCVD diamond samples. Therefore, a fluence offset between the samples was

derived. The offset of the sample `T15-43` was varied from $-0.5 \times 10^{15}\,\mathrm{p/cm^2}$ to $0.5 \times 10^{15}\,\mathrm{p/cm^2}$. A fluence offset of $0.1\,^{+0.2}_{-0.1} \times 10^{15}\,\mathrm{p/cm^2}$ was observed to yield a minimum goodness of fit when fitting the radiation damage model. The up and down variation in fluence offset resulting in a goodness of fit of $\chi^2_{\mathrm{min}}/N_{\mathrm{dof}} + 1$ were assigned as the uncertainty on the fluence offset and propagated to the systematic uncertainty of the radiation damage constant measurement.

In figure 11.13, the MFP is plotted as a function of 70 MeV proton fluence, with applied fluence offset. The data points were fitted with the radiation damage law and a radiation damage constant of

$$k = 1.64\,^{+0.09}_{-0.09}\,(\mathrm{stat})\,^{+0.24}_{-0.25}\,(\mathrm{syst}) \times 10^{-18}\,\mathrm{cm^2/(p\,\mu m)} \tag{11.5}$$

was derived. The fit was repeated separately for both polarities of the electric bias field. In addition, the fit was repeated using the results of the source measurement, before applying the zero voltage correction. The resulting differences were added in quadrature to the systematic uncertainty.

As cross check, the results of the clustering analysis were fitted, resulting in a radiation damage constant of

$$k = 1.71\,^{+0.09}_{-0.09}\,(\mathrm{stat})\,^{+0.26}_{-0.28}\,(\mathrm{syst}) \times 10^{-18}\,\mathrm{cm^2/(p\,\mu m)} \tag{11.6}$$

with a goodness of fit of $\chi^2/N_{\mathrm{dof}} = 4.05/8$. Like the results of 800 MeV protons, the results of the three methods were found in agreement within their uncertainties.

24 GeV Proton Radiation Damage

The radiation damage of 24 GeV protons in diamond has been characterised extensively [184–186]. Therefore, it may be used as a reference when comparing radiation damage of different particle species and energies in diamond. To minimise effects from different analysis methods, the measured CCDs after different 24 GeV proton fluences [186] were used to re-evaluate the radiation damage constant of 24 GeV protons.

Two sCVD (`071415` and `sCVD2`) and two pCVD diamond samples (`CD69` and `CD113`) have been probed. The inverse MFP, derived from the measured CCD, is plotted as a function of 24 GeV proton fluence in figure 11.14. An initial MFP of $2.5^{+40}_{-1.0} \times 10^3\,\mu\mathrm{m}$ was assumed for the sCVD diamond samples. The data points corresponding to the pCVD diamond samples start at a lower MFP than the sCVD diamond points. Consistent curves were observed when fitting the radiation damage model individually to the data points. A comparison of the individual slopes is depicted in figure 11.15. The combination of these slopes results in a radiation damage

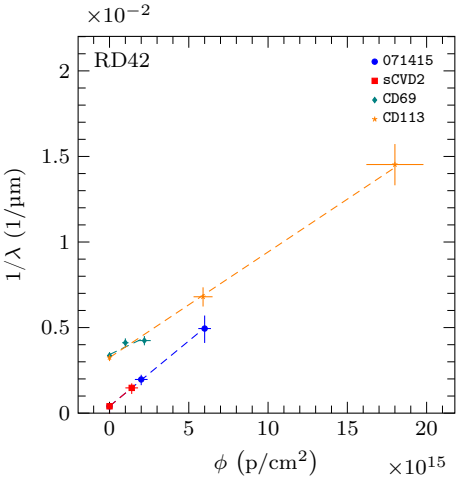

Figure 11.14: Inverse MFP as a function of 24 GeV proton fluence. The data points represent the MFP obtained by converting the measured CCD [186] at an electric bias field of 1 V/µm.

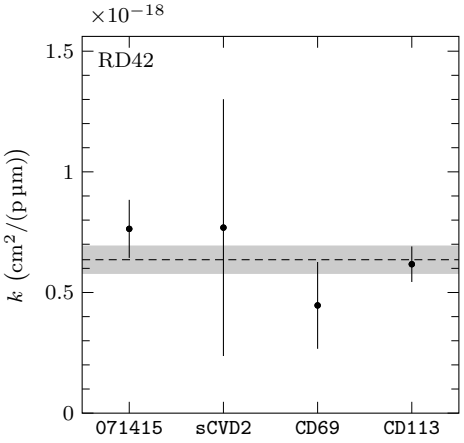

Figure 11.15: Radiation damage constants of 24 GeV protons measured with two sCVD diamond samples and two pCVD diamond samples. The combination of the individual damage constants is indicated by a dashed line and results in a goodness of fit of $\chi^2/N_{\text{dof}} = 2.36/3$.

constant of

$$k = 0.64\,^{+0.04}_{-0.04}\,(\text{stat})\,^{+0.05}_{-0.05}\,(\text{syst}) \times 10^{-18}\,\text{cm}^2/(\text{p}\,\mu\text{m}) \tag{11.7}$$

with a goodness of fit of $\chi^2/N_{\text{dof}} = 2.36/3$.

To verify consistency of the four samples, a single fit of the radiation damage model to their data points was performed using fluence offsets for the pCVD diamond samples. The fluence offsets, to account for the traps in the unirradiated state of pCVD diamond, were derived with the previously described offset scan, resulting in an offset of $4.3 \times 10^{15}\,\text{p/cm}^2$ and $4.2 \times 10^{15}\,\text{p/cm}^2$ for the samples `CD69` and `CD113`, respectively. Figure 11.16 shows the combined radiation damage curve. The radiation damage model was fitted to the data points, resulting in a radiation damage constant of

$$k = 0.671\,^{+0.04}_{-0.04}\,(\text{stat})\,^{+0.022}_{-0.022}\,(\text{syst}) \times 10^{-18}\,\text{cm}^2/(\text{p}\,\mu\text{m}) \tag{11.8}$$

with a goodness of fit of $\chi^2/N_{\text{dof}} = 3.63/9$. The fluence offset was scaled up and down by its uncertainty to propagate this systematic uncertainty to the radiation damage constant measurement. This re-evaluated result of the radiation damage of 24 GeV protons in diamond was found to be in good agreement with previous measurements [111, 184].

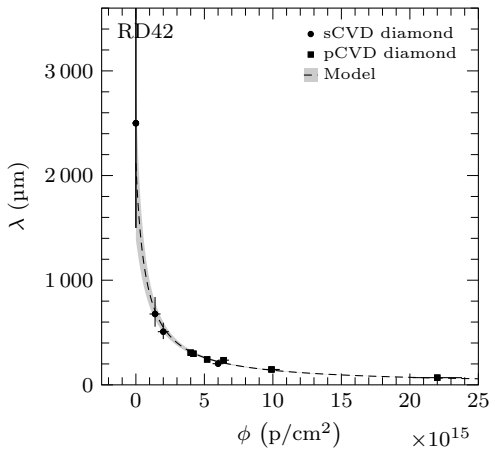

Figure 11.16: Mean free path as a function of 24 GeV proton fluence. The data points represent the mean free path obtained by converting the measured charge collection distance [186] at an electric bias field of 1 V/µm. The data points corresponding to pCVD diamond samples are shifted by a fluence offset of $3.8 \times 10^{15}\,\mathrm{p/cm^2}$. The damage model fit results in a goodness of fit of $\chi^2/N_{\mathrm{dof}} = 3.63/9$.

11.1.4 Neutron Radiation Damage

Like the damage induced by proton irradiation, the radiation tolerance of CVD diamond against fast neutrons is an important benchmark for applications of such devices in high energy physics experiments. Therefore, the pCVD diamond sample `L107-9` was irradiated with neutrons up to a total fluence of $(1.30 \pm 0.13) \times 10^{16}\,\mathrm{n/cm^2}$, as described in section 9.3.2.

After the irradiation, the sample was tested in two beam test campaigns. As above, the signal response was reconstructed with two algorithms. In the transparent analysis the individual signals of the surrounding strips were analysed. The charge was observed to be collected by the two strips closest to the predicted hit position. To account for possible tracking errors and multiple scattering, the signal response of the two highest adjacent strips within the ten closest strips was chosen as figure of merit. Figure 11.17 shows the observed signal response. The average measured pulse height corresponds to an SNR of 11.

In this regime of small signal response, the identification of signals against noise becomes challenging since the pulse height and noise distributions of single strips may start to overlap. For this reason, very low SNR thresholds of $t_{\mathrm{seed}} = 3$ and $t_{\mathrm{hit}} = 2$ to identify seed and hit strips, respectively, were chosen in the clustering analysis. Exclusive one and two strip clusters were required. These requirements result in a reconstruction efficiency of $(76.7 \pm 2.8)\,\%$. Including clusters with a size

ϕ (n/cm^2)	E_{bias} (V/µm)	f_{tr}	$\overline{r}_{\text{tr}}$ (µm)	$\overline{r}_{\text{cl}}$ (µm)	$\overline{r}'_{\text{cl}}$ (µm)
$1.30 \pm 0.13 \times 10^{16}$	+2	0.54 ± 0.04	23.0 ± 1.5	21.3 ± 3.3	25.2 ± 1.9
	−2	0.55 ± 0.06	22.3 ± 1.4	21 ± 4	24.6 ± 2.0

Table 11.5: Overview of the beam test results for the pCVD diamond sample `L107-9` after a neutron fluence of $(1.30 \pm 0.13) \times 10^{16}$ n/cm^2. The CCD reconstructed with the transparent and clustering algorithms are listed. The stated errors include statistical and systematic uncertainties. For the transparent method, the ratio of FWHM to MP value of the pulse height distribution, f, is shown.

of $\leq$4 strips would improve the reconstruction efficiency to a value of (81.1 ± 2.5) %. On average (14.7 ± 2.2) % of the events were rejected due to the reconstruction of multiple clusters. In figure 11.17, the pulse height distributions of both methods are compared. Both distributions may be described by a Landau distribution convoluted with a Gaussian. On average, the signal response reconstructed with the clustering algorithm was observed to be (92.7 ± 0.7) % of the value obtained with the transparent method. This bias by the cluster threshold is more pronounced than what was observed with other pCVD diamonds since the signals are smaller due to the high neutron fluence.

Table 11.5 summarises the beam test results. The observed ratio of the FWHM to MP value of the pulse height distribution is compatible with the values observed for the pCVD diamond sample `T15-33`. CCDs reconstructed with the clustering algorithm were observed smaller than the values reconstructed with the transparent method, but agree within the uncertainties. The corrected clustering method resulted in larger CCDs than the transparent algorithm, indicating an overcorrection for the missing charge of the second strip. Since the correction was estimated for higher seed and hit thresholds, such an overcorrection is expected. Between the two beam test campaigns, the DUT was disassembled. The result of the first beam test was confirmed in the second measurement.

The CCD before irradiation was obtained in a source measurement with pad electrodes at OSU [171, 180]. For this purpose, the signal response to a ^{90}Sr source was measured, as described before.

The CCD values measured were converted to MFP and are plotted as a function of neutron fluence in figure 11.18. The data points were fitted with the radiation damage model, described by equation (8.31), and a damage constant of

$$k = 3.05\,^{+0.23}_{-0.23}\,(\text{stat})\,^{+0.14}_{-0.14}\,(\text{syst}) \times 10^{-18}\,\text{cm}^2/(\text{n}\,\mu\text{m}) \tag{11.9}$$

was observed.

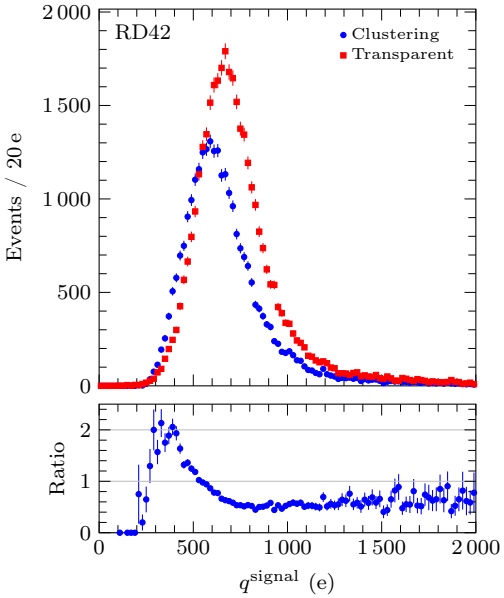

Figure 11.17: Pulse height distribution reconstructed with the transparent and clustering algorithms after a neutron fluence of $(1.30 \pm 0.13) \times 10^{16}\,\text{n/cm}^2$. The electric bias field was set to $+2\,\text{V/µm}$.

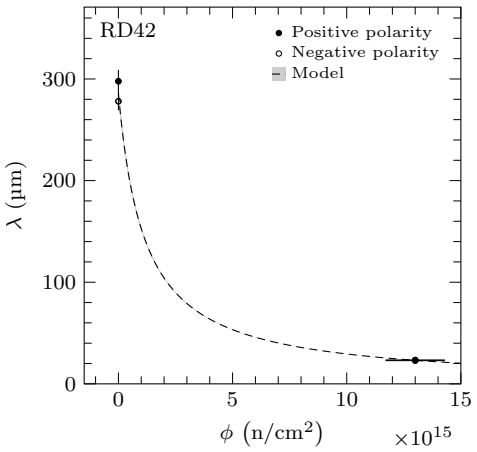

Figure 11.18: Mean free path as a function of neutron fluence. The data points represent the mean free path obtained by converting the measured charge collection distance with positive and negative bias polarity at each fluence. The damage model fit is shown by a dashed line and results in a goodness of fit of $\chi^2/N_{\text{dof}} = 1.97/2$.

Particle species	k (cm^2/µm)	κ
24 GeV protons	$0.67\,^{+0.04}_{-0.04} \times 10^{-18}$	1
800 MeV protons	$1.24\,^{+0.04}_{-0.04} \times 10^{-18}$	1.85 ± 0.13
70 MeV protons	$1.64\,^{+0.25}_{-0.27} \times 10^{-18}$	2.5 ± 0.4
25 MeV protons	$3.02\,^{+0.42}_{-0.36} \times 10^{-18}$	4.5 ± 0.6
Fast neutrons	$3.05\,^{+0.27}_{-0.27} \times 10^{-18}$	4.5 ± 0.5

Table 11.6: Radiation damage constants for different particle species. The measured radiation damage constants of 800 MeV protons, 70 MeV protons and fast neutrons are compared to the reference results of 24 GeV protons and to the previous result of 25 MeV protons [184]. The hardness factor κ is calculated using the 24 GeV proton radiation damage constant as reference.

Since the signal response reconstructed with the clustering method is highly biased by the applied thresholds, this is also true for the damage constant derived from these results. As a cross check, the results obtained with the clustering algorithm results were used to derive a radiation damage constant resulting in

$$k = 2.74\,^{+0.20}_{-0.20}\,(\text{stat})\,^{+0.16}_{-0.16}\,(\text{syst}) \times 10^{-18}\,\text{cm}^2/(\text{n}\,\mu\text{m}). \tag{11.10}$$

The cross check is smaller than the result using the transparent method but is in agreement within the uncertainties.

11.1.5 Comparison of Radiation Damage

The observed radiation damage constants of different particle energies and species are compared to previous measurements. Table 11.6 lists the measured radiation damage constants of 25 MeV protons and 24 GeV protons together with the results of this work. The quoted hardness factor κ was calculated using the 24 GeV proton result as reference.

The measured radiation damage constant predicts the radiation damage of 800 MeV protons 1.85 times higher than the radiation damage of 24 GeV protons, while 70 MeV protons were observed to yield a 2.5 times higher radiation damage. In the case of fast neutrons, a radiation damage constant was measured which is 4.5 times higher than the one of 24 GeV protons. The radiation damage constant of fast neutrons was observed to agree with the radiation damage constant of 25 MeV protons, $k = 3.02\,^{+0.42}_{-0.36} \times 10^{-18}\,\text{cm}^2/(\text{p}\,\mu\text{m})$ [184].

The MFP in sCVD and pCVD diamond follows the same radiation damage mechanism [147–149]. Due to its initial traps, pCVD diamond has a shorter initial MFP than sCVD diamond. When comparing sCVD and pCVD diamond, this characteristic may be regarded as a fluence offset of pCVD diamond. In the case of the 800 MeV proton and 24 GeV proton irradiated pCVD diamond samples, this fluence offset is included in the results of the offset scan. For the 70 MeV proton and fast neutron irradiated samples, the fluence offset of pCVD diamond, ϕ_0, was calculated by

$$\phi_0 = \frac{1}{k\lambda_0}. \tag{11.11}$$

After applying these offset corrections, the fluences were scaled to 24 GeV proton equivalent fluence by

$$\phi_{\text{eq}} = \kappa\phi \tag{11.12}$$

using the hardness factors of table 11.6. Figure 11.19 shows the MFP of sCVD and pCVD diamond samples as a function of 24 GeV proton equivalent fluence. All

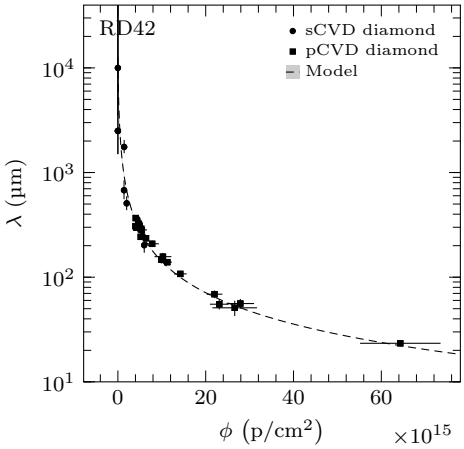

Figure 11.19: MFP as a function of 24 GeV proton equivalent fluence. A fluence offset correction is applied to the pCVD diamond samples. The 800 MeV proton, 70 MeV proton and fast neutron fluences are converted into 24 GeV proton equivalent fluence using the NIEL scaling hypothesis. The radiation damage model fitted to the data points results in a goodness of fit of $\chi^2/N_{\text{dof}} = 32.1/27$.

points were observed in agreement with the radiation damage model.

The point at the highest fluence was measured with the neutron irradiated pCVD diamond sample `L107-9`. Such a fluence may be comparable to fluences expected at the innermost layers of experiments at the HL-LHC. An important parameter for a sensor in such an environment is the SNR. An SNR of 10.8 ± 1.0 was measured with the sample `L107-9` after irradiation with the clustering algorithm, which may be used in a genuine detector application. Such an SNR is feasible for a detector application and thereby predicts CVD diamond a solid option for tracking detectors at the HL-LHC.

11.2 Signal Shape Study

As described in section 8.3, the measured pulse height depends on the number of electron-hole pairs created and the distance they move apart before getting trapped. The pulse height of monoenergetic incident particles is Landau distributed. For the probed sCVD and pCVD diamond samples, the shape of the pulse height distribution was studied as a function of fluence. The pulse height distribution's width represents a measure of the spread of the energy loss due to ionisation. In the further analysis, the relative width of the pulse height distribution reconstructed with the transparent algorithm, namely the ratio of the FWHM to MP value, f,

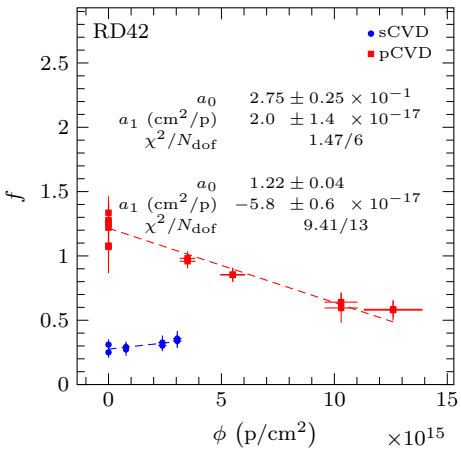

Figure 11.20: Energy resolution as a function of 800 MeV proton fluence. A slope is fitted to the data points corresponding to the sCVD and pCVD diamond samples, respectively.

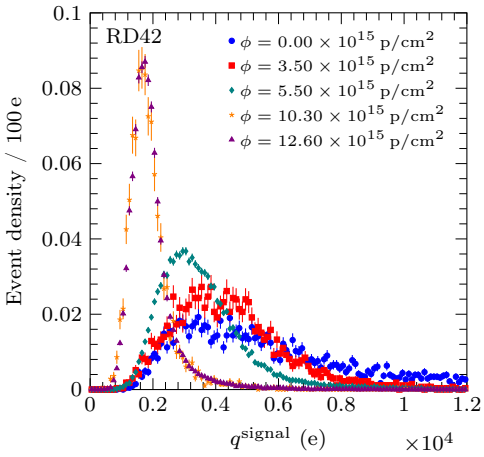

Figure 11.21: Pulse height distribution pCVD diamond samples after different accumulated 800 MeV proton fluences. The electric bias field of the runs shown was set to $-2\,\mathrm{V/\mu m}$. Each distribution's integral is scaled to unity.

was defined as figure of merit for the energy resolution of the sensor.

For the sCVD diamond sample `PW205B`, the ratio of the FWHM to MP value was derived from the pulse height distributions shown in figure 11.1. A systematic uncertainty of 0.04 was added in quadrature to the statistical uncertainty of the energy resolution to account for the differences between the measurements with opposite bias polarity. Figure 11.20 shows the resulting energy resolution as a function of 800 MeV proton fluence. The data points were fitted with a linear function, resulting in a slope of $(20 \pm 14) \times 10^{-18}\,\mathrm{cm^2/p}$, compatible with a constant function.

The pulse height distributions of the pCVD diamond samples irradiated with 800 MeV protons are shown in figure 11.21. In figure 11.20, the corresponding energy resolution is shown as function of fluence. The initial energy resolution of the sample `L107-11` was derived in a beam test as well as in a source measurement [180]. Both measurements were found in agreement. For the remaining two samples, the initial values were obtained in source measurements [180]. Unlike sCVD diamond, the energy resolution of these pCVD diamond samples improved with fluence. An average initial energy resolution of 1.23 ± 0.12 was observed, which decreased to a value of 0.582 ± 0.004 after a fluence of $(12.6 \pm 1.3) \times 10^{15}\,\mathrm{p/cm^2}$. This improvement in energy resolution may be described by a linear function. A slope of $(-58 \pm 6) \times 10^{-18}\,\mathrm{cm^2/p}$ was derived when fitting the data points with a

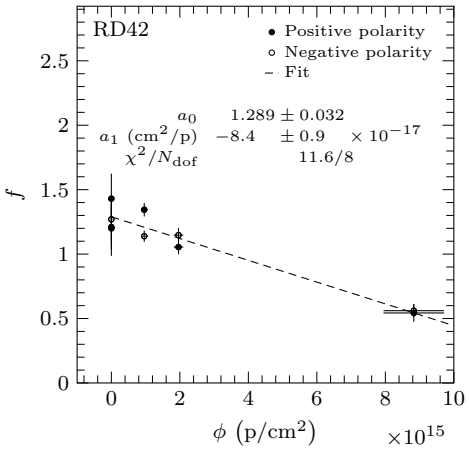

Figure 11.22: Energy resolution of the pCVD diamond samples `T15-33` and `T15-43` as a function of 70 MeV proton fluence.

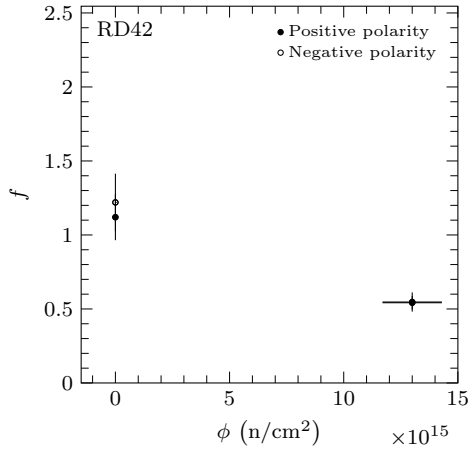

Figure 11.23: Energy resolution of the pCVD diamond sample `L107-9` as a function of neutron fluence.

linear function.

The relative width of the pulse height distribution measured with the pCVD diamond samples `T15-33` and `T15-43` is listed in table 11.4. Figure 11.22 shows the resulting energy resolution as a function of 70 MeV proton fluence. Like for the 800 MeV irradiated pCVD diamond samples, a linear decrease of the energy resolution was observed. From the source measurements an average initial energy resolution of 1.28 ± 0.09 was derived. After a fluence of $(8.8 \pm 0.9) \times 10^{15}\,\mathrm{p/cm^2}$, the value decreased to 0.54 ± 0.05. A linear function was fitted to the data points resulting in a slope of $(-84 \pm 9) \times 10^{-18}\,\mathrm{cm^2/p}$.

The energy resolution of the neutron irradiated pCVD diamond sample `L107-9` is plotted in figure 11.23. The initial and final values of the measured energy resolution agree with the observation above. However, to confirm the model of a linear decrease, more data points are necessary.

All pCVD diamond samples were observed to start with an initial relative width of their pulse height distribution of >1 which decreases to roughly 0.5 after irradiation. This may be related to the distribution of trapping centres in the diamond lattice. Due to the grain boundaries, the trapping centres of unirradiated pCVD diamond are distributed heterogeneously. With irradiation, additional trapping centres are introduced, resulting in an over all more homogeneous distribution of trapping centres. In sCVD diamond, the trapping centres are distributed uniformly. With the sCVD diamond sample, a relative width of the pulse height distribution of

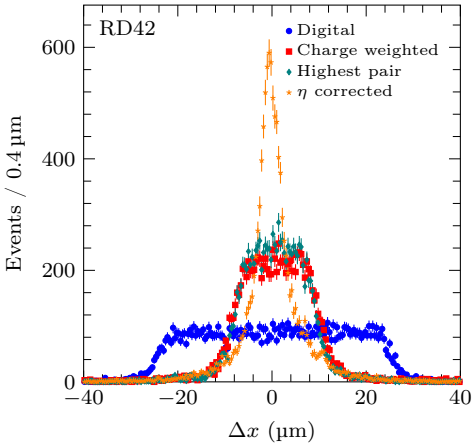

Figure 11.24: Residual distributions for different position reconstruction methods in the diamond plane, as described in section 10.2.3. Residuals obtained with digital positions, charge weighted positions, highest strip pair positions, and η corrected positions are drawn. In this order, the spatial resolution is improving.

roughly 0.3 was observed, independent of the fluence. Thus, sCVD diamond has a better energy resolution than pCVD diamond at all stages. However, further measurements are necessary to investigate the trend of the energy resolution of pCVD diamond at higher fluences. To elaborate a model of the energy resolution dependence on neutron fluence, further tests at intermediate fluences are needed.

11.3 Spatial Resolution Study

A possible application for diamond sensors is a position sensitive tracking detector. In such an application, the spatial resolution constitutes a key parameter of the device. Like the signal response, the spatial resolution is studied as a function of fluence of different particle species and energies.

11.3.1 Method

As described in section 10.2.3, different algorithms were used to reconstruct the hit position, yielding different spatial resolutions. The residual distributions in the diamond plane obtained with the algorithms studied are shown in figure 11.24, in the case of the sCVD diamond sample `PW205B`. A broad spectrum is observed with the digital position algorithm. It is centred around zero and has a standard deviation of 15.0 µm. The spectrum's FWHM is (49.34 ± 0.35) µm. However, its

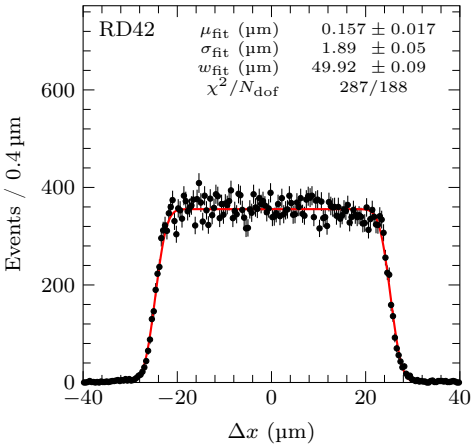

Figure 11.25: Digital residual distribution after an 800 MeV proton fluence of $(3.05 \pm 0.19) \times 10^{15}\,\text{p/cm}^2$. A rectangular function convoluted with a Gaussian is fitted to the data points.

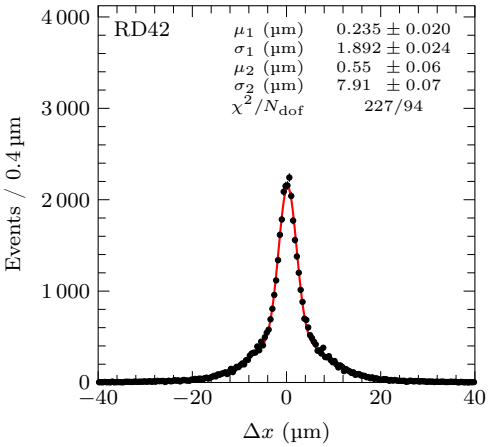

Figure 11.26: η corrected residual distribution after an 800 MeV proton fluence of $(3.05 \pm 0.19) \times 10^{15}\,\text{p/cm}^2$. The sum of two Gaussians is fitted to the data points in the range from −20 µm to 20 µm.

shape deviates slightly from a box function since the measured residual spectrum is convoluted with a Gaussian originating from the uncertainty on the predicted and measured position. The charge weighted algorithm clearly improves the spatial resolution. It results in a residual spectrum with an FWHM of (17.8 ± 0.6) µm and a standard deviation of 7.96 µm. When considering only the cluster's highest strip pair, the residual spectrum becomes slightly narrower with a standard deviation of 7.18 µm. This represents a slight improvement with respect to the previous method due to omitting channels with small SNRs. After correcting for non-linearities in the η distribution, a residual spectrum with an FWHM of (7.57 ± 0.15) µm and a standard deviation of 6.62 µm is obtained by the η corrected method.

In this study the digital position and the η corrected method were used. The digital resolution was used as first measure to verify well working devices. In figure 11.25, the digital residual distribution is shown after an 800 MeV proton irradiation of $(3.05 \pm 0.19) \times 10^{15}\,\text{p/cm}^2$. The distribution has an FWHM of (49.50 ± 0.29) µm and is centred at zero. A rectangular function convoluted with a Gaussian is used to fit the data points. The resulting width w_{fit} of the rectangular function is used as figure of merit for the digital spatial resolution. Various circumstances may influence the smeared edges, such as the resolution of the telescope, multiple scattering, tracking errors, or the geometry of the metallised strips. The width σ_{fit} of the convoluted Gaussian was therefore assigned as systematic uncertainty on the digital spatial resolution. To account for possible errors in the photolithography, an additional systematic uncertainty of 2 µm was added in quadrature.

The η corrected method exploits charge sharing between strips. Figure 11.26 shows the η corrected residual distribution after an 800 MeV proton fluence of $(3.05 \pm 0.19) \times 10^{15}\,\mathrm{p/cm^2}$. A narrow peak was observed on top of a broader distribution. The narrow peak may be associated with charge sharing events, while the broad distribution may originate from events in which the charge is collected by a single strip. The sum of two Gaussians was used to fit the shape of this distribution. To study the spatial resolution as a function of fluence, the width of the narrow charge sharing peak, represented by the fit parameter σ_1, was chosen as figure of merit. Half of the average difference when inverting the electric bias field was assigned as systematic uncertainty on the spatial resolution, similar to the systematic uncertainty on the signal response.

11.3.2 Radiation Dependence

Spatial Resolution after 800 MeV Proton Irradiation

Digital residuals were reconstructed for all beam test runs. Figure 11.27 shows the observed digital residual distributions of the sCVD diamond sample `PW205B` after each 800 MeV proton irradiations. At all fluences, a rectangular distribution was observed, in which no loss of charge was found at the edges, even for the highest dose. In figure 11.28, the resulting digital resolution is plotted as function of fluence. The digital resolution was observed independent of the fluence and is compatible with the strip pitch of 50 µm at all stages.

The η corrected residuals are shown in figure 11.29 after different accumulated 800 MeV proton fluences. At all stages, a narrow peak was observed on top of a broader distribution. Before irradiation the distribution is slightly shifted and the position of narrow peak was observed to be 3.8 µm. A small asymmetry was found in the tails of the distribution after a fluence of $(0.78 \pm 0.07) \times 10^{15}\,\mathrm{p/cm^2}$. Both effects may arise from charge feed across among the strips in the readout [149]. Figure 11.30 shows the measured spatial resolution as a function of fluence. After the first irradiation, an increase in spatial resolution was observed in the case of negative polarity of the electric bias field. The spatial resolutions after a fluence above $2 \times 10^{15}\,\mathrm{p/cm^2}$ improved compared to the initial values. These findings are compatible with previous studies [149].

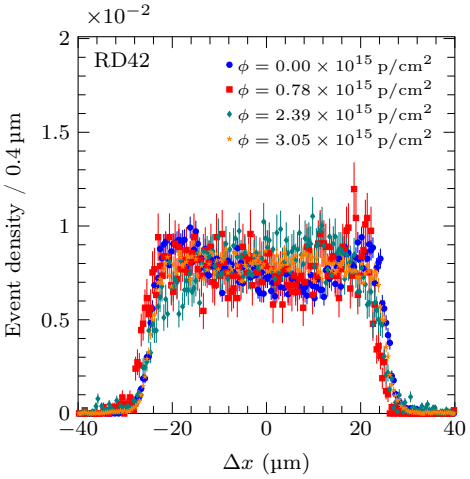

Figure 11.27: Digital residual distribution after different accumulated 800 MeV proton fluences, measured with positive polarity of the electric bias field.

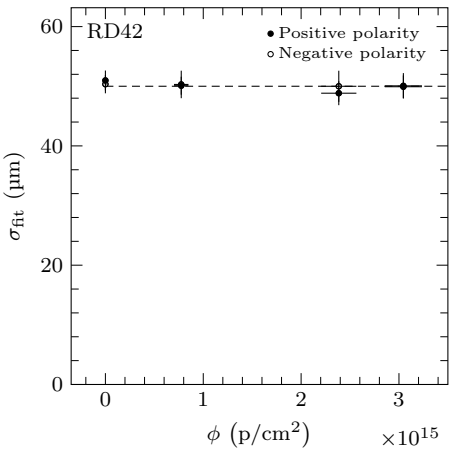

Figure 11.28: Digital resolution as a function of 800 MeV proton fluence. The dashed line indicates the strip pitch of 50 µm.

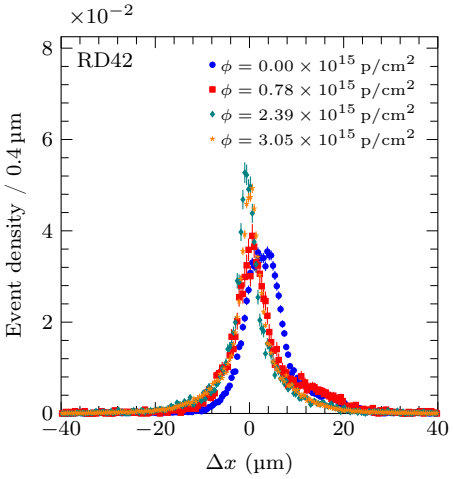

Figure 11.29: η corrected residual distribution after different accumulated 800 MeV proton fluences, measured with positive polarity of the electric bias field.

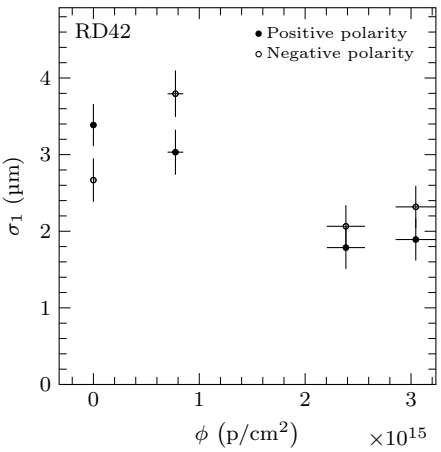

Figure 11.30: Spatial resolution as a function of 800 MeV proton fluence.

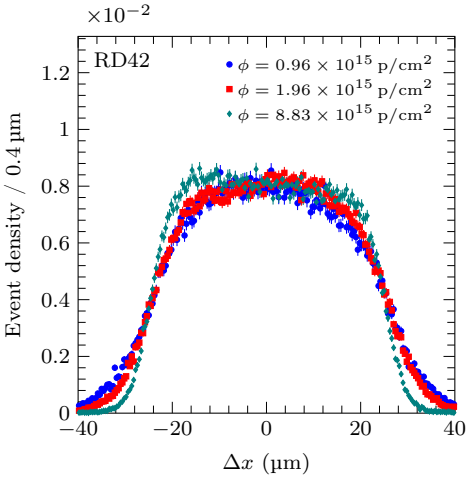

Figure 11.31: Digital residual distribution after different accumulated 70 MeV proton fluences, measured with positive polarity of the electric bias field.

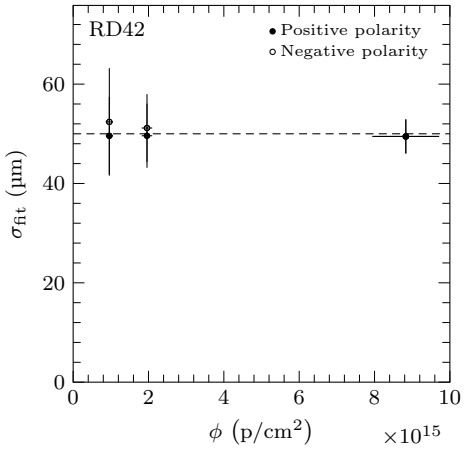

Figure 11.32: Digital resolution as a function of 70 MeV proton fluence. The strip pitch of 50 µm is indicated by a dashed line.

Spatial Resolution after 70 MeV Proton Irradiation

The two pCVD diamond samples `T15-33` and `T15-43` were tested as strip detectors after irradiation with 70 MeV protons. The digital residual distributions observed with these DUTs are shown in figure 11.31 after different accumulated 70 MeV proton fluences. At all fluence states, the distribution can be described by a rectangular function convoluted with a Gaussian. The related fit results in a width which is in agreement with the strip pitch of 50 µm, independent of the fluence, as shown in figure 11.32, where the digital resolution is plotted as a function of fluence. At the two lower fluence values, corresponding to the sample `T15-43`, the digital residual distribution was observed broader than at the highest fluence, corresponding to the sample `T15-33`. Thus, the fit of these broader distributions result in a larger width of the Gaussian, σ_{fit}, which is reflected in the larger uncertainties of corresponding data points in figure 11.32.

The residual distribution after different accumulated fluences using the η corrected algorithm is shown in figure 11.33. With increasing fluence the residual distribution was observed to get narrower. The distribution at all fluence values was fitted with the sum of two Gaussians. The width of the narrow Gaussian, σ_1, represents the spatial resolution and is plotted as a function of fluence in figure 11.34. Despite the large uncertainties, an improvement in spatial resolution with increasing fluence is observed. A better spatial resolution was measured with positive polarity of the electric bias potential at the first two fluence values. Furthermore, the agreement

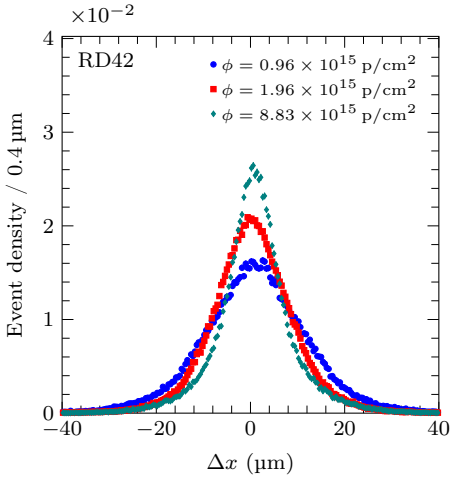

Figure 11.33: η corrected residual distribution after different accumulated 70 MeV proton fluences, measured with positive polarity of the electric bias field.

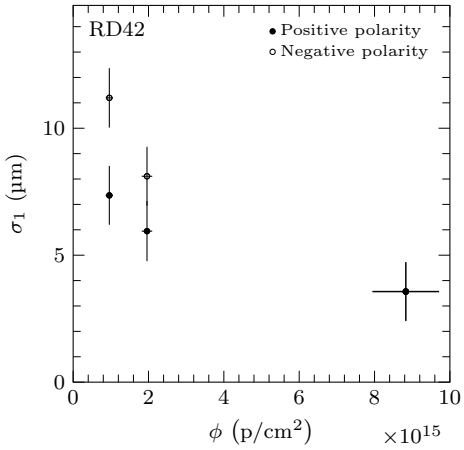

Figure 11.34: Spatial resolution as a function of 70 MeV proton fluence.

of the measurements with opposite bias polarity improved with fluence.

At all fluence values, both pCVD diamond samples yield a larger spatial resolution than the spatial resolution observed with the sCVD sample after 800 MeV proton irradiations. Due to the grain structure of pCVD diamond, the spatial resolution of pCVD diamond samples is expected to be worse than the one of sCVD diamond samples.

Spatial Resolution after Neutron Irradiation

After irradiation with fast neutrons to a fluence of $(1.30 \pm 0.13) \times 10^{16}\,\mathrm{n/cm^2}$, the pCVD diamond sample `L107-9` was probed as strip detector in two beam tests and its spatial resolution was measured. Figure 11.35 shows the digital residual distribution. The data points were fitted with a rectangular function convoluted with a Gaussian, resulting in a width of $(48.8 \pm 2.0)\,\mu\mathrm{m}$. This is in agreement with the expectations for a strip pitch of 50 µm and confirms a well working hit identification algorithm.

In figure 11.36, the η corrected residual distribution is shown. The distribution was fitted with the sum of two Gaussians and a spatial resolution of $(3.1 \pm 1.2)\,\mu\mathrm{m}$ was observed. This spatial resolution is compatible with the one observed after the highest 70 MeV proton irradiation and proves a well working device even after a neutron fluence of $(1.30 \pm 0.13) \times 10^{16}\,\mathrm{n/cm^2}$.

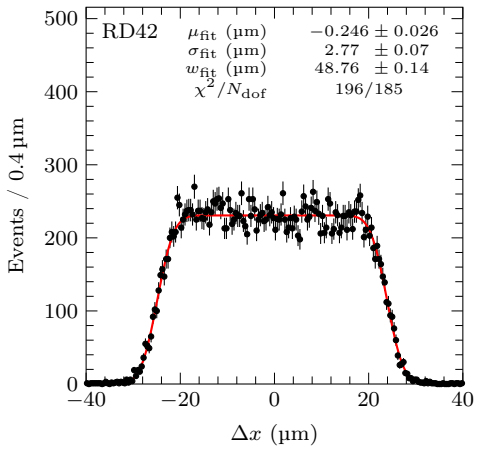

Figure 11.35: Digital residual distribution after a neutron fluence of $(1.30 \pm 0.13) \times 10^{16}\,\text{n/cm}^2$. The red line represents the fit of a rectangular function convoluted with a Gaussian.

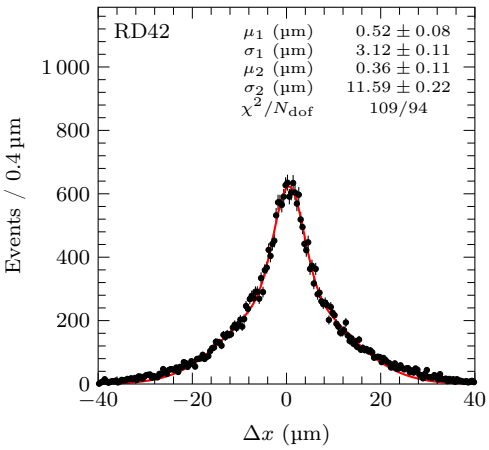

Figure 11.36: η corrected residual distribution after a neutron fluence of $(1.30 \pm 0.13) \times 10^{16}\,\text{n/cm}^2$. The sum of two Gaussians is fitted to the data points.

Chapter 12

Conclusion

A study of CVD diamond's radiation tolerance was presented. Seven CVD diamond samples were tested in several beam test campaigns. Between beam tests, an sCVD diamond sample and three pCVD diamond samples were irradiated with 800 MeV protons. Two pCVD diamond samples were irradiated with 70 MeV protons and a pCVD diamond was exposed to fast neutrons. The result of this work is a comparison of the radiation damage of 800 MeV protons, 70 MeV protons, and fast neutrons and represents the first such study performed.

Collected data of nine beam test campaigns were analysed with two different analysis techniques to derive CCDs at each fluence point. The clustered analysis reconstructed signals similar as it would be in an actual application. Analysed signals proved a well working device and were used as cross check. In the transparent analysis, signals were studied in more detail, independent of thresholds on the signal charge. Slightly higher signals were found compared to the clustering method. However, both techniques were found in agreement within uncertainties for the proton irradiated samples. A larger bias of the cluster thresholds was observed after the highest fast neutron fluence. With both algorithms, a discrepancy between the signal response measured with opposite direction of the applied electric bias field was observed. The different mobilities of electrons and holes in diamond may cause such a behaviour. However, further studies are necessary to probe if the observed difference is due to a property of diamond or caused by the readout system.

Resulting CCD points were converted into MFP and fitted with a damage curve for each particle species. Radiation damage constants of 800 MeV protons, 70 MeV protons, and fast neutrons were derived. The result for 800 MeV protons was found in agreement with other measurements [148, 149, 187]. The resulting damage constants of 800 MeV protons, 70 MeV protons, and fast neutrons were compared

to the corresponding values of 25 MeV and 24 GeV protons [184]. From these radiation damages constants, hardness factors were derived taking 24 GeV protons as reference. The radiation damage of these particle species and energies provides a good representation of the expected radiation damage in a high energy physics experiment.

A pCVD diamond sample was exposed to a fast neutron fluence comparable to fluences predicted at the HL-LHC. CVD diamond sensors were found to be capable of operating in such an environment expected within a future experiment at the HL-LHC. In such an application, a readout system which is able to handle small signals and operate at low thresholds will be necessary. However, the available sizes of sCVD diamond samples denote a limiting factor for an application on a large scale. Samples of pCVD diamond are available in larger sizes and follow the same damage law as sCVD diamond [147–149]. Due to its grain boundaries, pCVD diamond has more defects, and thus traps, than sCVD diamond and therefore has a smaller CCD in the unirradiated state. However, the quality of pCVD diamond is continuously improving and therefore its initial CCD.

The energy resolution of the probed samples was determined. For pCVD diamond, an improvement with irradiation was measured. All pCVD diamond samples reach a value of 0.5, while the energy resolution of sCVD diamond was observed constant at 0.3. A simple model was fitted to the data. However, for a better understanding of the underlying model, more data at intermediate and higher fluences are necessary.

The measured data were further used to study the fluence dependance of the spatial resolution of the probed detectors. Two algorithms, the digital and the η corrected position, were used to measure the resolution. The former method confirmed well working strip tracking detectors at all fluence levels. A slight improvement in resolution, obtained with the η corrected algorithm, was observed with increasing proton fluence for sCVD and pCVD diamond. A better spatial resolution was observed with the sCVD diamond samples than with the pCVD diamond samples, due to the grain boundaries of the latter. These results confirm CVD diamond detectors suitable for tracking applications in future experiments at the HL-LHC.

Finally, CVD diamond represents a radiation tolerant material for future particle physics detector applications. As reliable tracking detectors, CVD diamond sensors facilitate higher precision in SM measurements, such as the $t\bar{t}W$ cross section presented in the first part of this dissertation. Furthermore, such devices are essential to probe even rarer processes and provide the opportunity to search for new physics.

Acronyms

ADC	Analog-to-digital converter
ALICE	A Large Ion Collider Experiment
APD	Avalanche photodiode
ASIC	Application-specific integrated circuit
ATLAS	A Toroidal LHC ApparatuS
BaBar	$B\overline{B}$ experiment
b-jet	Bottom quark jet
CAMAC	Computer automated measurement and control
CB	Conduction band
CCD	Charge collection distance
CDF	Collider Detector at Fermilab
CERN	European Organization for Nuclear Research
CKM	Cabibbo-Kobayashi-Maskawa
CM	Common mode
CMC	Common mode corrected
CMN	Common mode noise
CMS	Compact Muon Solenoid
CSC	Cathode Strip Chamber
CSV	Combined Secondary Vertex
CTF	Combinatorial Track Finder
CVD	Chemical vapour deposition
CYRIC	Cyclotron and Radioisotope Center of Tohoku University
DØ	DZero
DAQ	Data Acquisition
DPS	Double parton scattering
DQM	Data Quality Monitoring
DT	Drift Tube
DUT	Device under test
EB	ECAL barrel
ECAL	Electromagnetic Calorimeter
EE	ECAL endcap
fcc	Face-centred cubic

FNAL Fermi National Accelerator Laboratory

FSR Final state radiation

FWHM Full width at half maximum

GSF Gaussian Sum Filter

GSW Glashow-Salam-Weinberg

HB HCAL barrel

HCAL Hadron Calorimeter

HE HCAL endcap

HF HCAL forward

HL-LHC High Luminosity LHC

HLT High-Level Trigger

HO HCAL outer barrel

HPHT High-pressure high-temperature

IPHC Institut Pluridisciplinaire Hubert Curien, Strasbourg

ISR Initial state radiation

JSI Jožef Stefan Institute

L1 Level-1 Trigger

LANSCE Los Alamos Neutron Science Center

LEIR Low Energy Ion Ring

LEP Large Electron-Positron Collider

LHAPDF Les Houches Accord PDF

LHC Large Hadron Collider

LHCb Large Hadron Collider beauty

Linac2 Linear accelerator 2

Linac3 Linear accelerator 3

LO Leading order

MC Monte Carlo

MFP Mean free path

MIP Minimum ionising particle

MP Most probable

MPF Missing transverse energy projection fraction

NIEL Non-ionising energy loss

NLO Next to leading order

OSU Ohio State University

pCVD Polycrystalline CVD

pdf Probability density function

PDF Parton density function

PF Particle-flow

PS Proton Synchrotron

PSB Proton Synchrotron Booster

PSI Paul Scherrer Institute

PU Pileup

PV Primary vertex

QCD Quantum Chromodynamics

QFT Quantum Field Theory

RD42 CVD Diamond Radiation Detector Development

RF Radiofrequency

RPC Resistive Plate Chamber

sCVD Single-crystalline CVD

SIROCCO Silicon strip read out CAMAC controller

SM Standard Model of Particle Physics

SNR Signal-to-noise ratio

SPS Super Proton Synchrotron

SV Secondary vertex

TEC Tracker Endcap

TIB Tracker Inner Barrel

TID Tracker Inner Disks

TOB Tracker Outer Barrel

TRIGA Training, Research, Isotopes, General Atomics

TRIUMF Tri-University Meson Facility

UCSB University of California, Santa Barbara

UCSD University of California, San Diego

UE Underlying event

VB Valence band

VPT Vacuum phototriode

List of Figures

II Radiation Tolerance of Diamond Sensors 91

List of Tables

Bibliography

[1] G. Aad et al. (The ATLAS Collaboration). «Observation of a new particle in the search for the Standard Model Higgs boson with the ATLAS detector at the LHC». In: *Physics Letters B* 716.1 (2012), pp. 1–29. ISSN: 0370-2693. DOI: 10.1016/j.physletb.2012.08.020.

[2] S. Chatrchyan et al. (The CMS Collaboration). «Observation of a new boson at a mass of 125 GeV with the CMS experiment at the LHC». In: *Physics Letters B* 716.1 (2012), pp. 30–61. ISSN: 0370-2693. DOI: 10.1016/j.physletb.2012.08.021.

[3] F. Abe et al. (The CDF Collaboration). «Observation of Top Quark Production in $\overline{p}p$ Collisions with the Collider Detector at Fermilab». In: *Phys. Rev. Lett.* 74 (14 Apr. 1995), pp. 2626–2631. DOI: 10.1103/PhysRevLett.74.2626.

[4] S. Abachi et al. (The D0 Collaboration). «Observation of the Top Quark». In: *Phys. Rev. Lett.* 74 (14 Apr. 1995), pp. 2632–2637. DOI: 10.1103/PhysRevLett.74.2632.

[5] The ATLAS, CDF, CMS, and D0 Collaborations. «First combination of Tevatron and LHC measurements of the top-quark mass». ATLAS-CONF-2014-008, CDF Note 11071, CMS PAS TOP-13-014, D0 Note 6416. 2014. arXiv: 1403.4427 [hep-ex].

[6] The ATLAS and CMS Collaborations. «Combination of ATLAS and CMS top-quark pair cross section measurements using proton-proton collisions at $\sqrt{s} = 7\,\text{TeV}$». Physics Analysis Summary ATLAS-CONF-2012-134, CMS PAS TOP-12-003. 2013. URL: http://cds.cern.ch/record/1541952.

[7] The ATLAS and CMS Collaborations. «Combination of ATLAS and CMS top quark pair cross section measurements in the eμ final state using proton-proton collisions at $\sqrt{s} = 8\,\text{TeV}$». Physics Analysis Summary ATLAS-CONF-2014-054, CMS PAS TOP-14-016. 2014. URL: http://cds.cern.ch/record/1950834.

[8] V. Khachatryan et al. (The CMS Collaboration). «Measurement of top quark-antiquark pair production in association with a W or Z boson in pp collisions at $\sqrt{s} = 8\,\text{TeV}$». In: *The European Physical Journal C* 74.9, 3060 (2014). ISSN: 1434-6044. DOI: 10.1140/epjc/s10052-014-3060-7. arXiv: 1406.7830 [hep-ex].

[9] I. J. R. Aitchison and A. J. G. Hey. *Gauge Theories in Particle Physics*. 4th ed. Vol. 1. CRC Press, 2013. ISBN: 978-1-4665-1299-3.

[10] I. J. R. Aitchison and A. J. G. Hey. *Gauge Theories in Particle Physics*. 4th ed. Vol. 2. CRC Press, 2013. ISBN: 978-1-4665-1307-5.

[11] A. Bettini. *Introduction to Elementary Particle Physics*. 2nd ed. Cambridge University Press, Feb. 2014. ISBN: 978-1-107-05040-2.

[12] F. Halzen and A. D. Martin. *Quarks and Leptons: An Introductory Course in Modern Particle Physics*. Wiley, 1984. ISBN: 978-0-471-88741-6.

[13] G. Arnison et al. (The UA1 Collaboration). «Experimental observation of isolated large transverse energy electrons with associated missing energy at $\sqrt{s} = 540\,\text{GeV}$». In: *Physics Letters B* 122.1 (1983), pp. 103–116. ISSN: 0370-2693. DOI: 10.1016/0370-2693(83)91177-2.

[14] M. Banner et al. (The UA2 Collaboration). «Observation of single isolated electrons of high transverse momentum in events with missing transverse energy at the CERN $\overline{\text{p}}\text{p}$ collider». In: *Physics Letters B* 122.5–6 (1983), pp. 476–485. ISSN: 0370-2693. DOI: 10.1016/0370-2693(83)91605-2.

[15] G. Arnison et al. (The UA1 Collaboration). «Experimental observation of lepton pairs of invariant mass around $95\,\text{GeV}/c^2$ at the CERN SPS collider». In: *Physics Letters B* 126.5 (1983), pp. 398–410. ISSN: 0370-2693. DOI: 10.1016/0370-2693(83)90188-0.

[16] P. Bagnaia et al. (The UA2 Collaboration). «Evidence for $\text{Z}^0 \to \text{e}^+\text{e}^-$ at the CERN $\overline{\text{p}}\text{p}$ collider». In: *Physics Letters B* 129.1 (1983), pp. 130–140. ISSN: 0370-2693. DOI: 10.1016/0370-2693(83)90744-X.

[17] K. A. Olive et al. (Particle Data Group). «Review of Particle Physics». In: *Chin. Phys.* C38 (2014), p. 090001. DOI: 10.1088/1674-1137/38/9/090001.

[18] D. D. Ryutov. «Using plasma physics to weigh the photon». In: *Plasma Physics and Controlled Fusion* 49.12B (2007), B429. DOI: 10.1088/0741-3335/49/12B/S40.

[19] Y. Fukuda et al. (The Super-Kamiokande Collaboration). «Evidence for Oscillation of Atmospheric Neutrinos». In: *Phys. Rev. Lett.* 81 (8 Aug. 1998), pp. 1562–1567. DOI: 10.1103/PhysRevLett.81.1562.

[20] Q. R. Ahmad et al. (The SNO Collaboration). «Direct Evidence for Neutrino Flavor Transformation from Neutral-Current Interactions in the Sudbury Neutrino Observatory». In: *Phys. Rev. Lett.* 89 (1 June 2002), p. 011301. DOI: 10.1103/PhysRevLett.89.011301.

[21] M. H. Ahn et al. (The K2K Collaboration). «Measurement of neutrino oscillation by the K2K experiment». In: *Phys. Rev. D* 74 (7 Oct. 2006), p. 072003. DOI: 10.1103/PhysRevD.74.072003.

[22] D. G. Michael et al. (The MINOS Collaboration). «Observation of Muon Neutrino Disappearance with the MINOS Detectors in the NuMI Neutrino Beam». In: *Phys. Rev. Lett.* 97 (19 Nov. 2006), p. 191801. DOI: 10.1103/PhysRevLett.97.191801.

[23] N. Cabibbo. «Unitary Symmetry and Leptonic Decays». In: *Phys. Rev. Lett.* 10 (12 June 1963), pp. 531–533. DOI: 10.1103/PhysRevLett.10.531.

[24] M. Kobayashi and T. Maskawa. «CP-Violation in the Renormalizable Theory of Weak Interaction». In: *Progress of Theoretical Physics* 49.2 (1973), pp. 652–657. DOI: 10.1143/PTP.49.652.

[25] G. Dissertori, I. G. Knowles and M. Schmelling. *Quantum Chromodynamics: High Energy Experiments and Theory*. Oxford University Press, 2009. ISBN: 978-0-19-956641-9. DOI: 10.1093/acprof:oso/9780199566419.001.0001.

[26] E. Noether. «Invariante Variationsprobleme». In: *Nachrichten von der Gesellschaft der Wissenschaften zu Göttingen, Mathematisch-Physikalische Klasse* 1918 (1918), pp. 235–257.

[27] D. J. Gross and F. Wilczek. «Ultraviolet Behavior of Non-Abelian Gauge Theories». In: *Phys. Rev. Lett.* 30 (26 June 1973), pp. 1343–1346. DOI: 10.1103/PhysRevLett.30.1343.

[28] H. D. Politzer. «Reliable Perturbative Results for Strong Interactions?» In: *Phys. Rev. Lett.* 30 (26 June 1973), pp. 1346–1349. DOI: 10.1103/PhysRevLett.30.1346.

[29] S. L. Glashow. «Partial-symmetries of weak interactions». In: *Nuclear Physics* 22.4 (1961), pp. 579–588. ISSN: 0029-5582. DOI: 10.1016/0029-5582(61)90469-2.

[30] A. Salam and J. C. Ward. «Electromagnetic and weak interactions». In: *Physics Letters* 13.2 (1964), pp. 168–171. ISSN: 0031-9163. DOI: 10.1016/0031-9163(64)90711-5.

[31] S. Weinberg. «A Model of Leptons». In: *Phys. Rev. Lett.* 19 (21 Nov. 1967), pp. 1264–1266. DOI: 10.1103/PhysRevLett.19.1264.

[32] S. L. Glashow, J. Iliopoulos and L. Maiani. «Weak Interactions with Lepton-Hadron Symmetry». In: *Phys. Rev. D* 2 (7 Oct. 1970), pp. 1285–1292. DOI: 10.1103/PhysRevD.2.1285.

[33] F. Englert and R. Brout. «Broken Symmetry and the Mass of Gauge Vector Mesons». In: *Phys. Rev. Lett.* 13 (9 Aug. 1964), pp. 321–323. DOI: 10.1103/PhysRevLett.13.321.

[34] P. W. Higgs. «Broken Symmetries and the Masses of Gauge Bosons». In: *Phys. Rev. Lett.* 13 (16 Oct. 1964), pp. 508–509. DOI: 10.1103/PhysRevLett.13.508.

[35] G. S. Guralnik, C. R. Hagen and T. W. B. Kibble. «Global Conservation Laws and Massless Particles». In: *Phys. Rev. Lett.* 13 (20 Nov. 1964), pp. 585–587. DOI: 10.1103/PhysRevLett.13.585.

[36] A. D. Martin et al. «Parton distributions for the LHC». In: *The European Physical Journal C* 63.2 (2009), pp. 189–285. ISSN: 1434-6044. DOI: 10.1140/epjc/s10052-009-1072-5.

[37] T. Gleisberg et al. «Event generation with SHERPA 1.1». In: *Journal of High Energy Physics* 2009.02 (2009), p. 007. DOI: 10.1088/1126-6708/2009/02/007. arXiv: 0811.4622 [hep-ph].

[38] F.-P. Schilling. «Top quark physics at the LHC: a review of the first two years». In: *International Journal of Modern Physics A* 27.17 (2012), p. 1230016. DOI: 10.1142/S0217751X12300165.

[39] R. Chierici. «Top quark physics at the LHC». In: *Riv. Nuovo Cim.* 37.02 (2014), pp. 47–123. DOI: 10.1393/ncr/i2014-10097-2.

[40] W. Bernreuther. «Top-quark physics at the LHC». In: *Journal of Physics G: Nuclear and Particle Physics* 35.8 (2008), p. 083001. DOI: 10.1088/0954-3899/35/8/083001. arXiv: 0805.1333 [hep-ph].

[41] M. Jeżabek and J. Kühn. «QCD corrections to semileptonic decays of heavy quarks». In: *Nuclear Physics B* 314.1 (1989), pp. 1–6. ISSN: 0550-3213. DOI: 10.1016/0550-3213(89)90108-9.

[42] J. M. Campbell and R. K. Ellis. «$t\bar{t}W^{\pm}$ production and decay at NLO». In: *Journal of High Energy Physics* 2012.7 (2012). DOI: 10.1007/JHEP07(2012)052.

[43] L. Evans and P. Bryant. «LHC Machine». In: *Journal of Instrumentation* 3.08 (2008), S08001. DOI: 10.1088/1748-0221/3/08/S08001.

[44] C. Lefèvre. «LHC: the guide. Guide du LHC». Feb. 2009.

[45] G. Aad et al. (The ATLAS Collaboration). «The ATLAS Experiment at the CERN Large Hadron Collider». In: *Journal of Instrumentation* 3.08 (2008), S08003. DOI: 10.1088/1748-0221/3/08/S08003.

[46] K. Aamodt et al. (The ALICE Collaboration). «The ALICE experiment at the CERN LHC». In: *Journal of Instrumentation* 3.08 (2008), S08002. DOI: 10.1088/1748-0221/3/08/S08002.

[47] S. Chatrchyan et al. (The CMS Collaboration). «The CMS experiment at the CERN LHC». In: *Journal of Instrumentation* 3.08 (2008), S08004. DOI: 10.1088/1748-0221/3/08/S08004.

[48] A. Augusto Alves Jr et al. (The LHCb Collaboration). «The LHCb Detector at the LHC». In: *Journal of Instrumentation* 3.08 (2008), S08005. DOI: 10.1088/1748-0221/3/08/S08005.

[49] M. Lamont. «LHC, HL-LHC and Beyond». In: *PoS* EPS-HEP2013 (2013), p. 149.

[50] M. Rossini. «Module Prototype Qualification for the CMS Pixel Detector Upgrade». PhD thesis. ETH Zürich, 2015. DOI: 10.3929/ethz-a-010594693.

[51] T. Sakuma and T. McCauley. «Detector and Event Visualization with SketchUp at the CMS Experiment». In: *Journal of Physics: Conference Series* 513.2 (2014), p. 022032. DOI: 10.1088/1742-6596/513/2/022032.

[52] A. Dominguez et al. (The CMS Collaboration). «CMS Technical Design Report for the Pixel Detector Upgrade». CERN-LHCC-2012-016, CMS-TDR-11. Sept. 2012. URL: http://cds.cern.ch/record/1481838.

[53] The CMS Collaboration. «Particle-Flow Event Reconstruction in CMS and Performance for Jets, Taus, and MET». Physics Analysis Summary CMS PAS PFT-09-001. Geneva: CERN, Apr. 2009. URL: http://cds.cern.ch/record/1194487.

[54] The CMS Collaboration. «Commissioning of the Particle-flow Event Reconstruction with the first LHC collisions recorded in the CMS detector». Physics Analysis Summary CMS PAS PFT-10-001. 2010. URL: http://cds.cern.ch/record/1247373.

[55] R. Frühwirth. «Application of Kalman filtering to track and vertex fitting». In: *Nuclear Instruments and Methods in Physics Research Section A: Accelerators, Spectrometers, Detectors and Associated Equipment* 262.2–3 (1987), pp. 444–450. ISSN: 0168-9002. DOI: 10.1016/0168-9002(87)90887-4.

[56] S. Chatrchyan et al. (The CMS Collaboration). «Description and performance of track and primary-vertex reconstruction with the CMS tracker». In: *Journal of Instrumentation* 9.10 (2014), P10009. DOI: 10.1088/1748-0221/9/10/P10009. arXiv: 1405.6569 [physics.ins-det].

[57] S. Chatrchyan et al. (The CMS Collaboration). «Performance of CMS muon reconstruction in pp collision events at $\sqrt{s} = 7\,\text{TeV}$». In: *Journal of Instrumentation* 7.10 (2012), P10002. DOI: 10.1088/1748-0221/7/10/P10002. arXiv: 1206.4071 [physics.ins-det].

[58] W. Adam et al. «Reconstruction of electrons with the Gaussian-sum filter in the CMS tracker at the LHC». In: *Journal of Physics G: Nuclear and Particle Physics* 31.9 (2005), N9. DOI: 10.1088/0954-3899/31/9/N01.

[59] M. Cacciari, G. P. Salam and G. Soyez. «The anti-k_t jet clustering algorithm». In: *Journal of High Energy Physics* 2008.04 (2008), p. 063. DOI: 10.1088/1126-6708/2008/04/063. arXiv: 0802.1189 [hep-ph].

[60] S. Chatrchyan et al. (The CMS Collaboration). «Determination of jet energy calibration and transverse momentum resolution in CMS». In: *Journal of Instrumentation* 6.11 (2011), P11002. DOI: 10.1088/1748-0221/6/11/P11002. arXiv: 1107.4277 [physics.ins-det].

[61] M. Cacciari, G. P. Salam and G. Soyez. «The catchment area of jets». In: *Journal of High Energy Physics* 2008.04 (2008), p. 005. DOI: 10.1088/1126-6708/2008/04/005. arXiv: 0802.1188 [hep-ph].

[62] M. Cacciari and G. P. Salam. «Pileup subtraction using jet areas». In: *Physics Letters B* 659.1–2 (2008), pp. 119–126. ISSN: 0370-2693. DOI: 10.1016/j.physletb.2007.09.077.

[63] B. Abbott et al. «Determination of the absolute jet energy scale in the DØ calorimeters». In: *Nuclear Instruments and Methods in Physics Research Section A: Accelerators, Spectrometers, Detectors and Associated Equipment* 424.2–3 (1999), pp. 352–394. ISSN: 0168-9002. DOI: 10.1016/S0168-9002(98)01368-0.

[64] S. Chatrchyan et al. (The CMS Collaboration). «Identification of b-quark jets with the CMS experiment». In: *Journal of Instrumentation* 8.04 (2013), P04013. DOI: 10.1088/1748-0221/8/04/P04013. arXiv: 1211.4462 [hep-ex].

[65] V. Khachatryan et al. (The CMS Collaboration). «Performance of the CMS missing transverse momentum reconstruction in pp data at $\sqrt{s} = 8\,\text{TeV}$». In: *Journal of Instrumentation* 10.02 (2015), P02006. DOI: 10.1088/1748-0221/10/02/P02006. arXiv: 1411.0511 [physics.ins-det].

[66] J. Alwall et al. «MadGraph 5: going beyond». In: *Journal of High Energy Physics* 2011.6, 128 (2011). DOI: 10.1007/JHEP06(2011)128.

[67] T. Sjöstrand, S. Mrenna and P. Skands. «PYTHIA 6.4 physics and manual». In: *Journal of High Energy Physics* 2006.05 (2006), p. 026. DOI: 10.1088/1126-6708/2006/05/026. arXiv: hep-ph/0603175.

[68] S. Agostinelli et al. (The GEANT4 Collaboration). «GEANT4—a simulation toolkit». In: *Nuclear Instruments and Methods in Physics Research Section A: Accelerators, Spectrometers, Detectors and Associated Equipment* 506.3 (2003), pp. 250–303. ISSN: 0168-9002. DOI: 10.1016/S0168-9002(03)01368-8.

[69] S. Chatrchyan et al. (The CMS Collaboration). «Search for new physics in events with same-sign dileptons and jets in pp collisions at $\sqrt{s} = 8\,\text{TeV}$». In: *Journal of High Energy Physics* 2014.1, 163 (2014). DOI: 10.1007/JHEP01(2014)163.

[70] The CMS Collaboration. «Measuring Electron Efficiencies at CMS with Early Data». Physics Analysis Summary CMS PAS EGM-07-001. Geneva: CERN, Dec. 2008. URL: http://cds.cern.ch/record/1194482.

[71] I. MacNeill. «Measurement of top quark-antiquark pair production in association with a Z boson with a trilepton final state in pp collisions at 8 TeV center of mass energy». PhD thesis. University of California, San Diego, 2015. ISBN: 978-1-321-82714-9. URL: http://escholarship.org/uc/item/0gt3c4cr.

[72] S. Chatrchyan et al. (The CMS Collaboration). «Measurement of associated production of vector bosons and top quark-antiquark pairs in *pp* collisions at $\sqrt{s} = 7\,\text{TeV}$». In: *Phys. Rev. Lett.* 110 (17 Apr. 2013), p. 172002. DOI: 10.1103/PhysRevLett.110.172002. arXiv: 1303.3239 [hep-ex].

[73] The CMS Collaboration. «Pileup Jet Identification». Physics Analysis Summary CMS PAS JME-13-005. Geneva: CERN, 2013. URL: http://cds.cern.ch/record/1581583.

[74] P. F. Harrison and H. R. Quinn (The BaBar Collaboration). *The BABAR physics book: Physics at an asymmetric B factory*. Ed. by P. F. Harrison and H. R. Quinn. 1998.

[75] A. Hoecker et al. «TMVA: Toolkit for Multivariate Data Analysis». In: *PoS* ACAT (2007), p. 040. arXiv: physics/0703039.

[76] R. Brun and F. Rademakers. «ROOT – An object oriented data analysis framework». In: *Nuclear Instruments and Methods in Physics Research Section A: Accelerators, Spectrometers, Detectors and Associated Equipment* 389.1 (1997), pp. 81–86. ISSN: 0168-9002. DOI: 10.1016/S0168-9002(97)00048-X.

[77] F. Abe et al. (The CDF Collaboration). «Evidence for top quark production in $\overline{p}p$ collisions at $\sqrt{s} = 1.8\,\text{TeV}$». In: *Phys. Rev. D* 50 (5 Sept. 1994), pp. 2966–3026. DOI: 10.1103/PhysRevD.50.2966.

[78] S. Abachi et al. (The D0 Collaboration). «Search for High Mass Top Quark Production in $p\overline{p}$ Collisions at $\sqrt{s} = 1.8\,\text{TeV}$». In: *Phys. Rev. Lett.* 74 (13 Mar. 1995), pp. 2422–2426. DOI: 10.1103/PhysRevLett.74.2422.

[79] B. Stieger. «Same-Sign Dileptons at CMS». PhD thesis. ETH Zürich, 2013. DOI: 10.3929/ethz-a-010378877.

[80] The CMS Collaboration. «Measurement of the WW, WZ and ZZ cross sections at CMS». Physics Analysis Summary CMS PAS EWK-11-010. 2012. URL: http://cdsweb.cern.ch/record/1370067.

[81] The CMS Collaboration. «Measurement of WZ production rate». Physics Analysis Summary CMS PAS SMP-12-006. 2013. URL: http://cds.cern.ch/record/1564318.

[82] V. Khachatryan et al. «Measurement of the WZ production cross section in pp collisions at $\sqrt{s} = 7\,\text{TeV}$ and $8\,\text{TeV}$ and search for anomalous triple gauge couplings at $\sqrt{s} = 8\,\text{TeV}$». In: *The European Physical Journal C* 77.4 (Apr. 2017), p. 236. ISSN: 1434-6052. DOI: 10.1140/epjc/s10052-017-4730-z.

[83] S. van der Meer. «Calibration of the effective beam height in the ISR». Tech. rep. ISR-PO-68-31. Geneva: CERN, 1968. URL: http://cds.cern.ch/record/296752.

[84] The CMS Collaboration. «CMS Luminosity Based on Pixel Cluster Counting – Summer 2013 Update». Physics Analysis Summary CMS PAS LUM-13-001. 2013. URL: http://cds.cern.ch/record/1598864.

[85] The ATLAS and CMS Collaborations. «Combination of ATLAS and CMS results on the mass of the top quark using up to 4.9 inverse femtobarns of data». Physics Analysis Summary CMS PAS TOP-13-005. 2013. URL: http://cds.cern.ch/record/1603490.

[86] T. Peiffer (The ATLAS, CDF, CMS, and D0 Collaborations). «Signal modeling uncertainties in top quark production». Conference Report CMS CR-2013-417. Geneva: CERN, Nov. 2013. DOI: 10.3204/DESY-PROC-2014-02/8.

[87] P. Torrielli and S. Frixione. «Matching NLO QCD computations with PYTHIA using MC@NLO». In: *Journal of High Energy Physics* 2010.4, 110 (2010). DOI: 10.1007/JHEP04(2010)110.

[88] D. Bourilkov, R. C. Group and M. R. Whalley. «LHAPDF: PDF Use from the Tevatron to the LHC». In: *TeV4LHC Workshop*. Batavia IL, USA, 2006. arXiv: hep-ph/0605240.

[89] J. Pumplin et al. «Uncertainties of predictions from parton distribution functions. II. The Hessian method». In: *Phys. Rev. D* 65 (1 Dec. 2001), p. 014013. DOI: 10.1103/PhysRevD.65.014013.

[90] The ATLAS and CMS Collaborations and The LHC Higgs Combination Group. «Procedure for the LHC Higgs boson search combination in Summer 2011». CMS-NOTE-2011-005, ATL-PHYS-PUB-2011-11. Geneva: CERN, Aug. 2011. URL: http://cds.cern.ch/record/1379837.

[91] S. Chatrchyan et al. (The CMS Collaboration). «Combined results of searches for the standard model Higgs boson in pp collisions at $\sqrt{s} = 7\,\text{TeV}$». In: *Physics Letters B* 710.1 (2012), pp. 26–48. ISSN: 0370-2693. DOI: 10.1016/j.physletb.2012.02.064.

[92] G. Cowan et al. «Asymptotic formulae for likelihood-based tests of new physics». In: *The European Physical Journal C* 71.2, 1554 (2011). ISSN: 1434-6044. DOI: 10.1140/epjc/s10052-011-1554-0.

[93] M. Garzelli et al. «$t\bar{t}W^{\pm}$ + $t\bar{t}Z$ hadroproduction at NLO accuracy in QCD with Parton Shower and Hadronization effects». In: *Journal of High Energy Physics* 2012.11, 56 (2012). DOI: 10.1007/JHEP11(2012)056. arXiv: 1208.2665 [hep-ph].

[94] G. Antchev et al. (The TOTEM Collaboration). «Luminosity-Independent Measurement of the Proton-Proton Total Cross Section at $\sqrt{s} = 8\,\text{TeV}$». In: *Phys. Rev. Lett.* 111 (1 July 2013), p. 012001. DOI: 10.1103/PhysRevLett.111.012001.

[95] G. Apollinari et al. *High-Luminosity Large Hadron Collider (HL-LHC): Preliminary Design Report*. CERN Yellow Reports: Monographs. Geneva: CERN, 2015. ISBN: 978-92-9083-423-6. DOI: 10.5170/CERN-2015-005.

[96] D. Contardo et al. *Technical Proposal for the Phase-II Upgrade of the CMS Detector*. CERN-LHCC-2015-010, LHCC-P-008, CMS-TDR-15-02. Geneva, June 2015. ISBN: 978-92-9083-417-5. URL: http://cds.cern.ch/record/2020886.

[97] R. S. Sussmann. *CVD Diamond for Electronic Devices and Sensors*. John Wiley, 2009. ISBN: 978-0-470-74039-2. DOI: 10.1002/9780470740392.

[98] S. F. Kozlov et al. «Preparation and Characteristics of Natural Diamond Nuclear Radiation Detectors». In: *IEEE Transactions on Nuclear Science* 22.1 (Feb. 1975), pp. 160–170. ISSN: 0018-9499. DOI: 10.1109/TNS.1975.4327634.

[99] C. Canali et al. «Electrical properties and performances of natural diamond nuclear radiation detectors». In: *Nuclear Instruments and Methods* 160.1 (1979), pp. 73–77. ISSN: 0029-554X. DOI: 10.1016/0029-554X(79)90167-8.

[100] A. Edwards et al. «Radiation monitoring with CVD diamonds in BABAR». In: *Nuclear Instruments and Methods in Physics Research Section A: Accelerators, Spectrometers, Detectors and Associated Equipment* 552.1–2 (2005), pp. 176–182. ISSN: 0168-9002. DOI: 10.1016/j.nima.2005.06.028.

[101] P. Dong et al. «Beam Condition Monitoring With Diamonds at CDF». In: *IEEE Transactions on Nuclear Science* 55.1 (Feb. 2008), pp. 328–332. ISSN: 0018-9499. DOI: 10.1109/TNS.2007.913492.

[102] V. Cindro et al. «The ATLAS Beam Conditions Monitor». In: *Journal of Instrumentation* 3.02 (2008), P02004. DOI: 10.1088/1748-0221/3/02/P02004.

[103] M. Červ. «The ATLAS Diamond Beam Monitor». In: *Journal of Instrumentation* 9.02 (2014), p. C02026. DOI: 10.1088/1748-0221/9/02/C02026.

[104] A. Bell et al. «Fast beam conditions monitor BCM1F for the CMS experiment». In: *Nuclear Instruments and Methods in Physics Research Section A: Accelerators, Spectrometers, Detectors and Associated Equipment* 614.3 (2010), pp. 433–438. ISSN: 0168-9002. DOI: 10.1016/j.nima.2009.12.056.

[105] M. Domke et al. «Commissioning of the beam conditions monitor of the LHCb experiment at CERN». In: *2008 IEEE Nuclear Science Symposium Conference Record*. Oct. 2008, pp. 3306–3307. DOI: 10.1109/NSSMIC.2008.4775052.

[106] M. H. Nazaré et al. «Development of diamond tracking detectors for high luminosity experiments at the LHC». R&D Proposal CERN/DRDC 94-21, DRDC/P56. Geneva: CERN, 1994. URL: http://cds.cern.ch/record/293000.

[107] F. Borchelt et al. «First measurements with a diamond microstrip detector». In: *Nuclear Instruments and Methods in Physics Research Section A: Accelerators, Spectrometers, Detectors and Associated Equipment* 354.2 (1995), pp. 318–327. ISSN: 0168-9002. DOI: 10.1016/0168-9002(94)01016-1.

[108] W. Adam et al. (The RD42 Collaboration). «Review of the development of diamond radiation sensors». In: *Nuclear Instruments and Methods in Physics Research Section A: Accelerators, Spectrometers, Detectors and Associated Equipment* 434.1 (1999), pp. 131–145. ISSN: 0168-9002. DOI: 10.1016/S0168-9002(99)00447-7.

[109] M. Friedl et al. (The RD42 Collaboration). «CVD diamond detectors for ionizing radiation». In: *Nuclear Instruments and Methods in Physics Research Section A: Accelerators, Spectrometers, Detectors and Associated Equipment* 435.1–2 (1999), pp. 194–201. ISSN: 0168-9002. DOI: 10.1016/S0168-9002(99)00586-0.

[110] W. Adam et al. «Radiation hard diamond sensors for future tracking applications». In: *Nuclear Instruments and Methods in Physics Research Section A: Accelerators, Spectrometers, Detectors and Associated Equipment* 565.1 (2006). Proceedings of the International Workshop on Semiconductor Pixel Detectors for Particles and Imaging PIXEL 2005, pp. 278–283. ISSN: 0168-9002. DOI: 10.1016/j.nima.2006.05.127.

[111] M. Mikuž et al. (The RD42 Collaboration). «Diamond Sensors in HEP». In: *36th International Conference on High Energy Physics*. 2012, p. 524.

[112] A. Oh et al. «A novel detector with graphitic electrodes in CVD diamond». In: *Diamond and Related Materials* 38 (2013), pp. 9–13. ISSN: 0925-9635. DOI: 10.1016/j.diamond.2013.06.003.

[113] F. Bachmair et al. «A 3D diamond detector for particle tracking». In: *Nuclear Instruments and Methods in Physics Research Section A: Accelerators, Spectrometers, Detectors and Associated Equipment* 786 (2015), pp. 97–104. ISSN: 0168-9002. DOI: 10.1016/j.nima.2015.03.033.

[114] L. Pauling. *The Nature of Chemical Bond*. 3rd ed. Cornell University Press, 1960.

[115] M. E. Wieser et al. «Atomic weights of the elements 2011 (IUPAC Technical Report)». In: *Pure and Applied Chemistry* 85 (5 Apr. 2013), pp. 1047–1078. ISSN: 1365-3075. DOI: 10.1351/PAC-REP-13-03-02.

[116] M. Levinshtein, S. Rumyanstev and M. S. Shur. *Handbook Series on Semiconductor Parameters*. Vol. 1: Si, Ge, C (Diamond), GaAs, GaP, GaSb, InAs, InP, InSb. World Scientific, 1996. ISBN: 978-981-02-2934-4.

[117] J. E. Field. *The properties of natural and synthetic diamond*. Academic Press, 1992.

[118] S. Kasap, P. Capper and C. Koughia. *Springer Handbook of Electronic and Photonic Materials*. Springer US, 2007. DOI: 10.1007/978-0-387-29185-7.

[119] O. Madelung. *Semiconductors Data Handbook*. Springer, 2004. ISBN: 978-3-642-62332-5. DOI: 10.1007/978-3-642-18865-7.

[120] C. Tschalär and H. Bichsel. «Mean Excitation Potential of Light Compounds». In: *Phys. Rev.* 175 (2 Nov. 1968), pp. 476–478. DOI: 10.1103/PhysRev.175.476.

[121] *Stopping Powers for Electrons and Positrons*. ICRU Report 37. International Commission on Radiation Units and Measurements, 1984.

[122] S. Tanuma, C. J. Powell and D. R. Penn. «Calculations of stopping powers of 100 eV – 30 keV electrons in 31 elemental solids». In: *Journal of Applied Physics* 103.6, 063707 (2008). DOI: 10.1063/1.2891044.

[123] W. de Boer et al. «Radiation hardness of diamond and silicon sensors compared». In: *physica status solidi (a)* 204.9 (2007), pp. 3004–3010. ISSN: 1862-6319. DOI: 10.1002/pssa.200776327.

[124] J. Koike, D. M. Parkin and T. E. Mitchell. «Displacement threshold energy for type IIa diamond». In: *Applied Physics Letters* 60.12 (1992), pp. 1450–1452. DOI: 10.1063/1.107267.

[125] C. Canali et al. «Measurements of the Average Energy Per Electron-Hole Pair Generation in Silicon between 5–320 K». In: *IEEE Transactions on Nuclear Science* 19.4 (Aug. 1972), pp. 9–19. ISSN: 0018-9499. DOI: 10.1109/TNS.1972.4326778.

[126] D. Meier. «CVD Diamond Sensors for Particle Detection and Tracking». PhD thesis. Universität Heidelberg, 1999.

[127] S. Zhao. «Characterization of the Electrical Properties of Polycrystalline Diamond Films». PhD thesis. The Ohio State University, 1994. URL: http://rave.ohiolink.edu/etdc/view?acc_num=osu1394810346.

[128] R. Tappert and M. C. Tappert. *Diamonds in Nature. A Guide to Rough Diamonds*. Springer Berlin Heidelberg, 2011. ISBN: 978-3-642-12572-0. DOI: 10.1007/978-3-642-12572-0.

[129] R. P. Mildren and J. R. Rabeau. *Optical Engineering of Diamond*. Wiley-VCH, 2013. ISBN: 978-3-527-41102-3. DOI: 10.1002/9783527648603.

[130] P. W. May. «Diamond thin films: a 21st-century material». In: *Philosophical Transactions of the Royal Society of London A: Mathematical, Physical and Engineering Sciences* 358.1766 (2000), pp. 473–495. ISSN: 1364-503X. DOI: 10.1098/rsta.2000.0542.

[131] P. K. Bachmann, D. Leers and H. Lydtin. «Towards a general concept of diamond chemical vapour deposition». In: *Diamond and Related Materials* 1.1 (1991), pp. 1–12. ISSN: 0925-9635. DOI: 10.1016/0925-9635(91)90005-U.

[132] *The Element Six CVD Diamond Handbook*. Element Six Technologies US Corporation. Santa Clara CA, USA, 2015.

[133] C. Grupen and I. Buvat. *Handbook of Particle Detection and Imaging*. Springer Berlin Heidelberg, 2012. ISBN: 978-3-642-13270-4. DOI: 10.1007/978-3-642-13271-1.

[134] H. Bethe. «Zur Theorie des Durchgangs schneller Korpuskularstrahlen durch Materie». In: *Annalen der Physik* 397.3 (1930), pp. 325–400. ISSN: 1521-3889. DOI: 10.1002/andp.19303970303.

[135] H. Bethe. «Bremsformel für Elektronen relativistischer Geschwindigkeit». In: *Zeitschrift für Physik* 76.5 (1932), pp. 293–299. ISSN: 0044-3328. DOI: 10.1007/BF01342532.

[136] F. Bloch. «Zur Bremsung rasch bewegter Teilchen beim Durchgang durch Materie». In: *Annalen der Physik* 408.3 (1933), pp. 285–320. ISSN: 1521-3889. DOI: 10.1002/andp.19334080303.

[137] R. M. Sternheimer. «The Density Effect for the Ionization Loss in Various Materials». In: *Phys. Rev.* 88 (4 Nov. 1952), pp. 851–859. DOI: 10.1103/PhysRev.88.851.

[138] R. M. Sternheimer and R. F. Peierls. «General Expression for the Density Effect for the Ionization Loss of Charged Particles». In: *Phys. Rev. B* 3 (11 June 1971), pp. 3681–3692. DOI: 10.1103/PhysRevB.3.3681.

[139] L. D. Landau. «On the energy loss of fast particles by ionization». In: *J. Phys. (USSR)* 8 (1944), pp. 201–205.

[140] P. V. Vavilov. «Ionization Losses of High-Energy Heavy Particles». In: *Soviet Physics JETP* 5 (1957), pp. 749–751.

[141] J. E. Moyal. «XXX. Theory of ionization fluctuations». In: *The London, Edinburgh, and Dublin Philosophical Magazine and Journal of Science* 46.374 (1955), pp. 263–280. DOI: 10.1080/14786440308521076.

[142] S. Behrends and A. C. Melissinos. «Properties of argon-ethane/methane mixtures for use in proportional counters». In: *Nuclear Instruments and Methods in Physics Research* 188.3 (1981), pp. 521–534. ISSN: 0167-5087. DOI: 10.1016/0029-554X(81)90263-9.

[143] H. Bichsel. «Straggling in thin silicon detectors». In: *Rev. Mod. Phys.* 60 (3 July 1988), pp. 663–699. DOI: 10.1103/RevModPhys.60.663.

[144] S. M. Sze and Kwok K. Ng. *Physics of Semiconductor Devices*. 3rd ed. John Wiley & Sons, Inc., 2006. ISBN: 978-0-470-06832-8. DOI: 10.1002/0470068329.

[145] A. Oh. «Particle detection with CVD diamond». PhD thesis. Hamburg: Universität Hamburg, 1999. URL: https://beluga.sub.uni-hamburg.de/vufind/Record/302747052.

[146] G. Kramberger. «Signal development in irradiated silicon detectors». PhD thesis. Univerza v Ljubljani, 2001.

[147] W. Trischuk (The RD42 Collaboration). «Recent Advances in Diamond Detectors». In: *Proceedings of the 34th International Conference in High Energy Physics*. Philadelphia, USA, 2008. arXiv: 0810.3429 [physics.ins-det].

[148] A. Oh (The RD42 Collaboration). «Diamond particle detectors systems in high energy physics». In: *Journal of Instrumentation* 10.04 (2015), p. C04038. DOI: 10.1088/1748-0221/10/04/C04038.

[149] F. Bachmair. «CVD Diamond Sensors In Detectors For High Energy Physics». PhD thesis. ETH Zürich, 2016. DOI: 10.3929/ethz-a-010748643.

[150] G. Lindström, M. Moll and E. Fretwurst. «Radiation hardness of silicon detectors – a challenge from high-energy physics». In: *Nuclear Instruments and Methods in Physics Research Section A: Accelerators, Spectrometers, Detectors and Associated Equipment* 426.1 (1999), pp. 1–15. ISSN: 0168-9002. DOI: 10.1016/S0168-9002(98)01462-4.

[151] Paul Scherrer Institut (PSI). Villigen, Switzerland. URL: http://www.psi.ch.

[152] P. W. Lisowski and K. F. Schoenberg. «The Los Alamos Neutron Science Center». In: *Nuclear Instruments and Methods in Physics Research Section A: Accelerators, Spectrometers, Detectors and Associated Equipment* 562.2 (2006). Proceedings of the 7th International Conference on Accelerator Applications – AccApp05, pp. 910–914. ISSN: 0168-9002. DOI: 10.1016/j.nima.2006.02.178.

[153] K. Ishii et al. «CYRIC Annual Report 2010–2011». Cyclotron and Radioisotope Center, Tohoku University, Jan. 2012.

[154] M. Glaser et al. «Radiation test facilities in the new PS East Hall at CERN». In: *Fifth European Conference on Radiation and Its Effects on Components and Systems*. 1999, pp. 136–141. DOI: 10.1109/RADECS.1999.858562.

[155] W. Hajdas et al. «The Proton Irradiation Facility at the Paul Scherrer Institute». In: *Nuclear Instruments and Methods in Physics Research Section B: Beam Interactions with Materials and Atoms* 113.1–4 (1996), pp. 54–58. ISSN: 0168-583X. DOI: 10.1016/0168-583X(95)01327-X.

[156] E. W. Blackmore. «Operation of the TRIUMF (20–500 MeV) proton irradiation facility». In: *IEEE Radiation Effects Data Workshop*. 2000, pp. 1–5. DOI: 10.1109/REDW.2000.896260.

[157] E. W. Blackmore, P. E. Dodd and M. R. Shaneyfelt. «Improved capabilities for proton and neutron irradiations at TRIUMF». In: *IEEE Radiation Effects Data Workshop*. July 2003, pp. 149–155. DOI: 10.1109/REDW.2003.1281368.

[158] ISIS pulsed neutron and muon source. Rutherford Appleton Laboratory. URL: http://www.isis.stfc.ac.uk.

[159] L. Snoj, G. Žerovnik and A. Trkov. «Computational analysis of irradiation facilities at the JSI TRIGA reactor». In: *Applied Radiation and Isotopes* 70.3 (2011), pp. 483–488. ISSN: 0969-8043. DOI: 10.1016/j.apradiso.2011.11.042.

[160] Element Six Technologies US Corporation. Santa Clara CA, USA. URL: http://e6cvd.com.

[161] *Short introduction to the use of the H6 beam*. Version 3.0. CERN. Geneva, May 2000.

[162] C. Colledani et al. «A submicron precision silicon telescope for beam test purposes». In: *Nuclear Instruments and Methods in Physics Research Section A: Accelerators, Spectrometers, Detectors and Associated Equipment* 372.3 (1996), pp. 379–384. ISSN: 0168-9002. DOI: 10.1016/0168-9002(95)01414-4.

[163] H. Spieler. *Semiconductor Detector Systems*. Oxford University Press, 2005. ISBN: 978-0-19-852784-8. DOI: 10.1093/acprof:oso/9780198527848.001.0001.

[164] *The VA2 Specifications*. Integrated Detector & Electronics AS. Høvik, Norway, 1999.

[165] N. Bingefors and M. Burns (DELPHI Microvertex Group). «SIROCCO IV: front end readout processor for DELPHI microvertex». In: *International Conference on the Impact of Digital Microelectronics and Microprocessors on Particle Physics*. Dec. 1988. URL: http://cds.cern.ch/record/194195.

[166] H. Kagan (The RD42 Collaboration). *Photograph of the diamond sensor PW205B*. Sept. 2015.

[167] W. Adam et al. (The RD42 Collaboration). «Pulse height distribution and radiation tolerance of CVD diamond detectors». In: *Nuclear Instruments and Methods in Physics Research Section A: Accelerators, Spectrometers, Detectors and Associated Equipment* 447.1–2 (2000), pp. 244–250. ISSN: 0168-9002. DOI: 10.1016/S0168-9002(00)00195-9.

[168] J. D. Jackson. *Classical Electrodynamics*. 3rd ed. Wiley, 1999. ISBN: 978-0-471-30932-1.

[169] U. Kötz et al. «Silicon strip detectors with capacitive charge division». In: *Nuclear Instruments and Methods in Physics Research Section A: Accelerators, Spectrometers, Detectors and Associated Equipment* 235.3 (1985), pp. 481–487. ISSN: 0168-9002. DOI: 10.1016/0168-9002(85)90097-X.

[170] P. Palni. «Evidence for the Heavy Baryon Resonance State Λ_b^{*0} Observed with the CDF II Detector, and Studies of New Particle Tracking Technologies Using the LANSCE Proton Beam». PhD thesis. University of New Mexico, 2014. URL: http://hdl.handle.net/1928/24334.

[171] M. Mikuž et al. «Study of polycrystalline and single crystal diamond detectors irradiated with pions and neutrons up to $3 \times 10^{15}/\mathrm{cm}^2$». In: *IEEE Nuclear Science Symposium Conference Record*. Vol. 3. Oct. 2007, pp. 2169–2172. DOI: 10.1109/NSSMIC.2007.4436581.

[172] «Neutron Fluence Measurements». Technical reports series 107. International Atomic Energy Agency (IAEA), 1970.

[173] E. S. Krištof. «Characterization of neutron flux in the exposure channel F19 of the TRIGA Mark II reactor in Ljubljana». In: *Nuclear Energy in Central Europe '98*. 1998, pp. 43–48.

[174] A. Abdel-Aziz. «Diamond Strip Detectors and Common Mode Correction». Student project thesis. University of Toronto, 2011.

[175] B. Rossi. *High-Energy Particles*. Prentice-Hall, 1952.

[176] R. Turchetta. «Spatial resolution of silicon microstrip detectors». In: *Nuclear Instruments and Methods in Physics Research Section A: Accelerators, Spectrometers, Detectors and Associated Equipment* 335.1 (1993), pp. 44–58. ISSN: 0168-9002. DOI: 10.1016/0168-9002(93)90255-G.

[177] E. Belau et al. «Charge collection in silicon strip detectors». In: *Nuclear Instruments and Methods in Physics Research* 214.2 (1983), pp. 253–260. ISSN: 0167-5087. DOI: 10.1016/0167-5087(83)90591-4.

[178] M. Huhtinen. «Delta Ray Effects in Silicon Strip Detectors». In: Report Series, Research Institute for High Energy Physics, University of Helsinki HU-SEFT-1992-06 (1992). ISSN: 0788-3587.

[179] M. Boronat et al. «Physical Limitations to the Spatial Resolution of Solid-State Detectors». In: *IEEE Transactions on Nuclear Science* 62.1 (Feb. 2015), pp. 381–386. ISSN: 0018-9499. DOI: 10.1109/TNS.2014.2376941.

[180] H. Kagan (The RD42 Collaboration). *CCD Measurement at Ohio State University*. Sept. 2007.

[181] H. Kagan (The RD42 Collaboration). *CCD Measurement at Ohio State University*. Mar. 2008.

[182] H. Kagan (The RD42 Collaboration). *CCD Measurement at Ohio State University*. Oct. 2010.

[183] J.-W. Tsung. «Diamond and Silicon Pixel Detectors in High Radiation Environments». PhD thesis. Universität Bonn, 2012.

[184] J.-W. Tsung et al. «Signal and noise of diamond pixel detectors at high radiation fluences». In: *Journal of Instrumentation* 7.09 (2012), P09009. DOI: 10.1088/1748-0221/7/09/P09009.

[185] D. Meier et al. (The RD42 Collaboration). «Proton irradiation of CVD diamond detectors for high-luminosity experiments at the LHC». In: *Nuclear Instruments and Methods in Physics Research Section A: Accelerators, Spectrometers, Detectors and Associated Equipment* 426.1 (1999), pp. 173–180. ISSN: 0168-9002. DOI: 10.1016/S0168-9002(98)01488-0.

[186] D. Asner et al. (The RD42 Collaboration). «Diamond pixel modules». In: *Nuclear Instruments and Methods in Physics Research Section A: Accelerators, Spectrometers, Detectors and Associated Equipment* 636.1, Supplement (2011). 7th International «Hiroshima» Symposium on the Development and Application of Semiconductor Tracking Detectors, S125–S129. ISSN: 0168-9002. DOI: 10.1016/j.nima.2010.04.096.

[187] S. Seidel. «Recent results on diamond radiation tolerance». In: vol. 9. 01. 2014, p. C01013. DOI: 10.1088/1748-0221/9/01/C01013.